The impact of confinement on deformable porous structures in flow

Simon M. Finney
Kellogg College
University of Oxford

A thesis submitted for the degree of
Doctor of Philosophy in Mathematics

Long vacation 2024

Acknowledgements

To my supervisors, Sarah Waters, Andreas Münch, and Matthew Hennessy, thank you for your mentorship and your invaluable insights into the problems presented in this thesis. It has been a great pleasure to be shaped by such brilliant minds, whose remarkable intellectual rigor is matched only by their thoughtful and supportive approach to supervision.

I have greatly enjoyed collaborating with researchers at the Universities of Birmingham and Edinburgh. In particular, Alicia El Haj, Melissa Vieira, Maria Chiara Arno, Amaziah Alipio, Stuart Forbes, Victoria Gadd, Wei-Yu Lu, Candice Ashmore-Harris. Thank you all for the engaging conversations and for the opportunity to bring an alternative perspective to challenging problems you face. Additional thanks to Evangelia Antonopoulou for her camaraderie, and to Ricardo Ruiz Baier for his guidance with FEniCS and multiphenics.

I thank my friends and colleagues, Aayushi Gupta, Ferdinand Valentin Mowinckel, Tilly Woods, Eddy Yeo, Nathalie Lövgren, Ben Walker, Joe Irving, Rory Cookman, Oscar Scrase, Patrick Sandbach, to name a few, for the welcome distractions and the constant sound of laughter.

To my family, thank you for nurturing my curiosity, and for the unending support and encouragement you have provided me. Finally, to my best friend Izzo, your kindness is unrivaled and your advice and support are two of my most valued things.

Statement of Originality

In Chapter 2, we consider an elastic particle translating axially along the centre-line of a rigid cylindrical tube. Two models are presented: an asymptotic solution in the small deformation limit which utilises a similar approach to Mietke et al. [1], and a non-linear numerical model which uses arbitrary Lagrangian-Eulerian approach, similar to Villone et al. [2]. The work presented in Chapter 2 extends these analyses by considering the first-order fluid problem, providing a comprehensive assessment of the range of validity of the asymptotic solutions, and by including an applied axial body force applied to the particle. The models and analyses presented in Chapter 2 have been published in the *IMA Journal of Applied Mathematics*.

The work in Chapters 3 and 4 contains, to our knowledge, the first mathematical consideration of finite thickness hydrogel-coated cells.

In Chapter 3 we model a hydrogel-coated cell in any unbounded Stokes flow, forming an extension to [3] who instead considered a spherical elastic particle in any unbounded Stokes flow. In the case of zero cell size, the framework reduces to model a spherical poroelastic particle in any unbounded Stokes flow, which extends the work of Young et al. [4] who considered a spherical poroelastic particle in the subset of surrounding flows which depend linearly on the spatial coordinates. A full analysis of this special case has been submitted to the *APS Physical Review Fluids* journal and is currently awaiting a reviewer response.

In Chapter 4 we model a hydrogel-coated cell translating axially along the centre-line of a cylindrical tube and driven by Poiseuille flow. Similarly to in Chapter 2, we again present both an asymptotic model in the small deformation limit and a non-linear numerical model, both of which form novel applications of the respective solution methods.

Abstract

This thesis explores the deformation and transport of deformable porous structures in flow and under confinement, the insights of which can be exploited in the development of next-generation cell therapies involving individually encapsulated cells. The study is divided into three main bio-inspired, fundamental fluid-structure interaction problems: an elastic particle in tube flow and subject to an axial body force, a hydrogel coated cell in an arbitrary unbounded flow, and the same coated cell in tube flow.

The first problem models an elastic particle translating axially along the centre-line of a rigid cylindrical tube in equilibrium with a background Newtonian viscous fluid. The flow is pressure-driven and an axial body force is applied to the particle. Semi-analytical solutions are obtained in the asymptotic limit of a small ratio of the viscous fluid forces to the elastic stiffness, highlighting how background flow, axial body force, and tube wall impact the particle's velocity, deformation, and shear stress. Additionally, a non-linear arbitrary Lagrangian-Eulerian finite element implementation is used, in conjunction with various existing results from the literature, to validate the semi-analytical solutions and interrogate their range of validity.

The second problem develops a framework to study a hydrogel-coated cell in an arbitrary, unbounded, three-dimensional Stokes flow. The coating is assumed to be poroelastic and stiff such that the equations of linear poroelasticity apply and interfacial conditions are linearised onto the undeformed surfaces. In steady state, the fluid inside the cell is stationary, and the cell pressure preserves the undeformed cell volume. Special attention is paid to the limiting case of zero cell size, which is shown to instead model an initially spherical poroelastic particle. To demonstrate the method, closed-form solutions for the translational velocity, rotation, and surface deformation are presented and analysed for a background

shear flow and Poiseuille flow. These solutions are shown to exactly reduce to solutions in the literature for the limiting case of an impermeable elastic particle with no-slip boundary conditions.

Finally, the tube flow analysis of the first problem is extended to model the coated cell to assess the effect of the tube confinement on the cell's mobility and deformation. Similarly, semi-analytical solutions in the small deformation limit are presented, along with non-linear finite element solutions. This comprehensive investigation provides significant insights into the mechanical cues experienced by a coated cell under tube confinement.

Contents

Chapter 1

Introduction

Cirrhosis and other liver diseases rank among the leading causes of death in the UK for those aged between 35 and 65 years [5, 6]. At present, the only curative treatment for end-stage liver disease is organ transplant, which is unsustainable with rising demand. Cell therapies, where donor cells injected directly into the blood stream transit through the vasculature and engraft (attach) into the damaged tissue to promote regeneration, hold promise as an alternative treatment to transplantation. Coating the injected cells with a hydrogel (common examples include alginate and hyaluronic acid) can enhance their effectiveness as the coating protects the injected cells from an immune response, while increasing the proportion of cells which engraft into the target tissue [7–9]. However, conventional coating methods can result in the formation of large cell aggregates in the host's blood vessels which may be life threatening. Recent advances in cell engineering allow for the binding of polymers directly to cell surfaces, allowing for individual cell encapsulation [10, 11]. This has important implications for the development of cell therapies as the encapsulations are homogeneous, have controllable thickness, and preserve the cell's morphology. Encapsulating a cell also impacts the mechanical cues it experiences from the surrounding environment. Upon exposure to mechanical stimuli, for example fluid pressure or shear stress, the intracellular cytoskeleton transfers stress to the cell nuclei, reproducibly upregulating expression of certain genes [12–15]. Importantly, a change in expression may directly correspond to a change in the cell's properties, with a key example being the expression of integrins (a family of proteins) on the cell surface which can improve cell adhesion [16]. The cell surface deformation is also important in this context. Stretching of the cell membrane can open ion channels, activating signalling cascades that again result in altered gene expression [17]. By adjusting the properties of the hydrogel coating, such as stiffness, permeability, slip, and thickness, the stresses and

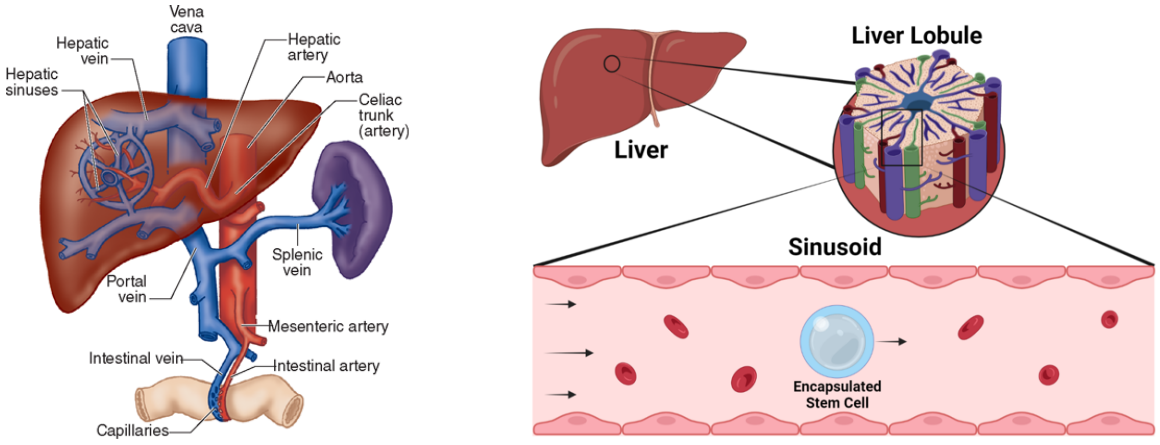

(a) (b)

Figure 1.1: (a) The liver and spleen anatomy. Taken from Butterworth et al. [20]. (b) Biological schematic of a hydrogel-coated cell travelling through a liver sinusoid.

deformation imposed on the cell are modulated. It is therefore important to understand how a hydrogel coating modulates the mechanical cues imposed on the cell to interpret observed changes in gene expression.

Mathematical modelling forms a natural route for predicting the role of coatings in cell therapies and has great potential for impact in biomedicine. Typically, the development of a novel therapy is divided into three stages: *in-vitro* experiments performed outside of a living body, *in-vivo* experiments which involve a living animal (typically rodents), and clinical trials with human participants. Waters et al. [18] outlined the common challenges in translating regenerative therapies to the patient, detailing the potential benefits of computational or *in-silico* modelling. One major benefit of *in-silico* models is that they can provide mechanistic insight into the many interactions which underpin complex biological phenomena. By comparison to biological experiments, *in-silico* models provide a rapid and low-cost tool to efficiently explore the parameter space and optimise the design of *in-vitro* or *in-vivo* experiments. Additionally, new components, for example the inclusion of an immune component, may be added to existing *in-silico* models to 'bridge the gap' between *in-vitro* and *in-vivo* data. When integrated into the research pipeline, *in-silico* models have the potential to reduce the number of *in-vitro* and *in-vivo* experiments required to reach clinical trials. Relevant to this thesis, in Ashmore-Harris et al. [19] we outline how mechanistic mathematical modelling can be utilised to accelerate the development of liver cell therapies.

Figure 1.1 summarises the hydrogel-coated cell therapy within the liver, which is

Vessel	d_0 (μm)	V_{avg} (μms^{-1})	Re
Portal Vein	10^3	10^5	100
Large Vessel	400	400	0.16
Small Vessel	70	40	0.003

Table 1.1: Average typical sizes and velocities with a rough estimate for the Reynolds number for different vessels in a mouse liver. Data for the portal vein from [22] and data for the large and small vessels from [23].

comprised of hexagonal liver lobules containing small vessels called sinusoids. The vessel structure within a liver is complex. Deoxygenated blood enters the liver through the portal vein, from which the vessel structure branches many hundreds of times, with vessels decreasing in size until the blood reaches the liver sinusoids. Then, the blood flows into the hepatic vein where it leaves to liver. In Table 1.1 we present the range of vessel sizes and flow rates for a typical mouse liver. We also present a rough estimation for the Reynolds number in each of these vessel types, $\text{Re} = \rho V_{\text{avg}} d_0/\mu_f$, where d_0 and V_{avg} are the typical vessel diameter and average fluid velocity, and ρ and μ_f are the fluid density and viscosity, respectively. For the estimates of the Reynolds number in Table 1.1 we use the density and viscosity of water. Since blood, which is a complex fluid comprised of red blood cells, immune cells, and platelets suspended in plasma, is shear thinning on the macro-scale [21], these estimates provide an upper bound for the Reynolds number for blood.

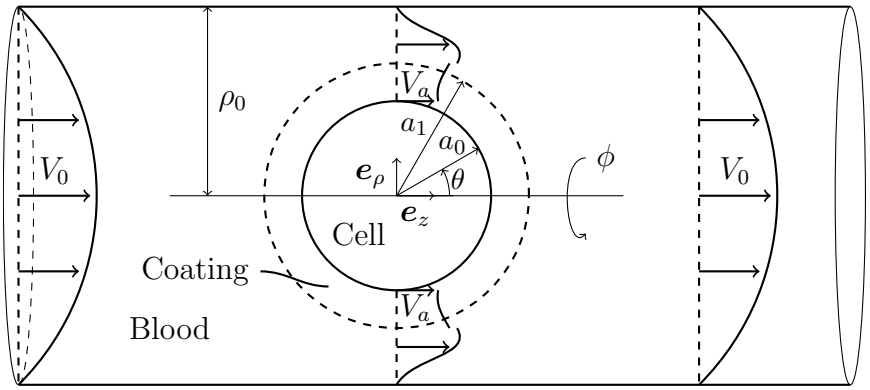

Figure 1.2: Mathematical schematic of a hydrogel-coated cell translating along the centre-line of a cylindrical tube with background Poiseuille flow far upstream and downstream ($V_0 = 2V_{\text{avg}}$), presented in the lab frame. The cell velocity in the lab frame is $V_a \boldsymbol{e}_z$.

The goal of this thesis is to develop a mechanistic mathematical model relevant

to an individual hydrogel-coated cell translating through a smaller vessel in the liver. To achieve this, we set up the canonical fluid-structure interaction (FSI) problem presented in Figure 1.2 which contains all the components of the biological problem: a cell region, a hydrogel coating region, a surrounding blood flow region, as well as the vessel confinement. This model aims to provide mechanistic insights which can be exploited in the development of next-generation cell therapies via a quantification of the mechanical cues imposed on the cell.

Throughout this thesis, we model the blood as an incompressible Newtonian fluid. This is motivated by the small shear rates for smaller vessels in Table 1.1 and a small size ratio of the native cell populations and the coated cells. For reference, in mice, a red blood cell has typical diameter $5.8 - 7.3$ μm [24] and a hepatocyte has a diameter of 50 μm [25]. The coating thickness inevitably depends on the coating process, and may be varied experimentally [11]. We assume the coatings are of finite thickness, and consider a wide range of different thicknesses. Motivated by the small Reynolds number for smaller vessels in Table 1.1 we also neglect inertial effects such that external fluid is described by the well-known Stokes equations. *In-vitro* studies typically use a phosphate-buffered saline (PBS) solution which has similar mechanical properties to water. Mimicking the geometry of a smaller vessel in the liver, we again expect a small Reynolds number, further validating the use of the Stokes equations in this context. For both *in-vitro* and *in-vivo* applications we assume the injected cells are dilute in the suspending fluid, and consequently consider only a single cell, omitting any interactions between the injected cells themselves. Since we focus on capturing the hydrodynamic (not chemical) interactions, we model the hydrogel coating as a homogeneous poroelastic material, and the cell as a sack of incompressible viscous fluid enclosed by an extensible membrane (fluid capsule). Cell membranes are composed of lipids and so are hydrophobic. However, molecules (including water) may diffuse across the cell membrane via the opening of ion channels [26]. For simplicity, we omit the passive diffusion of water molecules across the cell membrane due to osmosis and assume the cell membrane is impermeable to the surrounding fluid. Additionally, we assume the cell is soft in comparison with the coating and adopt a 'no-membrane' model such that we neglect any elastic response of the membrane. This assumption will be discussed in detail in Section 3.2.3.

The vessel wall is assumed to be rigid and impermeable. In reality, vessel walls are deformable, and are comprised of endothelial cells between which other cells may pass in a process called extravasation. *In-vitro* experiments often use plastic tubing when flowing cells which may be considered rigid. Whilst there have been efforts to

mathematically capture the geometric complexity of the liver, most notably Ho et al. [27] who developed a pipeline to generate a patient-specific, digitised vessel structure which may be used to predict the effect of surgery, in this thesis we assume the tube radius is constant. We also assume that the clearance between the cell and cylinder is finite, and do not model coated cells which contact the vessel boundary, or tightly fitting coated cells which squeeze through the vessel.

In building up the comprehensive system and understanding of this complex FSI problem, it is natural to consider various different sub-problems. For instance, in the limit in that the cell region shrinks to zero, we obtain the problem of a poroelastic particle in a confined Stokes flow. In the limit that the permeability goes to zero, this simplifies further to an elastic particle, and in the limit that the stiffness of the poroelastic particle tends to infinity, we instead obtain a rigid porous particle. The understanding gained from the interrogation of these various sub-problems builds our intuition and mechanistic insight into the comprehensive system. Due to the fundamental nature of these sub-problems (i.e., deformable porous structures coupled to viscous flow in confinement) we find additional motivation in a wealth of scientific applications. For example, the study of micro-gel beads [28], the characterisation of material properties of deformable particles including cells (flow cytometry) [29, 30], and cell and tissue engineering [31–34]. Further motivation comes from the use of hydrogel particles for drug delivery systems [35–37]. By injecting a solution containing drug-carrying hydrogel particles into the body, drug payloads can be delivered to specific sites in a minimally invasive procedure. However, the pressure-driven flow during injection can generate large shear stresses that damage the hydrogels and cause the premature release of drug molecules. Modern experimental techniques also motivate the study of biological cells exposed to a body force, which is included in Chapter 2. Yeo et al. [38] investigated how magnetically tagged cells are transported when exposed to a magnetic field and Zhang et al. [39] developed a method for dragging an individual cell in hydrodynamic flows using optical tweezers, which does not require direct contact with the cell itself.

We now provide an overview of the relevant mathematical literature surrounding each of the different components in the comprehensive system. In Sections 1.1.1 and 1.1.2 we review existing literature of particles in flow and under confinement. Next, we review existing literature of deformable fluid capsules in Section 1.1.3, which are often used as model for biological cells. We then consider the literature surrounding poroelastic shells and layers which are relevant to the coating, and the vessel wall, respectively. Finally, the specific problems considered in this thesis are outlined in

Section 1.2. Where necessary, we reserve more specific mathematical introductory material to each content chapter.

1.1 Relevant mathematical literature

1.1.1 Rigid particles in flow

1.1.1.1 Non-porous particles

Much of the mathematical literature surrounding the motion of particles in low Reynolds number flows is concerned with rigid impermeable bodies. Brenner and Happel [40] developed the method of reflections (MoR), a semi-analytical, meshless method to predict the flow surrounding an arbitrarily positioned small rigid particle under tube confinement. The work of Brenner and Happel [40] has been extended numerous times, including by Greenstein and Happel [41], who considered particle rotation and Leichtberg et al. [42], who considered up to nine rigid particles positioned along the tube centre-line, investigating the impacts of particle size and separation. Modern computing allows solutions obtained using the MoR to be far more accurate than their earlier counterparts. For example, more recently Bhattacharya et al. [43] and Yao et al. [44] used the MoR to calculate the velocity field around one and two rigid spheres arbitrarily positioned in a cylindrical tube, respectively, deriving relationships between the rigid particle velocities and the Stokes drag. These results form an extension to Faxen's law which describes the relationship between particle velocity and Stokes drag for a single rigid sphere in an unbounded Stokes flow.

Other analytical/semi-analytical methods have also been considered for a rigid particle in flow and under tube confinement. Bungay and Brenner [45] considered a tightly-fitting rigid spherical particle in a cylindrical tube, using a lubrication approximation in the thin gap to calculate the force and torque imposed on the sphere, as well as the change in pressure drop across the tube length. Yeh and Keh [46] used a boundary collocation technique to instead consider a rigid prolate particle, investigating the impact of the particle's size and aspect ratio on its drag.

1.1.1.2 Porous particles

Much work has been done to extend these analyses to consider the motion of a neutrally buoyant, rigid, porous particle suspended in a Stokes flow. Whittaker [47] used volume averaging to show that the macroscopic flow through a rigid porous medium with a small pore size is governed by Darcy's law, in which the fluid flow

is given by the product of the permeability and the pressure gradient. If the fluid volume fraction is large ($> 95\%$) an additional viscous term is added to Darcy's law, leading to Brinkman flow [48]. In this work we consider only Darcy's law to describe flow through porous structures, though we note that extension to Brinkman flow is possible [49].

Yang and Hong [50] obtained analytic expressions for the flow through a spherical Brinkman particle exposed to linear unbounded flows such as axisymmetric straining flow and linear shear flow. This work was later extended to consider the impact of an external planar interface on the particle's motion [51, 52]. More recently, Prakash and Sekhar [53] investigated the translational and rotational mobility of a spherical Brinkman annulus with a rigid impermeable core, confined within a spherical cavity filled with a viscous fluid, finding a reduction in mobility the closer the annulus was to the external boundary. Other studies have explored porous spheres in tubes of circular cross section, again focusing on how the confined geometry impacts mobility; Saad and Faltas [54] used a boundary collocation technique to study a single Brinkman sphere subject to a stress jump condition and Yao et al. [55] used the MoR to consider the motion of two Brinkman spheres positioned along the tube centre-line.

A large body of work has been concerned with the derivation of boundary conditions between a Stokes flow and a porous domain, rigid or deformable. This has lead to various proposed slip conditions on the interface between the two domains [56–61]. Most recently, Xu et al. [61] derived three sets of interfacial conditions between a Stokes flow and a deformable porous body, using a thermodynamic argument based on energy dissipation. Several simple driving flows were used to compare each set to those previously derived by Minale [60]. In this work we use boundary conditions similar to those employed by Ruiz-Baier et al. [62] and Badia et al. [63], and are summarized as the continuity of normal fluid flux, conservation of momentum, conservation of fluid normal stress, and the well-known Beavers & Joseph slip condition [56]. To be clear, it is not our aim to advocate for any one set of boundary conditions over another, and we stress that our framework is not limited to any particular choice.

1.1.2 Elastic and poroelastic particles in flow

Typically, poroelastic structures are modelled using a bi-phasic approach, where an elastic solid skeleton is coupled to an interstitial viscous fluid through conservation of mass and momentum [64, 65]. The theoretical study of poroelastic particles in a surrounding viscous flow has received less attention than their rigid counterpart. This is likely due to three main challenges:

(i) There exists a two-way poromechanical coupling within the particle, where internal flow drives solid deformation and vice-versa.

(ii) The surrounding flow is coupled to the particle shape through a fluid-structure interaction.

(iii) The internal flow in (i), and the surrounding flow in (ii), are themselves coupled through a non-trivial choice of conditions at the interface between the particle and surrounding viscous fluid.

Consequently, studies of poroelastic particles in a viscous flow are predominantly numerical, often utilising techniques such as the immersed boundary method [66] and the arbitrary Lagrangian-Eulerian (ALE) method to accurately capture the dynamics of the fluid-structure interaction [32, 34, 67, 68]. We note that studies involving an impermeable, elastic particle only require the consideration of (ii).

Small-deformation asymptotic reductions of fluid-structure (elastic or poroelastic structure) interaction problems are not uncommon, and greatly simplify the couplings between the fluid and solid mechanics [3, 4, 28, 69]. Specifically, by assuming the ratio of typical viscous stress in the exterior flow to the solid skeleton's elastic stiffness is small, the solid deformation of the particle will be small. Hence, the particle can be treated as linearly poroelastic and the interfacial conditions can be imposed on the undeformed geometry. Under this assumption, the governing equations describing the fluid flow, particle velocity, and particle rotation decouple from the particle deformation.

We first review the literature surrounding the simpler case of an elastic spherical particle coupled to a Stokes flow. Murata [70] modelled the sedimentation of an elastic sphere in an unbounded, stationary fluid in the limit of a small ratio of viscous forces to solid stiffness, showing the particle undergoes no shape change to leading order. Nasouri et al. [69] extended this framework to study the sedimentation of a two-sphere swimmer consisting of one rigid particle and one neo-Hookean particle in an unbounded, stationary fluid. Murata [3] modelled an elastic particle in a general unbounded flow, with a key example being Poiseuille flow. Murata's analytical framework determines the fluid flow by prescribing the background flow with no particle (this is given by the far-field flow) and adding a local correction to satisfy the interfacial conditions on the particle surface. Once calculated, the surface tractions are computed and used to calculate the resulting particle deformation. Importantly, the method does not fully consider the effect of a tube wall on the deformation. Mietke

et al. [1] utilised the MoR to properly account for the tube wall in the leading-order fluid problem, obtaining semi-analytical results for the small deformation of a particle in equilibrium which translates on the centre-line of a rigid cylindrical tube. By imaging the steady deformation of a single cell travelling through a microfluidic square channel, this model was then used to predict the Young's modulus of the cell. Later, Mokbel et al. [71] used a numerical method to model the large deformation of the elastic particle, predicting the Young's modulus of the cell using both a linearly elastic and neo-Hookean constitutive model. Villone and Maffettone [28] used an arbitrary Lagrangian-Eulerian (ALE) finite element method (FEM) to characterise the mobility and deformation of an incompressible, neo-Hookean particle, modelled as a drop of an upper-convected Maxwell viscoelastic fluid with infinite relaxation time, in different surrounding Newtonian and non-Newtonian flows. Within a cylindrical tube, Villone et al. [2] numerically calculated the lateral migration velocity of the particle for varying relative sizes and initial positions. Notably, these studies all omit the presence of a body force acting on the particle. Noichl and Schönecker [72] performed experiments investigating how the deformability of an elastic particle affects its sedimentation velocity in a channel of square cross section, finding poor agreement with existing analytical results [70]. This further motivates the study of how geometric confinement impacts deformable particles in viscous flow.

Returning now to poroelastic particles, where there is much less work, Young et al. [4] similarly used the small deformation asymptotic reduction to analytically calculate the equilibrium shape of a weakly deformable poroelastic particle under a linear flow, where the fluid velocity depends linearly on the spatial coordinates. This model was later utilised by Xu et al. [61] to investigate the impact of different interfacial conditions, concluding that a combination of complex flows and geometries is required to properly interrogate the effects of a particular choice.

1.1.3 Deformable fluid capsules

Biological cells have been modelled using a variety of different approaches. White blood cells may be simply modelled as a solid elastic bulk and bone cells are often modelled as viscoelastic fluids [73–75]. Softer cells such as red blood cells[1], and vesicles are typically modelled as an incompressible viscous fluid surrounded by an elastic

[1]We note that there exists a wealth of literature surrounding the mathematical description of red blood cells, including a spring membrane model and a viscoelastic membrane model (see Ju et al. [76] and references within).

membrane, or equivalently a fluid capsule [77, 78]. Mathematical studies of individual fluid capsules have been predominantly numerical, with particular interest paid to characterising the dynamics of the cells (hydrodynamic lift force, tank treading, tumbling) [78–80]. Analytical studies of spherical or elliptical capsules coupled to a viscous flow often involve unbounded simple shear flow [81, 82]. Several studies have considered the impact of confinement by modelling capsules transiting through a pipe with either cylindrical or square cross section, with the focus on understanding how this confinement impacts the capsule's shape and mobility [73, 83–87]. For example, Hu et al. [84] obtained three-dimensional numerical solutions assuming a neo-Hookean membrane and Barakat et al. [73] considered an inextensible membrane, obtaining both numerical and lubrication solutions in the limit of high confinement.

Understanding the impact of confinement on fluid capsules is of particular interest to the development of microfluidic systems which exploit the complex hydrodynamic interaction between the capsule and surrounding fluid to reliably sort cells based on their deformability [88]. Various experimental configurations have been proposed. For example, Guo et al. [89] sorted red blood cells through generations of tapered constrictions driven by oscillatory flow and Häner et al. [90] sorted individual capsules by flowing them through a partially obscured flow channel, showing that the path selection of the capsule depends on its stiffness. Additionally, several studies, experimental and computational, have used a branching flow channel to sort individual capsules, investigating how the capsule path selection depends on its deformation, initial position in the feeding channel, the surrounding flow inertia and the branch geometry [77, 91–93].

1.1.4 Poroelastic shells and coatings

The study of thin poroelastic bodies is motivated by a wide range of applications including deformable filters and biological membranes [94, 95]. Taber and Puleo [96] developed theories for the deformation of thin poroelastic plates and shells saturated by a viscous fluid based on the consolidation theory of Biot [64], with a key example being a poroelastic spherical shell. Later, Mikelić and Tambača [97] and Mikelić and Tambača [98] derived generalised models for poroelastic flexural shells, for example, cylindrical shells, conic shells, or plates, and poroelastic elliptical shells, respectively.

Motivated by the endothelial glycocalyx layer (EGL), a thin (~ 1 μm), gel-like layer that coats the inside of blood vessels [99], there are several theoretical studies that consider the impacts of a thin deformable porous coating on the inside of a rigid cylindrical tube. For instance, Secomb et al. [100] used lubrication theory to

model the motion of a red blood cell in a capillary with an endothelial surface layer, calculating the effect of the background flow velocity on the resultant cell shape and velocity. Similarly, Damiano et al. [101] used lubrication theory to model a rigid pellet translating through a cylindrical tube which is lined with a deformable porous layer, showing a reduction in the pressure gradient in the lubrication region when the porous layer is included. Relevant to this work, Wang and Parker [102] considered a tightly-fitting rigid particle translating through a rigid cylindrical tube, with both the particle and tube covered by a thin poroelastic layer. Using lubrication theory in the thin gap between the particle and the tube wall, they showed that in the limit of a thin layer, the effects of the porous layer reduce to a simple slip boundary condition. Following an extensive literature search, Wang and Parker [102] was the only mathematical work we found to explicitly model a deformable porous layer surrounding a particle in tube flow. The recent development of hydrogel-coated cells motivates the consideration of finite thickness deformable porous layers surrounding deformable particles/capsules.

1.2 Thesis outline

In Chapter 2, we model an elastic particle translating along the axis of the cylindrical tube which is filled with a Newtonian viscous fluid. The particle is subject to a background pressure-driven flow and an axial body force. This body force could reflect gravity for a sedimenting particle under confinement, or a magnetic force from tagging techniques in cell therapies [38]. We approach the problem using two different solution methods: In the first we perform an asymptotic reduction of the problem in the small deformation limit, utilising the MoR to calculate the leading-order and first-order fluid problems, and in the second we develop an ALE FEM framework to solve the full non-linear problem.

In Chapter 3 we consider a hydrogel-coated cell in any unbounded Stokes flow. Expanding on the work of Murata [3], we develop a framework to obtain closed-form solutions for the coated cell's velocity, rotation, and deformation in terms of the cell size, and the coating's permeability, slip, and Poisson's ratio in the small deformation limit. We present solutions for a hydrogel-coated cell under a background shear and Poiseuille flow, providing a comprehensive assessment of the impacts of the material parameters in both cases. Special attention is paid to the case of zero cell size, which is shown to instead model a poroelastic particle in any unbounded Stokes flow.

In Chapter 4, we consider a hydrogel-coated cell in tube flow. The coated cell is modelled identically to in Chapter 3 and translates axially along the centre-line of the

rigid cylindrical tube, subject to a background Poiseuille flow. Similar to Chapter 2, we utilise the MoR to solve the leading-order flow through the coating in the small deformation limit, using the associated tractions and Darcy pressure to analytically calculate the leading-order coating deformation. Additionally, we develop an ALE FEM framework to solve the full non-linear problem.

Finally, in Chapter 5 we summarise our work and discuss the key results obtained. We conclude by discussing potential extensions to the models.

Chapter 2

The impact of confinement on the deformation of an elastic particle under axisymmetric tube flow

2.1 Chapter summary

We model an elastic particle translating along the axis of the cylindrical tube which is filled with a Newtonian viscous fluid. The particle is subject to a background pressure-driven flow and an axial body force. We present the full non-linear problem and perform an asymptotic reduction in the limit of a small ratio of typical viscous forces to elastic stiffness, as described in Section 1.1.2. The leading-order fluid problem is shown to be pressure-driven Stokes flow past a rigid sphere which is subject to the axial body force, and is solved using the method of reflections, similar to [1]. The MoR has been previously utilised to calculate Poiseuille flow around a single rigid sphere [3, 40, 41, 103–105], with the main differences between publications being the convergence criteria used to truncate the infinite system of equations that arise after successive reflections of the flow from the spherical and cylindrical boundaries. While explicit solutions are presented in these works, their accuracy is restricted by only considering a small number of terms due to computational limitations.

Once calculated, the traction exerted by the fluid on the particle is used to analytically calculate the leading-order deformation of the particle. By considering the first-order fluid problem, the next-order correction to the translational velocity of the particle is shown to be zero. Depending on the magnitude of the ratio of applied body force to viscous forces, the particle can either have a bullet-like shape, an anti-bullet shape, or retain its original spherical shape. A finite element implementation is also presented to validate the MoR solutions, as well as interrogate their range of validity.

Previous authors have shown that the lateral migration forces acting on a deformable particle may be decomposed into an elastic restoring effect and a wall-induced lift, both of which push the particle toward the centre-line of the tube, together with inertial lift which pushes the particle away from the centre-line (see [85] and references within). Motivated by this, since we neglect fluid inertia, we assume the particle translates along the centre-line of the tube. We investigate steady flows and examine the individual effects of the background Poiseuille flow, axial body force, and the addition of the tube wall on the translational velocity of the particle, the resulting deformation, and the induced solid stress within the particle. We additionally investigate the impact of the particle deformation on the surrounding fluid, and show that the effect on the particle's velocity is weak. We use results from Murata [3], [45], and Villone et al. [2], along with our own non-linear ALE finite element simulations, to comprehensively assess the validity of the analytic results. The MoR solutions give deeper analytical insight than the ALE FEM solutions and provide a more practical tool for interrogating the effect of changing the background Poiseuille flow, axial body force and particle size. The ALE FEM solutions, however, solve the full non-linear problem and so may be used to the investigate finite deformations and to quantify the range of validity of the MoR solutions.

This chapter is structured as follows. In Section 2.2 we formulate the problem, non-dimensionalising through physical arguments. We then perform an asymptotic expansion in the limit of a small ratio of typical viscous fluid stress to elastic stiffness in Section 2.3. In Section 2.4, we present the semi-analytic MoR used to solve the leading-order and first-order fluid problems, alongside our non-linear ALE finite element method. In Section 2.6, we first study the cases of a particle exposed to a background Poiseuille flow only, and under an axial body force only, comparing our MoR solutions with pre-existing results from the literature and our ALE FEM solutions. We then use the MoR implementation to investigate the combined effects of a background Poiseuille flow and axial body force on the flow field, particle deformation and induced stress. Finally, we provide a closing discussion in Section 2.7.

2.2 Problem formulation

We model an initially spherical elastic particle translating axially along the centre-line of a cylindrical tube driven by Poiseuille flow in the far field and under the influence of an axial body force. We define spherical and cylindrical coordinate systems (r, ϕ, θ) and (ρ, ϕ, z), with corresponding unit vectors $(\boldsymbol{e}_r, \boldsymbol{e}_\phi, \boldsymbol{e}_\theta)$ and $(\boldsymbol{e}_\rho, \boldsymbol{e}_\phi, \boldsymbol{e}_z)$, respectively.

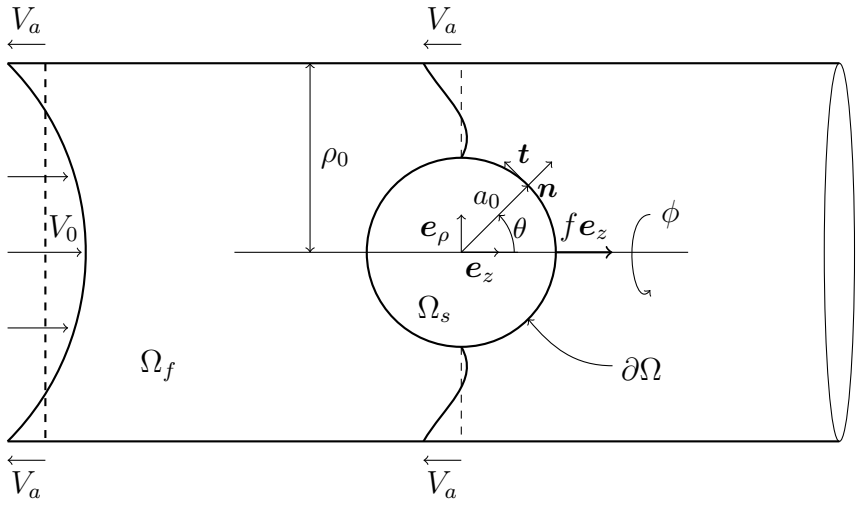

Figure 2.1: We consider an elastic particle translating with velocity $V_a\boldsymbol{e}_z$ along the centre-line of a cylindrical tube driven by Poiseuille flow in the far-field and subject to an axial body force $f\boldsymbol{e}_z$. We work in the frame of reference of the translating particle, resulting in sliding walls of velocity $-V_a\boldsymbol{e}_z$. The fluid domain and solid domains are denoted by Ω_f and Ω_s, respectively, with the interface between the two phases denoted by $\partial\Omega$.

We align the z-axis with the central axis of the tube and choose both origins to coincide with the centre of the particle as shown in Figure 2.1. We assume the problem is axisymmetric and has reached a steady equilibrium. The maximum magnitude of the background tube flow is V_0 in the lab frame and the undeformed particle and tube radii are given by a_0 and ρ_0, respectively. In the lab frame, the translational velocity of the particle, V_a, is unknown and will generally depend on the particle size and its material properties. We work in the frame of reference of the centre of mass of the particle such that we see sliding walls with velocity $-V_a\boldsymbol{e}_z$. The fluid and solid domains are denoted by Ω_f and Ω_s, respectively, with the interface between the two denoted by $\partial\Omega$.

2.2.1 Governing equations

The flow of fluid in the tube is governed by the incompressible Stokes equations,

$$\nabla \cdot \boldsymbol{\sigma}_f = \boldsymbol{0}, \tag{2.1}$$

$$\nabla \cdot \boldsymbol{v} = 0, \tag{2.2}$$

where $\boldsymbol{v}$ is the fluid velocity and $\boldsymbol{\sigma}_f$ is the stress tensor for a Newtonian viscous fluid given by

$$\boldsymbol{\sigma}_f = -p_f \boldsymbol{I} + \mu_f \left[\nabla \boldsymbol{v} + (\nabla \boldsymbol{v})^T\right], \tag{2.3}$$

with p_f the fluid pressure and μ_f the fluid viscosity. The superscript T denotes the transpose. The above expressions are presented using Eulerian coordinates, and we formulate the solid problem also in Eulerian coordinates.

The elastic particle is governed by the conservation of momentum equation,

$$\nabla \cdot \boldsymbol{\sigma}_s + f\boldsymbol{e}_z = \boldsymbol{0}, \tag{2.4}$$

where $\boldsymbol{\sigma}_s$ is the solid stress tensor and $f\boldsymbol{e}_z$ is a constant body force acting on the particle in the axial direction. For the elastic constitutive relation we choose an isotropic, incompressible neo-Hookean description,

$$\boldsymbol{\sigma}_s = -p_s \boldsymbol{I} + \mu_s(\boldsymbol{F} \cdot \boldsymbol{F}^T - \boldsymbol{I}), \tag{2.5}$$

where p_s is the solid pressure, $\frac{1}{2}\left(\boldsymbol{F} \cdot \boldsymbol{F}^T - \boldsymbol{I}\right)$ is the strain tensor and μ_s is the elastic shear modulus. The deformation gradient tensor, $\boldsymbol{F}$, is defined through its inverse $\boldsymbol{F}^{-1} = \boldsymbol{I} - \nabla \boldsymbol{u}$, where $\boldsymbol{u}$ is the displacement vector. The displacement vector is defined as $\boldsymbol{u}(\boldsymbol{x}) = \boldsymbol{x} - \boldsymbol{X}(\boldsymbol{x})$, where $\boldsymbol{X}$ is the position of a material point in the undeformed configuration and $\boldsymbol{x}$ is the current position vector of this point. The incompressibility condition is imposed as

$$\det(\boldsymbol{F}) = \frac{1}{\det(\boldsymbol{F}^{-1})} = 1. \tag{2.6}$$

Under the assumption of infinitesimal strain, Equations (2.5) and (2.6) reduce to the equations of incompressible linear elasticity,

$$\boldsymbol{\sigma}_s = -p_s \boldsymbol{I} + 2\mu_s \boldsymbol{e}, \tag{2.7}$$

$$\nabla \cdot \boldsymbol{u} = 0, \tag{2.8}$$

where $\boldsymbol{e} = \frac{1}{2}\left(\nabla \boldsymbol{u} + (\nabla \boldsymbol{u})^T\right)$ is the linear elastic strain tensor. Equations (2.7) and (2.8) are useful for informing the non-dimensionalsation and will guide our choice of perturbation parameter in Section 2.3.

We now present the boundary and interfacial conditions. Far upstream and downstream of the particle we impose Poiseuille flow of maximum magnitude V_0 in the lab frame in a tube whose walls have axial velocity $-V_a\boldsymbol{e}_z$,

$$\boldsymbol{v}(z \to \pm\infty) = V_0\left(1 - \frac{\rho^2}{\rho_0^2}\right)\boldsymbol{e}_z - V_a\boldsymbol{e}_z. \tag{2.9}$$

On the tube wall, $\rho = \rho_0$, we impose

$$\boldsymbol{v} = -V_a \boldsymbol{e}_z, \tag{2.10}$$

corresponding to no penetration and no-slip. Since we work in the frame of reference of the particle the no-slip and no-penetration boundary conditions on $\partial\Omega$ are given by

$$\boldsymbol{v} = \boldsymbol{0}. \tag{2.11}$$

We impose continuinty of stress on $\partial\Omega$,

$$\boldsymbol{\sigma}_f \cdot \boldsymbol{n} = \boldsymbol{\sigma}_s \cdot \boldsymbol{n}, \tag{2.12}$$

where $\boldsymbol{n}$ is the outward-pointing unit normal to the surface of the deformed particle.

The deformation of the interface is denoted by

$$\boldsymbol{u}(\boldsymbol{r}_s) = \boldsymbol{r}_s - a_0 \boldsymbol{e}_r, \tag{2.13}$$

where $\boldsymbol{r}_s$ is the position of the interface.

By integrating the stress balance (2.4), applying the divergence theorem and using the interfacial condition (2.12) we obtain the equilibrium relation,

$$\iiint_{\Omega_s} f \, \mathrm{d}V + F_z = 0, \quad \text{with} \quad F_z = \oiint_{\partial\Omega} \boldsymbol{e}_z \cdot \boldsymbol{\sigma}_f \cdot \boldsymbol{n} \, \mathrm{d}S, \tag{2.14}$$

where F_z is the viscous drag exerted by the fluid on the elastic particle in the axial direction. This will be useful later for predicting the translational velocity of the elastic particle V_a given a body force of magnitude f.

2.2.2 Non-dimensionalisation

We non-dimensionalise as follows, using stars to denote dimensionless variables,

$$\boldsymbol{\rho}^* = \frac{\boldsymbol{\rho}}{\rho_0}, \quad \boldsymbol{v}^* = \frac{\boldsymbol{v}}{V_0}, \quad p_f^* = \frac{\rho_0}{\mu_f V_0} p_f, \quad \boldsymbol{\sigma}_f^* = \frac{\rho_0}{\mu_f V_0} \boldsymbol{\sigma}_f. \tag{2.15}$$

We non-dimensionalise lengths with the tube radius ρ_0, velocities with V_0, and fluid pressure and stress with the viscous pressure scaling. Motivated by the interfacial stress condition (2.12), we non-dimensionalise the solid pressure and stress identically to the fluid stress, and scale the axial body force appropriately to the momentum equation for the solid phase (2.4),

$$p_s^* = \frac{\rho_0}{\mu_f V_0} p_s, \quad \boldsymbol{\sigma}_s^* = \frac{\rho_0}{\mu_f V_0} \boldsymbol{\sigma}_s, \quad f^* = \frac{\rho_0^2}{\mu_f V_0} f. \tag{2.16}$$

We introduce the parameter $\epsilon = \mu_f V_0/\mu_s \rho_0$ to characterise the size of the elastic strain, which is determined by dividing the solid stress by the shear modulus in (2.7). Having determined a scale for the elastic strain, it follows from the strain tensor that the solid displacement is of order $\epsilon\rho_0$, and is non-dimensionalised as,

$$\boldsymbol{u}^* = \frac{\boldsymbol{u}}{\epsilon\rho_0}. \tag{2.17}$$

We henceforth drop the stars for convenience.

The full dimensionless problem is then governed by

$$\nabla \cdot \boldsymbol{\sigma}_f = \boldsymbol{0}, \tag{2.18}$$

$$\nabla \cdot \boldsymbol{v} = 0, \tag{2.19}$$

$$\boldsymbol{\sigma}_f = -p_f \boldsymbol{I} + \left[\nabla \boldsymbol{v} + (\nabla \boldsymbol{v})^T\right], \tag{2.20}$$

in Ω_f, and

$$\nabla \cdot \boldsymbol{\sigma}_s + f\boldsymbol{e}_z = \boldsymbol{0}, \tag{2.21}$$

$$\boldsymbol{\sigma}_s = -p_s \boldsymbol{I} + \frac{1}{\epsilon}\left(\boldsymbol{F}\boldsymbol{F}^T - \boldsymbol{I}\right), \tag{2.22}$$

$$\det(\boldsymbol{F}) = 1, \tag{2.23}$$

in Ω_s, where

$$\boldsymbol{F} = \left(\boldsymbol{I} - \epsilon \nabla \boldsymbol{u}\right)^{-1}. \tag{2.24}$$

In the limit of small ϵ we have the following,

$$\boldsymbol{F} = \boldsymbol{I} + \epsilon \nabla \boldsymbol{u} + \mathcal{O}\left(\epsilon^2\right) \quad \text{and} \quad \det(\boldsymbol{F}) = 1 + \epsilon \nabla \cdot \boldsymbol{u} + \mathcal{O}\left(\epsilon^2\right), \qquad \text{as} \quad \epsilon \to 0. \tag{2.25}$$

The expansions (2.25) will be useful for the asymptotic analysis in Section 2.3.

The dimensionless boundary conditions in the far field are

$$\boldsymbol{v}(z \to \pm\infty) = \left(1 - \rho^2\right)\boldsymbol{e}_z - \mathcal{V}\boldsymbol{e}_z, \tag{2.26}$$

and on the walls of the cylindrical tube, $\rho = 1$,

$$\boldsymbol{v} = -\mathcal{V}\boldsymbol{e}_z. \tag{2.27}$$

On the fluid-particle interface, $\partial\Omega$, we have

$$\boldsymbol{v} = \boldsymbol{0} \tag{2.28}$$

$$\boldsymbol{\sigma}_f \cdot \boldsymbol{n} = \boldsymbol{\sigma}_s \cdot \boldsymbol{n}, \tag{2.29}$$

$$\epsilon \boldsymbol{u}(\boldsymbol{r}_s) = \boldsymbol{r}_s - \alpha \boldsymbol{e}_r. \tag{2.30}$$

In addition to ϵ we have two further dimensionless values: $\alpha = a_0/\rho_0$, the blockage factor, which is the ratio between the undeformed particle and tube radii, and $\mathcal{V} = V_a/V_0$ which represents the ratio between the translational velocity of the particle and the maximum magnitude of the Poiseuille flow in the lab frame. The equilibrium condition (2.14), used to calculate the particle's translational velocity, remains the same after non-dimensionalisation.

2.3 Asymptotic analysis of a stiff particle

We now assume that $\epsilon \ll 1$, corresponding to the limit of a stiff particle, and expand variables in powers of ϵ,

$$\boldsymbol{v} = \boldsymbol{v}^{(0)} + \epsilon \boldsymbol{v}^{(1)} + \cdots, \quad p_f = p_f^{(0)} + \epsilon p_f^{(1)} + \cdots, \quad \boldsymbol{\sigma}_f = \boldsymbol{\sigma}_f^{(0)} + \epsilon \boldsymbol{\sigma}_f^{(1)} + \cdots, \tag{2.31}$$

$$\boldsymbol{u} = \boldsymbol{u}^{(0)} + \epsilon \boldsymbol{u}^{(1)} + \cdots, \quad p_s = p_s^{(0)} + \epsilon p_s^{(1)} + \cdots, \quad \boldsymbol{\sigma}_s = \boldsymbol{\sigma}_s^{(0)} + \epsilon \boldsymbol{\sigma}_s^{(1)} + \cdots, \tag{2.32}$$

where the superscript i denotes the associated power of ϵ. We similarly expand the translational velocity of the elastic particle, the viscous drag, and the position of the interface,

$$\mathcal{V} = \mathcal{V}^{(0)} + \epsilon \mathcal{V}^{(1)} + \cdots, \quad F_z = F_z^{(0)} + \epsilon F_z^{(1)} + \cdots, \quad \text{and} \quad \boldsymbol{r}_s = \boldsymbol{r}_s^{(0)} + \epsilon \boldsymbol{r}_s^{(1)} + \cdots. \tag{2.33}$$

We proceed by assuming α, and the body force magnitude f, are $\mathcal{O}(1)$ as $\epsilon \to 0$. At each order in ϵ, we separate the problem into the respective fluid and solid parts. We show that the leading-order fluid problem decouples from the solid problem and is therefore not impacted by the deformation of the particle. The fluid stress provides a surface traction on the elastic particle which drives the leading-order solid problem.

In the analysis that follows, we impose a body force f, and calculate the translational velocity $\mathcal{V}$. We could equally solve the inverse problem using this framework by fixing the translational velocity and calculating the body force required to achieve this translational velocity equilibrium through (2.14). In this case we would asymptotically expand the body force f, as the translational velocity $\mathcal{V}$ is prescribed.

2.3.1 Limiting geometries

While not the focus of the present study, it is important to comment on the case when $\alpha \to 1$. Previously in Section 2.3, we characterised the solid strain by the dimensionless parameter ϵ, requiring $\epsilon \ll 1$ to satisfy the small strain assumption.

However, assuming the tube remains rigid, we expect the pressure in the lubrication layer between the tube wall and particle to increase such that assumption of infinitesimal strain is broken, even for $\epsilon \ll 1$. This suggests a restriction on ϵ related to the particle size α. Bungay and Brenner [45] studied a tightly-fitting, concentrically positioned rigid sphere in a cylindrical tube, finding that, for the cases of pressure-driven flow around a stationary particle and a particle translating through an otherwise stationary fluid, the fluid pressure in the lubrication region scales with $\delta^{-5/2}$ to leading order in δ, where $\delta = (1-\alpha)/\alpha$. It was also shown that the shear stress in the lubrication region scales with δ^{-2} such that the pressure forms the main contribution to the stresses acting on the particle. Thus, by using the pressure scale in the lubrication region as a measure of the fluid stress exerted on the particle and imposing stress conservation across the boundary, it follows that for $\alpha \to 1$, in order for the solid strain in the particle to be small, we require

$$\epsilon\delta^{-5/2} \ll 1. \tag{2.34}$$

We may also rearrange (2.34) to predict the range of suitable particle sizes for fixed ϵ,

$$1-\alpha \gg \epsilon^{2/5}. \tag{2.35}$$

We expect similar restrictions to apply with a general combination of pressure-driven flow and axial body force but these require a detailed asymptotic analysis that is beyond the scope of this thesis.

We can also consider the case $\alpha \to 0$. In this case, the spatial variables for the solid problem must be rescaled according to $x \to \alpha x$, in which case the stress tensor becomes

$$\boldsymbol{\sigma}_s = -p_s\boldsymbol{I} + \frac{1}{\epsilon\alpha}\left(\boldsymbol{F}\boldsymbol{F}^T - \boldsymbol{I}\right). \tag{2.36}$$

Consequently, for small α we require

$$\epsilon\alpha \ll 1, \tag{2.37}$$

to satisfy the infinitesimal strain assumption, suggesting the asymptotic expansion in ϵ remains valid for a wider range of ϵ for $\alpha \to 0$ compared with $\alpha \to 1$.

2.3.2 Leading-order fluid problem

The leading-order incompressible Stokes equations are

$$\nabla p_f^{(0)} = \nabla^2 \boldsymbol{v}^{(0)}, \tag{2.38}$$

$$\nabla \cdot \boldsymbol{v}^{(0)} = 0. \tag{2.39}$$

Expanding the kinematic condition (2.30) we find $\boldsymbol{r}_s^{(0)} = \alpha \boldsymbol{e}_r$, implying boundary conditions are applied on the undeformed particle surface, a sphere of radius α. The boundary conditions (2.26)–(2.28) at leading order give

$$\boldsymbol{v}^{(0)} \to \left(1 - \rho^2 - \mathcal{V}^{(0)}\right) \boldsymbol{e}_z \qquad \text{as } z \to \pm\infty, \tag{2.40}$$

$$\boldsymbol{v}^{(0)} = \boldsymbol{0} \qquad \text{at } r = \alpha, \tag{2.41}$$

$$\boldsymbol{v}^{(0)} = -\mathcal{V}^{(0)} \boldsymbol{e}_z \qquad \text{at } \rho = 1. \tag{2.42}$$

Equations (2.38)–(2.42) form a full description of the leading-order fluid problem. The particle does not deform at this order and so the leading-order fluid problem is equivalent to a rigid sphere under axisymmetric, pressure-driven tube flow subject to an axial body force. We note that the leading-order fluid pressure is determined up to an arbitrary constant and we choose to set $p_f = 0$ at $z = 0$ and $\rho = 1$. To leading order, the equilibrium condition (2.14) gives

$$\frac{4}{3} f \pi \alpha^3 + F_z^{(0)} = 0, \tag{2.43}$$

where the leading-order magnitude of the Stokes drag acting on the particle is given by

$$F_z^{(0)} = 2\pi\alpha^2 \int_0^\pi \boldsymbol{e}_z \cdot \boldsymbol{\sigma}_f^{(0)} \cdot \boldsymbol{e}_r \sin\theta \, \mathrm{d}\theta. \tag{2.44}$$

Noting that $\boldsymbol{v}^{(0)}$ depends linearly on the magnitude of the background Poiseuille flow and particle velocity, so too do $\boldsymbol{\sigma}_f^{(0)}$ and $F_z^{(0)}$. We can thus write a dimensionless, revised version of Faxen's law as

$$F_z^{(0)} = 6\pi\alpha \left(D^{(0)}(\alpha) - K^{(0)}(\alpha)\mathcal{V}^{(0)}\right), \tag{2.45}$$

defining $D^{(0)}(\alpha)$ and $K^{(0)}(\alpha)$ as the wall correction factors [55]. Substituting the expression for $F_z^{(0)}$ (2.45) into Equation (2.43) we obtain the explicit result for the leading-order translation velocity,

$$\mathcal{V}^{(0)} = \frac{D^{(0)}(\alpha)}{K^{(0)}(\alpha)} + \frac{2}{9} \frac{\alpha^2}{K^{(0)}(\alpha)} f. \tag{2.46}$$

Setting $f = 0$ in Equation (2.46) we obtain the leading-order translational velocity under no applied body force, motivating the decomposition

$$\mathcal{V}^{(0)} = \widehat{\mathcal{V}} + \widetilde{\mathcal{V}}, \quad \text{with} \quad \widehat{\mathcal{V}} = \frac{D^{(0)}(\alpha)}{K^{(0)}(\alpha)} \quad \text{and} \quad \widetilde{\mathcal{V}} = \frac{2}{9} \frac{\alpha^2}{K^{(0)}(\alpha)} f. \tag{2.47}$$

By decomposing the translational velocity in this way, we split the leading-order fluid problem into two parts: a rigid sphere under no body force driven by Poiseuille flow in the tube, resulting in the translational velocity $\widehat{\mathcal{V}}$, and a rigid sphere subject to an axial body force with no background flow, resulting in the translational velocity $\widetilde{\mathcal{V}}$. The explicit dependence on body force given by $\widetilde{\mathcal{V}}$ is similar to that obtained by Murata [70] for an elastic particle under a body force in an unbounded domain, with the addition of $1/K^{(0)}(\alpha)$ capturing the effect of the tube wall.

2.3.3 Leading-order solid problem

The leading-order equilibrium equation for the solid is

$$\nabla \cdot \boldsymbol{\sigma}_s^{(0)} + f\boldsymbol{e}_z = \boldsymbol{0}, \tag{2.48}$$

where combining (2.22) and (2.25) we reduce to a linearly elastic stress-strain relationship to leading order

$$\boldsymbol{\sigma}_s^{(0)} = -p_s^{(0)}\boldsymbol{I} + \nabla \boldsymbol{u}^{(0)} + \nabla \boldsymbol{u}^{(0)^T}. \tag{2.49}$$

The incompressibility condition is then given by Equation (2.25),

$$\nabla \cdot \boldsymbol{u}^{(0)} = 0, \tag{2.50}$$

such that the leading-order solid displacement and pressure are also governed by Stokes equations. The interfacial condition (2.29) gives,

$$\boldsymbol{\sigma}_f^{(0)} \cdot \boldsymbol{e}_r = \boldsymbol{\sigma}_s^{(0)} \cdot \boldsymbol{e}_r \quad \text{at } r = \alpha, \tag{2.51}$$

and the kinematic condition (2.30) at leading-order gives

$$\boldsymbol{r}_s^{(1)} = \boldsymbol{u}^{(0)} \quad \text{at } r = \alpha. \tag{2.52}$$

2.3.4 First-order fluid problem

We consider the first-order correction to the flow field around the elastic particle. We again have the Stokes equations relating fluid velocity and pressure at this order, Equations (2.38) and (2.39). The far-field condition (2.26) gives

$$\boldsymbol{v}^{(1)} \to -\mathcal{V}^{(1)}\boldsymbol{e}_z \quad \text{as } z \to \pm\infty, \tag{2.53}$$

where $\mathcal{V}^{(1)}$ captures how the leading-order deformation of the particle affects its translational velocity within the tube. The velocity condition on the tube wall is

$$\boldsymbol{v}^{(1)} = -\mathcal{V}^{(1)}\boldsymbol{e}_z \quad \text{at } \rho = 1, \tag{2.54}$$

while the velocity condition (2.28) at $\mathcal{O}(\epsilon)$ gives,

$$\boldsymbol{v}^{(1)}(r,\theta) = -\nabla \boldsymbol{v}^{(0)}(r,\theta)\cdot \boldsymbol{r}_s^{(1)}(r,\theta) = -u_r^{(0)}(r,\theta)\frac{\partial \boldsymbol{v}^{(0)}(r,\theta)}{\partial r} \quad \text{at } r=\alpha, \tag{2.55}$$

where we have used the fact that

$$\frac{\partial \boldsymbol{v}^{(0)}(\alpha,\theta)}{\partial \theta} = 0. \tag{2.56}$$

Expanding Equation (2.14), the viscous drag acting on the particle at first order is

$$\begin{aligned} 2\pi\alpha^2 f\int_0^\pi u_r^{(0)}\sin\theta\,\mathrm{d}\theta + 2\pi\alpha^2\int_0^\pi \boldsymbol{e}_z\cdot\boldsymbol{u}^{(0)}\cdot\nabla\boldsymbol{\sigma}_f^{(0)}\cdot\boldsymbol{e}_r\sin\theta\,\mathrm{d}\theta \\ + 2\pi\int_0^\pi \boldsymbol{e}_z\cdot\boldsymbol{\sigma}_f^{(0)}\cdot\left[\frac{\partial \boldsymbol{r}_s^{(0)}}{\partial\theta}\times\frac{\partial \boldsymbol{r}_s^{(1)}}{\partial\phi} + \frac{\partial \boldsymbol{r}_s^{(1)}}{\partial\theta}\times\frac{\partial \boldsymbol{r}_s^{(0)}}{\partial\phi}\right]\mathrm{d}\theta \\ + 2\pi\alpha^2\int_0^\pi \boldsymbol{e}_z\cdot\boldsymbol{\sigma}_f^{(1)}\cdot\boldsymbol{e}_r\sin\theta\,\mathrm{d}\theta = 0 \quad \text{at } r=\alpha, \end{aligned} \tag{2.57}$$

where $\times$ denotes the cross product and we have expanded the magnitude of the surface deformation as

$$|\boldsymbol{r}_s| = \alpha + \epsilon u_r^{(0)}(r,\theta) + \mathcal{O}(\epsilon^2) \quad \text{at } r=\alpha. \tag{2.58}$$

We show later in Section 2.4.1.4 that the first-order correction to the translational velocity $\mathcal{V}^{(1)} = 0$.

2.4 Solution methods

2.4.1 Semi-analytical implementation

Solving the leading-order fluid problem involves a mix of geometries; the cylindrical tube motivates the use of a cylindrical coordinate system, while the undeformed particle is more naturally considered via a spherical coordinate system. To account for this mix of geometries, we choose to employ the method of reflections (MoR), though we could equally select another suitable method, for example a collocation technique or boundary element method [54, 106].

In this subsection we introduce the MoR and apply it to the leading-order fluid problem. We then consider the leading-order solid problem, presenting general solutions for the deformation and relevant stress components. Finally, we consider the first-order fluid problem, showing the first-order correction to the translational velocity is zero.

2.4.1.1 Method of reflections

The method of reflections, originally developed by Brenner and Happel [40], is a meshless semi-analytic method which involves splitting up the problem such that only one set of boundary conditions, and consequently coordinate system, is considered at any time. We present full details of the MoR in Appendix A along the lines of Yao et al. [44, 55]. Due to the linearity of the Stokes equations and boundary conditions we can decompose the velocity field as follows,

$$\boldsymbol{v}^{(i)} = \boldsymbol{v}^{(i,0)} + \boldsymbol{v}^{(i,1)} + \boldsymbol{v}^{(i,2)} + \cdots, \quad p_f^{(i)} = p_f^{(i,0)} + p_f^{(i,1)} + p_f^{(i,2)} + \cdots, \tag{2.59}$$

where $\boldsymbol{v}^{(i,j)}$ corresponds to the j-th term in the series for $\boldsymbol{v}^{(i)}$, and $\boldsymbol{v}^{(i)}$ are the $\mathcal{O}(\epsilon^i)$ terms in the asymptotic expansion; see Section 2.3. Terms with odd j ($\boldsymbol{v}^{(i,\text{odd})}$, $p_f^{(i,\text{odd})}$) are calculated by solving Stokes equations using a spherical coordinate system and imposing the interfacial conditions on the particle, while terms with even j ($\boldsymbol{v}^{(i,\text{even})}$, $p_f^{(i,\text{even})}$) are calculated by solving Stokes equations using a cylindrical coordinate system and imposing the boundary conditions on the tube wall. Since each term corresponds to a reflection, the addition of a new term using either a spherical or cylindrical coordinate system, j is defined as the reflection number.

2.4.1.2 Leading-order fluid problem

We apply the MoR to solve the system of equations defining the leading-order fluid problem (2.38)–(2.42). We begin by choosing

$$\boldsymbol{v}^{(0,0)} = (1 - \rho^2 - \mathcal{V}^{(0)})\boldsymbol{e}_z, \tag{2.60}$$

which ensures all other velocity components must vanish for $z \to \pm\infty$, or equivalently for contributions in spherical coordinates, $r \to \infty$. Equation (2.60) guarantees we satisfy the far-field condition (2.40) and the boundary conditions on the tube wall (2.42). The only conditions left to satisfy are the boundary conditions on the surface of the sphere (2.41). To address this, we transform $\boldsymbol{v}^{(0,0)}$ to spherical coordinates (details given in Appendix A.1) and introduce $\boldsymbol{v}^{(0,1)}$ such that $\boldsymbol{v}^{(0,0)} + \boldsymbol{v}^{(0,1)}$ together satisfy the boundary conditions on the surface of the sphere. By including the velocity component $\boldsymbol{v}^{(0,1)}$ we disrupt the boundary conditions on the tube wall, (2.42). To reimpose these boundary conditions we convert the expression $\boldsymbol{v}^{(0,0)} + \boldsymbol{v}^{(0,1)}$ to cylindrical coordinates, and add $\boldsymbol{v}^{(0,2)}$ such that $\boldsymbol{v}^{(0,0)} + \boldsymbol{v}^{(0,1)} + \boldsymbol{v}^{(0,2)}$ satisfies Equation (2.42). This process repeats indefinitely with $\boldsymbol{v}^{(0,\text{even})}$ calculated by satisfying

Equation (2.42) using a cylindrical coordinate system, and $\boldsymbol{v}^{(0,\text{odd})}$ found by satisfying Equation (2.41) using a spherical coordinate system. We summarise the process via the following equations:

$$\boldsymbol{v}^{(0,0)} = (1-\rho^2-\mathcal{V}^{(0)})\boldsymbol{e}_z, \tag{2.61}$$

$$\boldsymbol{v}^{(0,1)} = \begin{cases} -\boldsymbol{v}^{(0,0)}, & r=\alpha, \\ 0, & r\to\infty, \end{cases} \tag{2.62}$$

$$\boldsymbol{v}^{(0,2)} = \begin{cases} -\boldsymbol{v}^{(0,1)}, & \rho=1, \\ 0, & z\to\pm\infty, \end{cases} \tag{2.63}$$

$$\boldsymbol{v}^{(0,3)} = \begin{cases} -\boldsymbol{v}^{(0,2)}, & r=\alpha, \\ 0, & r\to\infty, \end{cases} \tag{2.64}$$

$$\vdots$$

If we truncate the velocity series at an odd term then we fully satisfy the interfacial condition on the surface of the sphere, with an error on the tube wall. If we truncate the velocity series at an even term then the opposite is true. We define a solution as having converged when the most recent contribution to the net force acting on the sphere is at least five orders of magnitude smaller than the net force from all components. The details of this are presented in Appendix A.4.

The final solution obtained involves a combination of expressions in both spherical and cylindrical coordinate systems, which each individually satisfy Stokes equations, and when added satisfy both the boundary conditions on the tube wall and boundary conditions on the sphere surface simultaneously. Crucially, we can obtain semi-analytical expressions for the fluid velocity, pressure and stress on the undeformed boundary of the sphere at $r=\alpha$. The semi-analytic nature of these expressions originates from the integrals present in the general solution for the velocity field in cylindrical coordinates (A.17)–(A.19) which must be evaluated numerically. Consequently, the expressions for the total velocity field in spherical coordinates are of the form

$$v_r^{(0)}(\theta)|_{r=\alpha} = \sum_{n=2}^{\infty} \left[-\alpha^{-n-1}(A_n + B_n\alpha^2) + \tilde{v}_{(r,n)}\right] \mathcal{P}_{n-1}(\cos\theta), \tag{2.65}$$

$$v_\theta^{(0)}(\theta)|_{r=\alpha} = \sum_{n=2}^{\infty} \left[-\alpha^{-n-1}((n-1)A_n + (n-3)B_n\alpha^2) + \tilde{v}_{(\theta,n)}\right] \csc\theta\, \mathcal{C}_n(\cos\theta), \tag{2.66}$$

where $\mathcal{P}_n(\cos\theta)$ are the Legendre polynomials of order n and $\mathcal{C}_n$ are the Gegenbauer polynomials of order n and degree $-1/2$. The subscripts r and θ correspond to the

radial and azimuthal components of a vector in spherical coordinates, respectively, and the subscript n corresponds to the summation. We write the associated pressure field as,

$$p_f^{(0)}(\theta)|_{r=\alpha} = -2\sum_{n=2}^{\infty}\left[\frac{2n-3}{n}B_n\alpha^{-n} + \tilde{p}_{(n)}\right]\mathcal{P}_{n-1}(\cos\theta), \tag{2.67}$$

and the relevant stress components using the fluid constitutive relation (2.20),

$$\sigma_{f,rr}^{(0)}(\theta)|_{r=\alpha} = \sum_{n=2}^{\infty}\left[2\alpha^{-n-2}\left((n+1)A_n + \left(\frac{n^2+n-3}{n}\right)B_n\alpha^2\right) + \tilde{\sigma}_{(rr,n)}\right]\mathcal{P}_{n-1}(\cos\theta), \tag{2.68}$$

$$\sigma_{f,r\theta}^{(0)}(\theta)|_{r=\alpha} = \sum_{n=2}^{\infty}\left[2\alpha^{-n-2}\left((n^2-1)A_n + n(n-2)B_n\alpha^2\right) + \tilde{\sigma}_{(r\theta,n)}\right]\csc\theta\,\mathcal{C}_n(\cos\theta). \tag{2.69}$$

Here, the tensor components, $\sigma_{f,ij}^{(0)} = \boldsymbol{e}_i\cdot\boldsymbol{\sigma}_f^{(0)}\cdot\boldsymbol{e}_j$. In Equations (2.65)–(2.69) the coefficients A_n and B_n arise naturally from the stream function series for the velocity field in spherical coordinates, see (A.4), while the coefficients $\tilde{v}_{(r,n)}, \tilde{v}_{(\theta,n)}, \tilde{p}_{(n)}, \tilde{\sigma}_{(rr,n)}, \tilde{\sigma}_{(r\theta,n)}$ arise from projecting terms calculated using a cylindrical coordinate system onto the undeformed particle surface via Equations (A.9) and (A.10). All of these projections are performed numerically due to the difficulty of converting the general solutions for velocity and stress from cylindrical to spherical coordinates. To solve the leading-order fluid and solid problems, we use the first three non-zero terms in the stream function series which correspond to $n = 2, 4, 6$. This is because the far-field flow can be written exactly using terms with $n = 2$ and 4 and, under this external flow, the presence of the tube wall exclusively drives terms with even n in the stream function series. The impacts of this truncation choice on solution accuracy are discussed in Appendix A.4.

The fluid normal and shear stress calculated from the leading-order fluid problem act as tractions to drive a deformation of the elastic particle. From the MoR we have known, semi-analytic expressions for these forcing terms given by Equations (2.68) and (2.69).

2.4.1.3 Leading-order solid problem

At this order the solid displacement is governed by Stokes equations with a body force. Restricting to terms which remain finite as $r \to 0$, the solution is given by

Happel and Brenner [107],

$$u_r^{(0)}(r,\theta) = -\frac{1}{10} f r^2 \cos\theta - \sum_{n=2}^{\infty} r^{n-2}(C_n + r^2 D_n)\mathcal{P}_{n-1}(\cos\theta), \tag{2.70}$$

$$u_\theta^{(0)}(r,\theta) = \frac{1}{20} f r^2 \sin\theta + \sum_{n=2}^{\infty} r^{n-2}(nC_n + (n+2)r^2 D_n)\csc\theta\,\mathcal{C}_n(\cos\theta), \tag{2.71}$$

$$p_s^{(0)}(r,\theta) = -2\sum_{n=2}^{\infty} \frac{1+2n}{n-1} r^{n-1} D_n \mathcal{P}_{n-1}(\cos\theta). \tag{2.72}$$

We calculate the relevant stress components using the constitutive relation (2.49),

$$\sigma_{s,rr}^{(0)}(r,\theta) = -\frac{2}{5} f r\cos\theta - 2\sum_{n=2}^{\infty} r^{n-3}\left((n-2)C_n + \left(\frac{n^2-3n-1}{n-1}\right) r^2 D_n\right)\mathcal{P}_{n-1}(\cos\theta), \tag{2.73}$$

$$\sigma_{s,r\theta}^{(0)}(r,\theta) = \frac{3}{10} f r\sin\theta + 2\sum_{n=2}^{\infty} r^{n-3}(n(n-2)C_n + (n^2-1)r^2 D_n)\csc\theta\,\mathcal{C}_n(\cos\theta). \tag{2.74}$$

In general, C_n and D_n in Equations (2.73) and (2.74) are calculated by imposing continuity of traction on the particle surface (2.51). We then obtain the solid displacement by substituting C_n and D_n into Equations (2.70) and (2.71), with the position of the free surface given by Equation (2.52). The coefficient C_2 in Equation (2.70) corresponds to translation and so does not generate any stress in Equation (2.73) and (2.74). Since C_2 is not set by the interfacial conditions we must impose another condition to pin this translational degree of freedom. Here, we choose to set the net axial displacement to be zero via

$$\int_0^{\pi}\int_0^{\alpha} (\boldsymbol{e}_z \cdot \boldsymbol{u}^{(0)})\, r^2 \sin(\theta)\,\mathrm{d}r\,\mathrm{d}\theta = 0, \tag{2.75}$$

noting that another common choice is to set the particle displacement at the origin to zero. Substituting the above expressions for displacement (2.70) and (2.71) into (2.75) gives

$$C_2 = -\alpha^2\left(\frac{f}{10} + D_2\right), \tag{2.76}$$

such that the centre of mass of the particle is unchanged when deformed.

2.4.1.4 First-order correction to the translational velocity

We again apply the MoR to solve the first-order correction to the local flow field outlined by Equations (2.53)–(2.55). Since the leading-order fluid and solid problems

involve only terms with even n (see Section 2.4.1.2), we see the velocity condition on the particle surface (2.55) generates terms with odd n in $\boldsymbol{v}^{(1)}$ since $\boldsymbol{v}^{(0)}$ and $\boldsymbol{u}^{(0)}$ contain only terms with even n. Terms with even n arise due to the unknown first-order correction to the translational velocity, generated by the far-field condition (2.53) and the boundary conditions on the tube wall (2.54) since even n terms satisfy the wall conditions. Critically, in Equation (2.57) terms with odd n do not contribute to the net drag on the particle and so we find that

$$-6\pi\alpha K^{(0)}(\alpha)\mathcal{V}^{(1)} = 0, \tag{2.77}$$

such that the first-order correction to the translational velocity is zero. We interpret this result via a consideration of symmetry. We expect the velocity of a deformable particle to be an odd function of the applied body force and pressure gradient across the tube as inverting the direction of either changes the sign of the particle velocity. The leading-order velocity depends linearly on the applied body force and pressure drop and is the same for both a deformable particle and a rigid sphere of the same radius. The first-order contribution to the particle velocity is forced by (2.55) and so is quadratic (even) in both the applied body force and pressure drop. It is therefore necessary to calculate the second-order contribution to the particle velocity expansion to see a difference between rigid and deformable particles.

We note that the second-order contribution to the particle velocity could, in theory, be obtained through the use of the reciprocal theorem, which would avoid the explicit calculation of the full second-order velocity field [108]. This method relies on the construction of integral relations through the reciprocal theorem, which are simplified through knowledge of the boundary conditions on the second-order velocity field. The use of the reciprocal theorem to predict the second-order contribution to the particle velocity would require the calculation of the first-order particle deformation and is beyond the scope of the present study. Here, we instead utilise fully non-linear finite-element simulations to investigate higher-order contributions to the particle velocity and other quantities of interest.

2.5 Finite element implementation

To investigate the range of validity of the MoR solutions, we solve the full non-linear fluid-structure interaction (FSI) problem via the finite element method using an arbitrary Lagrangian-Eulerian (ALE) approach. We construct a steady, 2D axisymmetric

implementation which greatly improves efficiency (typically $\lesssim 1$ minute per simulation) compared to the previous time-dependent, 3D numerical study by [2] which took an average of $2-3$ days per simulation. For reference, calculation of the MoR solution takes < 1 second per simulation. In the finite element implementation, we instead work in the lab frame for convenience such that the particle translates with velocity $\mathcal{V}$. The ALE approach couples the Lagrangian solid problem with the Eulerian fluid problem, which is transformed into a Lagrangian frame via the fluid mesh displacement $\boldsymbol{u}_a \in \Omega_f$ such that the undeformed reference configuration is used as the computational domain. The fluid mesh displacement has no physical interpretation, and acts to project the solid displacement into the fluid domain. Consequently, an arbitrary governing equation may be used to calculate the fluid mesh displacement; in this study we use the equations of linear elasticity for the fluid mesh displacement. We use the finite element library `fenics` with the additional package `multiphenics` to implement the ALE method, generating meshes via `gmsh` [109–112]. We use P_2 elements for the fluid velocity, solid displacement, and fluid mesh displacement and use P_1 elements for the pressures.

We present an overview of our non-linear arbitrary Lagrangian-Eulerian (ALE) finite element model. The ALE method couples the Lagrangian solid problem and the Eulerian fluid problem. For clarity regarding these configurations, we again write $\boldsymbol{X}$ and $\boldsymbol{x}$ as the reference (Lagrangian) and current (Eulerian) configurations. For brevity, we present only the key details of the ALE problem set-up and refer the interested reader to Slyngstad [113]. To ensure accuracy in the finite element solutions we used the method of manufactured solutions to test the solid, fluid, and ALE solvers, presenting details in Appendix B.1.

2.5.1 Lagrangian solid problem

To distinguish between the Eulerian presentation of the solid problem in Section 2.2 and the Lagrangian solid problem we specify the Lagrangian gradient as $\nabla_{\boldsymbol{X}}$. It will also be useful to define the undeformed solid, fluid, and boundary domains as $\widehat{\Omega}_s, \widehat{\Omega}_f$, and $\partial\widehat{\Omega}$, respectively. The solid problem is then described by the balance of linear momentum,

$$\nabla_{\boldsymbol{X}} \cdot \boldsymbol{P} = \boldsymbol{0}, \tag{2.78}$$

where the first Piola-Kirchhoff stress tensor $\boldsymbol{P} = J\boldsymbol{\sigma}_s\boldsymbol{F}^{-T}$ and $\boldsymbol{F} = \boldsymbol{I} + \nabla_{\boldsymbol{X}}\boldsymbol{u}$. Again assuming the particle is incompressible, we have the further constraint (2.23).

2.5.2 Eulerian fluid problem

The Eulerian fluid problem is governed by the dimensionless Stokes equations (2.18)–(2.20). However, it is convenient to choose the undeformed reference configuration as the computational domain. To do this, we must transform the fluid equations to the reference configuration. We define the fluid mesh displacement associated with this transformation, and the associated deformation gradient tensor and Jacobian as

$$\boldsymbol{u}_a \in \widehat{\Omega}_f, \quad \boldsymbol{F}_a = \boldsymbol{I} + \nabla_{\boldsymbol{X}} \boldsymbol{u}_a, \quad J_a = \det \boldsymbol{F}_a, \tag{2.79}$$

respectively. Making use of Nansen's formula,

$$\boldsymbol{n} \mathrm{d}S = J_a \boldsymbol{F}^{-T} \cdot \boldsymbol{N} \mathrm{d}S_{\boldsymbol{X}}, \tag{2.80}$$

where $\boldsymbol{n}$ and $\boldsymbol{N}$ are the normal vectors in the deformed/reference configurations, respectively, we may write the stress balance across the fluid-solid interface (2.29) as

$$J_a \boldsymbol{\sigma}_f \boldsymbol{F}_a^{-T} \cdot \boldsymbol{N} = \boldsymbol{P} \cdot \boldsymbol{N}, \tag{2.81}$$

which is imposed on the undeformed particle boundary $\partial\widehat{\Omega}$. Nansen's formula (2.80) may also applied in conjunction with the divergence theorem to transform the Eulerian fluid equations to the reference configuration,

$$\nabla_{\boldsymbol{X}} \cdot (J_a \boldsymbol{\sigma}_f \boldsymbol{F}_a^{-T}) = \boldsymbol{0}, \tag{2.82}$$

$$\nabla_{\boldsymbol{X}} \cdot (J_a \boldsymbol{F}_a^{-1} \boldsymbol{v}) = 0, \tag{2.83}$$

$$\boldsymbol{\sigma}_f = -p_f \boldsymbol{I} + (\nabla_{\boldsymbol{X}} \boldsymbol{v}) \boldsymbol{F}_a^{-1} + \boldsymbol{F}_a^{-T} (\nabla_{\boldsymbol{X}} \boldsymbol{v})^T. \tag{2.84}$$

2.5.3 Arbitrary coupling

The solid displacement $\boldsymbol{u}_s \in \widehat{\Omega}_s$ is physically motivated and provides a mapping between the undeformed reference and deformed configurations. The fluid mesh displacement $\boldsymbol{u}_a \in \widehat{\Omega}_f$ has no such physical interpretation. We require continuity of displacement ($\boldsymbol{u}_a = \boldsymbol{u}_s$) along the fluid-solid interface and do not permit normal fluid displacements along non-moving boundaries. Under these boundary conditions, the fluid mesh displacement extends any solid displacement into the fluid domain, and may be solved for using arbitrary governing equations. Previous studies have required $\boldsymbol{u}_a$ satisfy Laplace's equation, the equations of linear or non-linear elasticity, or the biharmonic equation [113]. In this study we opt to use the equations of linear elasticity such that

$$\nabla_{\boldsymbol{X}} \cdot \boldsymbol{\sigma}_a = \boldsymbol{0} \tag{2.85}$$

$$\boldsymbol{\sigma}_a = \frac{\nu_a E_a}{(1+\nu_a)(1-2\nu_a)} \nabla_{\boldsymbol{X}} \cdot \boldsymbol{u}_a + \frac{E_a}{2(1+\nu_a)} \left[\nabla_{\boldsymbol{X}} \boldsymbol{u}_a + (\nabla_{\boldsymbol{X}} \boldsymbol{u}_a)^T \right], \tag{2.86}$$

where ν_a and E_a have no physical interpretation and in general do not have a consistent impact on problem convergence. After experimentation via a grid search, we opted to use $\nu_a = 0.1$ and $E_a = 1$ in this work. To be clear, ν_a and E_a are dimensionless, where E_a is defined relative to the corresponding properties of the particle.

2.5.4 Numerical implementation

In addition to the unknowns $\boldsymbol{v}, p_f, \boldsymbol{u}, p_s, \boldsymbol{u}_a$ we utilise several Lagrange multipliers to impose further constraints. These are, $L_d \in \widehat{\Omega}_s$ which ensures the mean solid displacement is zero, $\mathcal{V} \in \widehat{\Omega}_s$ which is the particle's translational velocity, $\boldsymbol{L}_f \in \partial\widehat{\Omega}$ which corresponds to the fluid traction acting on the solid, $L_p \in \widehat{\Omega}_f$ which ensures the mean fluid pressure is zero, and $\boldsymbol{L}_a \in \partial\widehat{\Omega}$ which enforces the continuity of the fluid and solid displacement.

In order to solve an axisymmetric implementation of the FSI problem we may extend the Cartesian equations to use a cylindrical coordinate system [62]. There are several facets to consider in this extension. For example, we write the axisymmetric (cylindrical) divergence as

$$\nabla_{\boldsymbol{X}} \cdot \boldsymbol{v} = \partial_z V_z + \frac{1}{\rho} \partial_\rho (\rho V_\rho) = \nabla_{\boldsymbol{X}}^{\text{Cart}} \cdot \boldsymbol{v} + \frac{V_\rho}{\rho}. \tag{2.87}$$

The axisymmetric gradient operator is identical to the Cartesian counterpart when applied to a scalar. When applied to vector we have

$$\nabla_{\boldsymbol{X}} \boldsymbol{v} = \nabla_{\boldsymbol{X}}^{\text{Cart}} \boldsymbol{v} + \frac{V_\rho}{\rho} \boldsymbol{e}_\phi \otimes \boldsymbol{e}_\phi, \tag{2.88}$$

which introduces further terms into the axisymmetric implementation. This can be seen, for example, in the determinant,

$$J = J^{\text{Cart}} \left(1 + \frac{u_\rho}{r} \right). \tag{2.89}$$

The final change comes from the differential volume and surface area,

$$\mathrm{d}X = \rho \, \mathrm{d}X^{\text{Cart}} = \rho \, \mathrm{d}\rho \, \mathrm{d}z, \tag{2.90}$$

$$\mathrm{d}S = \rho \, \mathrm{d}S^{\text{Cart}}. \tag{2.91}$$

We now present the weak variational problem for the non-linear axisymmetric ALE FSI problem. We define the test functions $\boldsymbol{w}, q_f, \boldsymbol{d}, q_s, \boldsymbol{d}_a, M_d, W, \boldsymbol{M}_f, M_p, \boldsymbol{M}_a$

associated with $\boldsymbol{v}, p_f, \boldsymbol{u}, p_s, \boldsymbol{u}_a, L_d, \mathcal{V}, \boldsymbol{L}_f, L_p, \boldsymbol{L}_a$, respectively. Multiplying the governing equations by the respective test function, integrating, and applying integration by parts the solid equations are

$$-\int_{\widehat{\Omega}_s} \boldsymbol{\sigma}_s : \nabla_{\boldsymbol{X}} \boldsymbol{d}\, \rho \,\mathrm{d}\rho \,\mathrm{d}z - \frac{1}{\epsilon}\int_{\widehat{\Omega}_s} \left(1 + \frac{u_\rho}{\rho}\right) d_\rho \,\mathrm{d}\rho \,\mathrm{d}z + \int_{\widehat{\Omega}_s} \left(\frac{1}{\epsilon} + p_s\right) d_\rho \frac{\rho}{\rho + u_\rho} \,\mathrm{d}\rho \,\mathrm{d}z + \int_{\widehat{\Omega}_s} f d_z \,\rho \,\mathrm{d}\rho \,\mathrm{d}z + \int_{\widehat{\Omega}_s} L_d d_z \,\rho \,\mathrm{d}\rho \,\mathrm{d}z - \int_{\partial\widehat{\Omega}_X} \boldsymbol{L}_f \cdot \boldsymbol{d}\, \rho \,\mathrm{d}S^{\mathrm{Cart}} = 0, \quad (2.92)$$

$$\int_{\widehat{\Omega}_s} (J-1) q_s \,\rho \,\mathrm{d}\rho \,\mathrm{d}z = 0. \quad (2.93)$$

Similarly, the fluid equations are

$$-\int_{\widehat{\Omega}_f} \boldsymbol{\sigma}_f : \nabla_{\boldsymbol{X}} \boldsymbol{w}\, \rho \,\mathrm{d}\rho \,\mathrm{d}z - \int_{\widehat{\Omega}_f} J \left(\frac{2V_\rho w_\rho}{(\rho + V_\rho)^2} - \frac{p_f w_\rho}{\rho} \frac{\rho}{\rho + V_\rho}\right) \rho \,\mathrm{d}\rho \,\mathrm{d}z + \int_{\partial\widehat{\Omega}_X} \boldsymbol{L}_f \cdot \boldsymbol{w}\, \rho \,\mathrm{d}S^{\mathrm{Cart}} = 0, \quad (2.94)$$

$$\int_{\widehat{\Omega}_f} \nabla_{\boldsymbol{X}} \cdot (J \boldsymbol{F}^{-1} \boldsymbol{v}) q_f \,\rho \,\mathrm{d}\rho \,\mathrm{d}z + \int_{\widehat{\Omega}_f} L_p q_f \,\rho \,\mathrm{d}\rho \,\mathrm{d}z = 0. \quad (2.95)$$

The fluid mesh displacement equations are

$$-\int_{\widehat{\Omega}_f} \boldsymbol{\sigma}_a : \nabla^{\mathrm{Cart}}_{\boldsymbol{X}} \boldsymbol{d}_a \,\rho \,\mathrm{d}\rho \,\mathrm{d}z - \int_{\widehat{\Omega}_f} \frac{1}{1+\nu_a} \frac{u_{a,\rho} d_{a,\rho}}{\rho} \,\mathrm{d}\rho \,\mathrm{d}z + \int_{\partial\widehat{\Omega}_X} \boldsymbol{L}_a \cdot \boldsymbol{d}_a \,\rho \,\mathrm{d}S^{\mathrm{Cart}} = 0. \quad (2.96)$$

We now use the various Lagrange multipliers to enforce their respective constraints. First, we impose the continuity of fluid velocity at the particle surface,

$$\int_{\partial\widehat{\Omega}_X} \boldsymbol{M}_f \cdot (\boldsymbol{v} - \mathcal{V}\boldsymbol{e}_z) \,\rho \,\mathrm{d}S^{\mathrm{Cart}} = 0, \quad (2.97)$$

the continuity of fluid and solid displacement at the particle surface,

$$\int_{\partial\widehat{\Omega}_X} \boldsymbol{M}_a \cdot (\boldsymbol{u} - \boldsymbol{u}_a) \,\rho \,\mathrm{d}S^{\mathrm{Cart}} = 0, \quad (2.98)$$

zero mean fluid pressure,

$$\int_{\widehat{\Omega}_f} p_f M_p \,\rho \,\mathrm{d}\rho \,\mathrm{d}z = 0, \quad (2.99)$$

zero mean axial solid displacement,

$$\int_{\widehat{\Omega}_s} u_z M_d \,\rho \,\mathrm{d}\rho \,\mathrm{d}z = 0, \quad (2.100)$$

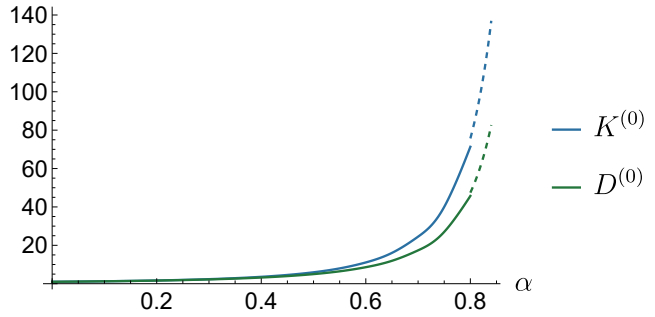

Figure 2.2: Wall correction factors, $K^{(0)}(\alpha)$ and $D^{(0)}(\alpha)$, for varying α. The solid lines are our MoR solutions and the dashed lines are adapted from Bungay and Brenner [45], and were obtained using a lubrication approximation with a rigid particle.

and balance the fluid drag with the axial body force,

$$\int_{\partial\widehat{\Omega}} (\boldsymbol{L}_f \cdot \boldsymbol{e}_z) W \, \rho \, \mathrm{d}S^{\mathrm{Cart}} - \int_{\widehat{\Omega}_s} f W \, \rho \, \mathrm{d}\rho \, \mathrm{d}z = 0. \tag{2.101}$$

These constraints together describe a particle under an axial body force f in equilibrium with the surrounding flow, and automatically calculates the equilibrium particle velocity.

2.6 Results

We now present results from both the MoR solutions and the non-linear ALE FEM solutions. We begin by considering the case of a particle in Poiseuille flow with $f = 0$, discussing the particle velocity and deformation. We then provide similar results for the case of a particle translating under an axial body force with no background Poiseuille flow. We use the ALE FEM solutions, along with relevant results from the literature where possible, to both validate the MoR solutions and probe their range of validity. Finally, we use the MoR implementation to investigate the combined impacts of the Poiseuille flow and body force on the particle shape, experienced stress, and the surrounding velocity field.

2.6.1 A particle in Poiseuille flow

We first present the wall corrections factors for the leading-order fluid problem in Figure 2.2, obtained by substituting the fluid stress into Equation (2.44) and isolating the parts which depend on the background Poiseuille flow and the particle velocity. We also present the equivalent results by Bungay and Brenner [45], obtained using a lubrication approximation for a rigid particle as $\alpha \to 1$.

Under no axial body force, the leading-order translational velocities are given by the ratio of $D^{(0)}$ and $K^{(0)}$ in Figure 2.2. We plot these MoR velocities against our FEM predictions for varying α in Figure 2.3a, using three different values of ϵ for the FEM predictions. We additionally plot the results by Murata [3] and Bungay and Brenner [45] which are valid for small and tightly-fitting rigid particles, respectively. The purely analytical solution by Bungay and Brenner [45], obtained in the limit $\alpha \to 1$, diverges quickly from the MoR and FEM solutions such that we observe a discrepancy from the FEM solution even for $\alpha = 0.9$. Conversely, the purely analytical solution by Murata [3] provides a good approximation for small α, but diverges as α increases. This too is expected, as Murata does not fully consider the tube wall, instead assuming the Poiseuille flow is unbounded. Murata's solution is identical to that obtained by the method of reflections with reflection number $j = 1$. If the particle size is small compared to the cross section of the tube then the influence of the tube wall on the flow, and thus its impact on the stresses at the particle's surface which result in the translation of the particle, is small. Both our MoR and FEM approaches impose no-slip on the tube wall, allowing the effect of the tube wall on the particle to be captured fully. This is ensured for the method of reflections if sufficient reflections are included for convergence and n in the spherical stream function series is large enough to accurately project cylindrical contributions to the undeformed surface of the particle when calculating $\tilde{v}_{(r,n)}, \tilde{v}_{(r,\theta)}, \tilde{\sigma}_{(rr,n)}$ and $\tilde{\sigma}_{(r\theta,n)}$ in Equations (2.65), (2.66), (2.68) and (2.69). Our MoR solutions are presented for $\alpha \leq 0.8$ since the number of reflections required for a solution increases with α and the choice of three non-zero terms in the spherical stream function series, corresponding to $n = 2, 4, 6$, is not enough for accurate projection when $\alpha > 0.8$. Both issues are discussed and quantified in Appendix A.4.

We observe strong agreement between our MoR and FEM solutions when ϵ is small, validating the method of reflections for this application. As α increases the non-linear predictions begin to diverge from the MoR predictions. In Figure 2.3b we quantify this divergence for three different particle sizes, presenting log-log plots of the norm of the absolute error between the FEM and MoR particle velocities over a wide range of ϵ. In each of these plots, we increase ϵ until the FEM implementation no longer converges, and note that the non-linear FEM predictions are in fact smaller than the MoR predictions. In each plot we observe a roughly straight line with average slope 2.17, indicating the predicted quadratic departure of the non-linear solution. We note that the data points with $\alpha = 0.2$ and $\epsilon = 0.05, 0.1$ are due to the accuracy limitations associated with the truncation choices in the MoR, and the

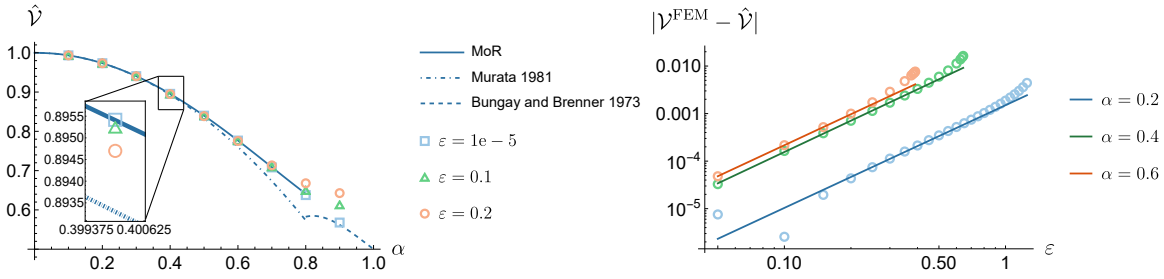

(a) (b)

Figure 2.3: (a) Predicted velocity of a particle under a background Poiseuille flow ($f = 0$) for varying α. Graphs are shown for the MoR (solid lines) and our finite element implementation for different ϵ (squares, triangles, and circles), as well as for the implementations by Murata [3] and Bungay and Brenner [45] which are valid for small and tightly-fitting rigid particles, respectively. (b) Log-log plots of the norm of the absolute error between the non-linear FEM solution and the MoR solutions, increasing ϵ for three different particle sizes. In each case, the non-linear particle velocity is smaller than the MoR prediction (see, for example, the inset in (a)). Linear lines of best fit are also presented, omitting the clear non-linear trend for $\epsilon > 0.5$. The average slope across the three lines is 2.17.

numerical nature of the FEM solution which are larger than the $\mathcal{O}(\epsilon^2)$ perturbation error. In general, we observe that the error increases with particle size for fixed ϵ as expected from (2.34) and (2.37), and note that with a smaller particle larger values of ϵ were attained before the FEM solver failed to converge. We acknowledge that the range of ϵ tested in Figure 2.3b is large, with the asymptotic solution predicting the non-linear particle velocity to within 1% when $\epsilon = 1$ and $\alpha = 0.2$. As $\alpha \to 0$, we expect the MoR solution to be robust to increases in ϵ as in this limit ϵ does not properly reflect the magnitude of the induced solid strain within the particle. This is because firstly, as previously discussed in Section 2.3.1, all lengths are scaled on the tube radius and so a factor of α is missing (see (2.37)). Additionally, the flow local to the particle approaches a uniform flow as $\alpha \to 0$, under which the particle surface deformation is $\mathcal{O}(\epsilon^2)$ [70]. These combined effects result in the observed strong agreement between the MoR and numerical methods for exceedingly large ϵ.

Interestingly, the sign of the discrepancy between the our MoR and FEM solutions is dependent on the particle size; though slight, the particle velocity decreases with ϵ when $\alpha \leq 0.6$ and increases with ϵ as $\alpha \to 1$. This is detailed in Figure 2.4a, where we present the difference between the deformed and undeformed particle velocities as predicted by the FEM solution method. Several particle sizes ranging from $\alpha = 0.1$ to 0.9 are presented over a range of ϵ. For reference, in Figure 2.4b we present the surface deformation of the particle for varying ϵ when $\alpha = 0.6$ and

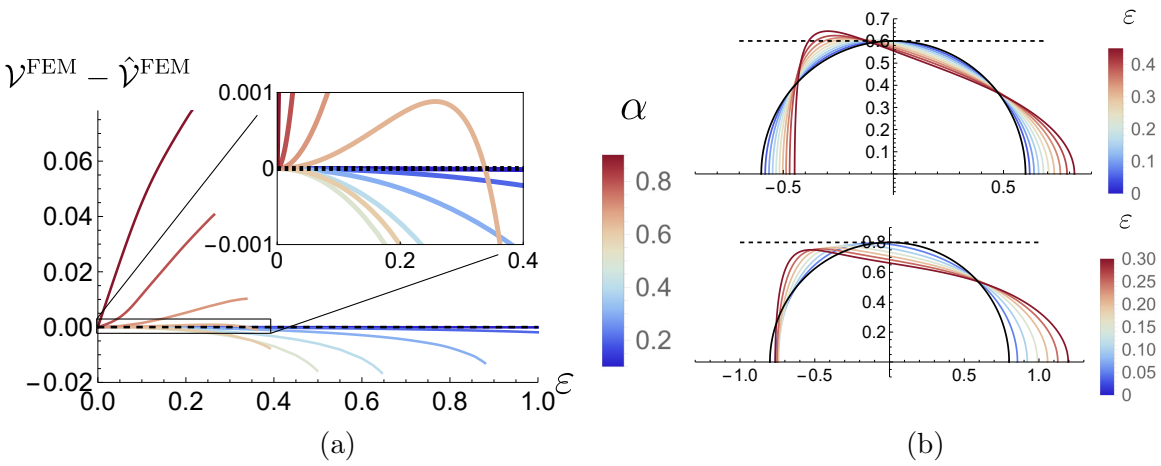

(a) (b)

Figure 2.4: (a) Difference between the deformed and rigid particle velocities using the FEM solution method, varying ϵ for several particle sizes. (b) Surface deformation (z-x plane) for various ϵ with $\alpha = 0.6$ (top) and $\alpha = 0.8$ (bottom).

$\alpha = 0.8$. For an elastic particle sedimenting in an unbounded flow, Nasouri et al. [69] showed that an incompressible particle's terminal velocity is slightly decreased ($\mathcal{O}(\epsilon^2)$) when compared with a rigid particle. This dependency is similarly observed here for particles with $\alpha \leq 0.6$ under tube confinement. We expect this is a result of the axial compression causing bulging of the particle out toward the tube wall, decreasing the minimum distance between the elastic particle and the tube wall, and increasing the particle's drag; see, for example, Figure 2.4b when $\alpha = 0.6$. For larger particles, however, we observe the reverse dependence. Here, the particle deformation involves an axial elongation (see Figure 2.4b with $\alpha = 0.8$), increasing the width of the lubrication layer between the particle and tube wall which we anticipate results in an increased particle velocity. This is analogous to the results of Barakat and Shaqfeh [87] who studied the motion of closely fitting vesicles under cylindrical confinement with varying initial shapes including spherical. We note also that the dependency of the particle velocity on ϵ is not strictly monotonic. In Figure 2.4a, when $\alpha = 0.65$, the particle velocity initially increases and then decreases with ϵ. We identify this particle size as the transition region between these two dependencies. Due to the limitations of our numerical method, it is unclear whether the graphs with larger α turn around if ϵ is increased further. More sophisticated numerical methods, or alternate asymptotic approaches are required to fully understand the limit of a soft particle ($\epsilon \to \infty$).

We now calculate the leading-order surface deformation of the particle, presenting results in Figure 2.5. Here, we compare our MoR and FEM solutions for various

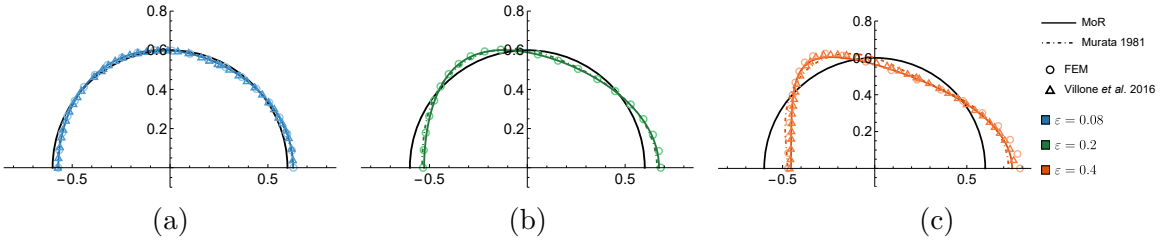

(a) (b) (c)

Figure 2.5: Surface deformation with $\alpha = 0.6$ and $f = 0$ for (a) $\epsilon = 0.08$, (b) $\epsilon = 0.2$, and (c) $\epsilon = 0.4$. Graphs are shown for both the MoR (solid, coloured lines) and our ALE FEM implementation (circles), as well as for the implementations by Murata [3] and where possible Villone et al. [2]. In each plot, we also show the undeformed particle boundary via the solid, black lines.

values of ϵ with the implementation by Murata [3], and, where possible, the ALE FEM fluid structure interaction simulations conducted by Villone et al. [2]. For small ϵ (Figure 2.5a), we see agreement between all four methods. As we increase ϵ, the analytical predictions begin to diverge from the non-linear FEM solutions. Murata [3] is the first to diverge due to the lack of proper consideration of the tube wall. With the tube wall properly considered, our MoR solutions more accurately mimic those predicted by both our FEM solutions and those by Villone et al. [2], achieving the predicted bullet-like shape at $\epsilon = 0.4$.

We quantify the performance of the MoR solution in comparison to Murata [3] in Figure 2.6, where we present log-log plots of the L^2-norm of the departure of the FEM displacement from the MoR solutions and those predicted by Murata [3], averaging across the particle boundary. For each α tested we observe a comparatively smaller error in the MoR deformation, as was qualitatively observed in Figure 2.5. The slope of each line of best fit reflects the dependence of the departure on ϵ. As expected, the MoR plots have an average slope of 2.00, since the MoR solutions accurately approximate the $\mathcal{O}(\epsilon)$ contribution to the particle deformation. Instead testing the Murata [3] predictions, we observe an average slope of 1.07, indicating the purely analytic solution does not predict the leading-order particle deformation as accurately as the MoR solution.

2.6.2 A particle under an axial body force

We now investigate the impact of applying an axial body force with magnitude f with no driving Poiseuille flow. We note that if the body force here is the effect of gravity, we model the sedimentation of a particle under tube confinement. In Section 2.2.2 we non-dimensionalised using the Poiseuille velocity V_0. In the absence of the background

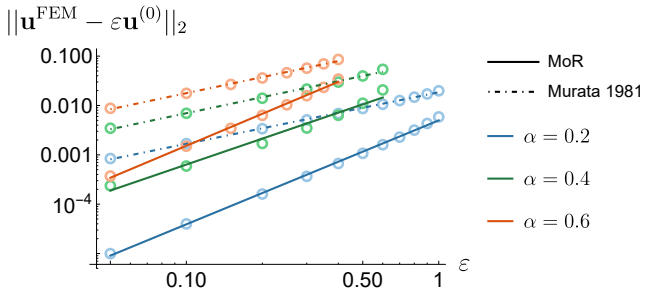

Figure 2.6: Log-log plots of the L^2-norm of the departure of the FEM displacement along the particle boundary from the MoR solutions (solid lines of best fit) and Murata [3] (dot-dashed lines of best fit) for three different values of ϵ. Here, the average gradient using the MoR solution is 2.00 and using Murata is 1.07.

Poiseuille flow, the velocity scale V_0 is redefined and determined by balancing viscous stresses with the body force to obtain $V_0 = \rho_0^2 f_0/\mu_f$, where f_0 is the typical body force magnitude. Using this scaling we recover Equation (2.47) which determines the relationship between the body force and particle velocity $\widetilde{\mathcal{V}}$. In Figure 2.7a we present $\widetilde{\mathcal{V}}$ for varying particle sizes, choosing the dimensionless $f = 10$ to obtain an ϵ range which is comparable to the above analysis for a particle in Poiseuille flow. We present MoR and FEM predictions, and also the results of Murata [70] and Bungay and Brenner [45], which describe rigid particles sedimenting in an unbounded flow and under strong tube confinement, respectively. We note that the behaviour as $\alpha \to 0$, $\widetilde{\mathcal{V}} \propto \alpha^2$, is a consequence of the choice of length scale ρ_0 which is convenient for the MoR. In this limit, the total body force applied to the particle is proportional to α^3 and the Stokes drag force is proportional to α, resulting in the observed behaviour. Re-dimensionalising (2.47) we recover consistency with the standard result for the sedimentation velocity of a rigid particle in an unbounded flow. Conversely, as $\alpha \to 1$, $\widetilde{\mathcal{V}}$ is decreased by the tube wall, since $K^{(0)} \propto \delta^{-5/2}, \delta = (1-\alpha)/\alpha$ in this limit. The trade-off between these two effects leads to a maximum translational velocity at an intermediate value when $\alpha \approx 0.4$. At this value we see the largest translational velocity for a given body force.

We see Murata's prediction, which considers an unbounded external flow, quickly diverges from the MoR solution for an equivalent particle under tube confinement. The prediction by Bungay and Brenner [45] also diverges from the MoR and FEM predictions when $\alpha = 0.8$. Unsurprisingly, the MoR and FEM predictions are consistent for small ϵ.

In Figure 2.7b we present log-log plots of the norm of the absolute error between the FEM and MoR predictions for the particle velocity over a wide range of ϵ, sim-

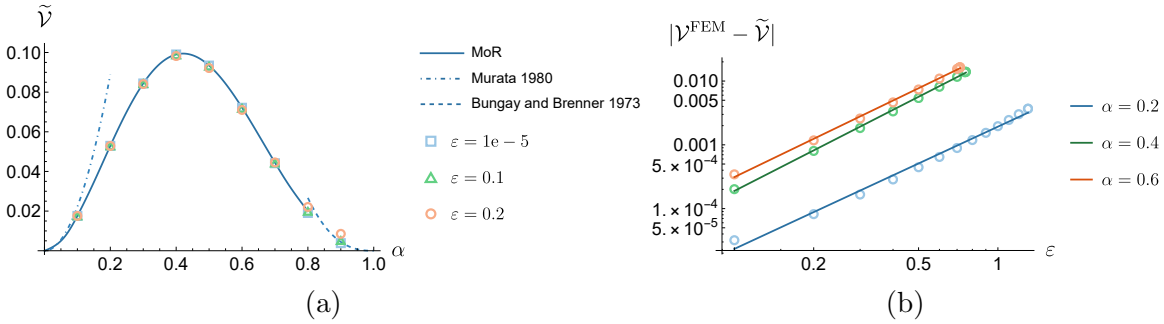

(a) (b)

Figure 2.7: (a) Equilibrium velocity of a particle with $f = 10$ and no background Poiseuille flow for varying α. Graphs are shown for the MoR (solid lines) and our finite element implementation for different ϵ (squares, triangles, and circles), as well as for the implementations by Murata [70] and Bungay and Brenner [45] which are valid for small and tightly-fitting rigid particles, respectively. (b) Log-log plots of the norm of the absolute error between the non-linear FEM solution from the MoR solutions, increasing ϵ for three different particle sizes. Linear lines of best fit are also presented with the average slope being 2.00.

ilar to Figure 2.3b for a particle in Poiseuille flow. We note the FEM predictions are smaller than the MoR solution for each presented α and again observe quadratic divergence, with the average slope of 2.00. We observe the absolute error is comparable to Figure 2.3b, though we note the relative error is larger than in the purely pressure-driven case since the particle velocity in Figure 2.7a is typically $\mathcal{O}(0.1)$.

For an elastic particle subject to an axial body force in an unbounded domain the leading-order surface deformation is zero [69, 70]. Consequently, any leading-order surface deformation predicted by our MoR and finite element implementations is caused directly by the tube walls. In Figure 2.8 we present surface deformation plots for varying ϵ, again choosing $f = 10$. For a positive f we observe a similar bullet-like shape to that induced by the Poiseuille flow, though note the particle appears to have a shorter axial length. We attribute the decrease in particle velocity in Figure 2.7a to the bulging effect this has on the particle, most visible in Figure 2.8 with $\epsilon = 0.7$ in the FEM solution, decreasing the gap width between the particle and tube wall. As $\alpha \to 1$ we expect instead that the particle is stretched along the $z-$axis, resulting in an increased gap width [87]. This stretching increases the particle velocity as observed in Figure 2.7a when $\alpha = 0.9$. We also computed $||\boldsymbol{u}^{\text{FEM}} - \boldsymbol{u}^{(0)}||_2$ along the particle boundary, which again indicated the error of the MoR solution was $\mathcal{O}(\epsilon^2)$.

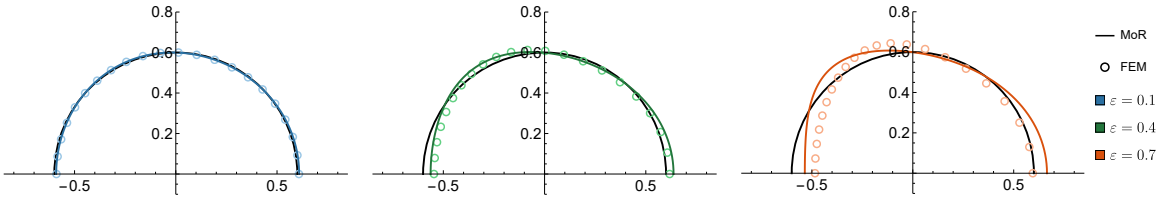

(a) (b) (c)

Figure 2.8: Surface deformation with $\alpha = 0.6$, $f = 10$, and no driving Poiseuille flow for (a) $\epsilon = 0.1$, (b) $\epsilon = 0.4$, and (c) $\epsilon = 0.7$. Graphs are shown for both the MoR (solid, coloured lines) and our ALE FEM implementation (circles). In each plot, we also show the undeformed particle boundary via the solid, black lines.

2.6.3 Combined effects of the Poiseuille flow and body force

Having validated the MoR solutions using the non-linear ALE FEM implementation, we proceed by only considering the MoR solutions, and operating within their tested range of validity. We investigate the combined effects of the driving Poiseuille flow and applied body force by linearly combining the velocities, stresses, and deformations obtained from separately solving the problems with no applied body force and no driving Poiseuille flow. For consistency, we again scale the velocity on the background Poiseuille flow by using V_0 as presented in (2.9). From these individual problems we observe both left and right-pointing bullet-like shapes suggesting that for a given α, there exists a negative (pointing upstream) body force magnitude such that these shapes approximately cancel. When this critical body force is applied, we see little surface deformation, though it is not identically zero. This critical body force at which we predict little surface deformation is represented in Figure 2.9 by the green line, where we use the deformation at $\theta = 0$ as a metric to represent this scenario. The surface displacement of the particle at $\theta = 0$ is positive above the green line and negative below such that Figure 2.9 forms a phase diagram, with the particle taking the shape of a rightward-pointing bullet above the green line, and a leftward-pointing bullet below it. Examples of these bullet-like shapes are inset in Figure 2.9, with each one corresponding to the closest red dot.

Within the context of mechanosensitive particles, it is important to consider how the solid stress, in particular the shear stress $\sigma^{(0)}_{s,r\theta}$, is distributed throughout the bulk of the particle. Figure 2.10 details the minimum and maximum values of $\sigma^{(0)}_{s,r\theta}$ with $\alpha = 0.6$ for a range of axial body forces; the range of stress values obtained throughout the bulk is contained in the shaded region. With $f = 0$ we have no body force and thus observe the stress developed purely due to the background Poiseuille flow. To study the induced stress in the bulk we consider three choices for the applied body force

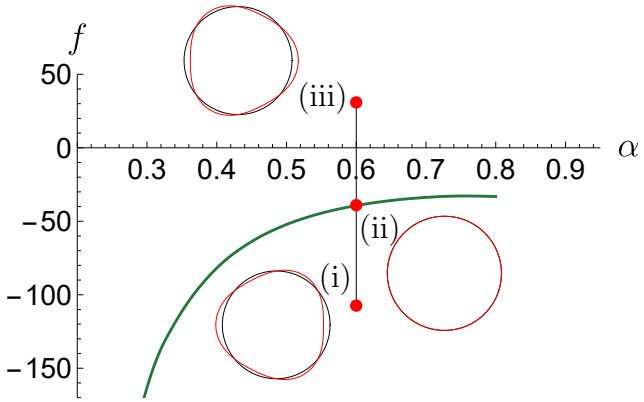

Figure 2.9: Deformation phase diagram for different f and α. The green line corresponds to the critical velocity at which there is little deformation of the particle boundary. Above this line the shape is that of a bullet pointing to the right, and below the shape is that of a bullet to the left. Examples of the surface deformation are given with $\epsilon = 0.1$ (undeformed particle in black), with each corresponding to the closest red dot. The applied body forces corresponding to the labels (i), (ii), and (iii) are $f = -107.7, -39.3$ and 31.0, respectively. Plots generated using our MoR implementation.

$f = -107.7, -39.3$ and 31.0 from left to right, which correspond to the translational velocities $\mathcal{V}^{(0)} = 0, 0.493$ and 1. As shown in Figure 2.9, these choices, marked by the red dots, serve as examples for the different kinds of surface deformation: a leftward-pointing bullet, little radial deformation at $r = \alpha$ and $\theta = 0$, and a rightward-pointing bullet. With $f = -107.7$ ($\mathcal{V}^{(0)} = 0$), the particle is pinned in the lab frame and so $\sigma^{(0)}_{s,r\theta}$ is negative in the upper half, corresponding to clockwise shear, and positive in the lower half, corresponding to anti-clockwise shear. For the plots with little deformation at $\theta = 0$, corresponding to $f = -39.3$ ($\mathcal{V}^{(0)} = 0.493$), we see a similar profile, except with a lower magnitude since the sliding wall reduces the shearing effect of the background Poiseuille flow on the particle surface. With $f = 31.0$ ($\mathcal{V}^{(0)} = 1$), we see that the shearing effect from the sliding wall now dominates such that $\sigma^{(0)}_{s,r\theta}$ with $r = \alpha$ and $\theta = \pi/2$ in the upper half is positive, corresponding to anti-clockwise shear. Closer to the tube axis, we still observe negative $\sigma^{(0)}_{s,r\theta}$ in the upper half, due to the shearing effect of the Poiseuille flow. By increasing the body force magnitude further, the sliding wall would dominate more strongly such that $\sigma^{(0)}_{s,r\theta}$ is completely positive in the upper half and negative in the lower half.

This is evident in Figure 2.11 where we present the corresponding leading-order and first-order streamline plots with the body force magnitudes $f = -107.7, -39.3, 100.3$ and $\alpha = 0.6$. In Figure 2.11a, when the particle is pinned in the lab frame, the streamlines divert around the sphere generating a large clockwise shear stress on the particle

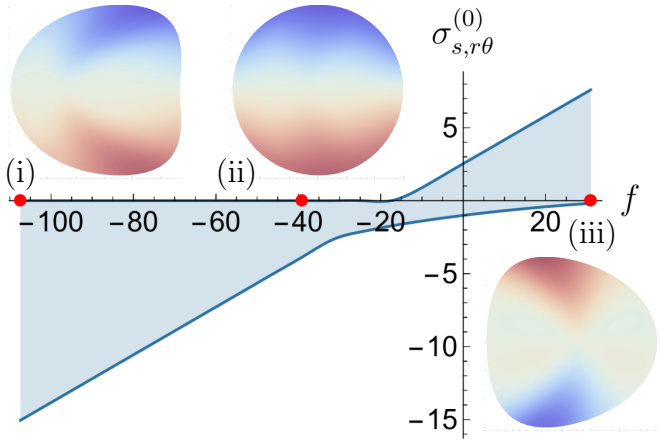

Figure 2.10: Maximal and minimal value of $\sigma^{(0)}_{s,r\theta}$ for varying translational velocities with $\alpha = 0.6$, where the shaded region indicates the range of values obtained throughout the particle bulk. For $f = -107.7, -39.3, 31.0$ ((i), (ii), (iii)) we present the stress throughout the bulk of the particle. These values are chosen identically to those in Figure 2.9, and are representative of the different key boundary shapes obtained by the particle. Here, red and blue correspond to positive (anti-clockwise) and negative (clockwise) stresses, respectively. The stress has been calculated using the MoR.

surface, concentrated around $\theta = \pi/2$. In Figure 2.11b, at the critical force in which we observe little deformation $f = -39.3$ ($\mathcal{V}^{(0)} = 0.493$), the streamlines are more horizontal, resulting in a reduced shear stress on the particle surface. In Figure 2.11c, where the particle velocity $\mathcal{V} = 1.5$, we observe a circulation region between the particle and the tube wall. Here, the body force instead forces the translational velocity of the particle to exceed the background Poiseuille flow. As a consequence of the tube wall the motion of the particle to the right forces fluid back upstream, resulting in the circulation region. The faster the particle, the more pronounced the circulation region. Consequently, the shear stress imposed on the sphere and the magnitude of the deformation are also larger. By manipulating the particle's velocity using a body force the traction in the upper half of the particle varies from clockwise to anticlockwise shear and determines the left and right-bullet shapes observed in Figures 2.9 and 2.10.

We also consider the effect of the leading-order deformation on the flow field, presenting streamline plots for the first-order correction in Figures 2.11d to 2.11f. Since the first-order contribution to the particle velocity is zero, the first-order correction to the flow field only accounts for the surface deformation of the particle through (2.55). The magnitude of the flow field is largest on the particle surface when $\theta = \pi/2$ where we observe the largest shear stress. The magnitude of the first-order correction de-

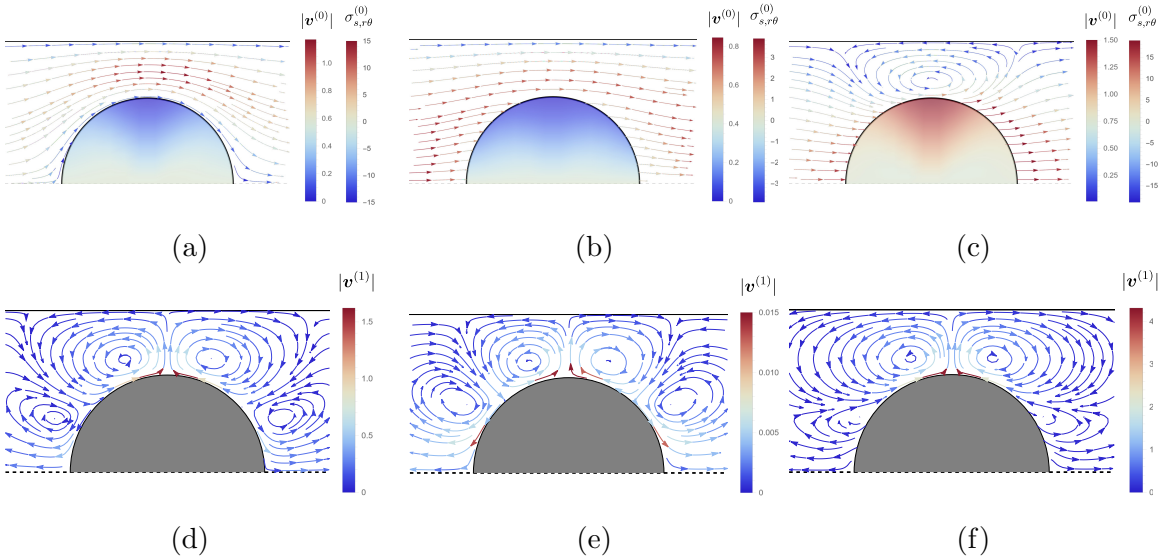

Figure 2.11: Leading-order ((a), (b), (c)) and first-order ((d), (e), (f)) streamline plots in the lab frame of reference with $\alpha = 0.6$ and $f = -107.7, -39.3, 100.3$. Plots generated using our MoR implementation. We present the corresponding $\sigma^{(0)}_{r\theta}$ in the leading-order plots throughout the undeformed particle bulk and note that here plots (a) & (b) correspond to (i) & (ii) as presented in Figure 2.10. The latter case $f = 100.3$, corresponding to a particle velocity $\mathcal{V}^{(0)} = 1.5$, is chosen to demonstrate the circulation region which is present when the particle is accelerated faster than the background Poiseuille flow.

cays quickly away from the particle surface to account for the remaining boundary conditions (2.53) and (2.54). We note that the magnitude of the first-order correction to the flow field is far smaller in Figure 2.11e which reflects the small leading-order displacement observed in Figure 2.9. The sign of the leading-order velocity field in the particle frame drives the direction of its resulting left-right bullet shape such that we observe similar circulation regions in each plot.

2.7 Conclusions

We present an asymptotic model for an elastic particle translating axially along the centre-line of a cylindrical tube, subject to an axial body force and driving Poiseuille flow. We work in the limit of a small ratio of viscous fluid stress to elastic stiffness and calculate the leading-order flow field, deformation, and relevant stress components. We show that the leading-order fluid problem decouples from the leading-order solid problem and solve for the fluid flow around a rigid sphere. The leading-order fluid tractions are substituted into the leading-order solid problem to calculate the result-

ing deformation and solid stress components. We then consider the first-order fluid problem and find that the leading-order deformation does not affect the next-order translational velocity. This was known for an elastic particle in an unbounded flow and has been extended here to include tube confinement. This result has important implications for interpreting the experimental results of Noichl and Schönecker [72] who observed large deviations in sedimentation velocity ($\sim 10\%$) for small, stiff, non-heavy particles ($\alpha \sim 0.1, \epsilon \sim 10^{-6}$) when compared with a rigid particle. One explanation for their observation of a large difference in velocity compared to our prediction of a small difference is that the experimental system does not reach steady state, which could be due to the effects of inertia in the fluid or the finite axial length of the domain. We also present a non-linear numerical finite element model used to validate the MoR solutions and investigate their range of validity. We find that the leading-order MoR solutions form an accurate simplification of the non-linear problem over a considerable range in ϵ and α, especially for the case of a particle in Poiseuille flow. Moreover, we quantify the quadratic departure between the two solution methods for the predicted particle velocity and surface displacement. Where possible, we also compare our solutions to those in the literature, finding the MoR provides semi-analytic solutions that hold across a range of α where previous analytical solutions do not apply.

The above results could be exploited in physical systems. For example, a body force could be selected in order to minimize deformation and preserve the initial spherical shape of a particle. A body force could equally be chosen to minimise the shearing effect on the particle or pin the particle in the flow. Due to the simplicity of the problem geometry the predicted surface deformation could be experimentally validated for either a sedimenting sphere in a quiescent fluid, a sphere in equilibrium with Poiseuille flow [1], or a combination of both. The translational velocities of rigid and deformable spheres could also be compared to verify the weak impact of surface deformation on translational velocity. Once validated experimentally, one could use these results as a tool for the characterisation of the elastic properties of the particle as has been done with previous studies [1, 29, 71]. If a greater precision is required, the MoR could again be used to solve the first-order solid problem. This could then be used in conjunction with the reciprocal theorem, or through calculation of the second-order fluid problem, to better understand the impact of elasticity on the particle velocity. Murata [70] showed that a compressible particle in an unbounded flow may have an increased or decreased velocity depending on its elastic constants. The effects of compressibility could also be investigated using our framework.

Code availability

Our ALE FEM implementation for an elastic particle translating through a fluid-filled tube is freely available at the GitHub repository: `https://github.com/finneysimon/stokes_elasticity_ALE_FSI.git`.

Chapter 3

Weakly deformable hydrogel-coated cell in an unbounded Stokes flow

3.1 Chapter summary

We provide a framework to analytically calculate the small deformation of a hydrogel coated cell modelled as an incompressible bag of viscous fluid surrounded by a linearly poroelastic coating when exposed to any unbounded Stokes flow. Importantly, the external Stokes flow may depend non-linearly on the spatial coordinates in the far field. Using our framework, the fluid flow is determined by prescribing the background flow with no coated cell (this is given by the far-field flow) and adding a local correction to satisfy the interfacial conditions on the cell and coating surfaces. Once calculated, the surface tractions and internal Darcy pressure are then computed and used to calculate the resulting coating deformation. Special attention is paid to the limiting case of zero cell size, which is shown to reduce to a linearly poroelastic particle in an unbounded Stokes flow. This limiting case forms a canonical FSI problem which warrants its own analysis, and forms a direct extension to the work of Young et al. [4], who considered a linearly poroelastic particle suspended in an unbounded Stokes flow which depends linearly on the spatial coordinates in the far field.

To demonstrate the power of the framework, we present two example far-field flow profiles, shear flow and Poiseuille flow. The former case was also considered by Young et al. [4], though we do not provide quantitative comparison since different interfacial conditions were imposed; the latter case is of interest to many biological applications, for example in drug delivery systems, and cannot be investigated using the approach of Young et al. [4].

When the external flow involves an external boundary, for example Poiseuille flow through a cylindrical tube, adding a local correction to the background flow disrupts the no-flow boundary conditions on the external tube wall. However, we note that this disruption is small if the particle is far from the boundary [3] and predictions in unbounded domains can be exploited. Maintaining the assumption of small deformation, semi-analytic methods, such as the method of reflections utilised in Chapter 2, may be used to capture the effect of an external boundary more accurately. When the particle surface and external boundary are close in proximity, the MoR converges poorly and a full numerical solution, or further asymptotic reductions, for example through the use of lubrication theory, are required to determine the flow.

Under the assumption of linear poroelasticity, the particle deformation is described by the Navier–Láme problem (compressible linear elasticity). Obtaining a complete, three-dimensional general solution to the Navier–Láme problem has been a debated topic over the last century, and still remains an active field [114–117]. Papkovich [118], Neuber [119] each independently derived the same non-unique harmonic solution, known as the Papkovich–Neuber representation. By removing one harmonic function, the Papkovich–Neuber representation was later shown to be complete for a radially convex domain, which includes a sphere [120–122]. More recently, the Papkovich–Neuber representation was extended using quaternion-valued potentials to provide a complete solution to the Navier–Láme problem irrespective of the choice of domain [116, 123]. In this work, we opt to use the Papkovich–Neuber representation since it is written explicitly using the solid spherical harmonic functions, which are convenient for coupling to Lamb's general solution for Stokes flow which also involves the solid spherical harmonics [124].

This chapter is structured as follows. In Section 3.2 we provide the dimensionless governing equations and boundary conditions describing the external Stokes flow, the linearly poroelastic coating, and the cell in the small deformation limit. We then present general solutions for the Stokes and poroelastic equations, and calculate the fluid flow and resulting deformation given a general background flow in Section 3.3. In Section 3.4 we detail two example background flow profiles, shear flow and Poiseuille flow. For each background flow, we present and analyse closed-form solutions for the coated cell's velocity, rotation, and deformation and investigate the impacts of the cell size, and the coating's permeability, slip, and Poisson's ratio. We also pay special attention to the limiting case of a poroelastic particle under any unbounded background Stokes flow. By choosing further limiting values of the problem parameters, we demonstrate exact agreement between our results and those obtained by

Murata [3] who considered an impermeable, incompressible elastic particle with no-slip boundary conditions in a general unbounded flow. Finally, we provide closing discussions and outline future extensions in Section 3.5.

3.2 Governing equations and boundary conditions

We consider a three-dimensional, initially spherical, hydrogel-coated cell fully immersed in an incompressible viscous fluid as shown in Figure 3.1. We assume the exterior flow is unbounded and driven solely by far-field conditions. The far-field conditions could reflect a flow involving an external boundary that is not explicitly considered here. We use spherical coordinates (r, θ, ϕ) with unit vectors $(\boldsymbol{e}_r, \boldsymbol{e}_\theta, \boldsymbol{e}_\phi)$ and align $r = 0$ with the centre of the coated cell. Here, $\theta \in [0, \pi)$ is the polar angle and $\phi \in [0, 2\pi)$ is the azimuthal angle. The cell, hydrogel, and external fluid domains are denoted by Ω_c, Ω_h, and Ω_f, respectively, with the interfaces between them denoted by $\partial\Omega_0$ and $\partial\Omega_1$. The cell and coating have undeformed radii a_0 and a_1, respectively, such that the undeformed boundaries $\partial\widehat{\Omega}_i$ are defined as $r = a_i, i = 0, 1$. We assume the system is in equilibrium and work in a frame of reference that translates with the particle, noting that the particle's translational velocity in the lab frame is unknown and given by $\boldsymbol{V}_{tr}$. In this frame the particle rotates according to

$$\boldsymbol{v}_\Omega = r[\boldsymbol{\Omega} \times \boldsymbol{e}_r], \tag{3.1}$$

where $\boldsymbol{\Omega}$ remains to be determined. It will also be useful to define the unit normal and tangents to the cell and coating as $\boldsymbol{n}_i$ and $\boldsymbol{t}_i^j$, $i = 0, 1$, $j = 1, 2$, respectively, where both $\boldsymbol{n}_i$ point toward the surrounding external fluid.

In the analysis that follows, we assume the coating deformation is small such that the well-known equations of linear poroelasticity apply in the coating [125], and interfacial conditions are linearised onto their respective undeformed surfaces. For brevity, we present only the dimensionless linearised problem in the main text. This is additionally derived in Appendix C as the leading-order asymptotic reduction of a non-linear poroelastic coating in the small-deformation limit. To avoid confusion, we define all necessary quantities in both the main text and in Appendix C such that each section is self contained.

The non-dimensionalisation choices are presented in Appendix C.3 and are summarised as follows. Lengths, velocities, and pressures/stresses are scaled on the outer coating radius a_1, the typical far-field velocity V_0 (see Figure 3.1 for examples of V_0),

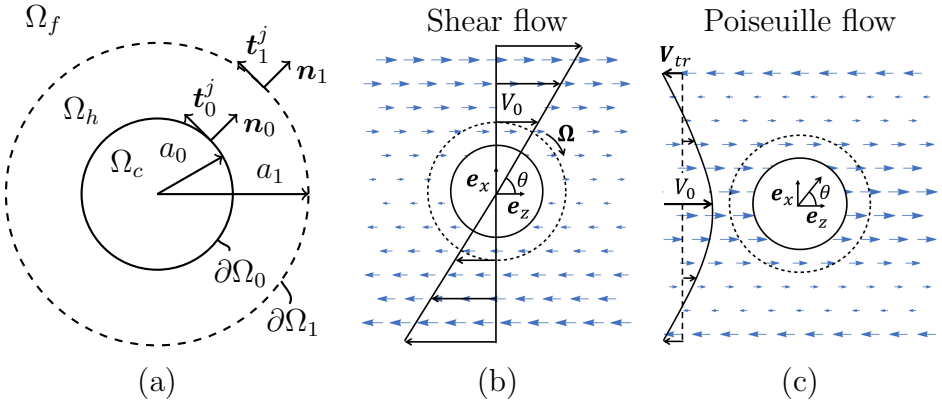

Figure 3.1: (a) Coated cell fully immersed in a Stokes flow. The cell, coating and fluid phases are denoted by Ω_c, Ω_h, and Ω_f, respectively. (b) Shear flow and (c) Poiseuille flow presented as far-field flows.

and $\mu_f V_0/a_1$ where μ_f is the fluid viscosity, respectively. The dimensionless parameter

$$\epsilon = \frac{\mu_f V_0}{\mu_s a_1}, \tag{3.2}$$

where μ_s is the shear modulus of the coating, forms a scale for the solid strain. Here, ϵ is defined as the ratio of typical viscous stresses in the external flow to the elastic stiffness of the solid skeleton. Finally, the deformation is scaled on ϵa_1. Assuming $\epsilon \ll 1$, we expect the solid strain and coating deformation to be small.

3.2.1 External flow

Neglecting inertial terms, the flow of external fluid in Ω_f is governed by the incompressible Stokes equations,

$$\nabla \cdot \boldsymbol{\sigma}_f = \mathbf{0}, \tag{3.3}$$

$$\nabla \cdot \boldsymbol{v} = 0, \tag{3.4}$$

where $\boldsymbol{v}$ is the fluid velocity and $\boldsymbol{\sigma}_f$ is the stress tensor for a Newtonian fluid given by

$$\boldsymbol{\sigma}_f = -p_f \boldsymbol{I} + \left[\nabla \boldsymbol{v} + (\nabla \boldsymbol{v})^T\right], \tag{3.5}$$

where P is the Stokes pressure. The superscript T denotes the transpose. The Stokes pressure is determined up to an arbitrary reference pressure that we will specify later.

We calculate the net force $\boldsymbol{F}_{\text{force}}$ and torque $\boldsymbol{T}$ exerted on the particle by the surrounding fluid via the surface integrals

$$\boldsymbol{F}_{\text{force}} = \int_{\phi=0}^{2\pi} \int_{\theta=0}^{\pi} \boldsymbol{\sigma}_f|_{r=1} \cdot \boldsymbol{n}_1 \ \sin\theta \ \mathrm{d}\theta \ \mathrm{d}\phi, \tag{3.6}$$

$$\boldsymbol{T} = \int_{\phi=0}^{2\pi} \int_{\theta=0}^{\pi} \boldsymbol{r} \times (\boldsymbol{\sigma}_f|_{r=1} \cdot \boldsymbol{n}_1) \ \sin\theta \ \mathrm{d}\theta \ \mathrm{d}\phi, \tag{3.7}$$

where to leading order in ϵ we have $\boldsymbol{n}_i = \boldsymbol{e}_r$. For a particle in equilibrium with the surrounding flow we impose

$$\boldsymbol{F}_{\text{force}} = \boldsymbol{T} = \boldsymbol{0}, \tag{3.8}$$

from which we determine the particle's translational and angular velocities, $\boldsymbol{V}_{tr}$ and $\boldsymbol{\Omega}$, respectively.

3.2.2 Hydrogel coating

We focus on capturing the hydrodynamic (not chemical) interactions and model the coating as a poroelastic material comprised of a porous and deformable solid phase (skeleton) fully saturated by an interstitial fluid phase which is identical to the external fluid. We assume both phases are individually incompressible, though compression of the solid skeleton is permitted through local changes to the internal pore structure.

The local volume fractions of the fluid and solid phases are denoted by ϕ_f and ϕ_s, respectively; ϕ_f is also called the porosity. Since the fluid fully saturates the solid skeleton, we have $\phi_f + \phi_s = 1$. Under the assumption of infinitesimal strain, the porosity is connected to the solid skeleton displacement $\boldsymbol{u}$ via

$$\frac{\phi_f - \phi_{f,0}}{1 - \phi_{f,0}} = \epsilon \nabla \cdot \boldsymbol{u}. \tag{3.9}$$

where $\phi_{f,0}$ is the initial porosity of coating in its relaxed/undeformed state which is assumed to be constant.

Flow in the coating relative to the solid skeleton is governed by Darcy's law,

$$\phi_{f,0}(\boldsymbol{v}_p - \boldsymbol{v}_s) = -\tilde{\kappa}_0 \nabla p_p, \tag{3.10}$$

where $\boldsymbol{v}_p$ is the fluid velocity in the coating, $\boldsymbol{v}_s$ is the velocity of the solid skeleton, p_p is the pore/Darcy pressure, and the Darcy number $\tilde{\kappa}_0 = \kappa_0 / a_1^2$, where $\kappa_0 = \kappa(\phi_{f,0})$ is the uniform permeability field associated with the initial porosity. In general the permeability will change as the solid skeleton deforms; however, under the assumption

of small strain, we treat the permeability as constant [125]. The solid velocity is given by the rigid-body rotation,

$$\boldsymbol{v}_s = \boldsymbol{v}_\Omega \tag{3.11}$$

since we seek steady solutions in a frame of reference that translates with the particle. It will also be useful to define the total internal volumetric flux $\boldsymbol{q}$ as

$$\boldsymbol{q} = \phi_{f,0}\boldsymbol{v}_p + (1-\phi_{f,0})\boldsymbol{v}_s = \phi_{f,0}(\boldsymbol{v}_p - \boldsymbol{v}_s) + \boldsymbol{v}_s, \tag{3.12}$$

where $\phi_{f,0}(\boldsymbol{v}_p - \boldsymbol{v}_s)$ is the Darcy flow appearing in (3.10). Conservation of mass for the fluid and solid phases gives,

$$\nabla \cdot \boldsymbol{v}_p = 0, \tag{3.13}$$

$$\nabla \cdot \boldsymbol{v}_s = 0, \tag{3.14}$$

where we note that since $\boldsymbol{v}_s$ is limited to the rigid body rotation (3.1), (3.14) is trivially satisfied.

To describe how the fluid and solid phases share internal stresses we write the total stress,

$$\boldsymbol{\sigma}_p = \boldsymbol{\sigma}' - p_p\boldsymbol{I}, \tag{3.15}$$

where $\boldsymbol{\sigma}'$ is Terzaghi's effective stress, which is the force per unit area carried by the solid skeleton. Details of this stress decomposition may be found in [125]. Under the assumption of infinitesimal strain, we use a linear elastic constitutive relation for effective solid stress of the coating,

$$\boldsymbol{\sigma}' = \frac{2\nu}{1-2\nu}\left(\nabla \cdot \boldsymbol{u}\right)\boldsymbol{I} + 2\boldsymbol{\varepsilon}, \tag{3.16}$$

where the Poisson's ratio ν is the of the ratio of the transverse contraction strain to the longitudinal extension strain in the direction of stretching force. Poisson's ratio typically varies between $\nu = 0$, where the material may be compressed without developing transverse strains, and $\nu = 1/2$, where the material is incompressible. The strain tensor $\boldsymbol{\varepsilon}$ in (3.16) is given by

$$\boldsymbol{\varepsilon} = \frac{1}{2}\left[\nabla\boldsymbol{u} + (\nabla\boldsymbol{u})^T\right]. \tag{3.17}$$

We note that the elastic constants ν and μ_s describe the mechanical properties of the solid skeleton and depend on both the skeleton material and its micro-structure. Balancing the total linear momentum between the fluid and solid phases we find

$$\nabla \cdot \boldsymbol{\sigma}_p = \nabla \cdot \boldsymbol{\sigma}' - \nabla p_p = \boldsymbol{0}. \tag{3.18}$$

3.2.3 Cell

We model the cell as a sack of incompressible viscous fluid enclosed by an impermeable elastic membrane. For simplicity, we will neglect the elastic resistance of the membrane, assuming it is small in comparison to the elastic resistance provided by the coating. To understanding this assumption, we begin by treating the cell membrane as an asymptotically thin spherical shell, whose deformation may be characterised by its bending stiffness M_c and in-plane stretching stiffness K_c,

$$M_c = \frac{E_c h_c^3}{12(1-\nu_c^2)}, \tag{3.19}$$

$$K_c = \frac{E_c h_c}{1-\nu_c^2}, \tag{3.20}$$

where μ_c, ν_c, and $E_c = 2\mu_c(1+\nu_c)$ are the shear modulus, Poisson's ratio, and the Young's modulus of the cell membrane, respectively, and $h_c \ll a_0$ is the shell thickness [126]. It may be shown that under the radial deflection ζ, the bending energy in the shell is $\sim M_c\zeta^2/a_0^4$ and the stretching energy in the shell is $\sim K_c\zeta^2/a_0^2$ [126]. The ratio of the two is then of the order $\propto h_c^2/a_0^2$, which is small. Importantly, a closed (no holes) spherical shell cannot be bent without stretching [126], and the dominant contribution to the elastic resistance of the cell is given by the shell's resistance to stretching (3.20). We note that this stretching dominant elastic response also holds for a thin coating, which will be important later in Section 3.4 where this case is considered. In general, a *membrane* is defined as a thin shell for which the bending stresses are small in comparison to the tensile stresses, and as such are disregarded [126].

As mentioned above, we neglect the elasticity of the cell membrane and assume the stretching stiffness of the cell membrane $K_c \ll K_h$, where K_h is the stretching stiffness of the hydrogel coating. Using (3.20), we approximate the stretching stiffness of the coating K_h as

$$K_h \propto \frac{E(a_1-a_0)}{1-\nu^2}, \tag{3.21}$$

where similarly $E = 2\mu_s(1+\nu)$ is the Young's modulus of the coating [127, 128].

We additionally assume the cell membrane is impermeable (see Chapter 1), and that there is no flow inside the cell. When undeformed, the cell pressure is given by the constant p_c^0, which we use as the reference pressure in the system. When deformed, we assume the constant cell pressure p_c, enforces the volumetric constraint,

$$\iiint_{\Omega_c} \mathrm{d}V = V_c = \frac{4}{3}\pi\alpha_0^3, \tag{3.22}$$

where V_c is the undeformed cell volume and $\alpha_0 = a_0/a_1$ is the dimensionless undeformed cell radius.

The deformed position of the interfaces $\partial\Omega_i$ are defined as

$$\boldsymbol{r}_i = \alpha_i \boldsymbol{e}_r + \epsilon \boldsymbol{u}(r = \alpha_i), \tag{3.23}$$

where $\alpha_1 = 1$ is the dimensionless undeformed coating radius. Taking the modulus of (3.23) we approximate the surface deformation of the particle as

$$|\boldsymbol{r}_i(\theta, \phi)| \approx \alpha_i + \epsilon\, \boldsymbol{u} \cdot \boldsymbol{e}_r|_{r=\alpha_i}. \tag{3.24}$$

Applying (3.24) to the volumetric constraint used to calculate the cell pressure (3.22) we have the expansion

$$2\pi \int_{\theta=0}^{\pi} \int_{r=0}^{\alpha_0+\epsilon u_r(r,\theta)} r^2 \sin\theta \mathrm{d}r\ \mathrm{d}\theta\ = \frac{4}{3}\pi\alpha_0^3 + 2\epsilon\pi \int_{\theta=0}^{\pi} u_r(r = \alpha_0) \sin\theta\ \mathrm{d}\theta + \mathcal{O}(\epsilon^2), \tag{3.25}$$

which requires

$$2\pi \int_{\theta=0}^{\pi} u_r(r = \alpha_0) \sin\theta\ \mathrm{d}\theta = 0. \tag{3.26}$$

We remind the reader that in (3.26) the cell pressure p_c is implicitly contained within the cell deformation, and is chosen to enforce this constraint.

3.2.4 Boundary conditions

Far from the coated cell we expect any disturbance to the external flow to be small such that

$$\boldsymbol{v} - \boldsymbol{V}_\infty - \boldsymbol{V}_{tr} \to 0 \quad \text{as} \quad r \to \infty, \tag{3.27}$$

where $\boldsymbol{V}_\infty$ and $\boldsymbol{V}_{tr}$ are the imposed external far-field flow and coated cell's constant translational velocity in the lab frame that will be determined, respectively.

On the undeformed surface between the external flow and the coating $\partial\widehat{\Omega}_1$, we impose the continuity of normal fluid flux, continuity of total stress, continuity of fluid stresses and the Beavers & Joseph slip condition [56],

$$\boldsymbol{v} \cdot \boldsymbol{n}_1 = \phi_{f,0} \boldsymbol{v}_p \cdot \boldsymbol{n}_1, \tag{3.28}$$

$$\boldsymbol{\sigma}_f \cdot \boldsymbol{n}_1 = \boldsymbol{\sigma}_p \cdot \boldsymbol{n}_1, \tag{3.29}$$

$$\boldsymbol{n}_1 \cdot \boldsymbol{\sigma}_f \cdot \boldsymbol{n}_1 = -p_p, \tag{3.30}$$

$$\boldsymbol{t}_1^j \cdot \boldsymbol{\sigma}_f \cdot \boldsymbol{n}_1 = \tilde{\gamma}((\boldsymbol{v} - \boldsymbol{q}) \cdot \boldsymbol{t}_1^j), \tag{3.31}$$

where the effective slip $\tilde{\gamma} = \gamma/\sqrt{\tilde{\kappa}_0}$ and the slip parameter γ is dependent on the material properties of the particle interface[1]. For reference, $\gamma = 0$ corresponds to a surface with perfect slip and $\gamma \to \infty$ corresponds to a surface with no-slip. To avoid confusion, we note that in Young et al. [4] the slip parameter is instead defined as $\sqrt{\tilde{\kappa}}_0/\gamma$; however, in this work we remain consistent with Beavers and Joseph [56]. These interfacial conditions form one of many viable choices for coupling a Stokes flow and poroelastic domain [56, 57, 61, 62]; the optimal choice of interfacial conditions will depend on the specific material choice and remains an active field of research [61]. By combining the interfacial conditions (3.29) and (3.30) we have the condition on $\partial\widehat{\Omega}_1$ ($r = 1$),

$$\boldsymbol{n} \cdot \boldsymbol{\sigma}' \cdot \boldsymbol{n} = 0, \tag{3.32}$$

which will be useful when calculating the particle deformation in Section 3.3.2. On the undeformed cell-coating interface, $\partial\widehat{\Omega}_0$, we impose no normal fluid flux and conservation of total stress,

$$\boldsymbol{v}_p \cdot \boldsymbol{n}_0 = 0, \tag{3.33}$$

$$\boldsymbol{\sigma}_p \cdot \boldsymbol{n}_0 = -p_c \boldsymbol{n}_0. \tag{3.34}$$

In (3.28) to (3.31), (3.33) and (3.34), $\boldsymbol{n}_i = \boldsymbol{e}_r$, $\boldsymbol{t}_i^1 = \boldsymbol{e}_\theta$, and $\boldsymbol{t}_i^2 = \boldsymbol{e}_\phi$ are the normal and tangential unit vectors to the undeformed particle surface.

3.2.5 Parameter values

We now consider the expected parameter values within the context of cell therapies. From Table 1.1, we expect the radius of a blood vessel in the liver ρ_0 to vary between $50\,\mu\text{m} < \rho_0 < 1\,\text{mm}$ [23]. We additionally assume the typical cell size ranges between $10\,\mu\text{m} < a_0 < 50\,\mu\text{m}$ where the upper bound is given by a mouse hepatocyte [25], and limit the coating thickness such that $a_1 < \rho_0$ to avoid consideration of large deformations occurring due to a cell squeezing through a small vessel. To justify the two-phase, poroelastic approach, the average pore size within the coating a_p must be small in comparison with the coating thickness, such that $a_p \ll a_1 - a_0$. In this work, we assume $10^{-2}\ \mu\text{m} < a_p < 1\ \mu\text{m}$. The permeability of the coating $\kappa_0 \sim a_p^2$ such that $10^{-16}\ \text{m}^2 < \kappa_0 < 10^{-12}\ \text{m}^2$, where the upper bound corresponds to the typical permeability for a saturated hydrogel [129, 130]. We thus expect the Darcy number to range between $10^{-10} < \tilde{\kappa}_0 < 10^{-3}$.

[1] To avoid the use of $\boldsymbol{t}_i^j$, which require a specific (and in general non-unique) parameterisation of the boundary to be chosen, (3.31) may instead be written as $\boldsymbol{n}_1 \times (\boldsymbol{\sigma}_f \cdot \boldsymbol{n}_1) = \tilde{\gamma}\boldsymbol{n}_1 \times (\boldsymbol{v} - \boldsymbol{q})$

We assume the typical viscosity of the fluid varies between $1\ \mathrm{mPa}\cdot\mathrm{s} < \mu_f < 10\ \mathrm{mPa}\cdot\mathrm{s}$, where the lower bound is water and the upper bound corresponds to the anticipated effective viscosity of blood under small shear rates [21]. As presented in Table 1.1, the external velocity scale V_0 may be as small as $40\,\mu\mathrm{m\,s^{-1}}$ in a small vessel in a mouse liver, or around $1\,\mathrm{mm\,s^{-1}}$ in a large vessel [23]. For hydrogels the Lamé constants typically range between 1 kPa and 1 MPa with a Poisson's ratio around 0.2 [4, 131]. We thus expect $10^{-9} < \epsilon < 10^{-3}$.

The membrane stiffness of a cell K_c varies hugely depending on the cell type. For instance, for red blood cells $K_c \sim 1\mu\mathrm{N\,m^{-1}}$ [132], while for macrophages $K_c \sim 100\mu\mathrm{N\,m^{-1}}$ [133]. To justify the 'no membrane' cell model we require $K_c \ll K_h$, where K_h is given by (3.21). Assuming $K_c \sim 100\mu\mathrm{N\,m^{-1}}$, it follows that we require $a_1 - a_0 \gg 0.1\mu\mathrm{m}$ for a soft hydrogel and $a_1 - a_0 \gg 0.1\mathrm{nm}$ for a stiff hydrogel, noting again that the cell size $10\,\mu\mathrm{m} < a_0 < 50\,\mu\mathrm{m}$. Other relevant cell types may be treated as an elastic bulk and characterised by a bulk Young's modulus. For example, hepatocytes have a bulk Young's modulus $E_c \sim 1\mathrm{kPa}$ [134]. In this case, we again require the elastic resistance provided by the cell to be small when compared to the resistance provided by the coating. For a soft coating, we expect the elastic contributions of a hepatocyte and its coating to be comparable; the analysis of this case forms a natural extension this thesis. In this work, we ignore the elasticity of the cell, assert that $\epsilon \ll 1$ such that the hydrogel coating is stiff, and investigate a wide range of $\tilde{\kappa}_0, \tilde{\gamma}, \alpha_0$ and α_1 to determine their effect on the mobility and deformation of the coated cell.

3.3 Method of solution

Under the assumption of infinitesimal strain, the fluid problem given by (3.3) to (3.5), (3.8), (3.10), (3.13), (3.27), (3.28), (3.30), (3.31) and (3.33) does not depend on the coating deformation, such that we have flow through a rigid porous annulus with an impermeable core. To determine the flow, we begin by prescribing the external flow in the absence of the coated cell. This is simply given by the far-field flow, to ensure the far-field condition (3.27) is satisfied. We then add a local correction due to the coated cell through the interfacial conditions (3.28), (3.30), (3.31) and (3.33) where the internal flow through the coating is given by the solution to (3.10) and (3.13).

Once the fluid problem is solved, the surface tractions and Darcy pressure drive the Navier–Láme problem (3.16) and (3.18), which can be solved subject to the boundary

conditions (3.29), (3.32) and (3.34) to calculate the particle deformation. In (3.18), p_p is known from the fluid problem and is treated as a body force.

3.3.1 The fluid problem

We first consider the external Stokes flow ($r > 1$), denoting the external velocity field in the absence of the particle by $\boldsymbol{v}^e$ and the local correction due to the particle by $\boldsymbol{v}^p$, such that

$$\boldsymbol{v} = \boldsymbol{v}^e + \boldsymbol{v}^p, \tag{3.35}$$

with the corresponding pressure fields p_f^e and p_f^p.

The far-field flow $\boldsymbol{v}^e$, given by (3.27), must satisfy Stokes equations (3.3)–(3.5) while remaining finite at the origin. Using the general solution in spherical coordinates derived by Lamb [124], we write

$$\boldsymbol{v}^e = \sum_{n=0}^{\infty} \left\{ \nabla \Phi_n^* + \nabla \times (\boldsymbol{r} \Psi_n^*) + \frac{n+3}{2(n+1)(2n+3)} r^2 \nabla P_n^* - \frac{n}{(n+1)(2n+3)} \boldsymbol{r} P_n^* \right\}, \tag{3.36}$$

$$p_f^e = \sum_{n=0}^{\infty} P_n^*, \tag{3.37}$$

where Φ_n^*, Ψ_n^*, and P_n^* are linear combinations of the regular solid spherical harmonics of degree n with constant coefficients as defined in Appendix D.1. To be clear, we write as an example,

$$\Phi_n^*(\boldsymbol{r}) = \sum_{m=-n}^{n} \Phi_{n,m}^{\mathcal{R}} \mathcal{R}_{n,m}(\boldsymbol{r}), \tag{3.38}$$

where $\mathcal{R}_{n,m}(\boldsymbol{r})$ are the regular solid spherical harmonics of degree n and order m and $\Phi_{n,m}^{\mathcal{R}}$ are the constant coefficients. The constants $\Phi_{n,m}^{\mathcal{R}}, \Psi_{n,m}^{\mathcal{R}}, P_{n,m}^{\mathcal{R}}$ are calculated to ensure the far-field condition (3.27) is satisfied.

The general solutions for the local correction to the flow and pressure fields, $\boldsymbol{v}^p$ and p_f^p, must decay as $r \to \infty$ in order to maintain the far-field condition (3.27). Hence, we find

$$\boldsymbol{v}^p = \sum_{n=1}^{\infty} \left\{ \nabla \Phi_{-n-1} + \nabla \times (\boldsymbol{r} \Psi_{-n-1}) - \frac{n-2}{2n(2n-1)} r^2 \nabla P_{-n-1} + \frac{n+1}{n(2n-1)} \boldsymbol{r} P_{-n-1} \right\}, \tag{3.39}$$

$$p_f^p = \sum_{n=1}^{\infty} P_{-n-1}, \tag{3.40}$$

where Φ_{-n-1}, Ψ_{-n-1}, and P_{-n-1} are linear combinations of the irregular solid spherical harmonics of degree n. Again, we write as an example

$$\Phi_{-n-1}(\boldsymbol{r}) = \sum_{m=-n}^{n} \Phi^{\mathcal{I}}_{n,m} \mathcal{I}_{n,m}(\boldsymbol{r}), \tag{3.41}$$

where $\mathcal{I}_{n,m}(\boldsymbol{r})$ are the irregular solid spherical harmonics and $\Phi^{\mathcal{I}}_{n,m}$ are the constant coefficients. The total velocity and pressure fields are then obtained by adding the external background flow and local correction via (3.35). For clarity, the above general solutions for the velocity field and pressure all use a spherical coordinate system.

If we instead consider the flow in the coating ($\alpha_0 < r < 1$), combining (3.10), (3.11) and (3.13), we see the internal pore pressure satisfies Laplace's equation,

$$\nabla^2 p_p = 0, \tag{3.42}$$

which has a general solution in spherical coordinates, given by

$$p_p = \sum_{n=0}^{\infty} p_n + \sum_{n=0}^{\infty} p_{-n-1}, \tag{3.43}$$

where p_n and p_{-n-1} are linear combinations of the regular and irregular solid spherical harmonics of degree n, respectively, similar to (3.38) and (3.41). The internal Darcy flow is then given by (3.10), and the total internal flux by (3.12).

The coefficients of the solid spherical harmonic functions $\Phi_{-n-1}, \Psi_{-n-1}, P_{-n-1}, p_n$, and p_{-n-1} are determined by the interfacial conditions (3.28), (3.30), (3.31) and (3.33). It is convenient to rewrite these interfacial conditions in terms of radial components and derivatives, the details of which are presented in Appendix D.3. By using (D.8) and (D.9) we obtain the reformulated boundary conditions

$$V_r|_{r=1} = -\tilde{\kappa}_0 \frac{\partial p_p}{\partial r}|_{r=1}, \tag{3.44}$$

$$\sigma_{f,rr}|_{r=1} = -p_p|_{r=1}, \tag{3.45}$$

$$\left[r\frac{\partial \sigma_{f,rr}}{\partial r} + 3(p_f + \sigma_{f,rr}) \right]_{r=1} = \tilde{\gamma} \left[r\frac{\partial V_r}{\partial r} + 2V_r + \tilde{\kappa}_0 \left(r\frac{\partial^2 p_f}{\partial r^2} + 2\frac{\partial p_p}{\partial r} \right) \right]_{r=1}, \tag{3.46}$$

$$\left[\boldsymbol{r} \cdot \nabla \times (\boldsymbol{\sigma}_f \cdot \boldsymbol{e}_r) \right]_{r=1} = \left[\boldsymbol{r} \cdot \nabla \times (\tilde{\gamma} \boldsymbol{v}) - \boldsymbol{r} \cdot \nabla \times (\tilde{\gamma} \boldsymbol{v}_s) \right]_{r=1}, \tag{3.47}$$

$$\frac{\partial p_p}{\partial r}|_{r=\alpha_0} = 0. \tag{3.48}$$

Substituting the general solutions for the Stokes velocity (3.36) and (3.39), Stokes pressure (3.37) and (3.40), and Darcy pressure (3.43) we obtain the system of equations presented in (D.31)–(D.35). Exploiting the linearity of the solid spherical harmonics, we solve this system of equations simultaneously at each degree $n \geq 0$ to

give,

$$\Phi_{-n-1} = n(2n-1)\Bigg[\frac{(2(n-1)n\tilde{\kappa}_0(2(n+2)+\tilde{\gamma})-\tilde{\gamma})}{\omega}\Phi_n^* - \frac{(4(n-1)(n+1)(n+2)+\tilde{\gamma}-2\tilde{\kappa}_0\tilde{\gamma}(3+n(5+n))}{(n+1)\omega}\alpha_0^{2n+1}\Phi_n^*\Bigg] + n(2n+1)\Bigg[\frac{(n+1+2\tilde{\kappa}_0(3+(n-1)n(n+1)(n+2)))}{(n+1)(2n+3)\omega}P_n^* + \frac{n-2\tilde{\kappa}_0(3+(n-1)n(n+1)(n+2))}{(n+1)(2n+3)\omega}\alpha_0^{2n+1}P_n^* - \frac{\tilde{\gamma}(n+1-2\tilde{\kappa}_0(n^3-2n^2-6n+3)))}{2(n+1)(2n+3)\omega}P_n^* - \frac{n\tilde{\gamma}-2\tilde{\kappa}_0\tilde{\gamma}(n^3+5n^2+n-6)}{2(n+1)(2n+3)\omega}\alpha_0^{2n+1}P_n^*\Bigg], \quad (3.49)$$

$$P_{-n-1} = 2n(4n^2-1)\Bigg[\frac{2\tilde{\kappa}_0 n(n^2+n-2)-1+\tilde{\gamma}(2\tilde{\kappa}_0(n-1)n-1)}{\omega}\Phi_n^* - \frac{2\tilde{\kappa}_0(n-1)n(n+1)(n+2)+n+n\tilde{\gamma}(1-2\tilde{\kappa}_0(n+1)(n+2))}{(n+1)\omega}\alpha_0^{2n+1}\Phi_n^*\Bigg] + n(2n-1)\Bigg[\frac{(4\tilde{\kappa}_0 n(n^2+n-2)+\tilde{\gamma}(2\tilde{\kappa}_0(n^2-3n-1)-1))}{\omega}P_n^* - \frac{4\tilde{\kappa}_0(n-1)n(n+1)(n+2)+n\tilde{\gamma}(1-2\tilde{\kappa}_0(n+1)(n+2))}{(n+1)\omega}\alpha_0^{2n+1}P_n^*\Bigg], \quad (3.50)$$

$$p_n = -\frac{2n(4n^2-1)(2(n+2)+\tilde{\gamma})}{\omega}\Phi_n^* - \frac{(2n+1)(2(n^2-1)+(n-2)\tilde{\gamma})}{\omega}P_n^*, \quad (3.51)$$

$$\Psi_{-n-1} = \begin{cases} \dfrac{(n-1)-\tilde{\gamma}}{(n+2)+\tilde{\gamma}}\Psi_n^* + \dfrac{2\tilde{\gamma}(\Omega^z\cos\theta+\Omega^x\cos\phi\sin\theta+\Omega^y\sin\theta\sin\phi)}{n(n+1)((n+2)+\tilde{\gamma})}, & n=1, \\ \dfrac{(n-1)-\tilde{\gamma}}{(n+2)+\tilde{\gamma}}\Psi_n^*, & n\neq 1, \end{cases} \quad (3.52)$$

$$p_{-n-1} = \frac{\alpha_0^{2n+1}}{r^{2n+1}}\frac{np_n}{n+1}, \quad (3.53)$$

where

$$\omega = 2((1+2n)(1+n+\alpha_0^{2n+1}n)+2\tilde{\kappa}_0(1-\alpha_0^{2n+1})n(n+2)(2n^2+1) + \tilde{\gamma}(1+n+\alpha_0^{2n+1}n)+\tilde{\gamma}\tilde{\kappa}_0 n(2n^2+1-2\alpha_0^{2n+1}(n+1)(2n+2))). \quad (3.54)$$

In (3.49)–(3.52) we have $r = 1$ and in (3.53) we have $r = \alpha_0$. We remind the reader that Φ_n^*, P_n^*, and Ψ_n^* are determined by the external background flow $\boldsymbol{v}^e$ through the far-field condition (3.27) which contains the cell's unknown translational velocity $\boldsymbol{V}_{tr}$. To calculate the cell's translational velocity, along with its rotational velocity $\boldsymbol{\Omega}$, we enforce the balances of linear and angular momentum (3.8). Substituting the solid spherical harmonic representation for $\boldsymbol{\sigma}_f$ into (3.6) and (3.7) we find

$$F^x_{\text{force}} = -4\pi P_{-2,1},\ F^y_{\text{force}} = -4\pi P_{-2,-1},\ F^z_{\text{force}} = -4\pi P_{-2,0}, \tag{3.55}$$

$$T^x = -8\pi\Psi_{-2,1},\ T^y = -8\pi\Psi_{-2,-1},\ T^z = -8\pi\Psi_{-2,0}, \tag{3.56}$$

where the superscripts x, y and z denote the x, y and z-components, respectively. Consequently, to satisfy (3.8) we require the further constraints

$$P_{-2,m} = 0, \quad \Psi_{-2,m} = 0, \quad m = 0, \pm 1, \tag{3.57}$$

which allow the relationship between the external flow and the particle's translation/rotation to be determined. The full solution for the fluid problem is given by combining (3.57) with (3.49)–(3.53).

3.3.2 The solid problem

The general solution to the Navier–Láme problem in three dimensions may be written using the Papkovich-Neuber potentials [115]

$$2\boldsymbol{u} = 2(1-\nu)\boldsymbol{\psi} - \nabla\left(\varphi + \frac{1}{2}\boldsymbol{r}\cdot\boldsymbol{\psi}\right), \tag{3.58}$$

where φ and $\boldsymbol{\psi}$ satisfy the Poisson equations

$$\nabla^2\boldsymbol{\psi} = \frac{\nabla p_p}{1-\nu} \qquad \text{and} \qquad \nabla^2\varphi = -\frac{\boldsymbol{r}\cdot\nabla p_p}{2(1-\nu)}. \tag{3.59}$$

We decompose φ and $\boldsymbol{\psi}$ into their complementary and particular components by writing

$$\varphi = \varphi_c + \varphi_p \qquad \text{and} \qquad \boldsymbol{\psi} = \boldsymbol{\psi}_c + \boldsymbol{\psi}_p, \tag{3.60}$$

where φ_c and $\boldsymbol{\psi}_c$ satisfy the homogeneous problem and φ_p and $\boldsymbol{\psi}_p$ are the particular solutions for the inhomogeneities in (3.59).

To solve (3.59), it is convenient to use a Cartesian (rather than spherical) basis for the vectors $\boldsymbol{\psi}_c$ and $\boldsymbol{\psi}_p$. Taking the x-component in the first equation in (3.59) as an example we have

$$\nabla^2\psi_p^x = \frac{1}{1-\nu}\frac{\partial p_p}{\partial x}, \tag{3.61}$$

where $\psi_p^x = \boldsymbol{\psi}_p \cdot \boldsymbol{e}_x$. Since p_p is harmonic, any partial derivative of p_p with respect to x, y or z is also harmonic. Applying the identity (D.9) with $l = 2$ we obtain exact expressions for the particular solutions,

$$\varphi_p(\boldsymbol{r}) = -\frac{r^2}{2(1-\nu)} \sum_{n=0}^{\infty} \frac{n p_n}{2(2n+3)} + \frac{(n+1)p_{-n-1}}{2(2n-1)}, \tag{3.62}$$

$$\psi_p^x(\boldsymbol{r}) = \frac{r^2}{1-\nu} \sum_{n=0}^{\infty} \frac{1}{2(2n+3)} \frac{\partial p_n}{\partial x} - \frac{1}{2(2n-1)} \frac{\partial p_{-n-1}}{\partial x}, \tag{3.63}$$

with similar expressions for ψ_p^y and ψ_p^z.

We now consider the complementary solutions to (3.59). Within a spherical or annular domain, we may set $\varphi_c = 0$ without loss of generality using the Papkovich-Neuber representation [121]. Studying (3.59), we see that the Cartesian components of $\boldsymbol{\psi}_c$ each satisfy Laplace's equation and are thus harmonic. Using Appendix D.1 we write their explicit forms as

$$\begin{aligned}
\psi_c^x(\boldsymbol{r}) = \boldsymbol{\psi}_c(\boldsymbol{r}) \cdot \boldsymbol{e}_x &= \sum_{n=0}^{\infty} \psi_n^x + \psi_{-n-1}^x = \sum_{n=0}^{\infty} \sum_{m=-n}^{n} \psi_{n,m}^{x,\mathcal{R}} \mathcal{R}_{n,m}(\boldsymbol{r}) + \psi_{n,m}^{x,\mathcal{I}} \mathcal{I}_{n,m}(\boldsymbol{r}), \\
\psi_c^y(\boldsymbol{r}) = \boldsymbol{\psi}_c(\boldsymbol{r}) \cdot \boldsymbol{e}_y &= \sum_{n=0}^{\infty} \psi_n^y + \psi_{-n-1}^x = \sum_{n=0}^{\infty} \sum_{m=-n}^{n} \psi_{n,m}^{y,\mathcal{R}} \mathcal{R}_{n,m}(\boldsymbol{r}) + \psi_{n,m}^{y,\mathcal{I}} \mathcal{I}_{n,m}(\boldsymbol{r}), \\
\psi_c^z(\boldsymbol{r}) = \boldsymbol{\psi}_c(\boldsymbol{r}) \cdot \boldsymbol{e}_z &= \sum_{n=0}^{\infty} \psi_n^z + \psi_{-n-1}^x = \sum_{n=0}^{\infty} \sum_{m=-n}^{n} \psi_{n,m}^{z,\mathcal{R}} \mathcal{R}_{n,m}(\boldsymbol{r}) + \psi_{n,m}^{z,\mathcal{I}} \mathcal{I}_{n,m}(\boldsymbol{r}),
\end{aligned} \tag{3.64}$$

where again $\mathcal{R}_{n,m}(\boldsymbol{r})$ and $\mathcal{I}_{n,m}(\boldsymbol{r})$ are the regular and irregular solid spherical harmonics, and $\psi_n^x, \psi_n^y, \psi_n^z, \psi_{-n-1}^x, \psi_{-n-1}^y$ and ψ_{-n-1}^z are linear combinations of the relevant solid spherical harmonics of degree n with the constant coefficients $\psi_{n,m}^{x,\mathcal{R}}, \psi_{n,m}^{y,\mathcal{R}}, \psi_{n,m}^{z,\mathcal{R}}, \psi_{n,m}^{x,\mathcal{I}}, \psi_{n,m}^{y,\mathcal{I}}$, and $\psi_{n,m}^{z,\mathcal{I}}$ as presented in (D.6). We note that when $\alpha_0 = 0$, such that we instead consider a spherical poroelastic particle, the displacement must remain finite at the origin. Consequently, in this case we only require the coefficients associated with the regular solid spherical harmonics, $\psi_{n,m}^{x,\mathcal{R}}, \psi_{n,m}^{y,\mathcal{R}}$ and $\psi_{n,m}^{z,\mathcal{R}}$, since $\psi_{n,m}^{x_i,\mathcal{I}} = 0$.

To calculate the solid displacement, it remains to calculate the constant coefficients $\psi_{n,m}^{x,\mathcal{R}}, \psi_{n,m}^{y,\mathcal{R}}, \psi_{n,m}^{z,\mathcal{R}}, \psi_{n,m}^{x,\mathcal{I}}, \psi_{n,m}^{y,\mathcal{I}}$ and $\psi_{n,m}^{z,\mathcal{I}}$ via the boundary conditions (3.29), (3.32) and (3.34).We again reformulate these boundary conditions by applying the divergence and curl to (3.29) and (3.34) to obtain

$$\sigma'_{rr}|_{r=1} = 0, \tag{3.65}$$

$$\left[r\frac{\partial p_f}{\partial r}+(3\lambda+2\mu_s)(\nabla\cdot\boldsymbol{u})-r\frac{\partial\sigma'_{rr}}{\partial r}-3p_f\right]_{r=1}=-\left[3p_f+r\frac{\partial\sigma_{f,rr}}{\partial r}\right]_{r=1}, \tag{3.66}$$

$$[\boldsymbol{r}\cdot\nabla\times(\boldsymbol{\sigma}'\cdot\boldsymbol{e}_r)]_{r=1}=[\boldsymbol{r}\cdot\nabla\times(\boldsymbol{\sigma}_f\cdot\boldsymbol{e}_r)]_{r=1}\,, \tag{3.67}$$

$$[-p_p+\sigma'_{rr}]\,|_{r=\alpha_0}=-p_c|_{r=\alpha_0}, \tag{3.68}$$

$$\left[r\frac{\partial p_f}{\partial r}+(3\lambda+2\mu_s)(\nabla\cdot\boldsymbol{u})-r\frac{\partial\sigma'_{rr}}{\partial r}-3(p_p-p_c))\right]_{r=\alpha_0}=0, \tag{3.69}$$

$$[\boldsymbol{r}\cdot\nabla\times(\boldsymbol{\sigma}'\cdot\boldsymbol{e}_r)]_{r=\alpha_0}=0, \tag{3.70}$$

with details of the reformulation provided in Appendix D.4. Finally, in order to calculate the cell pressure p_c, we impose the volumetric constraint (3.26).

Substituting the Papkovich-Neuber representation for the solid displacement (3.58) into the boundary conditions (3.65)–(3.70) we obtain

$$\begin{aligned}\sum_{n=0}^{\infty}\big[&\frac{1}{2}(3-4\nu-n)n[\boldsymbol{r}\cdot\boldsymbol{\psi}_c]_n-\frac{1}{2}(4(1-\nu)+n)(n+1)[\boldsymbol{r}\cdot\boldsymbol{\psi}_c]_{-n-1}\\&+\nu[\nabla\cdot\boldsymbol{\psi}_c]_n+\nu[\nabla\cdot\boldsymbol{\psi}_c]_{-n-1}+\left(\frac{n+4}{4}-\nu(n+1)\right)\frac{1}{1-\nu}\frac{np_n}{2n+3}\\&+\left(\frac{3-n}{4}-\nu n\right)\frac{1}{1-\nu}\frac{(n+1)p_{-n-1}}{2n-1}=0,\end{aligned} \tag{3.71}$$

$$\begin{aligned}&\sum_{n=0}^{\infty}(n-3)p_n-(n+4)p_{-n-1}+(1+\nu)[\boldsymbol{r}\cdot\boldsymbol{\psi}_c]_n+(1+\nu)[\boldsymbol{r}\cdot\boldsymbol{\psi}_c]_{-n-1}\\&\qquad-\nu(n-1)[\nabla\cdot\boldsymbol{\psi}_c]_n+\nu(n+2)[\nabla\cdot\boldsymbol{\psi}_c]_{-n-1}\\&-\frac{1}{2}(3-4\nu-n)n(n-1)[\boldsymbol{r}\cdot\boldsymbol{\psi}_c]_n-\frac{1}{2}(4(1-\nu)+n)(n+1)(n+2)[\boldsymbol{r}\cdot\boldsymbol{\psi}_c]_{-n-1}\\&\qquad+\left(1+\nu-(n+1)\left(\frac{n+2}{4}-\nu(n+1)\right)\right)\frac{1}{1-\nu}\frac{np_n}{2n+3}\\&\qquad+\left(1+\nu+n\left(\frac{1-n}{4}-\nu n\right)\right)\frac{1}{1-\nu}\frac{(n+1)p_{-n-1}}{2n-3}\\&=-\sum_{n=0}^{\infty}\big[2n(n-1)(n-2)\Phi^*_n+\frac{(n^2-n-3)n}{2n+3}P^*_n-2(n+1)(n+2)(n+3)\Phi_{-n-1}\\&\qquad+\frac{(n^2+3n-1)(n+1)}{2n-1}P_{-n-1}+3(P^*_n+P_{-n-1})\big],\end{aligned} \tag{3.72}$$

$$\sum_{n=0}^{\infty}(1-\nu)\Bigg[(n-1)\left(y\frac{\partial\psi_n^x}{\partial z}-z\frac{\partial\psi_n^x}{\partial y}+z\frac{\partial\psi_n^y}{\partial x}-x\frac{\partial\psi_n^y}{\partial z}+x\frac{\partial\psi_n^z}{\partial y}-y\frac{\partial\psi_n^z}{\partial x}\right)$$
$$-(n+2)\left(y\frac{\partial\psi_{-n-1}^x}{\partial z}-z\frac{\partial\psi_{-n-1}^x}{\partial y}+z\frac{\partial\psi_{-n-1}^y}{\partial x}-x\frac{\partial\psi_{-n-1}^y}{\partial z}+x\frac{\partial\psi_{-n-1}^z}{\partial y}-y\frac{\partial\psi_{-n-1}^z}{\partial x}\right)\Bigg]$$
$$=\sum_{n=0}^{\infty}\left[n(n+1)(n-1)\Psi_n^*-n(n+1)(n+2)\Psi_{-n-1}\right], \quad (3.73)$$

$$\sum_{n=0}^{\infty}\Big[\frac{1}{2\alpha_0^2}(3-4\nu-n)n[\boldsymbol{r}\cdot\boldsymbol{\psi}_c]_n-\frac{1}{2\alpha_0^2}(4(1-\nu)+n)(n+1)[\boldsymbol{r}\cdot\boldsymbol{\psi}_c]_{-n-1}$$
$$+\nu[\nabla\cdot\boldsymbol{\psi}_c]_n+\nu[\nabla\cdot\boldsymbol{\psi}_c]_{-n-1}+\left(\frac{n+4}{4}-\nu(n+1)\right)\frac{1}{1-\nu}\frac{np_n}{2n+3}$$
$$+\left(\frac{3-n}{4}-\nu n\right)\frac{1}{1-\nu}\frac{(n+1)p_{-n-1}}{2n-1}=\sum_{n=0}^{\infty}(p_n+p_{-n-1})-p_c, \quad (3.74)$$

$$\sum_{n=0}^{\infty}(n-3)p_n-(n+4)p_{-n-1}+(1+\nu)[\boldsymbol{r}\cdot\boldsymbol{\psi}_c]_n+(1+\nu)[\boldsymbol{r}\cdot\boldsymbol{\psi}_c]_{-n-1}$$
$$-\nu(n-1)[\nabla\cdot\boldsymbol{\psi}_c]_n+\nu(n+2)[\nabla\cdot\boldsymbol{\psi}_c]_{-n-1}$$
$$-\frac{1}{2\alpha_0^2}(3-4\nu-n)n(n-1)[\boldsymbol{r}\cdot\boldsymbol{\psi}_c]_n-\frac{1}{2\alpha_0^2}(4(1-\nu)+n)(n+1)(n+2)[\boldsymbol{r}\cdot\boldsymbol{\psi}_c]_{-n-1}$$
$$+\left(1+\nu-(n+1)\left(\frac{n+2}{4}-\nu(n+1)\right)\right)\frac{1}{1-\nu}\frac{np_n}{2n+3}$$
$$+\left(1+\nu+n\left(\frac{1-n}{4}-\nu n\right)\right)\frac{1}{1-\nu}\frac{(n+1)p_{-n-1}}{2n-3}=-p_c \quad (3.75)$$

$$\sum_{n=0}^{\infty}\frac{(1-\nu)}{\alpha_0}\Bigg[(n-1)\left(y\frac{\partial\psi_n^x}{\partial z}-z\frac{\partial\psi_n^x}{\partial y}+z\frac{\partial\psi_n^y}{\partial x}-x\frac{\partial\psi_n^y}{\partial z}+x\frac{\partial\psi_n^z}{\partial y}-y\frac{\partial\psi_n^z}{\partial x}\right)$$
$$-(n+2)\left(y\frac{\partial\psi_{-n-1}^x}{\partial z}-z\frac{\partial\psi_{-n-1}^x}{\partial y}+z\frac{\partial\psi_{-n-1}^y}{\partial x}-x\frac{\partial\psi_{-n-1}^y}{\partial z}+x\frac{\partial\psi_{-n-1}^z}{\partial y}-y\frac{\partial\psi_{-n-1}^z}{\partial x}\right)\Bigg]=0, \quad (3.76)$$

where using a Cartesian basis

$$[\boldsymbol{r}\cdot\boldsymbol{\psi}_c]_n=x\psi_n^x+y\psi_n^y+z\psi_n^z, \quad [\nabla\cdot\boldsymbol{\psi}_c]_n=\frac{\partial\psi_n^x}{\partial x}+\frac{\partial\psi_n^y}{\partial y}+\frac{\partial\psi_n^z}{\partial z}. \quad (3.77)$$

$$[\boldsymbol{r}\cdot\boldsymbol{\psi}_c]_{-n-1}=x\psi_{-n-1}^x+y\psi_{-n-1}^y+z\psi_{-n-1}^z, \quad [\nabla\cdot\boldsymbol{\psi}_c]_{-n-1}=\frac{\partial\psi_{-n-1}^x}{\partial x}+\frac{\partial\psi_{-n-1}^y}{\partial y}+\frac{\partial\psi_{-n-1}^z}{\partial z}. \quad (3.78)$$

For clarity, the boundary conditions (3.71)–(3.73) have $r = 1$ and the boundary conditions (3.74)–(3.76) have $r = \alpha_0$. In the current form, (3.71)–(3.76) are not diagonal and cannot be solved simultaneously at each degree n and order m as was done for the fluid problem. This is due to the terms

$$\frac{\partial \psi_n^x}{\partial x},\ \frac{\partial \psi_n^y}{\partial y},\ \frac{\partial \psi_n^z}{\partial z},\ x\psi_n^x,\ y\psi_n^y,\ z\psi_n^z,\ z\frac{\partial \psi_n^x}{\partial y},\ y\frac{\partial \psi_n^x}{\partial z},\ z\frac{\partial \psi_n^y}{\partial x},\ x\frac{\partial \psi_n^y}{\partial z},\ x\frac{\partial \psi_n^z}{\partial y},\ y\frac{\partial \psi_n^z}{\partial x}, \tag{3.79}$$

each of which involves the regular spherical harmonics, and the terms

$$\begin{aligned}\frac{\partial \psi_{-n-1}^x}{\partial x},\ \frac{\partial \psi_{-n-1}^y}{\partial y},\ \frac{\partial \psi_{-n-1}^z}{\partial z},\ x\psi_{-n-1}^x,\ y\psi_{-n-1}^y,\ z\psi_{-n-1}^z,\\ z\frac{\partial \psi_{-n-1}^x}{\partial y},\ y\frac{\partial \psi_{-n-1}^x}{\partial z},\ z\frac{\partial \psi_{-n-1}^y}{\partial x},\ x\frac{\partial \psi_{-n-1}^y}{\partial z},\ x\frac{\partial \psi_{-n-1}^z}{\partial y},\ y\frac{\partial \psi_{-n-1}^z}{\partial x},\end{aligned} \tag{3.80}$$

each of which involve the irregular spherical harmonics. The terms in (3.79) and (3.80) are not in general orthogonal with the solid spherical harmonic of degree n. To overcome this, we consider the general functions $\chi^{\mathcal{R}}(r,\theta,\phi)$ and $\chi^{\mathcal{I}}(r,\theta,\phi)$ which may be any term in (3.79) and (3.80), respectively. We project these terms to a spherical harmonic basis by writing, for example,

$$\chi^{\mathcal{R}}(r,\theta,\phi) = \sum_{n=0}^{\infty}\sum_{m=-n}^{n} \widetilde{\psi}_{n,m}^{\mathcal{R}}(r)\mathcal{R}_{n,m}(r,\theta,\phi), \tag{3.81}$$

$$\chi^{\mathcal{I}}(r,\theta,\phi) = \sum_{n=0}^{\infty}\sum_{m=-n}^{n} \widetilde{\psi}_{n,m}^{\mathcal{I}}(r)\mathcal{I}_{n,m}(r,\theta,\phi), \tag{3.82}$$

$$\widetilde{\psi}_{n,m}^{\mathcal{R}}(r) = \int_{\phi=0}^{2\pi}\int_{\theta=0}^{\pi} \frac{(2n+1)}{4\pi r^{2n}}\chi^{\mathcal{R}}(r,\theta,\phi)\mathcal{R}_{n,m}(r,\theta,\phi)\ \sin\theta\ \mathrm{d}\theta\ \mathrm{d}\phi \tag{3.83}$$

$$\widetilde{\psi}_{n,m}^{\mathcal{I}}(r) = -\int_{\phi=0}^{2\pi}\int_{\theta=0}^{\pi} \frac{(2n+1)}{4\pi r^{-2n-2}}\chi^{\mathcal{I}}(r,\theta,\phi)\mathcal{I}_{n,m}(r,\theta,\phi)\ \sin\theta\ \mathrm{d}\theta\ \mathrm{d}\phi, \tag{3.84}$$

where $\widetilde{\psi}_{n,m}^{\mathcal{R}}(r)$ and $\widetilde{\psi}_{n,m}^{\mathcal{I}}(r)$ are projected coefficients which generally depend on r. Projections for the terms in (3.79) and (3.80) may be similarly calculated. On the undeformed boundaries $\partial\widehat{\Omega}_i$, the projected coefficients (for example $\widetilde{\psi}_{n,m}^{\mathcal{R}}(r=\alpha_i)$ and $\widetilde{\psi}_{n,m}^{\mathcal{I}}(r=\alpha_i)$) are simply linear combinations of the unknown coefficients $\psi_{n,m}^{x,\mathcal{R}}, \psi_{n,m}^{y,\mathcal{R}}, \psi_{n,m}^{z,\mathcal{R}}, \psi_{n,m}^{x,\mathcal{I}}, \psi_{n,m}^{y,\mathcal{I}}$ and $\psi_{n,m}^{z,\mathcal{I}}$. Importantly, the sums for the projections all involve a finite number of terms. Therefore, by substituting projections similar to (3.81) and (3.82) for the terms in (3.79) and (3.80) into the boundary conditions (3.71)–(3.76) we may exploit the orthogonality of the spherical harmonics and solve (3.71)–(3.76) exactly by formulating a non-diagonal, finite-dimensional linear system

in terms of the unknown coefficients $\psi_{n,m}^{x,\mathcal{R}}, \psi_{n,m}^{y,\mathcal{R}}, \psi_{n,m}^{z,\mathcal{R}}, \psi_{n,m}^{x,\mathcal{I}}, \psi_{n,m}^{y,\mathcal{I}}$ and $\psi_{n,m}^{z,\mathcal{I}}$. For the sake of brevity the full solution is omitted from the text, however we do present the surface deformation (3.24) of the coating under a shear and Poiseuille flow in Section 3.4.

The cell pressure p_c enters the coating deformation via the reformulated interfacial conditions (3.74) and (3.75), and is calculated through enforcing the volumetric constraint (3.26). Under a background shear and Poiseuille flow, it may be shown that the volume constraint (3.25) is satisfied by $p_c = p_c^0$. This indicates the surface deformation of the cell is volume preserving to $\mathcal{O}(\epsilon)$, such that the cell pressure remains unaffected when deformed. To close the solid problem, the impact of the coating deformation on the porosity may be calculated via (3.9).

3.3.3 Spherical poroelastic particle

For the case of a spherical poroelastic particle, where the cell region is omitted and is replaced with further poroelastic material, we require $p_{-n-1} = 0$ and $\boldsymbol{\psi}_{-n-1} = \mathbf{0}$ to ensure the fluid flow and particle deformation remain finite at the origin. The interfacial conditions (3.33) and (3.34), along with the volumetric restriction (3.26) and cell pressure p_c, are also not required.

To recover the case of a spherical poroelastic particle from the coated cell model, we naively set $\alpha_0 = 0$ in the coated cell solutions. It is clear through (3.53) that by setting $\alpha_0 = 0$ we have $p_{-n-1} = 0$. Further, it may be shown that with $\alpha_0 = 0$, the reformulated boundary conditions (3.74)–(3.76) applied at the origin, require $\boldsymbol{\psi}_{-n-1} = \mathbf{0}$. Since the volumetric constraint (3.26) is trivially satisfied when $\alpha_0 = 0$, the cell pressure p_c simply reflects the total poroelastic stress at the origin, which is given by the reference pressure p_c^0 (undeformed cell pressure).

The only remaining interfacial condition is the no penetration condition (3.33). To interpret the no penetration condition, we consider the asymptotic limit $\alpha_0 \to 0$, where we expect the fluid problem may be written as an outer problem valid far from the origin, and an inner problem valid close to the cell surface ($r \sim \alpha_0$). The outer problem should be a spherical poroelastic particle coupled to an unbounded Stokes flow, and the inner problem should be unbounded uniform Darcy flow around the impermeable, perfect slip, undeformed cell surface. The magnitude of the uniform Darcy flow in the inner problem is given by the solution to the outer problem, which we anticipate will approach the Darcy flow through the centre of a spherical poroelastic particle (origin) when $\alpha_0 = 0$.

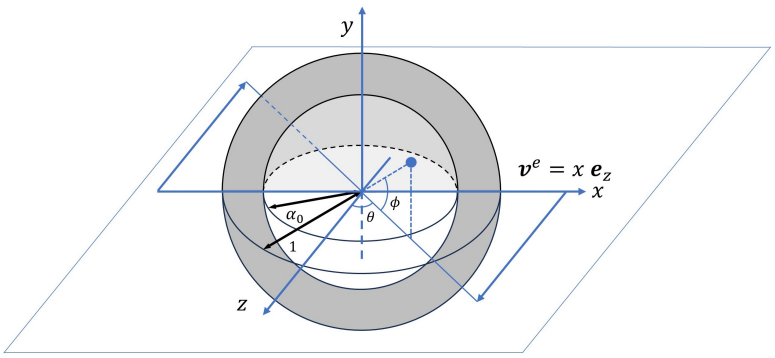

Figure 3.2: Schematic of a three-dimensional coated cell under a background shear flow.

3.4 Example flow profiles

We use the above framework to investigate the impacts of the Darcy number, slip, Poisson's ratio, and coating thickness on the cell's translational and angular velocity, and the coating deformation, under two example flow profiles, shear flow and Poiseuille flow. We first present analytical results for these key quantities, before studying the limiting case of a spherical poroelastic particle by setting $\alpha_0 = 0$. By taking the further limits $\tilde{\kappa}_0 \to 0, \gamma \to \infty$, and $\nu \to 1/2$ we model an incompressible, elastic particle[2] subject to no-slip boundary conditions in an unbounded flow, as studied by Murata [3]. We consider these limits in the case of both shear and Poiseuille background flows, and compare to Murata to validate our method. We then return to consider the full coated cell model ($\alpha_0 \neq 0$), to interpret how the dependencies of the coated cell's translation, rotation, and deformation on the Darcy number, slip, and Poisson's ratio change with coating thickness. Since lengths are non-dimensionalised on the outer coating radius, we note that as the coating thickness increases, the cell size decreases.

3.4.1 Shear flow

We first study the case of a background shear flow, as presented in Figure 3.2. In a Cartesian coordinate system, the dimensionless background shear flow is described by

$$v_x^e = 0, \quad v_y^e = 0, \quad v_z^e = x, \tag{3.85}$$

[2]Taking these limits, the Darcy pressure does not reduce to the elastic pressure in the particle. Further details of this reduction are provided in Appendix C.5.

We first write the external background flow using solid spherical harmonics,

$$\Psi_1^* = -\frac{1}{2} r \sin\theta \sin\phi, \tag{3.86}$$

$$\Phi_2^* = \frac{1}{4} r^2 \sin 2\theta \cos\phi. \tag{3.87}$$

From (3.57) it may be shown that the translational velocity of the coated cell $\boldsymbol{V}_{tr} = \boldsymbol{0}$, and that the torque balance requires

$$\frac{\tilde{\gamma}}{2(3+\tilde{\gamma})} + \frac{2\Omega^y \tilde{\gamma}}{2(3+\tilde{\gamma})} = 0 \implies \Omega^y = -\frac{1}{2}, \quad \Omega^x = \Omega^z = 0. \tag{3.88}$$

The left-hand side of (3.88) is composed of two terms. The first term is the torque imposed on a non-rotating coated cell under a background shear flow (see, for example, Figure 3.3b), and the second term is the torque experienced by a coated cell which rotates with angular velocity Ω^y in an unbounded, quiescent, Newtonian viscous fluid (see, for example, Figure 3.3c). Since these two terms scale identically with $\tilde{\kappa}_0$ and γ, and do not depend on α_0, the rotation of the coated cell is the same for all cell coatings. Special attention must be paid to the case when $\gamma = \tilde{\gamma} = 0$, such that there is perfect slip on the outer coating surface. This case forms a singular limit where $\boldsymbol{\Omega}$ is not uniquely determined. However, we note that $\boldsymbol{\Omega} = -\boldsymbol{e}_y/2$ in the limit as $\tilde{\gamma} \to 0$.

The surface deformations r_i are given by (3.24),

$$r_i = 1 + \frac{5}{4} \epsilon L_i^s(\tilde{\kappa}_0, \tilde{\gamma}, \nu, \alpha_0) \sin 2\theta \cos\phi, \tag{3.89}$$

where $L_i^s(\tilde{\kappa}_0, \tilde{\gamma}, \nu, \alpha_0)$ contain the dependencies of the surface deformations on $\tilde{\kappa}_0, \tilde{\gamma}, \nu$, and α_0. For brevity, we do not present the full solutions for $L_i^s(\tilde{\kappa}_0, \tilde{\gamma}, \nu, \alpha_0)$ here, though we do present closed form solutions for certain limiting cases below, along with several general plots across a wide range of parameter values. We note that the surface deformations (3.89) do not depend on the cell pressure $p_c = p_c^0$ since the cell pressure is not affected by the leading-order surface deformation in (3.26).

To interpret the coating deformation, it will be useful to consider the Darcy pressure p_p and the surface tractions, $\boldsymbol{\tau} = (\tau_r, \tau_\theta, \tau_\phi) = \boldsymbol{\sigma}_f|_{r=1} \cdot \boldsymbol{e}_r$ on r_1, which drive the resulting deformation of the coated cell through the governing equations (3.16) and (3.18) and boundary conditions (3.29) and (3.32). We note that through (3.30) we have $\tau_r = -p_p|_{r=1}$ and that the shearing tractions on the undeformed surface r_0 are zero through the boundary condition (3.34). For a coated cell under a shear flow we have

$$p_p = p_c^0 - 5M^s(\tilde{\kappa}_0, \tilde{\gamma}, \alpha_0, r) \sin 2\theta \cos\phi, \tag{3.90}$$

$$\tau_\theta = \frac{5}{2}T^s(\tilde{\kappa}_0, \tilde{\gamma}, \alpha_0)\cos 2\theta \cos\phi, \quad \tau_\phi = -\frac{5}{2}T^s(\tilde{\kappa}_0, \tilde{\gamma}, \alpha_0)\cos\theta \sin\phi, \tag{3.91}$$

where

$$M^s(\tilde{\kappa}_0, \tilde{\gamma}, \alpha_0, r) = \frac{3r^5 + 2\alpha_0^5}{3r^3}\frac{3(8+\tilde{\gamma})}{3(5+48\tilde{\kappa}_0+\tilde{\gamma}+6\tilde{\kappa}_0\tilde{\gamma}) + 2\alpha_0^5(5-72\tilde{\kappa}_0+\tilde{\gamma}-24\tilde{\kappa}_0\tilde{\gamma})}, \tag{3.92}$$

$$T^s(\tilde{\kappa}_0, \tilde{\gamma}, \alpha_0) = \frac{(3+\alpha_0^5(2-48\tilde{\kappa}_0))\tilde{\gamma}}{3(5+48\tilde{\kappa}_0+\tilde{\gamma}+6\tilde{\kappa}_0\tilde{\gamma}) + 2\alpha_0^5(5-72\tilde{\kappa}_0+\tilde{\gamma}-24\tilde{\kappa}_0\tilde{\gamma})}. \tag{3.93}$$

We additionally define the Darcy pressure magnitudes on the outer coating and cell surfaces,

$$M_i^s(\tilde{\kappa}_0, \tilde{\gamma}, \alpha_0) = M^s(r = \alpha_i). \tag{3.94}$$

We note that the denominators of M^s and T^s both contain the same dependencies on the Darcy number $\tilde{\kappa}_0$, slip $\tilde{\gamma}$, and cell size α_0. Although $\tilde{\gamma}$ appears in the solutions (3.89)–(3.91), it is important to recall that $\tilde{\gamma} = \gamma/\sqrt{\tilde{\kappa}_0}$ is composed of two independent and physically meaningful parameters, and below we choose to explore how γ and $\tilde{\kappa}_0$ impact the system rather than $\tilde{\gamma}$.

3.4.1.1 Spherical poroelastic particle

We first investigate the impacts of the Darcy number $\tilde{\kappa}_0$, slip $\tilde{\gamma}$, and Poisson's ratio ν, for the limiting case of a spherical poroelastic particle, which may be obtained by setting $\alpha_0 = 0$ (see Section 3.3.3). For brevity, we denote quantities with $\alpha_0 = 0$ via a hat; for instance, $\widehat{L}_i^s = L_i^s(\alpha_0 = 0)$. Removing the cellular region greatly simplifies the surface deformation,

$$\widehat{L}_1^s(\tilde{\kappa}_0, \tilde{\gamma}, \nu) = \frac{16(2+\nu) + \tilde{\gamma}(4+11\nu)}{(5+48\tilde{\kappa}_0+\tilde{\gamma}+6\tilde{\kappa}_0\tilde{\gamma})(7+5\nu)}, \tag{3.95}$$

where, since we work in a frame which translates with the particle, the deformation at the origin, $\widehat{L}_0^s = 0$. By taking the further limits $\tilde{\kappa}_0 \to 0$ (impermeable), $\gamma \to \infty$ (no-slip), and $\nu \to 1/2$ (incompressible), we recover the results obtained by Murata [3]; finding that $\widehat{L}_1^s \to 1$. The rigid body rotation of the particle given by (3.88) is identical to Murata's result regardless of the parameter choices, since the rotation of the particle is independent of its material parameters.

In Figure 3.3 we choose a small Darcy number $\tilde{\kappa}_0 = 10^{-3}$ and small slip $\gamma = 100$, presenting contour plots in the z-x plane for the flow through the poroelastic particle (Figure 3.3a) as a linear combination of the shear flow through a stationary, non-rotating particle (Figure 3.3b), and the flow associated with a rotating particle in a quiescent fluid (Figure 3.3c). Outside the particle we plot the velocity field $\boldsymbol{v}$ and

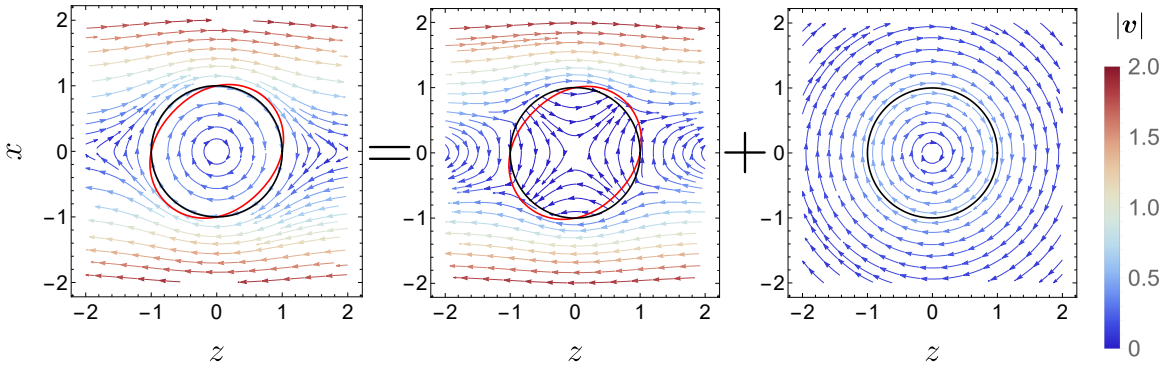

(a) Shear flow (b) No particle rotation and background shear flow (c) Pure particle rotation and zero background flow

Figure 3.3: Velocity contour plots in the z-x plane ($y = 0$) showing a decomposition of the internal and external flow. In all plots $\tilde{\kappa}_0 = 10^{-3}$ and $\gamma = 100$. The undeformed and deformed ($\epsilon = 0.1, \nu = 1/4$) particle surface are denoted by the black and red lines, respectively.

inside the particle we plot the total volume flux $\boldsymbol{q}$ (3.12); in each plot, the contour colour reflects the respective velocity magnitude. Under this decomposition, the total internal flux in Figure 3.3b is identical to the Darcy flow component ($\phi_{f,0}(\boldsymbol{v}_p - \boldsymbol{v}_s)$) of the total internal flux in Figure 3.3a, and the total internal flux $\boldsymbol{q}$ in Figure 3.3c is given exactly by the rigid body rotation $\boldsymbol{v}_s = \boldsymbol{v}_\Omega$. Additionally, the first term in the left-hand side of (3.88) is the torque experienced by the particle in Figure 3.3b, and the second term is the torque experienced by the particle in Figure 3.3c. In Figure 3.3b, where the particle does not rotate, the internal flow is extensional along a 45° angle to the flow, which we define as the major axis. We also define the minor axis as perpendicular to the major axis in the z-x plane. We note the contours cross the z-axis as a result of the particle; in the absence of a particle, the background flow has a line of stagnation points along $x = 0$. With small slip ($\gamma = 100$), the pure rotation of the particle in Figure 3.3c causes the external flow to circle the particle, decaying to zero far from the particle. Since there is no normal (radial) flow present in Figure 3.3c, the Darcy number $\tilde{\kappa}_0$ only affects the external flow through the Beavers and Joseph condition (3.31) via the effective slip $\tilde{\gamma} = \gamma/\sqrt{\tilde{\kappa}_0}$. With a smaller Darcy number, $\tilde{\gamma}$ is increased, reducing the effective slip on the particle surface such that the particle rotation generates a greater external flow. Combining the contours in Figures 3.3b and 3.3c, we obtain Figure 3.3a. Since the Darcy number is small here, the total internal flux is dominated by the particle rotation such that we observe circular contours. Due to the small slip, the external flow close to the particle boundary is dominated by the rotation such that the flow across the z-axis

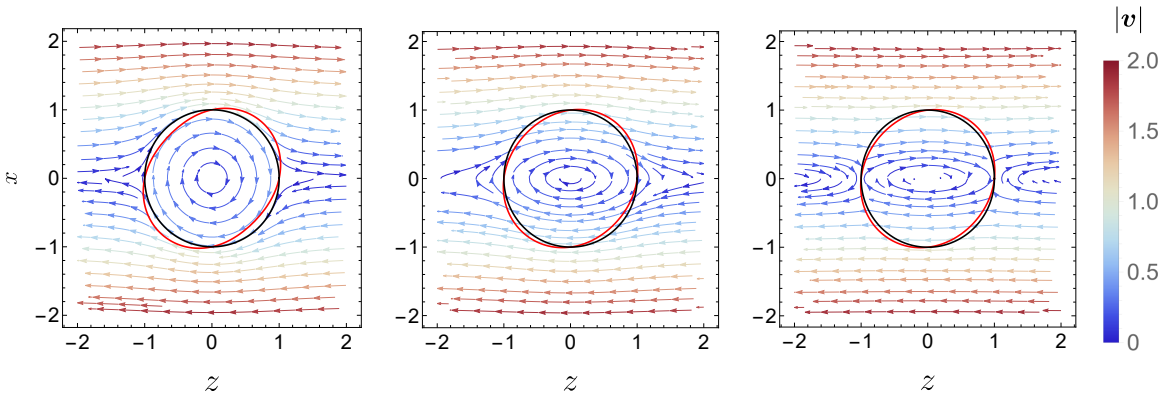

(a) $(\tilde{\kappa}_0, \gamma) = (10^{-3}, 10^{-2})$ (b) $(\tilde{\kappa}_0, \gamma) = (10^{-1}, 10^{2})$ (c) $(\tilde{\kappa}_0, \gamma) = (10^{-1}, 10^{-2})$

Figure 3.4: Velocity contour plots in the z-x plane for a poroelastic particle in shear flow varying $\tilde{\kappa}_0$ and γ with $y = 0$. The undeformed and deformed ($\epsilon = 0.1, \nu = 1/4$) particle surface are denoted by the black and red lines, respectively.

observed in Figure 3.3b changes direction and the external flow circles the particle. Far from the particle we recover the background shear flow.

Since no surface deformation is generated via the rigid body rotation of the particle, the deformed surfaces, presented via the red lines, are identical in Figures 3.3a and 3.3b. The particle deforms to a prolate spheroid aligned with the major axis of the extensional internal flow in Figure 3.3b. This is because the internal flow in Figure 3.3b is the Darcy flow (fluid flow relative to the solid) in Figure 3.3a.

In Figure 3.4 we present further 2-D cross sections (z-x plane) of the velocity contours and surface deformation under a shear flow for varying Darcy number and slip. In Figure 3.4a, the Darcy number is again small such that there is little internal fluid flow relative to the rotating skeleton. Consequently, the internal contours are near circular reflecting the particle rotation in (3.88). Comparing with Figure 3.3a, with a large slip ($\gamma = 0.01$) the external flow does not circle the particle, since the rotation of the particle generates little external flow. We note that the flow around the particle is faster since the greater slip reduces the resistance to tangential flow. In Figures 3.4b and 3.4c we increase the Darcy number and observe ellipsoidal contours within the particle due to the increased internal Darcy flow relative to the motion of the rigid skeleton. With a small slip in Figure 3.4b the external flow mimics the ellipsoidal contours near the interface. With a large slip (γ small) in Figure 3.4c the particle rotation does not generate a strong external flow such that we see a similar external flow structure to that observed in Figure 3.3b when rotation is neglected. We note that the external flow in Figure 3.4a is similar to that presented in Figure 3.4c along $x = 0$, though the flow across the z-axis is too subtle to be visible in the

contour plot. In all cases, far from the particle we recover the far-field shear flow with horizontal contours. The contours around $x = 2$ in Figures 3.3a and 3.4a to 3.4c are in general more strongly curved for a smaller Darcy number and slip, which indicates the disturbance to the flow is larger.

For all cases in Figure 3.4, the particle attains a similar prolate spheroidal shape to that observed in Figure 3.3. To interpret the surface deformation in (3.95), we consider the Darcy pressure within the particle and shearing surface tractions acting on the particle surface. The dependencies of the Darcy pressure and shearing tractions on the Darcy number and slip are obtained by setting $\alpha_0 = 0$ in (3.92) and (3.93),

$$\widehat{M}_1^s(\tilde{\kappa}_0, \tilde{\gamma}) = \frac{8 + \tilde{\gamma}}{5 + 48\tilde{\kappa}_0 + \tilde{\gamma} + 6\tilde{\kappa}_0\tilde{\gamma}}, \tag{3.96}$$

$$\widehat{T}^s(\tilde{\kappa}_0, \tilde{\gamma}) = \frac{\tilde{\gamma}}{5 + 48\tilde{\kappa}_0 + \tilde{\gamma} + 6\tilde{\kappa}_0\tilde{\gamma}}, \tag{3.97}$$

and $\widehat{M}_0^s = 0$. Setting $\alpha_0 = 0$ in (3.90), the Darcy pressure within the poroelastic particle under a shear flow is

$$p_p = p_c^0 - 5r^2\widehat{M}_1^s(\tilde{\kappa}_0, \tilde{\gamma}). \tag{3.98}$$

The shearing surface tractions on the particle surface are then given by

$$\tau_\theta = \frac{5}{2}\widehat{T}^s(\tilde{\kappa}_0, \tilde{\gamma})\cos 2\theta \cos\phi, \quad \tau_\phi = -\frac{5}{2}\widehat{T}^s(\tilde{\kappa}_0, \tilde{\gamma})\cos\theta \sin\phi, \tag{3.99}$$

In Figure 3.5 we present an example plot of the Darcy pressure within the particle with $\tilde{\kappa}_0 = 10^{-3}$, $\gamma = 100$, and $p_c^0 = 0$, along with $\widehat{M}_1^s$ and $\widehat{T}^s$ for varying $\tilde{\kappa}_0$ and γ. For reference, in Figure 3.5a we also present the major and minor axes, along with the direction of the shearing traction $\tau_\theta = \boldsymbol{\tau} \cdot \boldsymbol{e}_\theta$. In Figure 3.5a we see that the Darcy pressure is negative along the major axis and positive along the minor axis, resulting in the extensional internal Darcy flow as presented in Figure 3.3b. The Darcy pressure absorbs the normal surface traction through the interfacial condition (3.30), and generates deformation of the solid skeleton via the momentum equation (3.15). Since a positive pressure indicates compression and a negative pressure indicates extension, the Darcy pressure acts to stretch the solid skeleton along the major axis and compress it along the minor axis. Instead considering the shearing tractions in (3.99) with $y = 0$, we have $\tau_\phi = 0$ and τ_θ involves compression of the particle toward the major axis and stretching away from the minor axis, as indicated by the curved arrows near the particle surface in Figure 3.5a.

We present the dependencies of $\widehat{M}_1^s$ and $\widehat{T}^s$ on the Darcy number and slip in Figures 3.5b and 3.5c, observing that the Darcy pressure/normal surface traction

magnitude decrease with γ and that the shearing fluid tractions increase with γ. The normal surface traction is due to the pressure of the external fluid and the radial derivative of the normal component of the external velocity. It may be shown that with a larger slip (smaller γ), the external pressure is decreased since the resistance to the flow around the particle is decreased. However, with a larger slip the magnitude of the radial derivative of V_r is increased close to the particle surface, as was observed in Figures 3.3a and 3.4a. This increase in $\partial V_r/\partial r$ outweighs the reduction in the Stokes pressure, such that the normal surface traction, and hence Darcy pressure, increase with γ.

Increasing the Darcy number has two effects. Firstly, a greater internal fluid flow is permitted, which reduces the flow that is diverted around the particle. This effect decreases both the Darcy pressure and the shearing traction. Secondly, through (3.31) increasing the Darcy number decreases the effective slip $\tilde{\gamma} = \gamma/\sqrt{\tilde{\kappa}_0}$. This has the effect of increasing the Darcy pressure and further decreasing the shearing traction. The combination of these effects is evident in Figure 3.5b where increasing the Darcy number for small γ initially increases the pressure due to the effective reduction in slip via (3.31) until the Darcy number $\tilde{\kappa}_0 \sim 0.01$. When γ is larger, increasing the Darcy number only decreases $\widehat{M}_1^s$, since $\tilde{\gamma}$ remains large for all $\tilde{\kappa}_0$. If we instead consider the lines of constant $\tilde{\gamma}$ (dashed lines) in Figures 3.5b and 3.5c, the Darcy pressure and shearing traction only decrease with $\tilde{\kappa}_0$ since the effect of the Darcy number on slip is removed. For small $\tilde{\kappa}_0$, the contours are parallel to the lines of constant $\tilde{\gamma}$. This is because the internal Darcy flow is small such that the effect of increasing $\tilde{\kappa}_0$ on the Darcy pressure and shearing traction is due predominantly to the effective reduction in slip.

The combination of these forcing effects has non-trivial implications for the predicted surface deformation of the particle (3.95). In Figure 3.6 we present contour plots of $\widehat{L}_1^s(\tilde{\kappa}_0, \tilde{\gamma}, \nu)$, varying the Darcy number and slip for three values of the Poisson's ratio. When $\nu = 0$, no transverse strains develop when the particle is exposed to stretching or compressive forces. In this case, the shearing fluid traction presented in (3.97), which compresses the particle toward the major axis and stretches the particle away from the minor axis, does not cause the particle shape to deviate from a sphere. Consequently, only the Darcy pressure contributes to the resulting surface deformation such that the surface deformation magnitude has identical dependencies to $\widehat{M}^s(\tilde{\kappa}_0, \tilde{\gamma})$ as presented in Figure 3.5b. When $\nu = 1/2$, the particle is incompressible and the maximal transverse strains are induced when the particle is deformed. In this case, the shearing traction generates a transverse deformation which is positive along

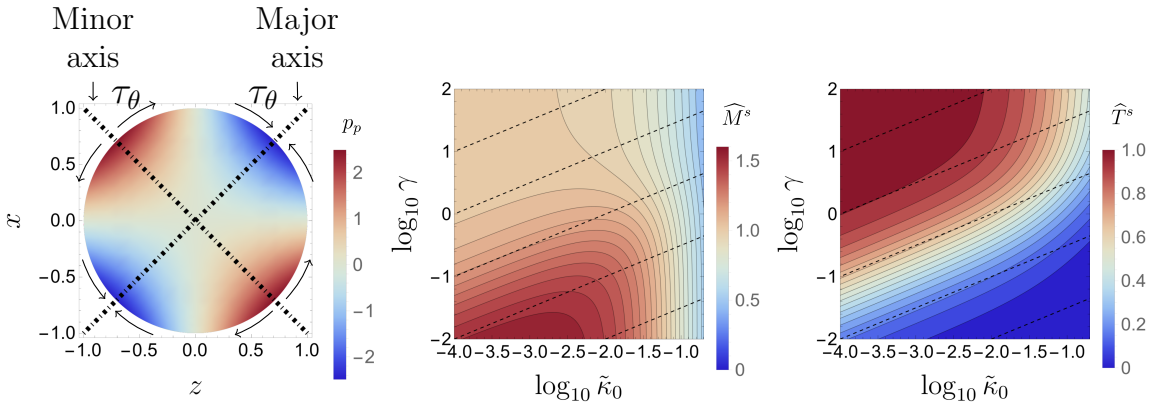

(a) (b) (c)

Figure 3.5: (a) Darcy pressure p_p within a poroelastic particle ($\alpha_0 = 0$) for $\tilde{\kappa}_0 = 10^{-3}$ and $\gamma = 100$ on $y = 0$. (b) Darcy pressure dependencies on $\tilde{\kappa}_0$ and γ, $\widehat{M}_1^s(\tilde{\kappa}_0, \tilde{\gamma})$. (c) Shearing traction dependencies on $\tilde{\kappa}_0$ and γ, $\widehat{T}^s(\tilde{\kappa}_0, \tilde{\gamma})$. In (b) and (c) the dashed lines are lines of fixed $\tilde{\gamma}$, and vary from 10^{-1} to 10^3 in powers of ten.

the major axis and negative along the minor axis. Consequently, the resulting surface deformation given by (3.23) is due to a combination of both the Darcy pressure and the transverse strains generated by the shearing traction. In this case, the surface deformation is dominated by the shearing traction and we observe that, in contrast to when $\nu = 0$, $\widehat{L}_1^s(\tilde{\kappa}_0, \tilde{\gamma}, \nu = 1/2)$ increases with γ as was observed with $\widehat{T}^s(\tilde{\kappa}_0, \tilde{\gamma})$ presented in Figure 3.5c. When $\nu = 1/4$ we observe that the surface deformation magnitude increases with γ when the Darcy number is large, and decreases with γ when the Darcy number is small. The Poisson's ratio therefore details the extent to which the shearing traction contributes to the resulting surface deformation. This interpretation motivates the decomposition

$$\widehat{L}_1^s(\tilde{\kappa}_0, \tilde{\gamma}, \nu) = \frac{2(2+\nu)}{7+5\nu}\widehat{M}_1^s(\tilde{\kappa}_0, \tilde{\gamma}) + \frac{9\nu}{7+5\nu}\widehat{T}^s(\tilde{\kappa}_0, \tilde{\gamma}), \tag{3.100}$$

where we can see clearly that when $\nu = 0$, the shear stress $\widehat{T}_s$ does not contribute to the resulting surface deformation, and when $\nu = 1/2$, contributes maximally to the dependencies on $\tilde{\kappa}_0$ and $\tilde{\gamma}$.

3.4.1.2 Coated cell

We now assume that $\alpha_0 \neq 0$ and investigate the impact of the coating thickness on the translational and rotational velocity, the Darcy pressure and shearing tractions, and the surface deformations of the coating. In Figure 3.7 we present contour plots in the (z-x) plane ($y = 0$) for $\alpha_0 = 0.25, 0.5$, and 0.75 using the same values for $\tilde{\kappa}_0$

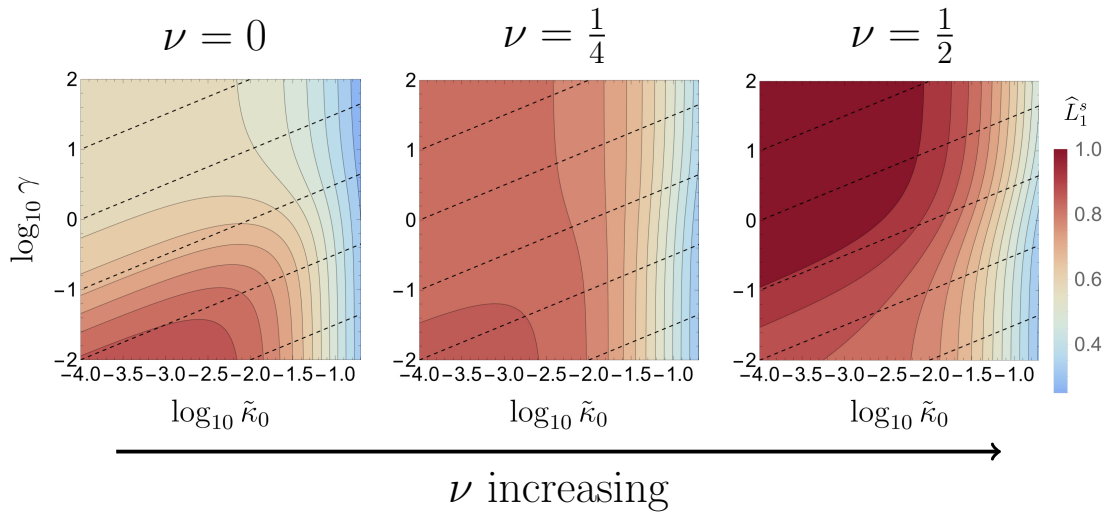

Figure 3.6: Contour plots of the magnitude of the particle surface deformation, $\widehat{L}_1^s(\tilde{\kappa}_0, \tilde{\gamma}, \nu)$. We continuously vary $\tilde{\kappa}_0$ and γ for $\nu = 0, 1/4, 1/2$. The dashed lines are lines of fixed $\tilde{\gamma}$, and vary from 10^{-1} to 10^3 in powers of ten.

and γ as in Figures 3.3 and 3.4. In the external region we plot the velocity field, $\boldsymbol{v}$, inside the coating we plot the total internal flux, $\boldsymbol{q}$. We do not present contours in the cell, since we assume no flow there. However, we remind the reader that the cell rotates with the coating according to (3.88).

In Figure 3.7 we present the surface deformations r_i by the red lines, setting $\epsilon = 0.025$, which is a quarter of the value used in Figure 3.4. We observe that the deformation increases considerably with α_0. To understand this behaviour, we define the coating thickness $\delta = 1 - \alpha_0$ and consider the limit $\delta \to 0$, corresponding to the case of an infinitesimally thin poroelastic coating. In this case, we have to leading order

$$L_i^s(\tilde{\kappa}_0, \tilde{\gamma}, \nu, \alpha_0 \to 1) = \frac{12\tilde{\kappa}_0\tilde{\gamma}(1+\nu) - \tilde{\gamma}(2+\nu) - 2(5+\nu)}{\delta((6\tilde{\kappa}_0 - 1)\tilde{\gamma} - 5)(1+\nu)} + \mathcal{O}(1), \tag{3.101}$$

such that the surface deformations r_i scale with the inverse of the coating thickness. We attribute this dependence of the deformation on the coating thickness to the stretching modulus of the coating (3.21). This is expected, as a thin closed shell may not bend without being stretched (see Section 3.2.3). It follows that in order for the infinitesimal strain assumption to remain valid, we require the normal displacement to be smaller than the coating thickness such that

$$\epsilon \ll (1 - \alpha_0)^2. \tag{3.102}$$

This result (3.102) is consistent with the expected scaling from linear shell theory [135], and suggests that stretching effects dominate the elastic response of the thin

coating. We expect (3.102) to be the correct bound on ϵ as $\alpha_0 \to 1$ for all unbounded flows; proper consideration of an external boundary would likely result in a different scaling when the coated cell is in close proximity to said boundary since the tractions imposed on the coating will increase.

In Figures 3.7a and 3.7b, we observe similar external contours to those presented in Figures 3.3a and 3.4a since in these plots the Darcy number is small such that the contours in the coating and cell both reflect the rigid body rotation given by (3.88). In particular, the external contours do not strongly depend on α_0. In Figures 3.7c and 3.7d, where the Darcy number is large, we can observe the impact of increasing α_0 on the contours. In general, increasing the cell size results in a larger disturbance to the flow field since the no penetration condition on the cell boundary (3.33) displaces the fluid around the cell.

To help interpret the coating deformation in (3.101) we also calculate the Darcy pressure/normal surface traction (3.92) and the shearing traction (3.93) in the limit $\alpha_0 \to 1$,

$$\widetilde{M}_i^s(\tilde{\kappa}_0, \tilde{\gamma}) = \frac{8 + \tilde{\gamma}}{5 + \tilde{\gamma} - 6\tilde{\kappa}_0\tilde{\gamma}} \tag{3.103}$$

$$\widetilde{T}^s(\tilde{\kappa}_0, \tilde{\gamma}) = \frac{\tilde{\gamma}(1 - 16\tilde{\kappa}_0)}{5 + \tilde{\gamma} - 6\tilde{\kappa}_0\tilde{\gamma}}, \tag{3.104}$$

where $\widetilde{M}_i^s = M_i^s(\alpha_0 \to 1)$ and $\widetilde{T}^s = T^s(\alpha_0 \to 1)$. It is apparent that both the normal traction and shearing traction blow up when $\gamma = 5\sqrt{\tilde{\kappa}_0}/(6\tilde{\kappa}_0 - 1)$ which admits realistic values of $\gamma > 0$ when $\tilde{\kappa}_0 > 1/6$. Moreover, the denominators in (3.92) and (3.93) may equal zero when $\alpha_0 > (3/8)^{1/5} \sim 0.82$, and γ and $\tilde{\kappa}_0$ are both large. We attribute this blow up to an invalid choice of parameters where the model assumptions beak down. As $\alpha_0 \to 1$, the Darcy number does not properly reflect the coating geometry, as the coating thickness is small compared with its radius. Consequently, $\tilde{\kappa}_0$ under-represents the actual Darcy number for the coating, and with $\tilde{\kappa}_0 = 1/6$ the coating approaches transparency. Since the cell size is large, flow which enters the coating is accelerated through the confined region to unrealistic speeds since there is no frictional resistance to moderate the flow in Darcy's law. Finally, when γ is large, the external flow on the coating surface must match this accelerated internal flow such that the unrealistic speeds are propagated into the external region. This gives in large velocity gradients close to the coating surface, resulting the blow up of the normal and shearing tractions. We expect that switching to Brinkman flow within the coating would remove this blow up, since the inclusion of a viscous dissipation term would restrict the magnitude of the internal velocity.

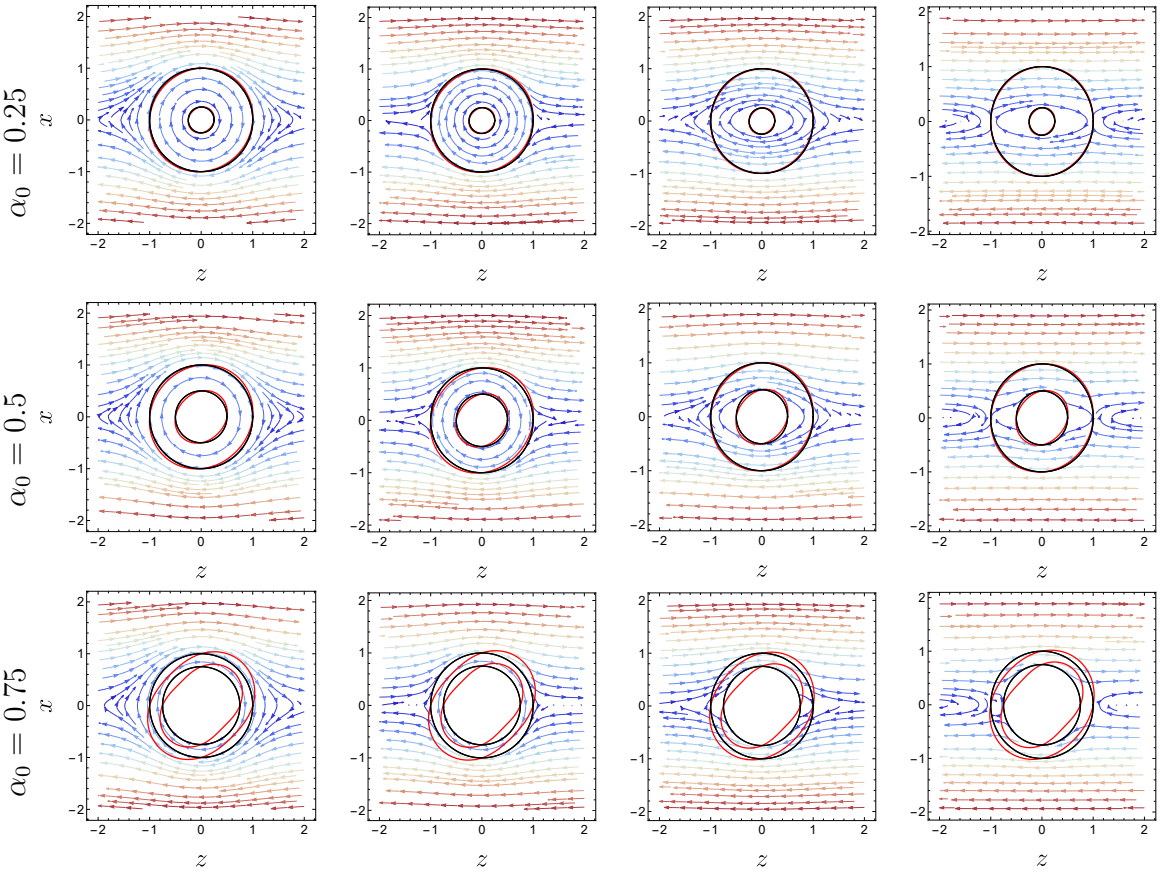

(a) $(\tilde{\kappa}_0, \gamma) = (10^{-3}, 10^2)$ (b) $(\tilde{\kappa}_0, \gamma) = (10^{-3}, 10^{-2})$ (c) $(\tilde{\kappa}_0, \gamma) = (10^{-1}, 10^2)$ (d) $(\tilde{\kappa}_0, \gamma) = (10^{-1}, 10^{-2})$

Figure 3.7: Velocity contour plots for the coated cell under an external shear flow varying $\tilde{\kappa}_0$ and $\tilde{\gamma}$ with $y = 0$. As with Figures 3.3 and 3.4 the contour colours reflect the velocity magnitude, with values ranging from 0 to 2. We also present the undeformed and deformed $(\epsilon = 0.025, \nu = 1/4)$ surfaces r_i by the black and red lines, respectively.

As in (3.100), we decompose the leading order surface deformation (3.101) in the limit of $\alpha_0 \to 1$ as

$$\widetilde{L}_i^s(\tilde{\kappa}_0, \tilde{\gamma}, \nu) = \frac{1}{1-\alpha_0}\left[\frac{5+\nu}{4(1+\nu)}\widetilde{M}_i^s(\tilde{\kappa}_0, \tilde{\gamma}) + \frac{3}{4}\widetilde{T}^s(\tilde{\kappa}_0, \tilde{\gamma})\right] + \mathcal{O}(1). \tag{3.105}$$

As was the case for a spherical poroelastic particle ($\alpha_0 = 0$) in (3.100), the contribution in (3.105) from the Darcy pressure is largest when $\nu = 0$. However, unlike in (3.100), the contribution from the shearing traction in (3.105) does not depend on the Poisson's ratio. Noting that the shearing traction on $r = \alpha_0$ is zero via the interfacial condition (3.34), as $\alpha_0 \to 1$, the coating is too thin for the transverse strains generated by the shearing traction to contribute to the resulting surface deformation. Instead, we anticipate the shearing traction generates a surface deformation through bending (and thus in-plane stretching) of the coating, the magnitude of which depends on the porous parameters $\tilde{\kappa}_0$ and γ, as well as the coating thickness and stiffness (through α_0 and ϵ).

The shearing traction in (3.104) is zero for all γ when $\tilde{\kappa}_0 = 1/16$. As the Darcy number increases, more fluid is permitted into the coating which must be diverted around the impermeable cell. In the limit of $\alpha_0 \to 1$, when $\tilde{\kappa}_0 = 1/16$, the tangential flow through the coating exactly matches the external tangential flow on $r = 1$. Consequently, the Beavers and Joseph boundary condition (3.31) is trivially satisfied by velocity continuity, such that the shearing traction is zero for all γ. Setting $\tilde{\kappa}_0 = 1/16$ in (3.103), we recover the Darcy pressure for an impermeable, perfect slip particle as was observed in Figure 3.5b. When the coating is infinitesimally thin, and the Beavers and Joseph condition is trivially satisfied for all γ, the resulting fluid problem reduces to flow around the undeformed cell, which is impermeable and has perfect slip.

We calculate the critical permeability at which the Beavers and Joseph condition is trivially satisfied for a given cell size by asserting $\partial L_i^s/\partial\gamma = 0$ and solving for $\tilde{\kappa}_0$,

$$\tilde{\kappa}_0^*(\alpha_0) = \frac{3+2\alpha_0^5}{80\alpha_0^5}. \tag{3.106}$$

When $\tilde{\kappa}_0 = \tilde{\kappa}_0^*(\alpha_0)$, the resulting fluid problem is independent of γ because the increased internal coating flow which is redirected around the cell exactly matches the external flow at $r = 1$. For Darcy numbers smaller than $\tilde{\kappa}_0^*(1) = 1/16$, the coating flow is smaller than the external flow for all cell sizes.

In Figures 3.8 and 3.9 we present the Darcy pressure (3.90) and shearing traction (3.91) magnitudes for a range of cell sizes α_0. In Figures 3.8a and 3.9a we fix $\gamma = 1$

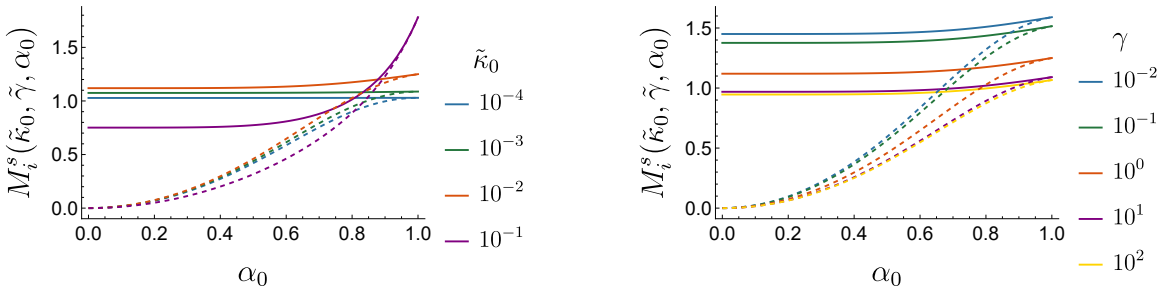

(a) $\gamma = 1$ (b) $\tilde{\kappa}_0 = 10^{-2}$

Figure 3.8: Darcy pressure dependencies $M^s(\tilde{\kappa}_0, \tilde{\gamma}, \alpha_0, r)$ given in (3.90) for varying α_0. In both plots, the solid and dashed lines have $r = 1$ and $r = \alpha_0$, respectively. In (a) we vary $\tilde{\kappa}_0$ for fixed $\gamma = 1$ and in (b) we vary γ for fixed $\tilde{\kappa}_0 = 10^{-2}$.

and present curves for different $\tilde{\kappa}_0$, and in Figures 3.8b and 3.9b we fix $\tilde{\kappa}_0 = 10^{-2}$ and present curves for different γ. In Figure 3.8, the solid and dashed lines correspond to M_1^s and M_0^s, respectively. In Figure 3.8a, we see when the Darcy number is small, the Darcy pressure on $r = 1$ is not affected by an increase in the cell size since the external flow is redirected around the coating. The Darcy pressure on $r = \alpha_0$ increases with the cell size up to the value on $r = 1$ in the limiting case of $\alpha_0 \to 1$. In general, increasing the cell size results in a larger Darcy pressure, with the effect exacerbated for a larger Darcy number. For a small cell size we see that an increase in the Darcy number initially increases the Darcy pressure due to the reduction in $\tilde{\gamma} = \gamma/\sqrt{\tilde{\kappa}_0}$ (greater effective slip), then decreases the Darcy pressure due to the greater fluid flow through the coating. As the cell size α_0 increases, this greater flow through the coating is redirected around the perfect-slip cell surface, increasing the Darcy pressure as it is harder to push the same volume of fluid through an effectively smaller area. In Figure 3.8b we instead fix $\tilde{\kappa}_0 = 10^{-2}$ and vary γ. Across all cell sizes, an increase in γ (decreased slip) decreases the Darcy pressure since the magnitude of the external flow is decreased. As the cell size increases the Darcy pressure increases; this effect is exacerbated for larger Darcy numbers, since a greater volume of fluid is redirected around the cell.

The analysis is similar for Figure 3.9 where we instead present the shearing traction dependencies given by T^s for varying $\tilde{\kappa}_0$ and γ. In Figure 3.9a, we again see that the shearing traction is not strongly affected by the cell size when the Darcy number is small. In general, an increase in the cell size decreases the shearing traction magnitude, with the relationship exacerbated for larger Darcy numbers and cell sizes. When the permeability is large (purple line) the shearing traction is negative for a large cell size. This is because the permeability is so large, the Darcy flow within

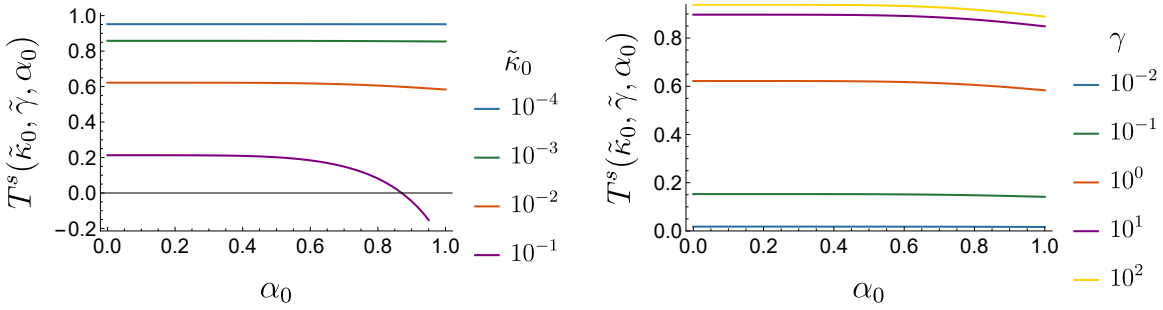

(a) $\gamma = 1$ (b) $\tilde{\kappa}_0 = 10^{-2}$

Figure 3.9: Shearing traction magnitude $T^s(\tilde{\kappa}_0, \tilde{\gamma}, \alpha_0)$ given in (3.91) for varying α_0. In (a) we vary $\tilde{\kappa}_0$ for fixed $\gamma = 1$ and in (b) we vary γ for fixed $\tilde{\kappa}_0 = 10^{-2}$.

the coating which is redirected around the impermeable cell surface is faster than the tangential external flow. Consequently, the shearing traction, which is determined via the Beavers & Joseph condition (3.31) is negative. The value of α_0 at which the shear stress is zero is predicted by inverting $\tilde{\kappa}_0^*(\alpha_0)$ in (3.106). At this point, the tangential flow in the coating exactly matches the external tangential flow on $r = 1$, such that changing γ has no effect on the solution. In Figure 3.9b we see that the shearing traction increases with γ, and again decreases with increasing cell size.

We now consider the effect of changing the cell size on the resulting surface deformations in Figures 3.10 to 3.12, noting that the cases of $\alpha_0 = 0$ and $\alpha_0 \to 1$ are related to the Darcy pressure and shearing tractions via the decompositions (3.100) and (3.105). In each plot, the solid and dashed lines correspond to the surface deformations r_1 and r_0 as described by L_1^s and L_0^s, respectively.

In Figure 3.10 we plot L_i^s for varying Darcy number, fixing $\gamma = 1$ and $\nu = 1/4$. When the cell size α_0 is small, the coating deformation magnitude L_1^s does not depend strongly on the cell size. The cell deformation magnitude L_0^s, however, scales linearly with α_0 when the cell is small, and vanishes when $\alpha_0 = 0$. We define the small α_0 behaviour as the bulk deformation mode, where the coated cell more accurately reflects a spherical poroelastic particle. Conversely, as $\alpha_0 \to 1$, both deformation magnitudes L_i^s strongly increase with α_0, and the cell deformation magnitude $L_0^s \sim L_1^s$. This reflects the expected thin coating limit calculated in (3.101), where the coating deformation scales with $1/(1 - \alpha_0)$, and is defined as the shell deformation mode. In Figure 3.10, we observe the transition between the bulk deformation and shell deformation modes occurs around $\alpha_0 = 1/2$ and is similar across all Darcy numbers.

When $\gamma = 1$ and $\nu = 1/4$ the effect of increasing $\tilde{\kappa}_0$ is similar to the case of a spherical poroelastic particle (Figure 3.6, middle panel) across all cell sizes. In fact,

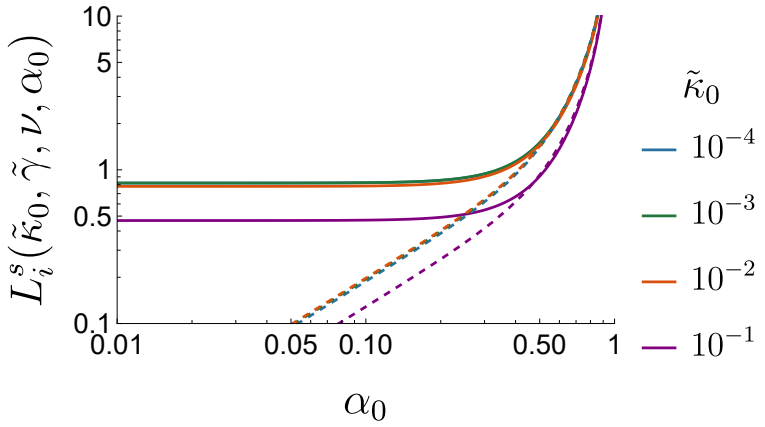

Figure 3.10: Surface deformation dependencies $L_i^s(\tilde{\kappa}_0, \tilde{\gamma}, \nu, \alpha_0)$, varying α_0 for several Darcy numbers while fixing $\gamma = 1$ and $\nu = 1/4$ throughout. The solid and dashed lines correspond to $i = 1$ and $i = 0$, respectively.

the dependencies on $\tilde{\kappa}_0$ observed in Figure 3.6 (middle panel) are similar for all $\tilde{\gamma}, \nu$, and α_0, with the coating deformation decreasing with increasing $\tilde{\kappa}_0$ except when the Darcy number and slip parameter are both small. This suggests that when α_0 is large, the increase to the Darcy pressure observed in Figure 3.8a as $\tilde{\kappa}_0$ increases is outweighed by the decrease to the shearing traction observed in Figure 3.9a.

In Figure 3.11a we instead vary γ, fixing $\tilde{\kappa}_0 = 10^{-2}$ and $\nu = 1/4$. Both the bulk and shell deformation modes are again apparent, though we observe the cell size at which $L_0^s \sim L_1^s$ increases with γ. As was similarly presented in Figure 3.6, for most cell sizes the surface deformations decrease with γ. This relationship flips for larger α_0, where the surface deformations instead increase with γ, since for a thin coating the shearing traction generates bending. For a given Darcy number and Poisson's ratio, the values of α_0 where the behaviour of L_i^s with γ changes are found by calculating $\partial L_i^s / \partial \gamma = 0$ and solving for α_0. In Figure 3.11b we present the cell size α_0 and Darcy number $\tilde{\kappa}_0$ at which this relationship flips for both L_1^s (solid lines) and L_0^s (dashed lines) over a range of Poisson's ratios. We also present $\tilde{\kappa}_0^*$ via the solid black line where, since the Darcy pressure and shearing tractions are independent of γ, we also expect L_i^s to be independent of γ. Above each curve, the respective surface deformation increases with γ; below the curve we have the opposite. For reference, the horizontal dot-dashed line corresponds to the parameter values in Figure 3.11a. For an incompressible coating ($\nu = 1/2$), L_1^s always increases with γ, regardless of the cell size. Hence, there is no solid yellow line visible in Figure 3.11b. Conversely, when $\nu = 0$, and the Darcy number is small, both L_i^s always increase with γ except in the limiting case of $\alpha_0 \to 1$. The transition points on $r = \alpha_0$ (L_0^s) are similar to those on

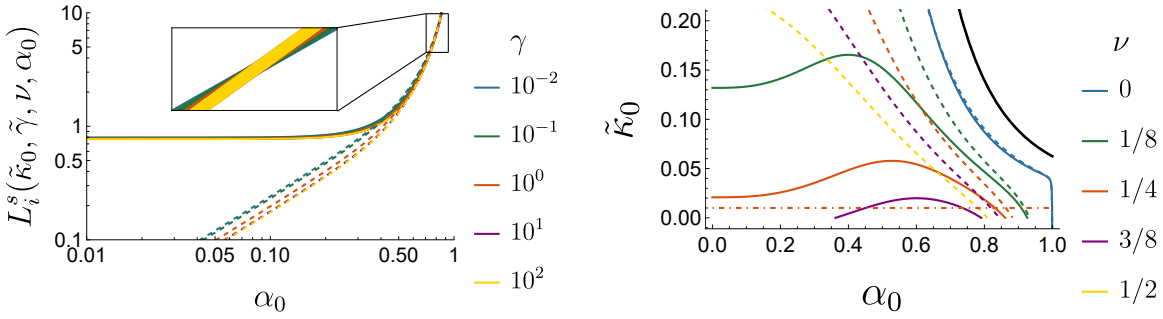

(a) $\tilde{\kappa}_0 = 10^{-2}, \nu = 1/4$ (b)

Figure 3.11: (a) Surface deformation dependencies $L_i^s(\tilde{\kappa}_0, \tilde{\gamma}, \nu, \alpha_0)$, varying α_0 for several γ while fixing $\tilde{\kappa}_0 = 10^{-2}$ and $\nu = 1/4$ throughout. (b) Curves in the $(\tilde{\kappa}_0, \alpha_0)$ space for which $\partial L_i^s/\partial\gamma = 0$ for several values of the Poisson's ratio, ν. In both plots, the solid and dashed lines correspond to $i = 1$ and $i = 0$, respectively. Above a given curve the respective surface deformation increases with γ; below the surface deformation decreases with γ.

$r = 1$ (L_1^s) when the cell size is large, since when the coating is thin we have $L_0^s \sim L_1^s$. Additionally, the transition points on $r = \alpha_0$ (L_0^s) are similar to those on $r = 1$ (L_1^s) when $\nu = 0$, since the shearing tractions, which act only on the outer coating surface $r = 1$, do not generate any surface displacement via transverse strains.

In Figure 3.12 we fix the Darcy number $\tilde{\kappa}_0 = 10^{-2}$ and slip γ and vary the Poisson's ratio ν. The cell size for which $L_0^s \sim L_1^s$, indicating the shell deformation mode, increases with ν. As was the case in Figure 3.6, for a small cell size a larger Poisson's ratio ν results in a larger surface deformation. This relationship is reversed for a larger cell size. Again, we interpret these relationships by considering the surface deformation in the limiting cases of a spherical poroelastic particle $\alpha_0 = 0$ (3.100), and an infinitesimally thin coating $\alpha_0 \to 1$ (3.105). When α_0 is small, the Poisson's ratio details the extent to which the shearing traction contributes to the surface deformation. When α_0 is large, the magnitude of the coating deformation is governed by its stretching modulus (3.21) (as bending generates stretching) which increases with ν.

3.4.2 Poiseuille flow

Figure 3.13 presents the problem schematic in a coordinate system translating with the centre of the coated cell. Here, R_0 is the dimensionless tube radius, the cell is a dimensionless distance β from the tube centre-line, and the wall velocity $\mathcal{V}\boldsymbol{e}_z = \boldsymbol{V}_{tr}/V_0$ is the normalised translational velocity of the particle in the lab frame. We note that the tube walls are represented by dashed lines, since the tube wall boundary conditions

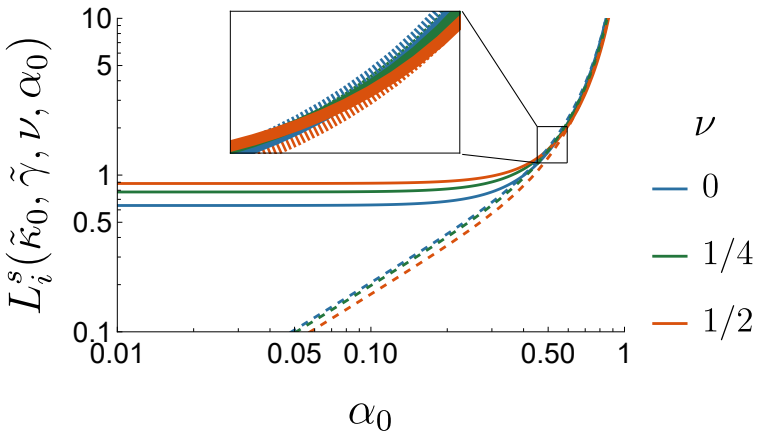

Figure 3.12: Surface deformation dependencies $L_i^s(\tilde{\kappa}_0, \tilde{\gamma}, \nu, \alpha_0)$, varying α_0 for various values of the Poisson's ratio while fixing $\gamma = 1$ and $\tilde{\kappa}_0 = 10^{-2}$ throughout. The solid and dashed lines correspond to $i = 1$ and $i = 0$, respectively.

are not satisfied in the solution framework. In order for the solution framework to remain valid, the particle must be sufficiently far from the tube wall. We therefore require

$$1 + \beta \ll R_0, \tag{3.107}$$

such that the particle does not disrupt the flow on the tube wall too strongly.

The dimensionless background Poiseuille flow may be written as,

$$v_x^e = v_y^e = 0, \quad v_z^e = (a + bx + c(x^2 + y^2)), \tag{3.108}$$

$$a = \left(1 - \frac{\beta^2}{R_0^2}\right) - U, \quad b = -\frac{2\beta}{R_0^2}, \quad c = -\frac{1}{R_0^2}. \tag{3.109}$$

The background Poiseuille flow is written exactly using the solid spherical harmonics by setting

$$\Phi_1^* = az, \quad \Phi_2^* = \frac{b}{2}xz, \quad \Phi_3^* = -\frac{c}{15}(5z^3 - 3r^2z), \quad P_1^* = 4cz, \quad \Psi_1^* = -\frac{b}{2}y. \tag{3.110}$$

Using (3.57) we obtain the translational and angular velocity of the particle. In particular, the translation velocity is given by

$$\mathcal{V} = 1 - R_0^{-2}\left(\beta^2 + \frac{2}{3}Q(\tilde{\kappa}_0, \tilde{\gamma}, \alpha_0)\right), \tag{3.111}$$

$$Q(\tilde{\kappa}_0, \tilde{\gamma}, \alpha_0) = \frac{(2 + \alpha_0^3(1 - 12\tilde{\kappa}_0) + 12\tilde{\kappa}_0)\tilde{\gamma}}{2(2 + \tilde{\gamma}) + \alpha_0^3(2 + (1 - 12\tilde{\kappa}_0)\tilde{\gamma})},$$

and the angular velocity is

$$\Omega^x = \Omega^z = 0, \quad \Omega^y = -\frac{b}{2} = \frac{\beta}{R_0^2}. \tag{3.112}$$

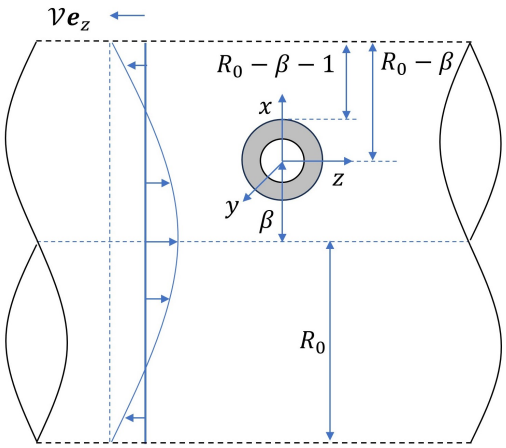

Figure 3.13: Schematic of a coated cell under Poiseuille flow in a frame of reference which translates with the cell. The coating has unit radius, the cell has radius α_0, the tube radius is R_0, and the particle is a distance β from the tube centre-line. The tube walls move with velocity $-\mathcal{V}\boldsymbol{e}_z = \boldsymbol{V}_{tr}$, corresponding to the translational velocity of the particle in the lab frame.

Here, the particle rotation is caused by the bx shearing term in (3.108) due to the particle being off-axis. The surface deformations are then given by

$$r_i = 1-\epsilon R_0^{-2}\left(\frac{5}{2}\beta L_i^s(\tilde{\kappa}_0,\tilde{\gamma},\nu,\alpha_0)\sin 2\theta\cos\phi - \frac{7}{16}L_i^p(\tilde{\kappa}_0,\tilde{\gamma},\nu,\alpha_0)(5\cos^3\theta-3\cos\theta)\right), \tag{3.113}$$

where $L_i^s(\tilde{\kappa}_0,\tilde{\gamma},\nu,\alpha_0)$, given in (3.89), is due to the shearing component of the background Poiseuille flow and is proportional to β, and $L_i^p(\tilde{\kappa}_0,\tilde{\gamma},\nu,\alpha_0)$ are the surface deformations when the coated cell is concentrically positioned in the tube ($\beta=0$). As with the case of a background shear flow, it may be shown that in order to satisfy the volume constraint (3.26) the cell pressure $p_c = p_c^0$, such that the cell pressure is not affected by the surface deformation.

We also again present the Darcy pressure and shearing tractions,

$$p_p = p_c^0 + \frac{5\beta}{2R_0^2}M^s(\tilde{\kappa}_0,\tilde{\gamma},\alpha_0,r)\sin 2\theta\cos\phi - \frac{7}{4R_0^2}M^p(\tilde{\kappa}_0,\tilde{\gamma},\alpha_0,r)(5\cos^3\theta-3\cos\theta) + \frac{1}{R_0^2}\frac{2r^3+\alpha_0^3}{r^2}\frac{4\tilde{\gamma}\cos\theta}{-2(2+\alpha_0^3)-(2+\alpha_0^3)\tilde{\gamma}+12\alpha_0^3\tilde{\kappa}_0\tilde{\gamma}}, \tag{3.114}$$

$$\tau_\theta = -\frac{5\beta}{2R_0^2}T^s(\tilde{\kappa}_0,\tilde{\gamma},\alpha_0)\cos 2\theta\cos\phi + \frac{7}{4R_0^2}T^p(\tilde{\kappa}_0,\tilde{\gamma},\alpha_0)\sin\theta(5\cos^2\theta-1) - \frac{1}{R_0^2}\frac{2(2+\alpha_0^3)\tilde{\gamma}\sin\theta}{-2(2+\alpha_0^3)-(2+\alpha_0^3)\tilde{\gamma}+12\alpha_0^3\tilde{\kappa}_0\tilde{\gamma}}, \tag{3.115}$$

$$\tau_\phi = \frac{5\beta}{2R_0^2} T^s(\tilde{\kappa}_0, \tilde{\gamma}, \alpha_0) \cos\theta \sin\phi, \tag{3.116}$$

where $M^s(\tilde{\kappa}_0, \tilde{\gamma}, \alpha_0, r)$ and $T^s(\tilde{\kappa}_0, \tilde{\gamma}, \alpha_0)$ given in (3.90) and (3.91) are due to the shearing component of the background flow when $\beta \neq 0$. The functions $M^p(\tilde{\kappa}_0, \tilde{\gamma}, \alpha_0, r)$ and $T^p(\tilde{\kappa}_0, \tilde{\gamma}, \alpha_0)$ are due to the background Poiseuille flow when the coated cell is concentrically positioned ($\beta = 0$) and are given by

$$M^p(\tilde{\kappa}_0, \tilde{\gamma}, \alpha_0, r) = \frac{7(8r^7 + 75\alpha_0^7)(10 + \tilde{\gamma})}{20r^4(4(7 + \tilde{\gamma}) + 57\tilde{\kappa}_0(10 + \tilde{\gamma}) + 3\alpha_0^7(7 + \tilde{\gamma} - 10\tilde{\kappa}_0(19 + 4\tilde{\gamma})))}, \tag{3.117}$$

$$T^p(\tilde{\kappa}_0, \tilde{\gamma}, \alpha_0) = \frac{(4 + 3\alpha_0^7(1 - 70\tilde{\kappa}_0))\tilde{\gamma}}{4(7 + \tilde{\gamma}) + 57\tilde{\kappa}_0(10 + \tilde{\gamma}) + 3\alpha_0^7(7 + \tilde{\gamma} - 10\tilde{\kappa}_0(19 + 4\tilde{\gamma}))}. \tag{3.118}$$

We note that the denominators in (3.117) and (3.118) are again identical and that T^p does not feature in τ_ϕ since the background Poiseuille flow is axisymmetric when $\beta = 0$. Similarly to (3.94), we additionally define

$$M_i^p(\tilde{\kappa}_0, \tilde{\gamma}, \alpha_0) = M^p(\tilde{\kappa}_0, \tilde{\gamma}, \alpha_0, r = \alpha_i). \tag{3.119}$$

It may be shown that the final terms in (3.114) and (3.115) generate a deformation which does not represent a departure from a sphere; specifically, they correspond to a translation of the coated cell along the z-axis. We note that this translation is omitted in (3.113).

Similar to (3.92) and (3.93), the denominators in (3.117) and (3.118) may equal zero when α_0, $\tilde{\kappa}_0$, and γ are all large. In this limit, we similarly expect unrealistic velocities within the confined region of the coating, which are propagated through to the external region via the Beavers & Joseph boundary condition. Again, we attribute this to the lack of a viscous dissipation term in Darcy's law, and expect that switching to Brinkman flow inside the coating would remove this blow up.

3.4.3 Poroelastic particle

As in Section 3.4.1.1, we first analyse the case of a poroelastic particle in a Poiseuille flow by taking $\alpha_0 = 0$. Denoting the magnitudes for a spherical poroelastic particle with a hat, for example $Q(\alpha_0 = 0) = \widehat{Q}(\alpha_0 = 0)$, we have the particle velocity

$$\mathcal{V} = 1 - R_0^{-2}\left(\beta^2 + \frac{2}{3}\widehat{Q}(\tilde{\kappa}_0, \tilde{\gamma})\right), \quad \widehat{Q}(\tilde{\kappa}_0, \tilde{\gamma}) = \frac{\tilde{\gamma}(1 + 6\tilde{\kappa}_0)}{2 + \tilde{\gamma} + 4\tilde{\kappa}_0\tilde{\gamma}}, \tag{3.120}$$

the surface deformation (3.113) with $\widehat{L}_0^p = 0$ and

$$\widehat{L}_1^p(\tilde{\kappa}_0, \tilde{\gamma}, \nu) = \frac{4(30(3 + \nu) + \tilde{\gamma}(5 + 23\nu))}{(4(7 + \tilde{\gamma}) + 57\tilde{\kappa}_0(10 + \tilde{\gamma}))(13 + 7\nu)}, \tag{3.121}$$

the Darcy pressure (3.114) with $\widehat{M}_0^p = 0$ and

$$\widehat{M}_1^p(\tilde{\kappa}_0, \tilde{\gamma}) = \frac{4(10+\tilde{\gamma})}{4(7+\tilde{\gamma}) + 57\tilde{\kappa}_0(10+\tilde{\gamma})}, \tag{3.122}$$

and the shearing traction (3.115) with

$$\widehat{T}^p(\tilde{\kappa}_0, \tilde{\gamma}, \alpha_0 = 0) = \frac{4\tilde{\gamma}}{4(7+\tilde{\gamma}) + 57\tilde{\kappa}_0(10+\tilde{\gamma})}. \tag{3.123}$$

We note that by again taking the further limits which correspond to an impermeable ($\tilde{\kappa}_0 \to 0$), no-slip ($\gamma \to \infty$), incompressible ($\nu \to 1/2$), elastic particle we have $\widehat{Q} \to 1$, $\widehat{L}_1^p \to 1$, $\widehat{M}_1^p \to 1$, and $\widehat{T}^p \to 1$, and again exactly recover the results obtained by Murata [3]. As with the case of shear flow, the rigid body rotation of the particle is identical regardless of the parameter choices.

In Figure 3.14, we present contour plots for the translational velocity of the particle (3.120) positioned along the centre-line of the tube ($\beta = 0$) with $R_0 = 2$. To interpret Figure 3.14, we first consider the dashed lines of constant $\tilde{\gamma}$, which controls the effective slip through the Beavers & Joseph condition (3.31). Increasing $\tilde{\kappa}_0$ along these dashed lines leads to a decrease in $\mathcal{V}$, since the fluid flows through the particle rather than driving it downstream. Increasing the effective slip by decreasing $\tilde{\gamma}$, we observe the particle velocity decreases. This is because the increased slip reduces the particle drag. In the limiting case of perfect slip ($\gamma = 0$), we have the maximal particle velocity $\mathcal{V} = 1$ regardless of the Darcy number $\tilde{\kappa}_0$, since the external fluid preferentially slips around the particle rather than flow through it. We now consider the impacts of the Darcy number $\tilde{\kappa}_0$ on its own, noting that, through (3.31), increasing the Darcy number decreases $\tilde{\gamma} = \gamma/\sqrt{\tilde{\kappa}_0}$ which effectively increases the slip on the particle surface. We see that when γ is small, increasing the Darcy number increases the particle velocity due to this effective reduction in slip. When γ is instead large, $\tilde{\gamma}$ is large for all Darcy numbers, such that $\mathcal{V}$ only decreases with $\tilde{\kappa}_0$. In general, the effect of the Darcy number is smaller when γ is small since the greater slip leads to the fluid preferentially flowing around the particle rather than through it. When the particle is off-axis ($\beta \neq 0$), the particle velocity $\mathcal{V}$ contains the additive constant $-\beta^2/R_0^2$ which is independent of γ and $\tilde{\kappa}_0$. Increasing β has the effect of decreasing the average velocity of the surrounding flow, while inducing the rotation captured in (3.112).

We present 2-D cross sections (z-x plane) of the velocity contours and equilibrium particle shape under Poiseuille flow in Figure 3.15, fixing $\beta = 0$ such that the particle is in the centre of the tube, and varying $\tilde{\kappa}_0$ and γ. In the external region we plot the

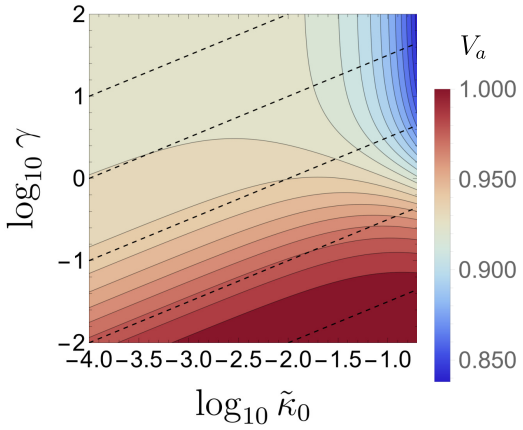

Figure 3.14: Contour plots varying $\tilde{\kappa}_0$ and γ for the particle velocity positioned along the centre-line of the tube ($\beta = 0$) with $R_0 = 2$. The dashed lines are lines of fixed $\tilde{\gamma}$, and vary from 10^{-1} to 10^3 in powers of ten.

velocity field $\boldsymbol{v}$ and inside the particle we plot the total internal volumetric flux $\boldsymbol{q}$; the contour colour reflects the velocity magnitude. We set $R_0 = 2$ throughout and choose $\epsilon = 0.2R_0^2$ such that the surface deformation is comparable to those presented in Figure 3.4. We note that since the particle translates in the lab frame, with its translational velocity $\boldsymbol{V}_{tr} = \mathcal{V}\boldsymbol{e}_z$ given by (3.120), the tube wall velocity differs slightly in each plot, as detailed in the figure caption. In all plots, flow close to the tube wall moves to the left (upstream) due to the sliding wall and flow close to the centre-line moves to the right (downstream) due to the Poiseuille flow.

Figures 3.15a and 3.15b have small Darcy number such that the internal flow is small. When γ is large in Figure 3.15a the external contours bend such that the upstream flow closer to the tube wall and downstream flow close to the tube axis are connected. In Figure 3.15b when γ is small, these bends occur over a shorter vertical distance, since the reduced friction on the particle surface causes the particle velocity to increase. In Figure 3.15c we again have a small slip ($\gamma = 100$) and increase the Darcy number. This increase in the Darcy number reduces the downstream force imposed on the particle by the external fluid, calculated via the stress integral (3.6), decreasing the particle velocity. Further, the external contours are more horizontal, since less fluid is diverted around the particle surface. Increasing the slip ($\gamma = 0.01$) in Figure 3.15d the particle mobility is again increased and we observe a similar internal flow profile to that in Figure 3.15b, since fluid may more easily slip around the particle rather than travel through it. Compared with Figure 3.15b, the increase in Darcy number results in recirculation regions which cross the particle surface. We

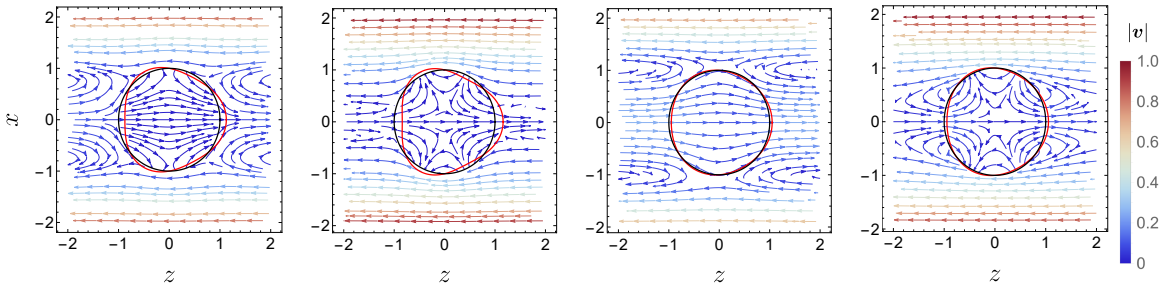

(a) $(\tilde{\kappa}_0, \gamma) = (10^{-3}, 10^2)$ (b) $(\tilde{\kappa}_0, \gamma) = (10^{-3}, 10^{-2})$ (c) $(\tilde{\kappa}_0, \gamma) = (10^{-1}, 10^2)$ (d) $(\tilde{\kappa}_0, \gamma) = (10^{-1}, 10^{-2})$

Figure 3.15: Velocity contour plots under an external Poiseuille flow varying $\tilde{\kappa}_0$ and γ; $\beta = 0$ and $R_0 = 2$ in all plots. The undeformed and deformed ($\epsilon = 0.2R_0^2, \nu = 1/4$) particle surfaces are presented via the black and red lines, respectively. From left to right the particle velocities are $0.83, 0.99, 0.74, 0.99$.

note that these recirculation regions are a result of the reference frame and are not present in the lab frame.

In Figure 3.16 we present further 2-D contour plots for an off-axis poroelastic particle in Poiseuille flow, fixing $\beta = 1/3$ and varying $\tilde{\kappa}_0$ and γ. Compared with Figure 3.15 the particle velocity is decreased by β^2/R_0^2 and the particle rotates according to (3.112). With a small Darcy number in Figures 3.16a and 3.16b, the internal total flux contours are circular due to this rotation. However increasing the Darcy number in Figures 3.16c and 3.16d, we observe a large Darcy flow through the particle. In both Figures 3.15 and 3.16, we note that the tube wall boundary conditions are not strongly disrupted, especially when the Darcy number is larger. In fact, only the topmost contours in Figures 3.16a and 3.16b, where the particle is closest to the tube wall, are visibly perturbed from horizontal.

When on the centre-line ($\beta = 0$), the particle adopts a bullet-like shape which is consistent with previous observations for an elastic particle [3, 28, 136]. When off-axis, the particle shape is a linear combination of a bullet-like deformation associated with the Poiseuille flow and the prolate spheroid deformation associated with a shear flow of strength b. With $\beta = 1/3$, $b = -2\beta/R_0^2$ is negative, such that the major and minor axes presented in Figure 3.5a are flipped and the rotation (3.112) is anticlockwise. From (3.113), we note that the surface deformation is proportional to R_0^{-2}. This is expected since in the limiting case of $R_0 \to \infty$ the background flow is uniform, which generates no surface deformation for a non-porous elastic particle [69].

Since the particle surface deformation associated with the shear flow contribution ($\widehat{L}_1^s$) was analysed in Figure 3.6, we now focus on the Poiseuille flow contribution for a particle on the centre-line of the surrounding tube ($\widehat{L}_1^p$), presenting contour plots in

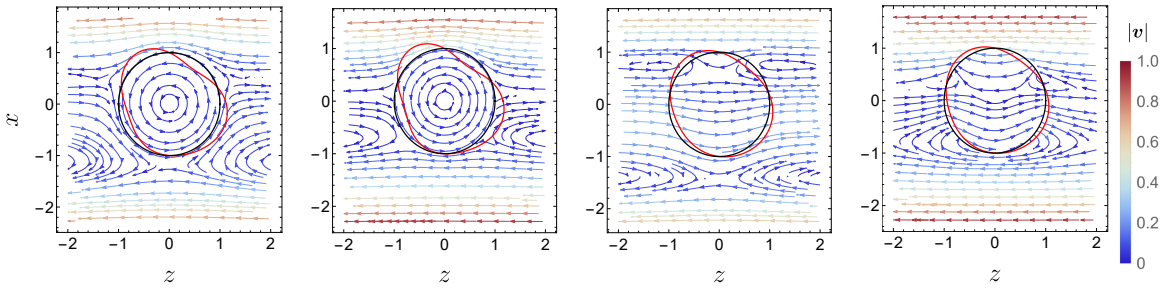

(a) $(\tilde{\kappa}_0, \gamma) = (10^{-3}, 10^2)$ (b) $(\tilde{\kappa}_0, \gamma) = (10^{-3}, 10^{-2})$ (c) $(\tilde{\kappa}_0, \gamma) = (10^{-1}, 10^2)$ (d) $(\tilde{\kappa}_0, \gamma) = (10^{-1}, 10^{-2})$

Figure 3.16: Velocity contour plots under an external Poiseuille flow varying $\tilde{\kappa}_0$ and γ; $\beta = 1/3$ and $R_0 = 2$ in all plots. The undeformed and deformed ($\epsilon = 0.2R_0^2, \nu = 1/4$) particle surfaces are presented via the black and red lines, respectively. From left to right the particle velocities are $0.80, 0.95, 0.71, 0.97$.

(3.121). The Darcy number $\tilde{\kappa}_0$ and slip parameter γ are varied continuously for the discrete values of Poisson's ratio, $\nu = 0, 1/4, 1/2$. We observe similar dependencies on $\tilde{\kappa}_0, \gamma$ and ν which we again attribute to the effects of the Darcy pressure and normal/shearing fluid tractions. With large γ (smaller slip) the sliding wall generates a larger shearing traction on the particle surface. As before, with $\nu = 1/2$ transverse strains develop within the particle such that an increase in γ increases the surface deformation magnitude. With $\nu = 0$, no such transverse strains are developed such that we observe the reverse dependency. Similar to (3.100), we write the surface deformation (3.121) as a combination of the Darcy pressure (3.122) and shearing traction (3.123),

$$\widehat{L}_1^p(\tilde{\kappa}_0, \tilde{\gamma}, \nu) = \frac{3(3+\nu)}{(13+7\nu)}\widehat{M}_1^p(\tilde{\kappa}_0, \tilde{\gamma}) + \frac{4(5\nu-1)}{(13+7\nu)}\widehat{T}^p(\tilde{\kappa}_0, \tilde{\gamma}). \tag{3.124}$$

Similar to (3.100), we see that as ν increases, the contribution from the Darcy pressure decreases, and the contribution from the shearing traction increases. However, unlike in (3.100), here the shearing traction generates a surface deformation when $\nu = 0$. We attribute this to the more complex θ dependence (larger n in the solid spherical harmonic functions) of the shearing traction in (3.115). When $\nu = 1/5$, we see that the base contribution (when $\nu = 0$) of the shearing traction to the surface deformation exactly cancels the contribution due to the transverse strains developed within the particle.

3.4.4 Coated cell

We now consider the general case when $\alpha_0 \neq 0$ such that we again model the cell region, with the aim to predict how the cell size/coating thickness impacts the cell

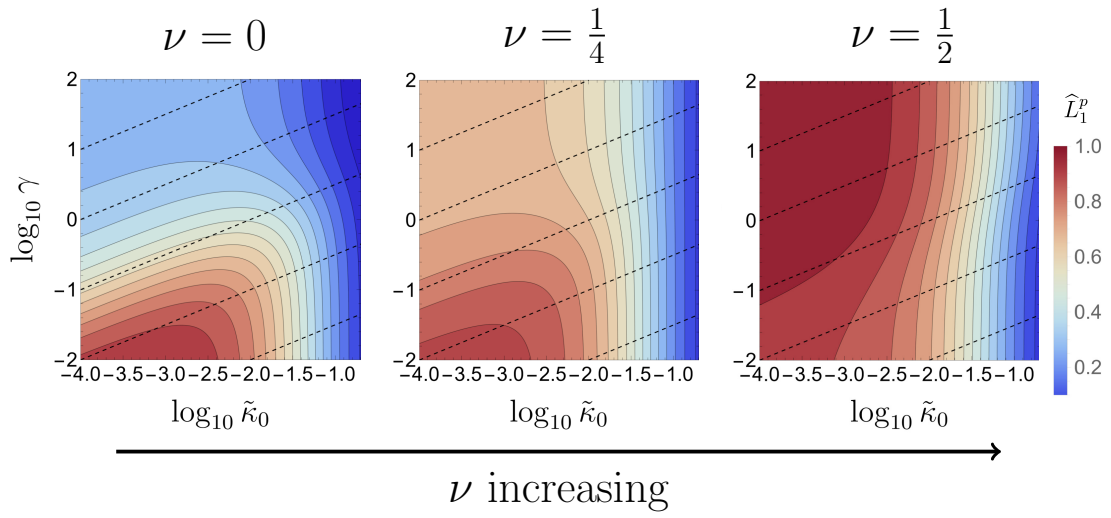

Figure 3.17: Contour plots of the magnitude of the particle surface deformation, $L_1^p(\tilde{\kappa}_0, \tilde{\gamma}, \nu, \alpha_0 = 0)$. We continuously vary $\tilde{\kappa}_0$ and γ for $\nu = 0, 1/4, 1/2$. The dashed lines are lines of fixed $\tilde{\gamma}$, and vary from 10^{-1} to 10^3 in powers of ten.

velocity and the resulting surface deformations. We first consider the particle velocity given in (3.111). Since there is a factor of $\alpha_0^3(1 - 12\tilde{\kappa}_0)\tilde{\gamma}$ in both the numerator and denominator of $Q(\tilde{\kappa}_0, \tilde{\gamma}, \alpha_0)$, the cell velocity is not strongly dependent on the cell size and is instead determined primarily by the Darcy number $\tilde{\kappa}_0$ and slip parameter γ. We argue this is because the cell surface has perfect slip, such that fluid which is displaced by the cell surface does not strongly affect the total drag of the coated cell. When $\tilde{\kappa_0} \to 0$, corresponding to an impermeable coating, Q is not dependent on the cell size since there is no flow within the coating. As was the case in Figure 3.14, when $\gamma = 0$, corresponding to a perfect slip, the fluid preferentially flows around the coating rather than through it, such that the cell velocity equals $\mathcal{V} = 1$ for all Darcy numbers and cell sizes when $\beta = 0$.

To visualise the flow, we present the selection of velocity contour plots in Figure 3.18 for the cell sizes $\alpha_0 = 1/4, 1/2$, and $3/4$. We choose a large Darcy number $\tilde{\kappa}_0 = 10^{-1}$ in each plot, since the external flow is not strongly affected by the cell size when the Darcy number is small, and vary the slip parameter γ and eccentricity β. The coated cell velocities differ in each plot, as indicated above each plot. The cell size does not have a strong effect on the cell velocity, such that each column in Figure 3.18 has a similar translational velocity. In the external region we plot the velocity field $\boldsymbol{v}$, and inside the coating we plot the total internal volumetric flux $\boldsymbol{q}$. We do not plot contours inside the cell region, though note the cell rotates according to (3.112). The contour colour reflects the velocity magnitude, with values varying

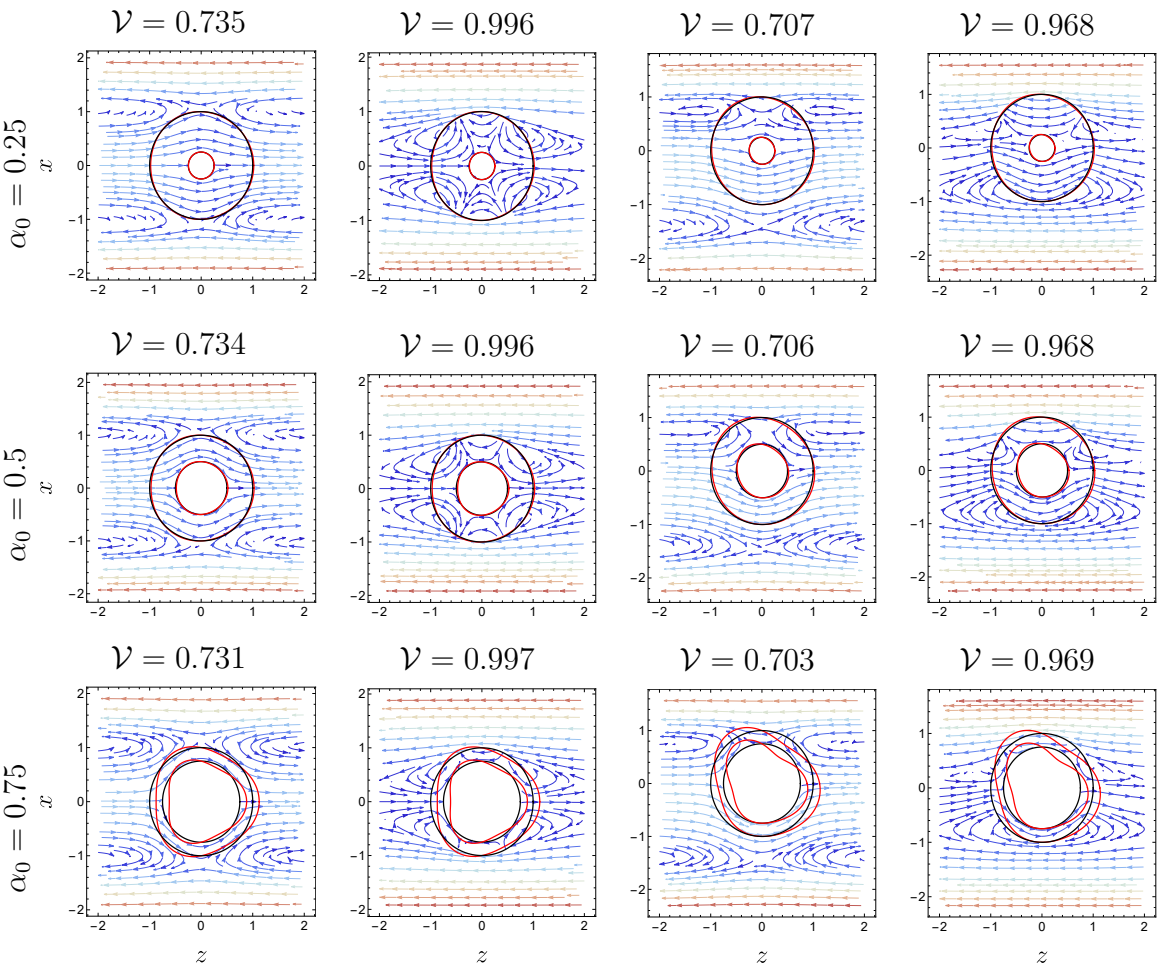

(a) $(\gamma, \beta) = (10^2, 0)$ (b) $(\gamma, \beta) = (10^{-2}, 0)$ (c) $(\gamma, \beta) = (10^2, 1/3)$ (d) $(\gamma, \beta) = (10^{-2}, 1/3)$

Figure 3.18: Velocity contour plots of the coated cell under an external Poiseuille flow varying γ and β for fixed $\tilde{\kappa}_0 = 10^{-1}$ with $y = 0$. In the external region we plot the velocity field, $\boldsymbol{v}$ and inside the coating we plot the flux, $\boldsymbol{q}$. As with Figures 3.15 and 3.16 the contour colours reflect the velocity magnitude, with values ranging from 0 to 1 (see Figure 3.15). We also present the undeformed and deformed $(\epsilon = 0.075R_0^2, \nu = 1/4)$ surfaces r_i by the black and red lines, respectively.

from 0 to 1 (see Figure 3.15). We set $R_0 = 2$ throughout and choose $\epsilon = 0.075R_0^2$ such that the surface deformation is comparable to those presented in Figures 3.15 and 3.16. In Figures 3.18a and 3.18c, which may be compared directly with Figures 3.15c and 3.16c, we have a small slip ($\gamma = 100$). As the cell size is increased, flow in the coating is increased. This does not strongly affect the external flow, or the cell's translational velocity, since the cell surface has perfect slip, and the tangential flow on the cell surface is not penalised via friction. In Figures 3.18b and 3.18d, which may be compared directly with Figures 3.15d and 3.16d, we have a large slip ($\gamma = 10^{-2}$). Consequently, the particle velocity is large since the fluid preferentially flows around the coating rather than through it. This is reflected in the velocity contours by the small magnitude of internal flow. Once again, the external Stokes flow is also not strongly affected by increasing the cell size. As expected, the coating obtains a similar deformed shape when compared with Figures 3.15 and 3.16, with the deformation magnitude increasing strongly with the cell size.

To avoid repetition, we do not present the Poiseuille flow components of the Darcy pressure and surfaces shearing tractions presented in (3.114) and (3.115) since the dependencies are similar to those observed in Figures 3.8 and 3.9. For completeness, we present the dependencies of the surface deformation associated with the background Poiseuille flow L_i^p in Figure 3.19, though we note that these are similar to those presented in Figures 3.10 to 3.12.

To aid the interpretation of the surface deformation we again consider the limiting case of a thin coating, $\alpha_0 \to 1$. We expand the surface deformation to leading order in $1 - \alpha_0$ to obtain,

$$\widetilde{L}_1^p(\tilde{\kappa}_0, \tilde{\gamma}, \nu) = \frac{1}{1-\alpha_0} \frac{24\tilde{\kappa}_0\tilde{\gamma}(1+\nu) - \tilde{\gamma}(3+\nu) - 2(11+\nu)}{(7+\tilde{\gamma}-9\tilde{\kappa}_0\tilde{\gamma})(1+\nu)} + \mathcal{O}(1), \tag{3.125}$$

which, by similarly setting $\alpha_0 \to 1$ in (3.117) and (3.118) may be written as

$$\widetilde{L}_i^p(\tilde{\kappa}_0, \tilde{\gamma}, \nu) = \frac{1}{1-\alpha_0} \left[\frac{11+\nu}{5(1+\nu)} \widetilde{M}_i^p(\tilde{\kappa}_0, \tilde{\gamma}) + \frac{4}{5} \widetilde{T}^p(\tilde{\kappa}_0, \tilde{\gamma}) \right] + \mathcal{O}(1), \tag{3.126}$$

where

$$\widetilde{M}_i^p(\tilde{\kappa}_0, \tilde{\gamma}) = \frac{10+\tilde{\gamma}}{7+\tilde{\gamma}-9\tilde{\kappa}_0\tilde{\gamma}}, \tag{3.127}$$

$$\widetilde{T}^p(\tilde{\kappa}_0, \tilde{\gamma}) = \frac{\tilde{\gamma}(1-30\tilde{\kappa}_0)}{7+\tilde{\gamma}-9\tilde{\kappa}_0\tilde{\gamma}}. \tag{3.128}$$

Similar to (3.105), the contribution of the shearing traction to the surface displacement does not depend on ν.

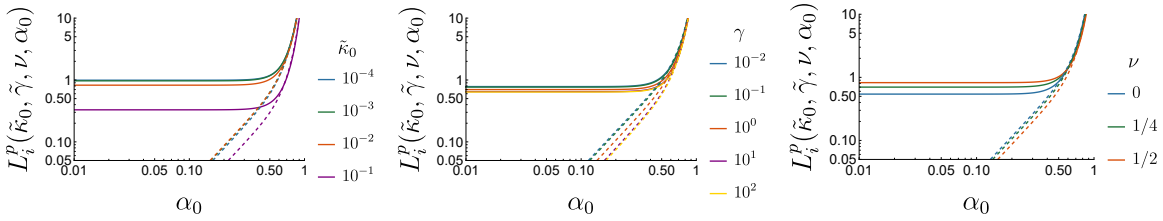

(a) (b) (c)

Figure 3.19: Surface deformation dependencies $L_i^p(\tilde{\kappa}_0, \tilde{\gamma}, \nu, \alpha_0)$ (see (3.113)), varying α_0 for (a) several values of the Darcy number $\tilde{\kappa}_0$, fixing $\gamma = 1$ and $\nu = 1/4$, (b) several values of the slip parameter γ, fixing $\tilde{\kappa}_0 = 10^{-2}$ and $\nu = 1/4$, and (c) several values of the Poisson's ratio ν, fixing $\tilde{\kappa}_0 = 10^{-2}$ and $\gamma = 1$. In all plots, the solid and dashed lines correspond to $i = 1$ and $i = 0$, respectively.

In Figure 3.19 we again see a clear distinction between the bulk deformation mode, where the surface deformation on $r = 1$ is not strongly affected by an increase to the cell size, and the shell deformation mode, in which $L_0^p = L_1^p$ and both scale with the inverse of the coating thickness. Distinct from the case of a background shear flow (Figures 3.10 to 3.12), where the cell deformation L_0^s scaled with the cell size α_0, in Figure 3.19 we see that when α_0 is small, L_0^p instead scales with α_0^2.

3.5 Summary and discussion

We develop a framework to model an initially spherical coated cell exposed to a general background Stokes flow. We assume the ratio of the viscous fluid stress to the elastic stiffness is small such that the coating is governed by the equations of linear poroelasticity. Using this framework we are able to analytically investigate the impacts of Darcy number, slip, Poisson's ratio, and cell size on the translation, rotation, and deformation of the coated cell. We present results for two example background flow profiles, shear flow and Poiseuille flow. In the latter, the results are valid provided the coated cell is sufficiently far from the external boundary. The presented framework allows the theoretical consideration of external flows involving any external boundary, provided they can be treated as unbounded, that is, the background flow may be written as a finite sum of spherical harmonics. We also consider the special case of zero cell size, in which we show the solutions describe an initially spherical poroelastic particle in an unbounded flow. Taking further limits, we show that for both a background shear and Poiseuille flow, our solutions agree exactly with those presented by Murata [3] in the limiting case of a non-porous, incompressible elastic particle with no-slip boundary conditions.

Under a shear flow the coated cell rotates, with different flow patterns observed for varying slip. Interestingly, the leading-order cell rotation does not depend on its material properties or the coating thickness, since the torque imposed on the coated cell by the background shear flow scales identically with the torque experienced by a coated cell which rotates in an unbounded quiescent fluid. We separate the surface deformation of the coated cell into two modes: a bulk deformation mode when the cell size is small, and a shell deformation mode when the cell size is large (thin coating). The transition between these two modes is shown to depend on the slip parameter γ and the Poisson's ratio ν. In general, we find that the surface displacement decreases with increasing Darcy number and, surprisingly, may either increase or decrease with increasing slip, depending on the Poisson's ratio and cell size. We interpret these dependencies by considering the Darcy pressure and fluid tractions which drive the resulting deformation, presenting explicit decompositions in the limiting cases of a spherical poroelastic particle and a thin coating. When the coating is thin (shell deformation mode), the coating deformation scales with the reciprocal of its thickness which is consistent with the expected result of a thin spherical shell. Consequently, for a thin coating the dependence of the surface deformation on the Darcy number, slip, and Poisson's ratio are small when compared with the coating thickness. Under a background Poiseuille flow the coated cell translates; its mobility is decreased with the Darcy number and enhanced by a large slip. When positioned on the tube centre-line the coated cell obtains a bullet-like shape, with similar dependencies to those observed for a shear flow. When off-axis, a shearing component is introduced in the background flow which causes the cell to translate more slowly, rotate, and deform according to the magnitude of the shear. Under a Poiseuille flow, we predict the deformation magnitude depends on the inverse square of the tube radius. Additionally, under both flows, we find that the leading-order surface deformation does not affect the cell pressure.

The framework developed in this chapter may be generally applied to any unbounded Stokes flow. However, it does not ensure any external wall boundary conditions are satisfied. This is important when the coated cell is in close proximity to the external boundary. In Chapter 4, we utilise similar solution methods to Chapter 2 (MoR and ALE FEM) to investigate the impacts of tube confinement on the coated cell, comparing to the unbounded solutions presented here where possible.

Chapter 4

The impact of confinement on the mobility and deformation of a hydrogel-coated cell in a tube

4.1 Chapter summary

In this chapter, we consider a hydrogel-coated cell in tube flow. This forms a direct extension from Chapter 2, where the elastic particle is replaced by the hydrogel-coated cell model detailed in Chapter 3. The coated cell translates axially along the centre-line the rigid cylindrical tube and is subject to a background Poiseuille flow. We seek steady solutions and investigate how the material properties of the coating and problem geometry impact the translational velocity and deformation of the cell, the change in pressure drop across the tube length, and the cell pressure. Similar to Chapter 2, we again solve the leading-order problem in the limit of a small ratio of typical viscous forces to coating stiffness, utilising the MoR to calculate the leading-order flow. We also develop an ALE FEM framework to solve the full non-linear problem, allowing the range of validity of the MoR solutions, along with the non-linear effects associated with the finite deformation of the coating, to be interrogated. While this work is strongly motivated by the application to cell therapies described in Chapter 1, the results in this paper aim to provide general fluid mechanical insight into the impacts of tube confinement.

This chapter is structured as follows. In Section 4.2 we provide the non-linear governing equations for the external fluid, hydrogel coating, and cell, and present all boundary and interfacial conditions. We then non-dimensionalise and perform an asymptotic expansion in the limit of a small ratio of typical viscous fluid stress to elastic stiffness in Section 4.3, showing that the problem is identical to that presented in

Chapter 3 under an axisymmetric background Poiseuille flow with additional boundary conditions which explicitly account for the tube wall. In Section 4.4, we present two methods for solving these problems, both of which are direct applications of those presented in Chapter 2. The first involves the semi-analytical method of reflections (MoR), and the second is an ALE numerical scheme, which we use to validate the MoR solutions and interrogate their range of validity. In Section 4.5, we investigate the impacts of the Darcy number, slip parameter, Poisson's ratio, and the cell size and coating thickness on the cell velocity, pressure, and resulting deformation, comparing results where possible to the unbounded case presented in Section 3.4.2. Finally, we provide closing discussions and outline future extensions in Section 4.6.

4.2 Governing equations and boundary conditions

We model an initially spherical, hydrogel-coated cell translating axially along the centre-line of a cylindrical tube driven by Poiseuille flow far in the far-field. We define spherical and cylindrical coordinate systems (r, ϕ, θ) and (ρ, ϕ, z), with corresponding unit vectors $(\boldsymbol{e}_r, \boldsymbol{e}_\phi, \boldsymbol{e}_\theta)$ and $(\boldsymbol{e}_\rho, \boldsymbol{e}_\phi, \boldsymbol{e}_z)$, respectively. We align the z-axis with the central axis of the tube and choose both origins to coincide with the centre of the cell as shown in Figure 4.1. We assume the problem is axisymmetric in ϕ and has reached a steady state in a frame moving with the centre of mass of the cell. The maximum magnitude of the background tube flow is V_0 in the lab frame and the undeformed cell, undeformed hydrogel coating, and tube radii are given by a_0, a_1, and ρ_0, respectively. The tube wall has velocity $-V_a\boldsymbol{e}_z$ where V_a is the translational velocity of the cell in the lab frame. This cell velocity is unknown and depends on the problem geometry and the coating's material properties. The fluid, hydrogel coating, and cell domains are denoted by Ω_f, Ω_h, and Ω_c, respectively, with the interfaces between them denoted by $\partial\Omega_1$ and $\partial\Omega_0$. It will also be useful to define the unit normal and tangent to the cell and its coating as $\boldsymbol{n}_i$ and $\boldsymbol{t}_i = \boldsymbol{e}_\phi \times \boldsymbol{n}_i$, $i = 0, 1$, respectively, where both $\boldsymbol{n}_i$ point toward the surrounding external fluid.

The surrounding fluid, hydrogel coating, and cell are modelled using the framework presented in Appendices C.1 and C.2. To avoid repetition, we present the non-linear dimensionless governing equations and boundary conditions here, redefining all necessary quantities such that the presentation is standalone. The non-dimensionlisation choices are similar to those presented in Appendix C.3, with the only difference being the choice of length scale. Remaining consistent with Chapter 2 (see Section 2.2.2), we non-dimensionalise lengths with ρ_0, velocities with V_0, pressures and stresses with

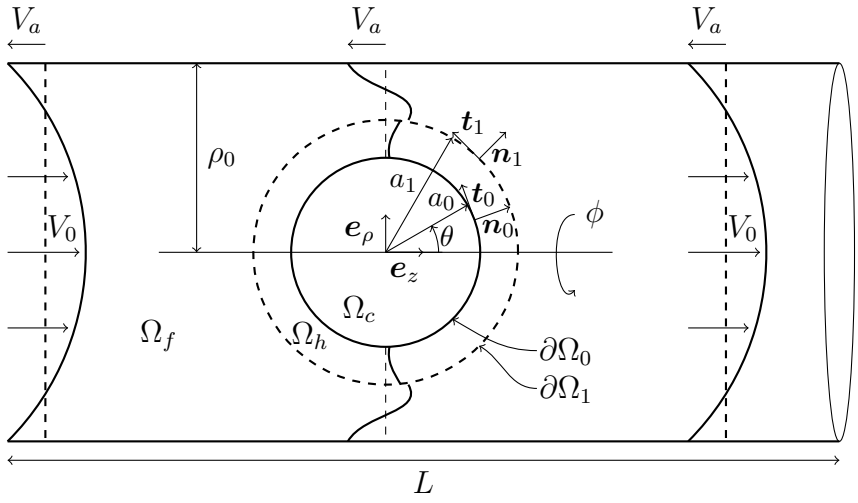

Figure 4.1: Schematic of a hydrogel-coated cell translating along the centre-line of a cylindrical tube with background Poiseuille flow far upstream and downstream, presented in the frame of reference of the cell. The cell velocity in the lab frame is $V_a\boldsymbol{e}_z$.

the viscous pressure scale $\rho_0/\mu_f V_0$, where μ_f is the fluid viscosity. We again introduce the dimensionless parameter

$$\epsilon = \frac{\mu_f V_0}{\mu_s \rho_0}, \tag{4.1}$$

where μ_s is the shear modulus of the coating, and ϵ is the ratio of typical viscous stresses in the external flow to the elastic stiffness of the solid skeleton. It follows that the coating deformation is scaled on $\epsilon\rho_0$.

4.2.1 Surrounding Fluid

The surrounding flow is modelled as a Newtonian viscous fluid and, neglecting inertial terms, is governed by the incompressible Stokes equations,

$$\nabla \cdot \boldsymbol{\sigma}_f = \boldsymbol{0}, \tag{4.2}$$

$$\nabla \cdot \boldsymbol{v} = 0, \tag{4.3}$$

where $\boldsymbol{v}$ is the fluid velocity and $\boldsymbol{\sigma}_f$ is the fluid stress tensor given by

$$\boldsymbol{\sigma}_f = -p_f \boldsymbol{I} + \left[\nabla \boldsymbol{v} + (\nabla \boldsymbol{v})^T\right], \tag{4.4}$$

with p_f the fluid pressure and the superscript T denotes the transpose. We note that the external fluid pressure is determined up to an arbitrary constant. Here, we choose

to set $p_f = 0$ far downstream from the hydrogel-coated cell; for the purposes of this work we choose $p_f = 0$ at $(z, \rho) = (10, 0)$. To avoid dependence on this arbitrary constant we additionally define the extra pressure drop across the tube as,

$$\Delta P^+ = \lim_{L\to\infty} \left(\Delta p_f - \Delta P^{\text{Pois}}\right) = \lim_{L\to\infty} \left(\Delta p_f - 4L\right), \tag{4.5}$$

where L is the dimensionless tube length and ΔP^{Pois} is the Poiseuille flow contribution to the pressure field. The extra pressure drop ΔP^+ was similarly presented in Barakat et al. [73] and measures the change in pressure drop along the tube due to the coated cell independent of the tube length.

4.2.2 Hydrogel coating

We model the hydrogel coating as a poroelastic material comprised of a porous and deformable solid skeleton which is fully saturated by the external fluid. The material of the solid skeleton is assumed to be incompressible, though compression of the coating is permitted through local changes to the pore structure. To facilitate coupling to the external Newtonian fluid, we adapt the non-linear Eulerian presentation of the equations of poroelasticity in MacMinn et al. [125].

The local volume fractions of the fluid and solid phases are denoted by ϕ_f and ϕ_s, respectively; ϕ_f is also called the porosity. Since the fluid fully saturates the solid skeleton, we have $\phi_f + \phi_s = 1$.

We define the displacement of the solid skeleton as

$$\epsilon \boldsymbol{u}(\boldsymbol{x}) = \boldsymbol{x} - \boldsymbol{X}(\boldsymbol{x}), \tag{4.6}$$

where $\boldsymbol{X}$ is the position of a material point in the undeformed configuration and $\boldsymbol{x}$ is the current position vector of this point. The deformation gradient tensor $\boldsymbol{F}$ is defined via

$$\boldsymbol{F}^{-1} = \nabla \boldsymbol{X} = \boldsymbol{I} - \epsilon \nabla \boldsymbol{u}. \tag{4.7}$$

We further define the left Cauchy-Green deformation tensor $\boldsymbol{B} = \boldsymbol{F}\boldsymbol{F}^{\mathrm{T}}$ and the Jacobian

$$J(\boldsymbol{x}) = \det(\boldsymbol{F}) = \frac{1}{\det(\boldsymbol{F}^{-1})}, \tag{4.8}$$

which measures the local volume change of the coating. The Jacobian is directly related to the porosity via

$$J(\boldsymbol{x}) = \frac{1 - \phi_{f,0}}{1 - \phi_f(\boldsymbol{x})}, \tag{4.9}$$

where $\phi_{f,0} = \phi_f(\boldsymbol{x} - \epsilon\boldsymbol{u}(\boldsymbol{x}))$ is the porosity of the undeformed coating, which we assume is constant.

We assume the internal fluid flow is governed by Darcy's law [47],

$$\boldsymbol{q} = \phi_f(\boldsymbol{v}_p - \boldsymbol{v}_s) = -\tilde{\kappa}_0\kappa(\phi_f)\nabla p_p, \tag{4.10}$$

where $\boldsymbol{q}$ is the Darcy flow, κ is the permeability of the coating, and $\tilde{\kappa}_0 = \kappa_0/\rho_0^2$ is the Darcy number. Here, κ_0 is the dimensional permeability of the undeformed coating such that we have $\kappa(\phi_{f,0}) = 1$. The internal fluid velocity and solid skeleton velocity are $\boldsymbol{v}_p$ and $\boldsymbol{v}_s$, respectively, and the Darcy pressure is denoted by p_p. In general the permeability will change as the solid skeleton deforms, which is captured through its dependence on porosity. Imposing conservation of mass for the internal fluid and solid phases we have

$$\nabla \cdot (\phi_f \boldsymbol{v}_p) = 0, \quad \nabla \cdot (\phi_s \boldsymbol{v}_s) = 0, \tag{4.11}$$

such that by combining (4.10) and (4.11) we have

$$\nabla \cdot (\boldsymbol{q} + \boldsymbol{v}_s) = 0 \tag{4.12}$$

Since we seek steady solutions, choose a reference frame which translates with the coated cell, and do not expect the coated cell to rotate due to system symmetry, the solid skeleton velocity $\boldsymbol{v}_s = \boldsymbol{0}$. When solving the governing equations numerically in Section 4.4.2 it will instead be convenient to work in the lab frame such that $\boldsymbol{v}_s = \mathcal{V}\boldsymbol{e}_z$, where $\mathcal{V} = V_a/V_0$ is the dimensionless cell velocity in the lab frame.

To describe how the fluid and solid phases support the local mechanical load we write the total stress as

$$\boldsymbol{\sigma}_p = \boldsymbol{\sigma}' - p_p\boldsymbol{I}, \tag{4.13}$$

where $\boldsymbol{\sigma}'$ is Terzaghi's effective stress tensor, defined as the force per unit total area supported by the solid skeleton through deformation. We adopt a compressible neo-Hookean description as an effective stress strain relationship within the solid skeleton,

$$\boldsymbol{\sigma}' = \lambda(J-1)\boldsymbol{I} + \frac{\mu_s}{J}\left(\boldsymbol{B} - \boldsymbol{I}\right), \tag{4.14}$$

where λ is Lamé's first parameter and $\frac{1}{2}\left(\boldsymbol{B} - \boldsymbol{I}\right)$ is the strain which is assumed to be finite. We additionally define the Poisson's ratio $\nu = \lambda/(2(\lambda + \mu_s))$ which quantifies the magnitude of the transverse strains induced in the material under stretching or compression. Imposing mechanical equilibrium we have

$$\nabla \cdot \boldsymbol{\sigma}_p = \nabla \cdot \boldsymbol{\sigma}' - \nabla p_p = \boldsymbol{0}. \tag{4.15}$$

4.2.3 Cell

We model the cell as a sack of incompressible viscous fluid enclosed by an impermeable membrane. As discussed in Section 3.2.3, the elastic resistance provided by this membrane is characterised predominantly by its stretching modulus,

$$K_c = \frac{E_c h_c}{1 - \nu_c^2}, \tag{4.16}$$

where E_c is the Young's modulus of the membrane, h_c is the membrane thickness, and ν_c is the Poisson's ratio of the membrane. This is because a closed spherical shell may not be bent without being stretched [126]. Here, we neglect the elasticity of the membrane and assume the stretching stiffness of the hydrogel coating $K_h \gg K_c$. In dimensional terms, K_h may be approximated as

$$K_h \propto E(a_1 - a_0), \tag{4.17}$$

where $E = \mu_s(3\lambda + 2\mu_s)/(\lambda + \mu_s) = 2\mu_s(1 + \nu)$ is the Young's modulus of the coating [127, 128].

Since the cell membrane is assumed to be impermeable (see Chapter 1) and we seek steady solutions, we assume no flow inside the cell. Moreover, we assume the pressure in the cell, denoted by p_c, enforces the volumetric constraint,

$$\iiint_{\Omega_c} \mathrm{d}V = V_c = \frac{4}{3}\pi\alpha_0^3, \tag{4.18}$$

where V_c is the undeformed cell volume and $\alpha_0 = a_0/\rho_0$ is the dimensionless cell radius.

4.2.4 Boundary conditions

Far upstream and downstream of the coated cell we impose Poiseuille flow, expressed in the frame of reference of the cell as

$$\boldsymbol{v}(z \to \pm\infty) = \left(1 - \frac{\rho^2}{\rho_0^2}\right)\boldsymbol{e}_z - \mathcal{V}\boldsymbol{e}_z. \tag{4.19}$$

On the tube wall, $\rho = \rho_0$, we impose the no-slip and no-normal-flow conditions,

$$\boldsymbol{v} = -\mathcal{V}\boldsymbol{e}_z. \tag{4.20}$$

The deformed position of the interfaces $\partial\Omega_i$ are defined as

$$\boldsymbol{r}_i = \alpha_i \boldsymbol{e}_r + \epsilon \boldsymbol{u}(\boldsymbol{r}_i), \tag{4.21}$$

where $\alpha_i = a_i/\rho_0$ and we assume the hydrogel coating is covalently bonded to the cell membrane such that there is no relative movement between them.

On the fluid-coating interface, $\partial\Omega_1$, we impose the continuity of normal fluid flux, continuity of total stress, continuity of normal fluid stress, and the well-known Beavers & Joseph slip condition [56],

$$\boldsymbol{v} \cdot \boldsymbol{n}_1 = \phi_f \boldsymbol{v}_p \cdot \boldsymbol{n}_1, \tag{4.22}$$

$$\boldsymbol{\sigma}_f \cdot \boldsymbol{n}_1 = \boldsymbol{\sigma}_p \cdot \boldsymbol{n}_1, \tag{4.23}$$

$$\boldsymbol{n}_1 \cdot \boldsymbol{\sigma}_f \cdot \boldsymbol{n}_1 = -p_p, \tag{4.24}$$

$$\boldsymbol{t}_1 \cdot \boldsymbol{\sigma}_f \cdot \boldsymbol{n}_1 = -\tilde{\gamma} \left(\boldsymbol{v} - \phi_f \boldsymbol{v}_p\right) \cdot \boldsymbol{t}_1, \tag{4.25}$$

where $\tilde{\gamma} = \gamma/\sqrt{\tilde{\kappa}_0 \kappa(\phi_f)}$ is defined as the effective slip and the slip parameter γ is dependent on the material properties of the coating. For reference, $\gamma = 0$ corresponds to a surface with perfect slip and $\gamma \to \infty$ corresponds to a surface with no-slip. These interfacial conditions form one of many viable choices for coupling a Stokes flow and poroelastic domain [56, 57, 61, 62]; the optimal choice of interfacial conditions will depend on the specific material choice and remains an active field of research [61].

On the cell-coating interface, $\partial\Omega_0$, we impose no normal fluid flux and continuity of total stress,

$$\phi_f \boldsymbol{v}_p \cdot \boldsymbol{n}_0 = 0, \tag{4.26}$$

$$\boldsymbol{\sigma}_p \cdot \boldsymbol{n}_0 = -p_c \boldsymbol{n}_0. \tag{4.27}$$

By integrating the stress balance (4.15), applying the divergence theorem and using the interfacial condition (4.23) we obtain the condition that the net axial total drag exerted by the external fluid on the coated cell is zero,

$$F_z = \oiint_{\partial\Omega_1} \boldsymbol{e}_z \cdot \boldsymbol{\sigma}_f \cdot \boldsymbol{n}_1 \, \mathrm{d}S = 0, \tag{4.28}$$

which is expected from a force balance in the absence of external forces. This will be useful later for predicting the translational velocity of the cell $\mathcal{V}$.

4.3 Asymptotic reduction

We now assume $\epsilon \ll 1$ and expand the variables, $\boldsymbol{v}, p_f, \boldsymbol{\sigma}_f, \phi_f, \boldsymbol{v}_p, \kappa, p_p, \boldsymbol{u}, \boldsymbol{\sigma}'$ and p_c in powers of ϵ, e.g.

$$\boldsymbol{v} = \boldsymbol{v}^{(0)} + \epsilon \boldsymbol{v}^{(1)} + \cdots, \tag{4.29}$$

where the superscript (i) denotes the associated power of ϵ. We similarly expand the translational velocity of the coating, the viscous drag, and the positions of the interfaces $\partial\Omega_i$ as

$$\mathcal{V} = \mathcal{V}^{(0)} + \epsilon\mathcal{V}^{(1)} + \cdots, \quad F_z = F_z^{(0)} + \epsilon F_z^{(1)} + \cdots, \quad \text{and} \quad \boldsymbol{r}_i = \boldsymbol{r}_i^{(0)} + \epsilon\boldsymbol{r}_i^{(1)} + \cdots. \tag{4.30}$$

We proceed by assuming the parameters $\alpha_i, \phi_{f,0}, \tilde{\lambda}, \tilde{\kappa}_0$ and $\tilde{\gamma}$ remain fixed as $\epsilon \to 0$. Similar to Section 2.3, we expand the governing equations and boundary conditions in powers of ϵ, and show that the leading-order fluid flow decouples from the solid deformation.

4.3.1 Leading-order fluid problem

The leading-order incompressible Stokes equations are simply

$$\nabla p_p^{(0)} = \nabla^2 \boldsymbol{v}^{(0)}, \tag{4.31}$$

$$\nabla \cdot \boldsymbol{v}^{(0)} = 0. \tag{4.32}$$

In the limit of infinitesimal strain we have the expansions

$$\boldsymbol{F} = \boldsymbol{I} + \epsilon\nabla\boldsymbol{u} + \mathcal{O}\left(\epsilon^2\right), \tag{4.33}$$

$$\det(\boldsymbol{F}) = 1 + \epsilon\nabla\cdot\boldsymbol{u} + \mathcal{O}\left(\epsilon^2\right). \tag{4.34}$$

The porosity is given by expanding (4.8) and (4.9) and using (4.34) to write

$$\phi_f = \phi_{f,0} + \epsilon(1-\phi_{f,0})\nabla\cdot\boldsymbol{u}^{(0)} + \cdots, \tag{4.35}$$

such that $\phi_f^{(0)} = \phi_{f,0}$. Expanding (4.10), the leading-order flow in the coating is governed by Darcy's law with constant porosity $\phi_{f,0}$ and associated permeability $\tilde{\kappa}_0$,

$$\phi_{f,0}\boldsymbol{v}_f^{(0)} = -\tilde{\kappa}_0\nabla p_p^{(0)}. \tag{4.36}$$

The incompressibility condition (4.11) at leading order is

$$\phi_{f,0}\nabla\cdot\boldsymbol{v}_p^{(0)} = 0. \tag{4.37}$$

Expanding the kinematic condition (4.21) gives the deformation of the interfaces $\partial\Omega_i$,

$$\boldsymbol{r}_i = \alpha_i\boldsymbol{e}_r + \epsilon\boldsymbol{u}^{(0)}(\boldsymbol{r}_i) + \mathcal{O}(\epsilon^2), \tag{4.38}$$

such that $\boldsymbol{r}_i^{(0)} = \alpha_i\boldsymbol{e}_r$, implying interfacial conditions are applied on the undeformed cell and coating surfaces with $\boldsymbol{n}_i^{(0)} = \boldsymbol{e}_r$ and $\boldsymbol{t}_i^{(0)} = \boldsymbol{e}_\theta$.

The far-field and no-slip conditions (4.19) and (4.20) are

$$\boldsymbol{v}^{(0)} \to \left(1-\rho^2-\mathcal{V}^{(0)}\right)\boldsymbol{e}_z, \qquad \text{as } z \to \pm\infty, \tag{4.39}$$

$$\boldsymbol{v}^{(0)} = -\mathcal{V}^{(0)}\boldsymbol{e}_z, \qquad \text{at } \rho = 1. \tag{4.40}$$

The interfacial conditions for the flow problem (4.22) and (4.24) to (4.26) at leading order give

$$\boldsymbol{v}^{(0)}\cdot\boldsymbol{e}_r = \phi_{f,0}\boldsymbol{v}_p^{(0)}\cdot\boldsymbol{e}_r, \qquad \text{at } r=\alpha_1, \tag{4.41}$$

$$\boldsymbol{e}_r\cdot\boldsymbol{\sigma}_f^{(0)}\cdot\boldsymbol{e}_r = -p_f^{(0)}, \qquad \text{at } r=\alpha_1, \tag{4.42}$$

$$\boldsymbol{e}_\theta\cdot\boldsymbol{\sigma}_f^{(0)}\cdot\boldsymbol{e}_r = \tilde{\gamma}\left(\boldsymbol{v}^{(0)}-\phi_{f,0}\boldsymbol{v}_p^{(0)}\right)\cdot\boldsymbol{e}_\theta, \qquad \text{at } r=\alpha_1, \tag{4.43}$$

$$\boldsymbol{v}_p^{(0)}\cdot\boldsymbol{e}_r = 0, \qquad \text{at } r=\alpha_0. \tag{4.44}$$

Finally, the equilibrium condition (4.28) at leading order gives

$$F_z^{(0)} = 2\pi\alpha^2\int_0^\pi \boldsymbol{e}_z\cdot\boldsymbol{\sigma}_p^{(0)}\cdot\boldsymbol{e}_r\sin\theta\,\mathrm{d}\theta = 0. \tag{4.45}$$

Equations (4.31), (4.32), (4.36), (4.37) and (4.39) to (4.45) form a full description of the leading-order fluid flow. Similar to Section 2.3.2, the impact of the coating deformation does not enter at this order, and the fluid problem is equivalent to flow through a rigid spherical porous annulus with an impermeable core subject to axisymmetric, pressure-driven tube flow.

Similar to Section 2.3.2, we note that $\boldsymbol{v}^{(0)}$, and thus $\boldsymbol{\sigma}_f^{(0)}$ and $F_z^{(0)}$, depend linearly on the magnitude of the background Poiseuille flow and the cell velocity. Consequently, we can write the dimensionless, revised version of Faxen's law,

$$F_z^{(0)} = 6\pi\alpha_1(D^{(0)}(\alpha_0,\alpha_1,\tilde{\kappa}_0,\gamma) - K^{(0)}(\alpha_0,\alpha_1,\tilde{\kappa}_0,\gamma)\mathcal{V}^{(0)}). \tag{4.46}$$

The only difference between (4.46) and the equivalent relation with an elastic particle (see (2.45)) is that here the wall correction factors $D^{(0)}$ and $K^{(0)}$ now also depend on the cell size α_0, the Darcy number $\tilde{\kappa}_0$, and the slip parameter γ. As a reminder, $D^{(0)}$ captures the leading-order drag exerted by the background Poiseuille flow on a stationary coated cell, and $K^{(0)}$ captures the leading-order drag exerted by the surrounding fluid on a coated cell which is translating through a tube filled with an otherwise quiescent viscous Newtonian fluid. Substituting (4.46) into (4.45) we predict the leading-order translation velocity,

$$\mathcal{V}^{(0)} = \frac{D^{(0)}(\alpha_0,\alpha_1,\tilde{\kappa}_0,\gamma)}{K^{(0)}(\alpha_0,\alpha_1,\tilde{\kappa}_0,\gamma)}. \tag{4.47}$$

4.3.2 Leading-order solid problem

The leading-order mechanical equilibrium equation for the solid skeleton is given by expanding (4.13),

$$\nabla \cdot \boldsymbol{\sigma}_p^{(0)} = \nabla \cdot \boldsymbol{\sigma}'^{(0)} - \nabla p_p^{(0)} = \mathbf{0}, \tag{4.48}$$

where expanding (4.14) and using (4.33) we obtain a linearly elastic stress-strain relationship,

$$\boldsymbol{\sigma}'^{(0)} = \tilde{\lambda}(\nabla \cdot \boldsymbol{u}^{(0)})\boldsymbol{I} + 2\boldsymbol{e}^{(0)}, \tag{4.49}$$

where $\boldsymbol{e}^{(0)} = \frac{1}{2}\left(\nabla \boldsymbol{u}^{(0)} + \left(\nabla \boldsymbol{u}^{(0)}\right)^T\right)$ is the linear elastic strain.

Taking the modulus of (4.38) we have

$$|\boldsymbol{r}_i| = \alpha_i + \epsilon u_r^{(0)}(r = \alpha_i) + \mathcal{O}(\epsilon^2), \tag{4.50}$$

Applying (4.50) to the volumetric constraint used to calculate the cell pressure (4.18) we have the expansion

$$2\pi \int_{\theta=0}^{\pi} \int_{r=0}^{\alpha_0 + \epsilon u_r(r,\theta) + \mathcal{O}(\epsilon^2)} r^2 \sin\theta \mathrm{d}r \, \mathrm{d}\theta \; = \frac{4}{3}\pi\alpha_0^3 + 2\epsilon\pi \int_{\theta=0}^{\pi} u_r^{(0)}(r = \alpha_0) \sin\theta \, \mathrm{d}\theta + \mathcal{O}(\epsilon^2), \tag{4.51}$$

so that

$$2\pi \int_{\theta=0}^{\pi} u_r^{(0)}(r = \alpha_0) \sin\theta \, \mathrm{d}\theta = 0. \tag{4.52}$$

We remind the reader that in (4.52) the cell pressure p_c is implicitly contained within the cell deformation, and is chosen to enforce this constraint.

Expanding the remaining interfacial conditions (4.23) and (4.27) to leading order and using (4.42) gives

$$0 = \boldsymbol{e}_r \cdot \boldsymbol{\sigma}'^{(0)} \cdot \boldsymbol{e}_r, \qquad \text{at } r = \alpha_1, \tag{4.53}$$

$$\boldsymbol{e}_\theta \cdot \boldsymbol{\sigma}_f^{(0)} \cdot \boldsymbol{e}_r = \boldsymbol{e}_\theta \cdot \boldsymbol{\sigma}'^{(0)} \cdot \boldsymbol{e}_r, \qquad \text{at } r = \alpha_1, \tag{4.54}$$

$$\boldsymbol{e}_r \cdot \boldsymbol{\sigma}'^{(0)} \cdot \boldsymbol{e}_r - p_p^{(0)} = -p_c^{(0)}, \qquad \text{at } r = \alpha_0, \tag{4.55}$$

$$\boldsymbol{e}_\theta \cdot \boldsymbol{\sigma}'^{(0)} \cdot \boldsymbol{e}_r = 0, \qquad \text{at } r = \alpha_0. \tag{4.56}$$

Once the Darcy pressure and surface tractions are computed by solving the leading order fluid problem, Equations (4.48), (4.49) and (4.53) to (4.56), are used to calculate the resulting surface deformations given by (4.38). Finally, the effect of this deformation on the porosity field may then be calculated via (4.35).

4.4 Solution methods

We now outline two solutions methods for obtaining the desired solutions. In the first we first solve the leading-order fluid problem using the semi-analytical MoR. We then use these results to analytically calculate the resulting leading-order coating deformation. In the second we solve the fully coupled, non-linear problem numerically using an ALE FEM approach.

4.4.1 Semi-analytical implementation

Solving the leading-order fluid problem (Equations (4.31), (4.32), (4.36), (4.37) and (4.39) to (4.45)) involves a mix of geometries; the cylindrical tube motivates the use of a cylindrical coordinate system, while the flow through the coating is more naturally considered via a spherical coordinate system. To account for this mix of geometries, we again choose to employ the method of reflections (MoR), though other methods, for example a collocation technique or boundary element method, may be used [54, 87, 106]. Once the leading-order fluid flow is calculated, the leading-order solid problem (Equations (4.48), (4.49) and (4.53) to (4.56)) is solved analytically using a spherical coordinate system, since we only require a solution inside the coating region.

Having previously introduced the MoR in Section 2.4.1.1, we now apply it to solve the leading-order fluid problem. Again, further details on the coordinate transformations, general solutions to the Stokes equations, and convergence of the solution are left to Appendix A.

4.4.1.1 Application of the MoR to the leading-order fluid problem

The method of reflections, originally developed by Brenner and Happel [40] to model Stokes flow around a small, rigid, impermeable particle in a cylindrical tube, is a meshless semi-analytic method which splits the problem such that only one set of boundary conditions, and consequently coordinate system, are considered at any time. Due to the linearity of the Stokes equations and boundary conditions we can decompose the external velocity and pressure fields as follows

$$\boldsymbol{v}^{(i)} = \boldsymbol{v}^{(i,0)} + \boldsymbol{v}^{(i,1)} + \boldsymbol{v}^{(i,2)} + \cdots, \quad p_f^{(0)} = p_f^{(i,0)} + p_f^{(i,1)} + p_f^{(i,2)} + \cdots, \tag{4.57}$$

where $\boldsymbol{v}^{(i,j)}$ corresponds to the j-th term (where j is called the reflection number) in the series for $\boldsymbol{v}^{(i)}$, and $\boldsymbol{v}^{(i)}$ are the $\mathcal{O}(\epsilon^i)$ terms in the asymptotic expansion; see Section 2.3. We also decompose the leading-order internal velocity field, Darcy pressure,

and cell pressure as follows,

$$\boldsymbol{v}_p^{(i)} = \boldsymbol{v}_p^{(i,1)} + \boldsymbol{v}_p^{(i,3)} + \cdots, \quad p_p^{(i)} = p_p^{(i,1)} + p_p^{(i,3)} + \cdots, \quad p_c^{(i)} = p_c^{(i,1)} + p_c^{(i,3)} + \cdots. \tag{4.58}$$

Terms with odd j ($\boldsymbol{v}^{(i,\text{odd})}$, $p_f^{(i,\text{odd})}$, etc.) are calculated by imposing the interfacial conditions on the coating using a spherical coordinate system, while terms with even j ($\boldsymbol{v}^{(i,\text{even})}$, $p_f^{(i,\text{even})}$) are calculated by imposing the boundary conditions on the tube wall using a cylindrical coordinate system. Contributions to the internal velocity field, Darcy pressure, and cell pressure are only ever required to satisfy the interfacial conditions on the coating and thus their expansions do not contain terms with even j.

Similar to Section 2.4.1.2, we begin by choosing

$$\boldsymbol{v}^{(0,0)} = (1 - \rho^2 - \mathcal{V})\boldsymbol{e}_z, \tag{4.59}$$

to satisfy both the boundary conditions on the tube wall (4.40) and the far-field condition (4.39) such that all other external velocity components must vanish for $z \to \pm\infty$, or equivalently $r \to \infty$ for contributions in spherical coordinates. We then transform $\boldsymbol{v}^{(0,0)}$ to spherical coordinates (details given in Appendix A.1) and introduce $\boldsymbol{v}^{(0,1)}$ and $\boldsymbol{v}_p^{(0,1)}$ to satisfy the remaining interfacial conditions on the coating (4.41)–(4.44). By including the external velocity component $\boldsymbol{v}^{(0,1)}$ we disrupt the boundary conditions on the tube wall, (4.40). To reimpose these boundary conditions we convert the expression $\boldsymbol{v}^{(0,0)} + \boldsymbol{v}^{(0,1)}$ to cylindrical coordinates, and include $\boldsymbol{v}^{(0,2)}$ such that $\boldsymbol{v}^{(0,0)} + \boldsymbol{v}^{(0,1)} + \boldsymbol{v}^{(0,2)}$ satisfies (4.40). The process repeats indefinitely and is summarised

by the following equations:

$$(j=0)\begin{cases}\boldsymbol{v}^{(0,0)}=(1-\rho^2-\mathcal{V})\boldsymbol{e}_z, & \end{cases} \tag{4.60}$$

$$(j=1)\begin{cases}\left(\boldsymbol{v}^{(0,1)}+\boldsymbol{v}^{(0,0)}\right)\cdot\boldsymbol{e}_r=\phi_{f,0}\boldsymbol{v}_p^{(0,1)}\cdot\boldsymbol{e}_r, & r=\alpha_1,\\ \boldsymbol{e}_r\cdot\left(\boldsymbol{\sigma}_f^{(0,1)}+\boldsymbol{\sigma}_f^{(0,0)}\right)\cdot\boldsymbol{e}_r=-p_f^{(0,1)}, & r=\alpha_1,\\ \boldsymbol{e}_\theta\cdot\left(\boldsymbol{\sigma}_f^{(0,1)}+\boldsymbol{\sigma}_f^{(0,0)}\right)\cdot\boldsymbol{e}_r & \\ \quad=\tilde{\gamma}\left(\boldsymbol{v}^{(0,1)}+\boldsymbol{v}^{(0,0)}-\phi_{f,0}\boldsymbol{v}_p^{(0,1)}\right)\cdot\boldsymbol{e}_\theta, & r=\alpha_1,\\ \boldsymbol{v}_p^{(0,1)}\cdot\boldsymbol{e}_r=0, & r=\alpha_0,\\ \boldsymbol{v}^{(0,1)}\to 0, & r\to\infty,\end{cases} \tag{4.61}$$

$$(j=2)\begin{cases}\boldsymbol{v}^{(0,2)}=-\boldsymbol{v}^{(0,1)}, & \rho=1,\\ \boldsymbol{v}^{(0,2)}\to 0, & z\to\pm\infty,\end{cases} \tag{4.62}$$

$$(j=3)\begin{cases}\left(\boldsymbol{v}^{(0,3)}+\boldsymbol{v}^{(0,2)}\right)\cdot\boldsymbol{e}_r=\phi_{f,0}\boldsymbol{v}_p^{(0,3)}\cdot\boldsymbol{e}_r, & r=\alpha_1,\\ \boldsymbol{e}_r\cdot\left(\boldsymbol{\sigma}_f^{(0,3)}+\boldsymbol{\sigma}_f^{(0,2)}\right)\cdot\boldsymbol{e}_r=-p_f^{(0,3)}, & r=\alpha_1,\\ \boldsymbol{e}_\theta\cdot\left(\boldsymbol{\sigma}_f^{(0,3)}+\boldsymbol{\sigma}_f^{(0,2)}\right)\cdot\boldsymbol{e}_r & \\ \quad=\tilde{\gamma}\left(\boldsymbol{v}^{(0,3)}+\boldsymbol{v}^{(0,2)}-\phi_{f,0}\boldsymbol{v}_p^{(0,3)}\right)\cdot\boldsymbol{e}_\theta, & r=\alpha_1,\\ \boldsymbol{v}_p^{(0,3)}\cdot\boldsymbol{e}_r=0, & r=\alpha_0,\\ \boldsymbol{v}^{(0,3)}\to 0, & r\to\infty,\end{cases} \tag{4.63}$$

$$\vdots$$

where $\boldsymbol{\sigma}_f^{(0,j)}$ are the stress components corresponding to the external velocity and pressure components with the same j. If we truncate the velocity series at an odd term then we satisfy the interfacial conditions on the coating surface, with an error on the tube wall. If we truncate the velocity series at an even term then the opposite is true. We define a solution as having converged when the most recent contribution to the net force acting on the sphere is at least five orders of magnitude smaller than the net force from all components. The details of the convergence criteria are presented in Appendix A.4.

4.4.1.2 General solutions

The general solutions for the external Stokes flow are identical to those presented in Section 2.4.1.1, with the general solutions to the Stokes equations (4.31) and (4.32) using both a spherical and cylindrical coordinate system given in Appendix A.2 and Appendix A.3, respectively. For clarity, we restate Equations (2.65)–(2.69), which

give the Stokes velocity, pressure, and relevant stress components on $r = \alpha_1$,

$$v_r^{(0)}(\theta)|_{r=\alpha_1} = \sum_{n=2}^{\infty} \left[-\alpha_1^{-n-1}(A_n + B_n\alpha_1^2) + \tilde{v}_{(r,n)}\right] \mathcal{P}_{n-1}(\cos\theta), \tag{4.64}$$

$$v_\theta^{(0)}(\theta)|_{r=\alpha_1} = \sum_{n=2}^{\infty} \left[-\alpha_1^{-n-1}((n-1)A_n + (n-3)B_n\alpha_1^2) + \tilde{v}_{(\theta,n)}\right] \csc\theta\, \mathcal{C}_n(\cos\theta), \tag{4.65}$$

$$p_f(\theta)|_{r=\alpha_1} = p_0 - 2\sum_{n=2}^{\infty} \left[\frac{2n-3}{n} B_n\alpha_1^{-n} + \tilde{p}_{(n-1)}\right] \mathcal{P}_{n-1}(\cos\theta), \tag{4.66}$$

$$\sigma_{f,rr}^{(0)}(\theta)|_{r=\alpha_1} = -p_o + \sum_{n=2}^{\infty} \left[2\alpha_1^{-n-2} \left((n+1)A_n + \left(\frac{n^2+n-3}{n}\right) B_n\alpha_1^2\right) + \tilde{\sigma}_{(rr,n-1)}\right] \mathcal{P}_{n-1}(\cos\theta), \tag{4.67}$$

$$\sigma_{f,r\theta}^{(0)}(\theta)|_{r=\alpha_1} = \sum_{n=2}^{\infty} \left[2\alpha_1^{-n-2} \left((n^2-1)A_n + n(n-2)B_n\alpha_1^2\right) + \tilde{\sigma}_{(r\theta,n)}\right] \csc\theta\, \mathcal{C}_n(\cos\theta), \tag{4.68}$$

where $\mathcal{P}_n(\cos\theta)$ are the Legendre polynomials of order n and $\mathcal{C}_n$ are the Gegenbauer polynomials of order n and degree $-1/2$, and p_0 is a constant which is used to ensure $p_f = 0$ at $(z, \rho) = (10, 0)$. The subscripts r and θ correspond to the radial and azimuthal components of a vector in spherical coordinates, respectively, and the tensor components, $\sigma_{f,kl} = \boldsymbol{e}_k \cdot \boldsymbol{\sigma}_f \cdot \boldsymbol{e}_l$. The coefficients A_n and B_n arise from the streamfunction series using spherical coordinates (A.4) (odd j), while the coefficients $\tilde{v}_{(r,n-1)}, \tilde{v}_{(\theta,n)}, \tilde{p}_{(n-1)}, \tilde{\sigma}_{(rr,n-1)}, \tilde{\sigma}_{(r\theta,n)}$ arise from projecting terms calculated using the general solution in cylindrical coordinates (A.15) and (A.16) (even j) on $r = \alpha_1$ via (A.9) and (A.10). These projections are performed numerically due to the difficulty of converting the general solutions for velocity, pressure, and stress from cylindrical to spherical coordinates.

Since the Darcy pressure p_p and the associated velocity field $\boldsymbol{v}_p$ are composed only of terms with odd j, see (4.58), their general solution may be written exactly using a spherical coordinate system throughout the entire coating domain. Taking the divergence of (4.36) and using (4.37) we see the Darcy pressure satisfies the Laplace's

equation and thus has the general solution as

$$p_p^{(0)}(r,\theta) = p_0 + \sum_{n=2}^{\infty} \left[C_n r^{n-1} + D_n r^{-n}\right] \mathcal{P}_{n-1}(\cos\theta), \tag{4.69}$$

$$v_{p,r}^{(0)}(r,\theta) = -\frac{\tilde{\kappa}_0}{\phi_{f,0}} \sum_{n=2}^{\infty} \left[(n-1)C_n r^{n-2} - nD_n r^{-n-1}\right] \mathcal{P}_{n-1}(\cos\theta), \tag{4.70}$$

$$v_{p,\theta}^{(0)}(r,\theta) = \frac{\tilde{\kappa}_0}{\phi_{f,0}} \sum_{n=2}^{\infty} n(n-1) \left[C_n r^{n-2} + D_n r^{-n-1}\right] \csc\theta \, \mathcal{C}_n(\cos\theta). \tag{4.71}$$

Each of the above series (4.64)–(4.71) theoretically contains an infinite number of terms in summation over n, however we only consider the first three non-zero terms to solve the leading-order fluid problem, corresponding to $n = 2, 4, 6$. This is because the far-field flow (4.59) can be written exactly in spherical coordinates using terms with $n = 2$ and 4 and, under this external flow, the presence of the tube wall exclusively drives terms with even n in the stream function series. A discussion of the impacts of this truncation choice on the solution error is presented in Appendix A.4. The restriction to even n may also be interpreted via a consideration of symmetry through $z = 0$, as we now explain. We expect the following to be true,

$$v_\rho^{(0)}(\rho,z) = -v_\rho^{(0)}(\rho,-z), \quad v_z^{(0)}(\rho,z) = v_z^{(0)}(\rho,-z), \tag{4.72}$$

with the same relations true for the internal velocity field. Transforming the above expressions for the external and internal velocity fields into cylindrical coordinates we see that terms with odd n break these symmetries and are thus not generated by the external tube wall.

4.4.1.3 Leading-order solid problem

The fluid stresses and Darcy pressure calculated from the leading-order fluid problem drive the deformation of the coating and the cell. To leading order, the solid displacement is governed by the Navier-Lamé equations (4.48) and (4.49) with the Darcy pressure gradient acting as a body force in (4.48). Exploiting separation of

variables, we obtain the following general solutions for the deformation,

$$u_r^{(0)}(r,\theta) = \sum_{n=2}^{\infty} \Bigg(C_n \frac{(n-1)r^n(1+n(\tilde{\lambda}+3))}{2(2n-1)(2n+1)(\tilde{\lambda}+2)} + D_n \frac{nr^{1-n}((n-1)\tilde{\lambda}+(3n-4))}{2(2n-3)2n-1)(\tilde{\lambda}+2)} + r^{n-2}((n-1)E_n + nr^2(n-3+\frac{2\tilde{\lambda}}{\tilde{\lambda}+1})F_n) + r^{-n-1}(nG_n + (n-1)r^2(n+2-\frac{2\tilde{\lambda}}{\tilde{\lambda}+1})H_n) \Bigg) \mathcal{P}_{n-1}(\cos\theta), \tag{4.73}$$

$$u_\theta^{(0)}(r,\theta) = \sum_{n=2}^{\infty} \Bigg(C_n \frac{r^n((n+2)\tilde{\lambda}+3(n+1))}{2(2n-1)(2n+1)(\tilde{\lambda}+2)} - D_n \frac{r^{1-n}((n-3)\tilde{\lambda}+3(n-2))}{2(2n-3)(2n-1)(\tilde{\lambda}+2)} + r^{n-2}(E_n + r^2(n+4-\frac{2\tilde{\lambda}}{\tilde{\lambda}+1})F_n) + r^{-n-1}(-G_n + r^2(5-n-\frac{2\tilde{\lambda}}{\tilde{\lambda}+1})H_n) \Bigg) \mathcal{P}_{n-1}(\cos\theta). \tag{4.74}$$

We calculate the relevant stress components using the constitutive relation (4.49), and use the boundary conditions (4.52)–(4.56) to solve for the unknown constants E_n, F_n, G_n and H_n, and the leading-order constant cell pressure $p_c^{(0)}$. By substituting the general solutions for the displacement (4.73) and (4.74) into the volume constraint (4.52), it may be shown that with n even we always require $p_c^{(0)} = p_0$, such that the leading-order deformation does not impact the cell pressure. Since, with even n, the Legendre polynomials contributing to the Darcy and Stokes pressures (4.66) and (4.69) are anti-symmetric across $z = 0$, we have $p_f^{(0)}(\theta = \pi/2) = p_f^{(0)}(\theta = \pi/2) = p_c^{(0)} = p_0$. Consequently, the cell pressure is directly related to the extra pressure drop across the tube length ΔP^+, defined in (4.5). Due to the geometric symmetry through $z = 0$, an extra pressure drop of ΔP^+ across the tube length implies an increased cell pressure of $\Delta P^+/2$ when compared with the background Poiseuille flow contribution. Since we set $p_f = 0$ at $(z, \rho) = (10, 0)$, we write the leading-order cell pressure

$$p_c^{(0)} = \frac{\Delta P^{\text{Pois}} + \Delta P^+}{2} = 40 + \frac{\Delta P^+}{2}. \tag{4.75}$$

The coefficient E_2 in (4.73) and (4.74) corresponds to a translation and so does not generate any stress. Hence, the coefficient E_2 is not set by the interfacial stress conditions (4.53)–(4.56) and we must impose another condition to pin this degree of freedom. We choose to set the net axial displacement of the coating to be zero

through the constraint

$$\int_0^{\pi} \int_{\alpha_0}^{\alpha_1} (\boldsymbol{e}_z \cdot \boldsymbol{u}^{(0)})\, r^2 \sin(\theta)\, \mathrm{d}r\, \mathrm{d}\theta = 0, \tag{4.76}$$

thereby removing the translational invariance of the problem.

4.4.2 Finite element implementation

To investigate the range of validity of the MoR solutions, we solve the full non-linear fluid-structure interaction (FSI) problem via the finite element method using a similar arbitrary Lagrangian-Eulerian (ALE) approach to that proposed in Section 2.5. We construct a steady, 2D axisymmetric implementation, again choosing to work in the lab frame such that the particle translates with (dimensionless) velocity $\mathcal{V}$ for convenience. The ALE approach couples the Lagrangian solid problem with the Eulerian fluid problem, which is transformed into a Lagrangian frame via the mesh displacements $\boldsymbol{u}_a \in \widehat{\Omega}_f$ and $\boldsymbol{u}_c \in \widehat{\Omega}_c$ such that the undeformed reference configuration is used as the computational domain. The mesh displacements $\boldsymbol{u}_a$ and $\boldsymbol{u}_c$ extend the surface deformation of the hydrogel coating $\boldsymbol{u} \in \widehat{\Omega}_h$ into the fluid and cell domains, respectively, and are solved for using an arbitrary governing equation. We use the finite element library `fenics` with the additional package `multiphenics` to implement the ALE method, generating meshes via `gmsh` [109–112]. We use P_2 elements for the Stokes fluid velocity, solid displacement, and mesh displacements, P_1 elements for the pressures, and use P_0 elements for the Darcy velocity.

We present an overview of our non-linear arbitrary Lagrangian-Eulerian (ALE) finite element model for the coated cell. We again clarify $\boldsymbol{X}$ and $\boldsymbol{x}$ as the reference (Lagrangian) and current (Eulerian) configurations. To verify accuracy in the finite element solutions we conduct a mesh refinement study in Appendix B.2.

4.4.2.1 External Stokes flow

We begin by defining the Lagrangian gradient $\nabla_{\boldsymbol{X}}$, distinct from the Eulerian gradient used throughout Section 4.2. We also define the undeformed fluid, hydrogel coating, cell, and boundary domains as $\widehat{\Omega}_f, \widehat{\Omega}_s$, $\widehat{\Omega}_c$, and $\partial\widehat{\Omega}_i, i = 0, 1$, respectively.

The Eulerian fluid problem is governed by the dimensionless Stokes equations (4.2)–(4.4). However, it is convenient to choose the undeformed reference configuration as the computational domain which requires us to transform the fluid equations to the reference configuration. We define the fluid mesh displacement associated with

this transformation, and the associated deformation gradient tensor and Jacobian as

$$\boldsymbol{u}_a \in \widehat{\Omega}_f, \quad \boldsymbol{F}_a = \boldsymbol{I} + \nabla_{\boldsymbol{X}} \boldsymbol{u}_a, \quad J_a = \det \boldsymbol{F}_a, \tag{4.77}$$

respectively. We write Nansen's formula,

$$\boldsymbol{n} \mathrm{d}S = J_a \boldsymbol{F}^{-T} \cdot \boldsymbol{N} \mathrm{d}S_{\boldsymbol{X}}, \tag{4.78}$$

where $\boldsymbol{n}$ and $\boldsymbol{N}$ are the normal vectors in the deformed/reference configurations, respectively, which may be used in conjunction with the divergence theorem to transform the Eulerian fluid equations (4.2)–(4.4) to the reference configuration,

$$\nabla_{\boldsymbol{X}} \cdot (J_a \boldsymbol{\sigma}_p \boldsymbol{F}_a^{-T}) = \boldsymbol{0}, \tag{4.79}$$

$$\nabla_{\boldsymbol{X}} \cdot (J_a \boldsymbol{F}_a^{-1} \boldsymbol{v}) = 0, \tag{4.80}$$

$$\boldsymbol{\sigma}_f = -p_f \boldsymbol{I} + (\nabla_{\boldsymbol{X}} \boldsymbol{v}) \boldsymbol{F}_a^{-1} + \boldsymbol{F}_a^{-T} (\nabla_{\boldsymbol{X}} \boldsymbol{v})^T. \tag{4.81}$$

4.4.2.2 Hydrogel coating

We similarly transform the Eulerian internal fluid flow to the reference domain $\widehat{\Omega}_s$ via the solid displacement $\boldsymbol{u}$, noting that in a Lagrangian frame the deformation gradient tensor $\boldsymbol{F} = \boldsymbol{I} + \nabla_{\boldsymbol{X}} \boldsymbol{u}$. Defining the nominal Darcy flow $\boldsymbol{Q} = J\boldsymbol{F}^{-1}\boldsymbol{q}$ we rewrite Darcy's law as

$$\boldsymbol{Q} = -\boldsymbol{K} \nabla_{\boldsymbol{X}} p_p, \tag{4.82}$$

where $\boldsymbol{K} = \tilde{\kappa}_0 J \boldsymbol{C}^{-1}$ is defined as the permeability tensor and $\boldsymbol{C} = \boldsymbol{F}^T \boldsymbol{F}$ is the right Cauchy-Green tensor. The incompressibility condition is similarly transformed as

$$\nabla_{\boldsymbol{X}} \cdot (\boldsymbol{Q} + J\boldsymbol{F}^{-1} \boldsymbol{v}_s) = 0. \tag{4.83}$$

The skeleton velocity $\boldsymbol{v}_s = \mathcal{V} \boldsymbol{e}_z$ appears in (4.83) since we work in the lab frame.

The skeleton deformation is governed by the balance of linear momentum,

$$\nabla_{\boldsymbol{X}} \cdot \boldsymbol{P} = \boldsymbol{0}, \tag{4.84}$$

where the first Piola-Kirchhoff stress tensor is decomposed as $\boldsymbol{P} = J\boldsymbol{\sigma}' \boldsymbol{F}^{-T} - p_p J \boldsymbol{F}^{-T}$.

4.4.3 Cell

Within the cell we use the cell pressure p_c to enforce the volumetric constraint (4.18). This is achieved by assuming the cell is incompressible,

$$J_c - 1 = 0, \tag{4.85}$$

where the Jacobian $J_c = \det \boldsymbol{F}_c$ and $\boldsymbol{F}_c = \boldsymbol{I} + \nabla_{\boldsymbol{X}} \boldsymbol{u}_c$.

4.4.3.1 Interfacial conditions

Making use of Nansen's formula (4.78), we first transform the interfacial conditions on $\partial\widehat{\Omega}_1$ to the reference frame. The continuity of normal flux (4.22)is transformed to

$$J_a \boldsymbol{F}_a^{-1}\boldsymbol{v}\cdot\boldsymbol{N} = (\boldsymbol{Q} + J\boldsymbol{F}^{-1}\boldsymbol{v}_s)\cdot\boldsymbol{N}, \tag{4.86}$$

The stress balance (4.23) is

$$J_a\boldsymbol{\sigma}_p\boldsymbol{F}_a^{-T}\cdot\boldsymbol{N} = \boldsymbol{P}\cdot\boldsymbol{N}. \tag{4.87}$$

It is convenient to combine the remaining conditions (4.24) and (4.25) into a traction condition. To do this, we decompose the velocities into the normal and tangential components such that in an Eulerian frame we have

$$\boldsymbol{v}-\boldsymbol{q}-\boldsymbol{v}_s = ([\boldsymbol{v}-\boldsymbol{q}-\boldsymbol{v}_s]\cdot\boldsymbol{n})\boldsymbol{n} + ([\boldsymbol{v}-\boldsymbol{q}-\boldsymbol{v}_s]\cdot\boldsymbol{t})\boldsymbol{t}, \tag{4.88}$$

where using (4.22) the normal component of (4.88) vanishes. Using (4.88), the interfacial conditions (4.24) and (4.25) are combined and transformed to give the traction condition

$$J_a\boldsymbol{\sigma}_p\boldsymbol{F}_a^{-T}\cdot\boldsymbol{N} = -Jp_p\boldsymbol{F}^{-T}\boldsymbol{N} + \tilde{\gamma}J|\boldsymbol{F}^{-T}\boldsymbol{N}|(\boldsymbol{v}-\frac{1}{J}\boldsymbol{F}\boldsymbol{Q}-\mathcal{V}\boldsymbol{e}_z). \tag{4.89}$$

On $\partial\widehat{\Omega}_0$ we then have the no penetration (4.26)

$$\tilde{\kappa}_0\boldsymbol{F}^{-T}\nabla_{\boldsymbol{X}}p_p\cdot\boldsymbol{N} = 0 \tag{4.90}$$

and the stress balance (4.27)

$$\boldsymbol{P}\cdot\boldsymbol{N} = -J_c p_c\boldsymbol{F}^{-T}\boldsymbol{N}. \tag{4.91}$$

4.4.3.2 Arbitrary couplings

The fluid mesh displacements $\boldsymbol{u}_a$ and $\boldsymbol{u}_c$ extend the coated cell deformation into the domains $\widehat{\Omega}_f$ and $\widehat{\Omega}_c$, respectively. To do this, we require continuity with $\boldsymbol{u}$ on $\partial\widehat{\Omega}_i$

$$\boldsymbol{u}_a = \boldsymbol{u} \quad \text{on } \partial\widehat{\Omega}_1 \tag{4.92}$$

$$\boldsymbol{u}_c = \boldsymbol{u} \quad \text{on } \partial\widehat{\Omega}_0, \tag{4.93}$$

and restrict $\boldsymbol{u}_a\cdot\boldsymbol{N} = \boldsymbol{u}_c\cdot\boldsymbol{N}$ on non-moving boundaries. Under these boundary conditions, $\boldsymbol{u}_a$ and $\boldsymbol{u}_c$ may be solved for using arbitrary governing equations, with

previous studies using Laplace's equation, linear elasticity, or the biharmonic equation [113]. In this study we opt to use the equations of linear elasticity for $\boldsymbol{u}_a$ such that

$$\nabla_{\boldsymbol{X}} \cdot \boldsymbol{\sigma}_a = \boldsymbol{0} \tag{4.94}$$

$$\boldsymbol{\sigma}_a = \frac{\nu_a E_a}{(1+\nu_a)(1-2\nu_a)} \nabla_{\boldsymbol{X}} \cdot \boldsymbol{u}_a + \frac{E_a}{2(1+\nu_a)} \left[\nabla_{\boldsymbol{X}} \boldsymbol{u}_a + (\nabla_{\boldsymbol{X}} \boldsymbol{u}_a)^T \right], \tag{4.95}$$

where ν_a and E_a have no physical interpretation and in general do not have a consistent impact on the parameter range in which we obtain numerical convergence [113]. After experimentation via a grid search, we opted to use $\nu_a = 0.1$ and $E_a = 1$ in this work. To calculate $\boldsymbol{u}_c$ we instead use Laplace's equation,

$$\nabla_{\boldsymbol{X}} \cdot \boldsymbol{\sigma}_c = \boldsymbol{0}, \quad \boldsymbol{\sigma}_c = \nabla_{\boldsymbol{X}} \boldsymbol{u}_c. \tag{4.96}$$

4.4.3.3 Numerical implementation

In addition to the unknowns $\boldsymbol{v}, p_f, \boldsymbol{u}, p_p, \mathcal{V}, \boldsymbol{u}_a, p_c$, and $\boldsymbol{u}_c$ we utilise several Lagrange multipliers to impose further constraints. These are: $f_0 \in \widehat{\Omega}_s$ which is used to enforce the equilibrium constraint (4.28); $L_d \in \widehat{\Omega}_s$ which ensures the mean solid displacement is zero; $\boldsymbol{L}_t^i \in \partial\widehat{\Omega}_i$ which correspond to the surface tractions acting on the coating: $L_p \in \widehat{\Omega}_f$ which ensures the mean fluid pressure is zero[1]: $\boldsymbol{L}_a^i \in \partial\widehat{\Omega}_i$ which enforce the continuity of displacement; $\boldsymbol{L}_v^i \in \partial\widehat{\Omega}_i$ which correspond to the normal flux through $\partial\widehat{\Omega}_i$.

Similar to Section 2.5.4, it is convenient to write the axisymmetric implementation of the FSI problem as an extension of the 2-D Cartesian problem [62]. There are several facets to consider in this extension. For example, we write the axisymmetric (cylindrical) divergence as

$$\nabla_{\boldsymbol{X}} \cdot \boldsymbol{v} = \partial_z v_z + \frac{1}{\rho} \partial_\rho (\rho v_\rho) = \nabla_{\boldsymbol{X}}^{\text{Cart}} \cdot \boldsymbol{v} + \frac{v_\rho}{\rho}. \tag{4.97}$$

The axisymmetric gradient operator is identical to the Cartesian counterpart when applied to a scalar. When applied to vector $\boldsymbol{v}$ we have

$$\nabla_{\boldsymbol{X}} \boldsymbol{v} = \nabla_{\boldsymbol{X}}^{\text{Cart}} \boldsymbol{v} + \frac{v_\rho}{\rho} \boldsymbol{e}_\phi \otimes \boldsymbol{e}_\phi, \tag{4.98}$$

which introduces further terms into the axisymmetric implementation. This can be seen, for example, in the determinant,

$$J = J^{\text{Cart}} \left(1 + \frac{u_\rho}{r} \right). \tag{4.99}$$

[1]For comparison with the MoR solution we require $p_f = 0$ when $(z, x) = (10, 0)$. This may be obtained by simply subtracting the pressure at this point from the FEM solution which enforces zero mean pressure across the fluid domain.

The final change comes from the differential volume and surface area,

$$\mathrm{d}X = \rho\,\mathrm{d}X^{\mathrm{Cart}} = \rho\,\mathrm{d}\rho\,\mathrm{d}z, \tag{4.100}$$

$$\mathrm{d}S = \rho\,\mathrm{d}S^{\mathrm{Cart}}. \tag{4.101}$$

We now present the weak variational problem for the non-linear axisymmetric ALE FSI problem. We present the test functions for each associated variable

Trial	$\boldsymbol{v}$	p_p	$\boldsymbol{u}$	p_p	$\boldsymbol{u}_a$	p_c	$\boldsymbol{u}_c$	L_d	$\mathcal{V}$	$\boldsymbol{L}_t^0$	$\boldsymbol{L}_t^1$	L_p	$\boldsymbol{L}_a^0$	$\boldsymbol{L}_a^1$	$\boldsymbol{L}_v^0$	$\boldsymbol{L}_v^1$
Test	$\boldsymbol{w}$	q_f	$\boldsymbol{d}$	q_p	$\boldsymbol{d}_a$	q_c	$\boldsymbol{d}_c$	M_d	W	$\boldsymbol{M}_t^0$	$\boldsymbol{M}_t^1$	M_p	$\boldsymbol{M}_a^0$	$\boldsymbol{M}_a^1$	$\boldsymbol{M}_v^0$	$\boldsymbol{M}_v^1$

Multiplying the governing equations by the respective test function, integrating, and applying integration by parts the fluid equations are

$$-\int_{\widehat{\Omega}_f} \boldsymbol{\sigma}_p : \nabla_{\boldsymbol{X}} \boldsymbol{w}\,\rho\,\mathrm{d}\rho\,\mathrm{d}z - \int_{\widehat{\Omega}_f} J\left(\frac{2v_\rho w_\rho}{(\rho+v_\rho)^2} - \frac{p_p w_\rho}{\rho}\frac{\rho}{\rho+v_\rho}\right)\rho\,\mathrm{d}\rho\,\mathrm{d}z + \int_{\partial\widehat{\Omega}_1} \boldsymbol{L}_t^1 \cdot \boldsymbol{w}\,\rho\,\mathrm{d}S^{\mathrm{Cart}} = 0, \tag{4.102}$$

$$\int_{\widehat{\Omega}_f} \nabla_{\boldsymbol{X}} \cdot (J\boldsymbol{F}^{-1}\boldsymbol{v}) q_f\,\rho\,\mathrm{d}\rho\,\mathrm{d}z + \int_{\widehat{\Omega}_f} L_p q_f\,\rho\,\mathrm{d}\rho\,\mathrm{d}z = 0. \tag{4.103}$$

Similarly, the coating equations are

$$-\int_{\widehat{\Omega}_s} \boldsymbol{\sigma}_s : \nabla_{\boldsymbol{X}} \boldsymbol{d}\,\rho\,\mathrm{d}\rho\,\mathrm{d}z - \frac{1}{\epsilon}\int_{\widehat{\Omega}_s}\left(1+\frac{u_\rho}{\rho}\right) d_\rho\,\mathrm{d}\rho\,\mathrm{d}z + \int_{\widehat{\Omega}_s}\left(\frac{1}{\epsilon} - \frac{\lambda}{\epsilon}(J-1)J + Jp_s\right) d_\rho \frac{\rho}{\rho+u_\rho}\,\mathrm{d}\rho\,\mathrm{d}z + \int_{\widehat{\Omega}_s} L_d d_z\,\rho\,\mathrm{d}\rho\,\mathrm{d}z - \int_{\partial\widehat{\Omega}_1} \boldsymbol{L}_t^1 \cdot \boldsymbol{d}\,\rho\,\mathrm{d}S^{\mathrm{Cart}} + \int_{\partial\widehat{\Omega}_0} \boldsymbol{L}_t^0 \cdot \boldsymbol{d}\,\rho\,\mathrm{d}S^{\mathrm{Cart}} = 0, \tag{4.104}$$

$$-\int_{\widehat{\Omega}_s} \boldsymbol{K}\nabla_{\boldsymbol{X}} p_p : \nabla_{\boldsymbol{X}} q_p\,\rho\,\mathrm{d}\rho\,\mathrm{d}z - \int_{\widehat{\Omega}_s} J\boldsymbol{F}^{-1}\mathcal{V}\boldsymbol{e}_z \cdot \nabla_{\boldsymbol{X}} q_p\,\rho d_\rho\,\mathrm{d}\rho\,\mathrm{d}z + \int_{\partial\widehat{\Omega}_1} \boldsymbol{L}_v^1 q_p\,\rho\,\mathrm{d}S^{\mathrm{Cart}} - \int_{\partial\widehat{\Omega}_0} \boldsymbol{L}_v^0 q_p\,\rho\,\mathrm{d}S^{\mathrm{Cart}} = 0. \tag{4.105}$$

Imposing the continuity of normal velocity (4.86) and the traction condition (4.89) in $\widehat{\Omega}_1$ we have

$$\int_{\partial\widehat{\Omega}_1} \left(\boldsymbol{v} + \tilde{\kappa}_0 \boldsymbol{F}^{-T}\nabla_{\boldsymbol{X}} p_p - \mathcal{V}\boldsymbol{e}_z\right) \cdot \boldsymbol{N} M_v^1\,\rho\,\mathrm{d}S^{\mathrm{Cart}}, \tag{4.106}$$

$$\int_{\partial\widehat{\Omega}_1} \boldsymbol{L}_t^1 \cdot \boldsymbol{M}_t^1\,\rho\,\mathrm{d}S^{\mathrm{Cart}} - \int_{\partial\widehat{\Omega}_1} Jp_p \boldsymbol{F}^{-T}\boldsymbol{N} \cdot \boldsymbol{M}_t^1\,\rho\,\mathrm{d}S^{\mathrm{Cart}} + \tilde{\gamma}\int_{\partial\widehat{\Omega}_1} J|\boldsymbol{F}^{-T}\boldsymbol{N}|\left(\boldsymbol{v} + \tilde{\kappa}_0\boldsymbol{F}^{-1}\nabla_{\boldsymbol{X}} p_p - \mathcal{V}\boldsymbol{e}_z\right) \cdot \boldsymbol{M}_t^1\,\rho\,\mathrm{d}S^{\mathrm{Cart}} = 0. \tag{4.107}$$

Similarly, we impose the no penetration condition (4.90) and the stress balance (4.91) on $\widehat{\Omega}_0$,

$$\int_{\partial\widehat{\Omega}_0} \left(\tilde{\kappa}_0 \boldsymbol{F}^{-T} \nabla_{\boldsymbol{X}} p_p\right) \cdot \boldsymbol{N} M_v^0 \, \rho \, \mathrm{d}S^{\mathrm{Cart}} = 0, \tag{4.108}$$

$$\int_{\partial\widehat{\Omega}_0} \boldsymbol{L}_t^0 \cdot \boldsymbol{M}_t^0 \, \rho \, \mathrm{d}S^{\mathrm{Cart}} - \int_{\partial\widehat{\Omega}_0} J_c p_c \boldsymbol{F}^{-T} \boldsymbol{N} \cdot \boldsymbol{M}_t^0 \, \rho \, \mathrm{d}S^{\mathrm{Cart}} = 0. \tag{4.109}$$

Within the cell domain $\widehat{\Omega}_c$ we use the cell pressure to enforce the incompressibility condition

$$\int_{\widehat{\Omega}_c} (J_c - 1) q_c \, \rho \, \mathrm{d}S^{\mathrm{Cart}} = 0. \tag{4.110}$$

The mesh displacement equations are

$$- \int_{\widehat{\Omega}_f} \boldsymbol{\sigma}_a : \nabla_{\boldsymbol{X}}^{\mathrm{Cart}} \boldsymbol{d}_a \, \rho \, \mathrm{d}\rho \, \mathrm{d}z - \int_{\widehat{\Omega}_f} \frac{1}{1+\nu_a} \frac{u_{a,\rho} d_{a,\rho}}{\rho} \, \mathrm{d}\rho \, \mathrm{d}z + \int_{\partial\widehat{\Omega}_1} \boldsymbol{L}_a^1 \cdot \boldsymbol{d}_a \, \rho \, \mathrm{d}S^{\mathrm{Cart}} = 0, \tag{4.111}$$

in $\widehat{\Omega}_f$ and in $\widehat{\Omega}_c$ we have

$$- \int_{\widehat{\Omega}_c} \boldsymbol{\sigma}_c : \nabla_{\boldsymbol{X}}^{\mathrm{Cart}} \boldsymbol{d}_c \, \rho \, \mathrm{d}\rho \, \mathrm{d}z - \int_{\widehat{\Omega}_c} \frac{u_{c,\rho} d_{c,\rho}}{\rho} \, \mathrm{d}\rho \, \mathrm{d}z + \int_{\partial\widehat{\Omega}_0} \boldsymbol{L}_a^0 \cdot \boldsymbol{d}_c \, \rho \, \mathrm{d}S^{\mathrm{Cart}} = 0. \tag{4.112}$$

We also impose zero mean axial solid displacement,

$$\int_{\widehat{\Omega}_s} u_z M_d \, \rho \, \mathrm{d}\rho \, \mathrm{d}z = 0. \tag{4.113}$$

to calculate the coated cell velocity and ensure the coated cell is in equilibrium with the surrounding flow,

$$\int_{\partial\widehat{\Omega}_1} (\boldsymbol{L}_t^1 \cdot \boldsymbol{e}_z) W \, \rho \, \mathrm{d}S^{\mathrm{Cart}} = 0. \tag{4.114}$$

We impose continuity of displacement on both interfaces $\widehat{\Omega}_i$,

$$\int_{\partial\widehat{\Omega}_1} \boldsymbol{M}_a^1 \cdot (\boldsymbol{u} - \boldsymbol{u}_a) \, \rho \, \mathrm{d}S^{\mathrm{Cart}} = 0, \tag{4.115}$$

$$\int_{\partial\widehat{\Omega}_0} \boldsymbol{M}_a^0 \cdot (\boldsymbol{u}_c - \boldsymbol{u}_a) \, \rho \, \mathrm{d}S^{\mathrm{Cart}} = 0. \tag{4.116}$$

and finally we impose zero mean fluid pressure,

$$\int_{\widehat{\Omega}_f} p_p M_p \, \rho \, \mathrm{d}\rho \, \mathrm{d}z = 0. \tag{4.117}$$

These constraints together describe a coated cell in equilibrium with a background Poiseuille flow.

4.4.4 Comparison with the unbounded Poiseuille flow

To quantify the impact of using the MoR to properly account for the tube confinement on the resulting solutions, in Section 4.5 we compare the MoR and FEM implementation with the unbounded framework, presented in Chapter 3. The unbounded framework is identical to the MoR solution with reflection number $j = 1$, since the disturbance to the external Stokes flow created by the coated cell is never reflected back to the tube wall. In order to accurately compare these predictions, we must re-scale the results of Chapter 3 such that lengths are non-dimensionalised on the tube radius ρ_0 rather than the size of the coated cell α_1. This is easily achieved by setting

$$\tilde{\kappa}_0 \to \frac{\tilde{\kappa}_0}{\alpha_1^2}, \rho_0 \to \frac{1}{\alpha_1}, \alpha_0 \to \frac{\alpha_0}{\alpha_1}, r \to \frac{1}{\alpha_1}, \tag{4.118}$$

in all results presented in Section 3.4.2. Additionally, we update the unbounded solutions in Chapter 3 to impose the constraint (4.76) ((4.113) in the FEM implementation) which ensures the net axial translation of the coating is zero. Rescaling the unbounded solutions in Chapter 3 according to (4.118) and imposing the additional constraint (4.76) allows for accurate comparison to the MoR solutions.

4.5 Results

We now present results for the cell's velocity, deformation, and pressure, as well as the effect of the coated cell on the extra pressure drop across the tube over a wide range of geometric and material parameters. We present predictions using the MoR and FEM solution methods, along with the unbounded external flow implementation with the adjustments described in Section 4.4.4, Since we only consider the leading order fluid and solid problems in the MoR and unbounded implementations, we omit any asymptotic superscripts and instead distinguish the numerical implementation via the superscript 'FEM'.

4.5.1 Effect of the material parameters

In this subsection we fix the problem geometry, choosing $\alpha_0 = 0.4$ and $\alpha_1 = 0.6$, and investigate the effects of changing the Darcy number $\tilde{\kappa}_0$, slip parameter γ, and shear modulus μ_s. We begin by studying the translational velocity of the cell. In general the cell velocity is determined by a competition between the axial drag force exerted on a stationary coated cell by the surrounding Poiseuille flow (D) and the axial drag force exerted by an external quiescent fluid on a coated cell translating with velocity

$\mathcal{V}$ (K), with the balance depending on the Darcy number and slip for fixed geometry. In Figure 4.2 we present the wall correction factors D and K, and the cell velocity $\mathcal{V}$ as a function of γ for different $\tilde{\kappa}_0$. In Figure 4.2, and throughout this chapter, the solid lines are our MoR solutions, the dot-dashed lines are our unbounded solutions from Chapter 3, and the circles are from our FEM solutions. Here, we use the numerical solutions purely to validate the MoR solutions by setting $\epsilon = 10^{-5}$ in our numerical simulations; the effect of increasing ϵ will be investigated later.

In Figures 4.2a and 4.2b we observe that both D and K increase with γ, with the effect greater for smaller Darcy numbers. With low Darcy number the flow is directed around the coating such that a reduction in slip (increase in γ) generates larger fluid tractions and consequently a larger axial force. This acts to increase both (D) and (K). By increasing the Darcy number we permit more fluid into the coating which reduces the fluid tractions on the coating such that we observe a smaller increase in the drag. In Figure 4.2c we see that the cell velocity decreases with increasing γ, with the effect amplified for larger Darcy numbers. We observe that the cell velocity increases with the Darcy number when γ is small and increases with the Darcy number when γ is large. The cell velocity is determined by (4.47), and the impact of γ on $\mathcal{V}$ is captured via the dependence of D and K on γ. It is clear from Figure 4.2c that D increases comparatively less than K with γ. When separating the background plug flow generated by the sliding wall, and the pressure-driven flow through a stationary tube, we find the flow around the coating is larger than the flow through the coating for the plug flow component. Therefore, the effect of increasing γ is greater for K than for D and a smaller magnitude of sliding wall velocity is required for the coated cell to be in equilibrium as γ increases. With a large Darcy number, flow through the coating is enhanced, and the effect of increasing γ is comparatively even greater for K than for D, resulting in a small cell velocity when $\tilde{\kappa}_0$ and γ are both large.

The unbounded predictions (dot-dashed lines) that are adapted from Section 3.4.2 and are equivalent to limiting the reflection number to $j = 1$ in the MoR, hugely under-predict the effect of the tube wall for the wall correction factors D and K. This is expected, as the unbounded solutions do not properly account for the tube wall boundary conditions. Studying Figure 4.2c, we observe that the unbounded solutions over-predict the cell velocity when γ is small and under-predict the cell velocity when γ is large. When γ is small, the unbounded solutions predict that the cell velocity approaches one, corresponding to the maximum velocity of the background Poiseuille flow, regardless of the permeability. With the tube wall properly considered, mass conservation requires that any movement of the coated cell downstream generates

upstream flow within the tube. Without this upstream flow, the cell velocity does not feel the restriction by the tube wall, and the cell attains the maximum velocity when the slip is large (small γ). Instead, when γ is large, we expect the unbounded solutions to under-predict the cell velocity, as was observed in Figure 2.3a for an impermeable, elastic particle with no-slip boundary conditions. The FEM predictions with $\epsilon = 10^{-5}$ (circles) align with our MoR solutions, since the tube wall boundary conditions are properly accounted for.

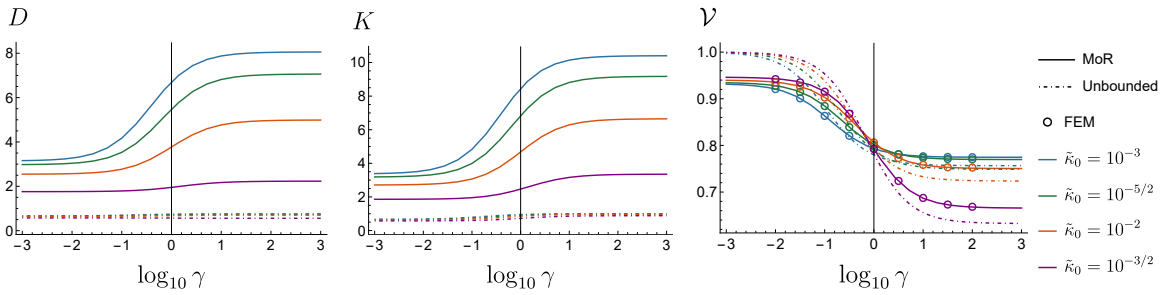

(a) (b) (c)

Figure 4.2: The wall correction factors D (a) and K (b), and the cell velocity $\mathcal{V}$ (c) as a function of γ for different $\tilde{\kappa}_0$ with $\alpha_1 = 0.6$ and $\alpha_0 = 0.4$. The solid and dot-dashed lines are the MoR and unbounded solutions, and the data points marked via circles are validatory FEM solutions with $\epsilon = 10^{-5}$.

In Figure 4.3 we use the FEM solution method to investigate the effect of increasing ϵ on the cell velocity. In Figure 4.3a we fix $\tilde{\kappa}_0 = 10^{-5/2}$ throughout and present the difference between the FEM and MoR velocity predictions for various γ. We see that for all γ an increase in ϵ decreases the particle velocity. This result was similarly observed for an elastic particle of the same size in Figure 2.3a. Further tests confirmed this relationship over the range of Darcy numbers considered in Figure 4.2. We note that the missing data points are due to the limited convergence of our solutions with large γ, which is discussed in Appendix B.2.1. In Figure 4.3b we again fix $\tilde{\kappa}_0 = 10^{-5/2}$ and present log-log plots of the norm of the absolute error between the FEM and MoR particle velocities, varying γ over a wide range of ϵ. For each γ considered, we observe an approximately linear relationship between the error and ϵ, where the slope increases with γ. We attribute the shallower slope when $\gamma = 10^{-2}$ in part to the larger error between the MoR and FEM solutions when $\epsilon = 10^{-5}$. This can be seen in the blue line in Figure 4.3a, which indicates a larger error between the FEM and MoR predictions for small γ. A similar analysis comparing just the FEM solutions ($\mathcal{V}^{\text{FEM}} - \mathcal{V}^{\text{FEM}}(\epsilon = 10^{-5})$ not shown) shows parallel lines of slope ~ 2 (quadratic departure), though again the error increases with decreasing γ for all ϵ.

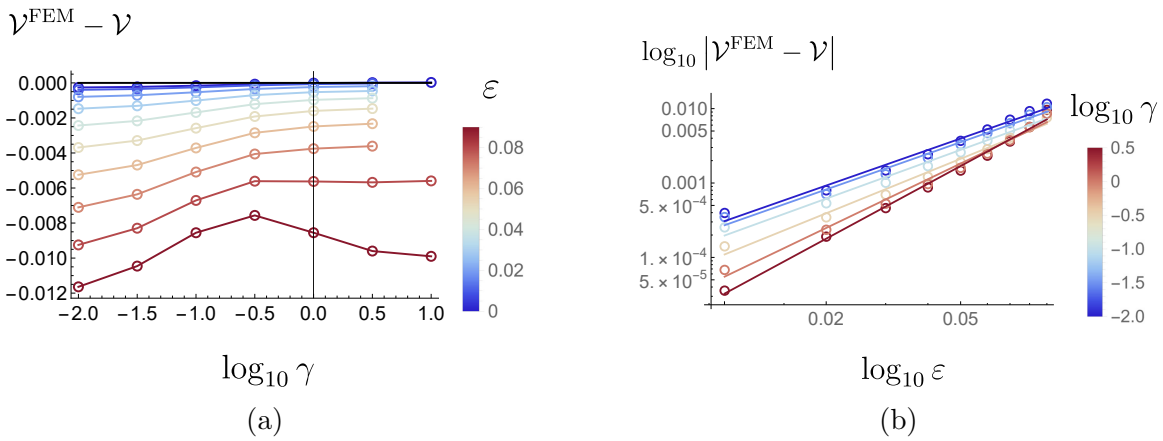

(a) (b)

Figure 4.3: The difference between the nonlinear FEM and MoR velocity predictions for fixed $\alpha_1 = 0.6, \alpha_0 = 0.4$, $\tilde{\kappa}_0 = 10^{-5/2}$, and $\tilde{\lambda} = 1 (\nu = 0.25)$. In (a) we vary γ for several ϵ values and in (b) we present log-log plots for the absolute error in the MoR velocity predictions, varying ϵ for several γ. The slopes range from 1.65 when $\gamma = 10^{-2}$ to 2.40 when $\gamma = 10^{1/2}$, with the mean slope across all lines being 1.89.

Even with the error, the mean slope in Figure 4.3b is 1.89, capturing the quadratic departure of the nonlinear FEM solutions from the linearised MoR solutions in ϵ.

Figure 4.4 details streamline plots for $\alpha_0 = 0.4, \alpha_1 = 0.6$ with four different combinations of $\tilde{\kappa}_0$ and γ. The values $\tilde{\kappa}_0 = 10^{-3/2}$ and $10^{-5/2}$ in Figure 4.4 correspond to a large and small Darcy number, respectively. Setting $\gamma = 10^{-2}$ we have large slip along $r = \alpha_1$ and with $\gamma = 100$ small slip; as $\gamma \to \infty$ we recover a no-slip boundary condition. In the frame of reference of the cell, the background Poiseuille flow drives fluid to the right and the sliding wall drives flow to the left. These combined forcings result in the apparent shearing nature of the flow away from the coated cell, where fluid is forced to the right in the central region of the tube and to the left in the region of the tube boundaries. If the cell velocity is larger the sliding wall dominates more. We also note the apparent presence of stagnation points in the streamline plots which are artifacts of the frame of reference and represent points at which the fluid translates with the coated cell in the lab frame. In Figure 4.4a we have large γ and small $\tilde{\kappa}_0$ such that we observe small slip and restricted flow into the coating. In Figure 4.4b we instead have a large Darcy number and more fluid flows within the coating. In Figures 4.4c and 4.4d $\gamma = 10^{-2}$ such that we have a large slip on $r = \alpha_1$. In Figure 4.4c we have small Darcy number and little flow into the coating. Since the flow may slip around the coating we observe a larger cell velocity (see the discussion surrounding Figure 4.2) and consequently a stronger impact of the sliding wall on the flow. Increasing the Darcy number in Figure 4.4d permits more

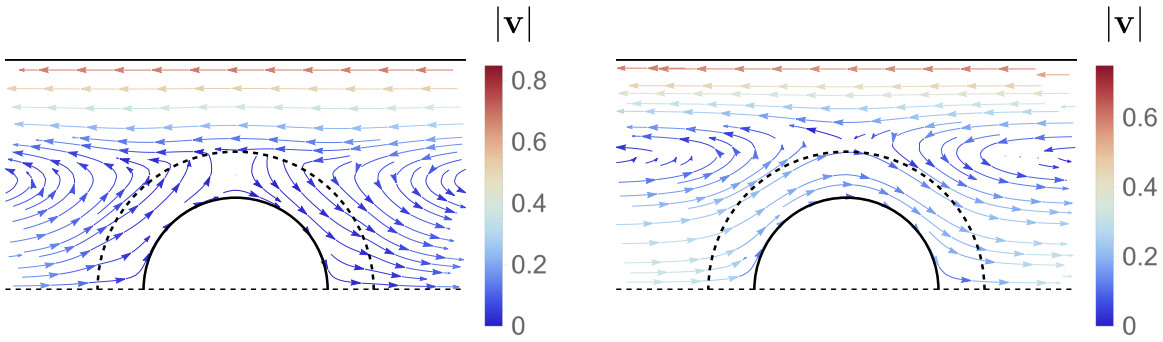

(a) $(\tilde{\kappa}_0, \tilde{\gamma}) = (10^{-5/2}, 10^2), \mathcal{V} = 0.770$ (b) $(\tilde{\kappa}_0, \tilde{\gamma}) = (10^{-3/2}, 10^2), \mathcal{V} = 0.668$

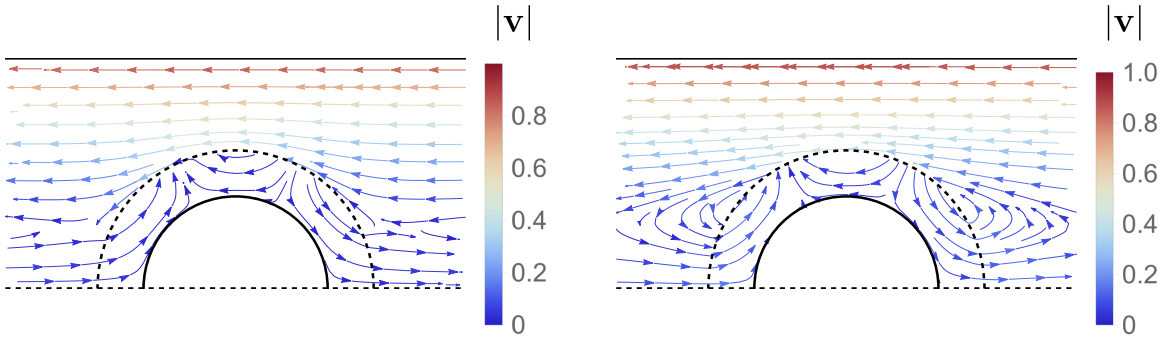

(c) $(\tilde{\kappa}_0, \tilde{\gamma}) = (10^{-5/2}, 10^{-2}), \mathcal{V} = 0.928$ (d) $(\tilde{\kappa}_0, \tilde{\gamma}) = (10^{-3/2}, 10^{-2}), \mathcal{V} = 0.943$

Figure 4.4: Streamline plots with $\alpha_1 = 0.6$ and $\alpha_0 = 0.4$ for varying $\tilde{\kappa}_0$ and γ, calculated using the MoR. The top two plots ((a) & (b)) have large $\gamma = 10^2$ and the bottom two plots ((c) & (d)) have small $\gamma = 10^{-2}$. The leftmost two plots ((a) & (c)) have small $\tilde{\kappa}_0 = 10^{-5/2}$, and the rightmost two plots ((b) & (d)) have large $\tilde{\kappa}_0 = 10^{-3/2}$. Each individual plot is in equilibrium and has a different cell velocity $\mathcal{V}$, corresponding to the magnitude of the sliding wall in the cell frame. In the external region we plot the velocity field and inside the coating we plot the total internal flux, $\boldsymbol{q} = \phi_{f,0}\boldsymbol{v}_p$. The velocity scale for each plot is given in the corresponding colour bar.

fluid flow within the coating, resulting in the apparent re-circulation regions around $\theta = \pi/4, 3\pi/4$. Despite the larger Darcy number, here, the fluid preferentially flows around the coating rather than through it, such that the internal velocity is similar between Figures 4.4c and 4.4d.

Figure 4.5a shows the extra pressure drop across the tube length ΔP^+, defined in (4.5), for varying $\tilde{\kappa}_0$ and γ with $\alpha_1 = 0.6$ and $\alpha_0 = 0.4$. We note that equivalent unbounded solutions are omitted since the extra pressure drop is trivially zero. This is because the local correction to the Stokes pressure decays as $r \to \infty$, see (3.40). In general, we see that for all values of $\tilde{\kappa}_0$ we have a positive ΔP^+ for large γ (less slip) and a negative ΔP^+ for small γ (more slip). This suggests that with small slip a greater pressure drop is required to push the coated cell along the tube as

has been similarly predicted by Barakat et al. [73] for an elastic capsule. However, surprisingly, we predict that with small γ (large slip), a smaller pressure drop is required to generate the Poiseuille fluid flux prescribed in the far field. To understand this effect, we consider a coated cell which is pinned by some body force such that it is stationary within the tube. In this case, we would expect the pressure drop across the tube to increase as the coated cell blocks the fluid flow. Additionally, we expect that pinned cells with a greater slip (smaller γ) have a reduced ΔP^+ in comparison to those with a smaller slip (larger γ) due to a reduction in friction on the coating surface. By reducing the body force which pins the coated cell in place, the cell begins to translate downstream and we expect the pressure drop across the tube to decrease. Similarly, we expect this reduction in the pressure drop to decrease with a increasing slip due to a reduction in the friction on the coating surface. For all material properties, the greater the cell velocity, the greater the reduction in the pressure drop across the tube required to generate the far-field flux, since the motion of the coated cell also drives this downstream flux. Importantly, we showed in Figure 4.2c that the translational velocity of the coated cell is much larger for a small γ (large slip) compared with a large γ (small slip). Consequently, for a large slip, the net pressure drop across the tube is reduced and ΔP^+ is negative. For a small slip, the cell velocity is smaller and the net pressure drop across the tube is increased such that ΔP^+ is positive. For ΔP^+ negative, this prediction suggests that it is more efficient (lower pressure required for identical far-field flux) to drive a coated cell downstream tube than to simply drive the same volume of viscous fluid. In Figure 4.5a we also see that in general an increase in the Darcy number further decreases the pressure drop across the tube length. By increasing the Darcy number, we increase flow through the coating such that less fluid is redirected around the coating, decreasing the pressure drop across the tube.

In Figure 4.5b we fix $\tilde{\kappa}_0 = 10^{-5/2}$ and use the FEM solution method to investigate the impact of increasing ϵ. Several plots are presented for varying γ, to coincide with the velocities presented in Figure 4.3a. We see that the elasticity of the coated cell exacerbates the dependencies observed in Figure 4.5a; for small γ an increase in ϵ decreases the extra pressure drop across the tube and for large γ an increase in ϵ increases the extra pressure drop across the tube.

As detailed in Section 4.4.1.3, the leading-order cell pressure is related to the extra pressure drop via (4.75) which is effectively presented in Figure 4.5a. In Figure 4.6 we present the effect of ϵ on the cell pressure, choosing $\tilde{\kappa}_0 = 10^{-5/2}$ and $\tilde{\lambda} = 1$ ($\nu = 0.25$) throughout. We present the FEM cell pressure relative to the background Poiseuille

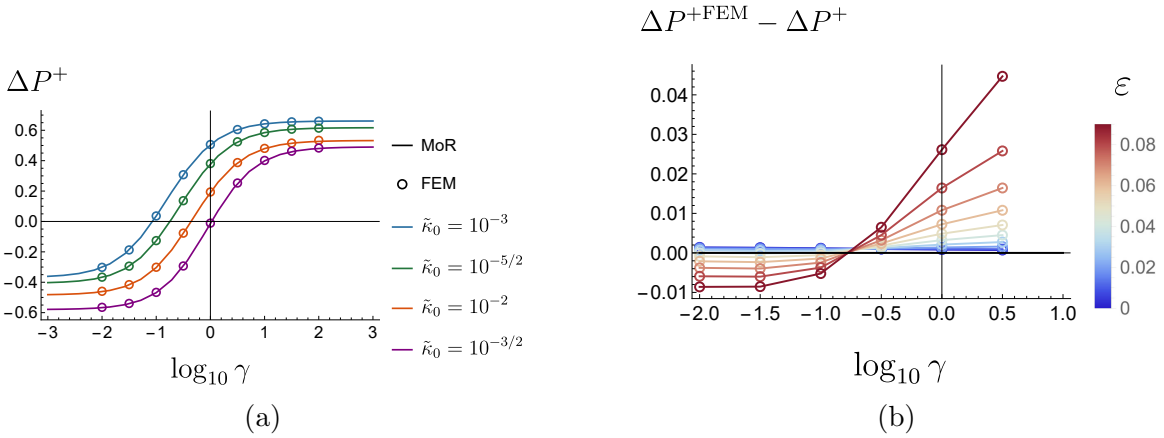

Figure 4.5: (a) The extra pressure drop across the tube length, given by ΔP^+, with $\alpha_1 = 0.6$ and $\alpha_0 = 0.4$. The dependence γ is given for varying $\tilde{\kappa}_0$. The marked data points are our validatory FEM solutions with $\epsilon = 10^{-5}$. (b) The difference between the FEM and MoR predictions for the extra pressure drop with $\tilde{\kappa}_0 = 10^{-5/2}$.

flow contribution in Figure 4.6a and the FEM cell pressure relative to the leading-order MoR cell pressure in Figure 4.6b. We see that in general the cell pressure increases with ϵ, which we interpret as the cell resisting compressive forces. We note the effect of increasing ϵ on the cell pressure is also due in part to the change in pressure drop across the tube as presented in Figure 4.5. For fixed ϵ we expect the coating deformation increase with γ (see, for example, Figure 4.9 which will be discussed in full later) such that the effects of the coating deformation on the cell pressure are greater for larger γ.

We now calculate the leading-order surface deformation of the particle, presenting results in Figure 4.7. Here, we compare our MoR and FEM solutions for various values of ϵ, along with the unbounded implementation presented in Chapter 3, choosing $\tilde{\kappa}_0 = 10^{-5/2}$, $\gamma = 1$, and $\tilde{\lambda} = 1$ ($\nu = 0.25$) throughout. For small ϵ (Figure 4.7a), we see agreement between all methods. As we increase ϵ, the analytical predictions begin to diverge from the non-linear FEM solutions, with the unbounded solutions diverging to a greater degree than the MoR solutions. This divergence is quantified in Figure 4.8, where we present log-log plots of the L^2-norm of the departure of the FEM displacement from the MoR (solid lines) and unbounded (dot-dashed lines) solutions, averaging across the cell boundary $r = \alpha_0$. Similar to Figure 4.3b, we fix $\tilde{\kappa}_0 = 10^{-5/2}$ and present plots for varying γ. Each plot forms a straight line whose slope reflects the dependence of the departure on ϵ. We find that the mean slope for the MoR solutions is 2.09 since the MoR solutions accurately approximate the $\mathcal{O}(\epsilon)$ contribution to the particle deformation. The unbounded solutions on the other hand have a higher base

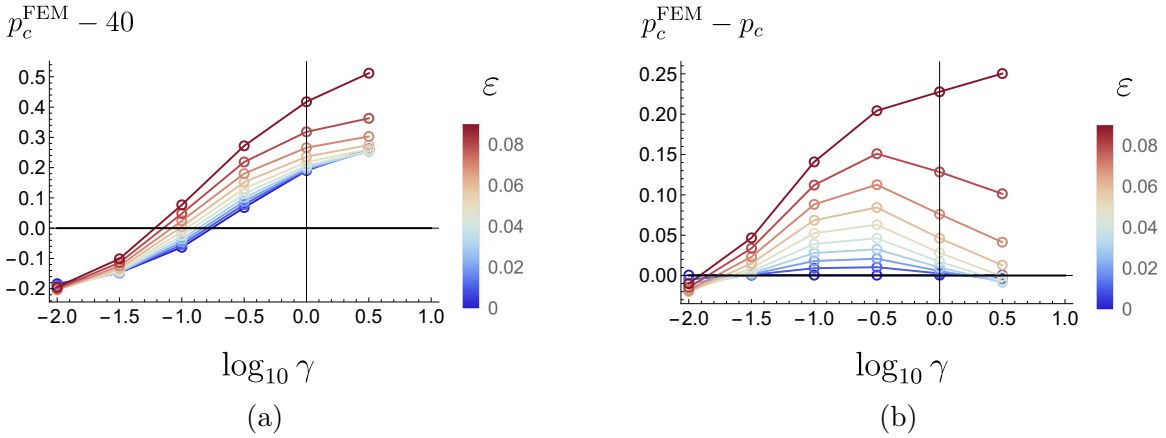

Figure 4.6: The difference between the FEM cell pressure and (a) the background Poiseuille flow and (b) the leading-order MoR cell pressure predictions with $\tilde{\kappa}_0 = 10^{-5/2}$ and $\tilde{\lambda} = 1$ ($\nu = 0.25$).

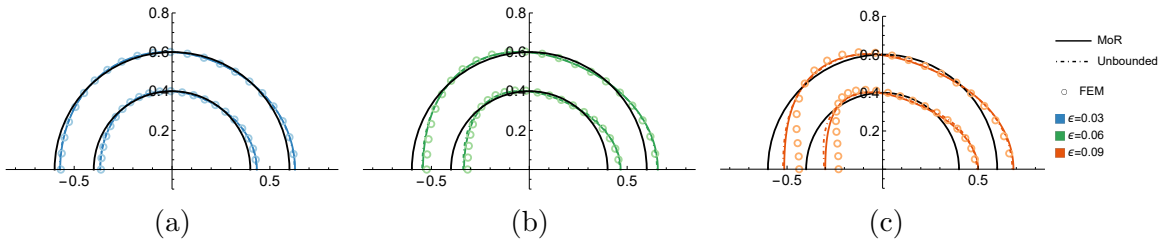

Figure 4.7: Surface deformation with $\tilde{\kappa}_0 = 10^{-5/2}$, $\gamma = 1$, $\tilde{\lambda} = 1$ ($\nu = 0.25$), $\alpha_1 = 0.6$ and $\alpha_0 = 0.4$ for (a) $\epsilon = 0.03$, (b) $\epsilon = 0.06$, and (c) $\epsilon = 0.09$. Graphs are shown for both the MoR (solid, coloured lines) and our FEM implementation (circles), as well as for the unbounded implementation adapted from Chapter 3 (dot-dashed lines). In each plot, we also show the undeformed cell and coating boundaries via the solid, black lines.

error and a mean slope of 1.11. As expected, each case in Figure 4.7 predicts the expected bullet-like shape, however with $\epsilon = 0.09$ in Figure 4.7c, neither the MoR nor the unbounded solutions are able to accurately capture the concave bending of the coating predicted by the FEM method at $\theta = \pi$.

We proceed by choosing the cell surface deformation with $\theta = 0$ as a measurement of the deformation magnitude, and investigate the impacts of the slip and Darcy number in Figure 4.9a with $\tilde{\lambda} = 1$ ($\nu = 0.25$). We observe in Figure 4.9a that in general a reduction in the permeability results in a larger deformation magnitude. We attribute this to a reduction in the normal tractions imposed on the coating surface as more fluid is permitted to enter the coating. Further, we observe that an increase in γ, corresponding to a reduction in the slip, results in an increase in the deformation magnitude, with the effect amplified for large $\tilde{\kappa}_0$. The unbounded solutions predict a

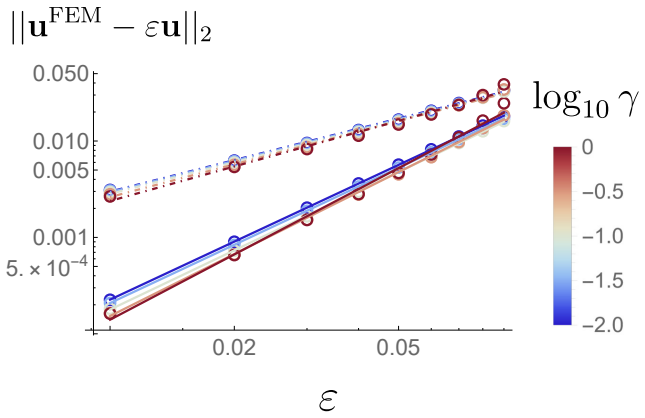

Figure 4.8: Log-log plots of the L^2-norm of the departure of the FEM displacement along the particle boundary from the MoR solutions (solid lines of best fit) and the unbounded solutions (dot-dashed lines of best fit) for several different values of γ with $\tilde{\kappa}_0 = 10^{-5/2}$, $\tilde{\lambda} = 1$ ($\nu = 0.25$), $\alpha_0 = 0.4$, and $\alpha_1 = 0.6$. The mean slope using the MoR solution is 2.09 and using the unbounded solution is 1.1.

similar qualitative behaviour to the MoR solutions, though are considerably different for small Darcy numbers. Surprisingly, the unbounded solutions perform well when the Darcy number is very large, despite the different predicted velocity in Figure 4.2c. The FEM solutions with $\epsilon = 10^{-5}$ agree with the MoR solutions across the entire parameter space.

4.5.2 Effect of geometric parameters

We now investigate the effect of changing the cell and the encapsulation sizes, α_0 and α_1. Throughout this subsection, we consider three different cell sizes $\alpha_0 = 0.1, 0.3,$ and 0.5. For each cell size, we continuously vary the coating thickness.

In Figure 4.10 we fix $\tilde{\kappa}_0 = 10^{-5/2}$ and $\gamma = 1$, and present the wall correction factors K and D, and predicted translational velocity $\mathcal{V}$, varying the encapsulation size α_1 for three different cell sizes. In Figure 4.10a we see that both K and D increase with coating thickness, since a thicker coating increases the disturbance to the flow as more fluid is displaced around the coated cell. This leads to larger tractions on the coating surface and results in a larger drag force acting on the coating. We also observe that the wall correction factors are slightly larger for a large cell and thin coating, when compared with a small cell and thicker coating. With a larger Darcy number, a greater flow is expected within the coating, such that we expect the cell size to have a greater impact on the wall correction factors for fixed encapsulation size α_1. For $\tilde{\kappa}_0 \to 0$ we permit no flow into the coating, such that the cell size would not impact K and D

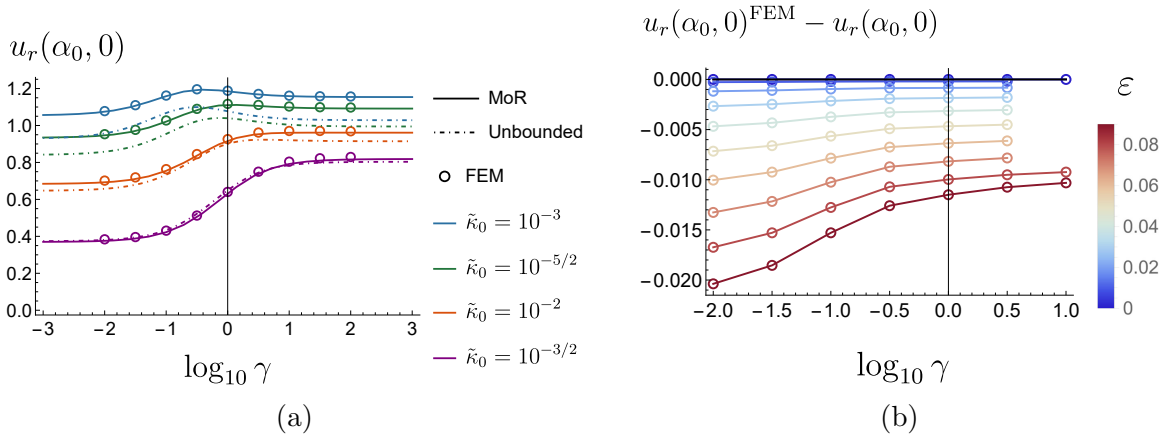

Figure 4.9: (a) The deformation magnitude, given by $u_r(\alpha_0, 0)$, with $\alpha_1 = 0.6$ and $\alpha_0 = 0.4$. The dependence on γ is given for varying $\tilde{\kappa}_0$. The solid lines correspond to our MoR predictions and the dot-dashed lines correspond to our unbounded predictions. The data points marked via a circles are our validatory FEM solutions with $\epsilon = 10^{-5}$. (b) The difference between the nonlinear FEM and MoR deformation predictions for fixed $\alpha_1 = 0.6, \alpha_0 = 0.4$, $\tilde{\kappa}_0 = 10^{-5/2}$, and $\tilde{\lambda} = 1$ ($\nu = 0.25$).

for fixed α_1. The unbounded solutions (dot-dashed lines) quickly diverge from the MoR solutions for increasing encapsulation size (α_1) and again hugely under-predict K and D when α_1 is large. This is because the unbounded solution, equivalent to setting the maximum reflection number $j = 1$ in the MoR solutions, do not properly account for the tube wall boundary conditions which are more impactful the larger the coated cell.

In Figure 4.10b we predict that an increase in coating thickness with fixed cell size α_0 decreases the cell's velocity; this is typical for an elastic particle [136] or a capsule [73] translating through a tube. Further investigation (results not shown) showed that this relationship holds across all $\tilde{\kappa}_0$ and γ considered. Since little fluid is permitted into the coating when $\tilde{\kappa}_0 = 10^{-5/2}$, for a fixed encapsulation size, the cell size has a small effect on its velocity. Though slight, we observe that for the same encapsulation size, a larger cell and thin coating has a greater translational velocity than a smaller cell and thicker coating. We expect this is due to the perfect slip on the cell surface (4.56) decreasing the drag of the total encapsulation. As expected, when $\epsilon = 10^{-5}$ the nonlinear solutions strongly agree with the MoR predictions, and the unbounded predictions diverge more strongly as the encapsulation size increases as the impact of the tube wall becomes more important. Referring back to Figure 4.2c, we expect the unbounded solution to perform especially poorly when γ is small or large, over-predicting the particle velocity when γ is small and under-predicting when

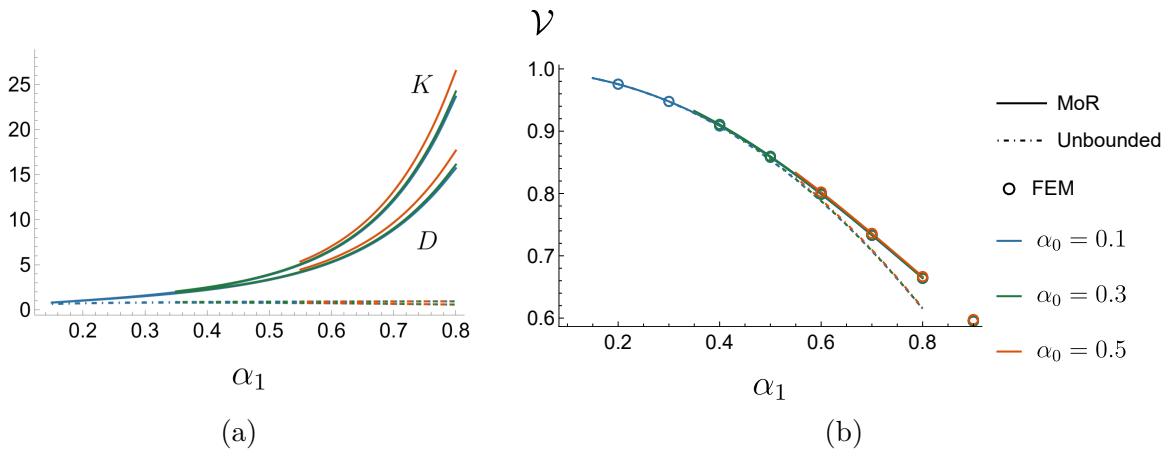

Figure 4.10: (a) The wall correction factors D and K and (b) the cell velocity $\mathcal{V}$ as a function of the encapsulation size for three different fixed cell sizes which are indicated by the colours. The Darcy number $\tilde{\kappa}_0 = 10^{-5/2}$ and slip parameter $\gamma = 1$ are fixed. The solid and dot-dashed lines are the MoR and unbounded solutions, and the data points marked via circles are validatory FEM solutions with $\epsilon = 10^{-5}$.

γ is large.

In Figure 4.11, we use the FEM solutions to investigate the impact of ϵ on the cell velocity, fixing $\tilde{\kappa}_0 = 10^{-5/2}$, $\gamma = 1$, and $\alpha_0 = 0.5$ for varying coating thicknesses. We see that when the encapsulation size is smaller the cell velocity decreases with ϵ. When the encapsulation size is large we observe the reverse. This is analogous to the results in Figure 2.4, where we predicted that the velocity of an elastic particle with radius $\alpha \geq 0.65$ increases with ϵ, though we note that in Figure 4.11 the cell velocity decreases with ϵ for a larger range of encapsulation sizes (see, for example, when $\alpha_1 = 0.8$). This is similarly interpreted by considering the deformation of the coating in Figure 4.11b. We see that the minimum distance between the coated cell and the tube wall is decreased under deformation when $\alpha_1 = 0.7$, such that the coated cell bulges out toward the tube wall. We expect that this bulging effect increases the drag of the coated cell such that it translates with a slower velocity. When compared with Figure 2.4b, here we observe that the coated cell bulges out for larger α_1 (α in Figure 2.4b). We expect this is due to the buckling of the coating observed at $\theta = \pi$ in Figure 4.11b. As the encapsulation size is increased, the bending and stretching moduli of the coating increase, and the pressure in the gap between the coated cell and the tube wall increases, both of which restrict the bulging effect such that the minimum distance between the coated cell and the tube wall instead increases with deformation. Consequently, when $\alpha_1 = 0.9$, the cell velocity increases with ϵ.

We also observe that the effect of ϵ on the cell velocity decreases in magnitude

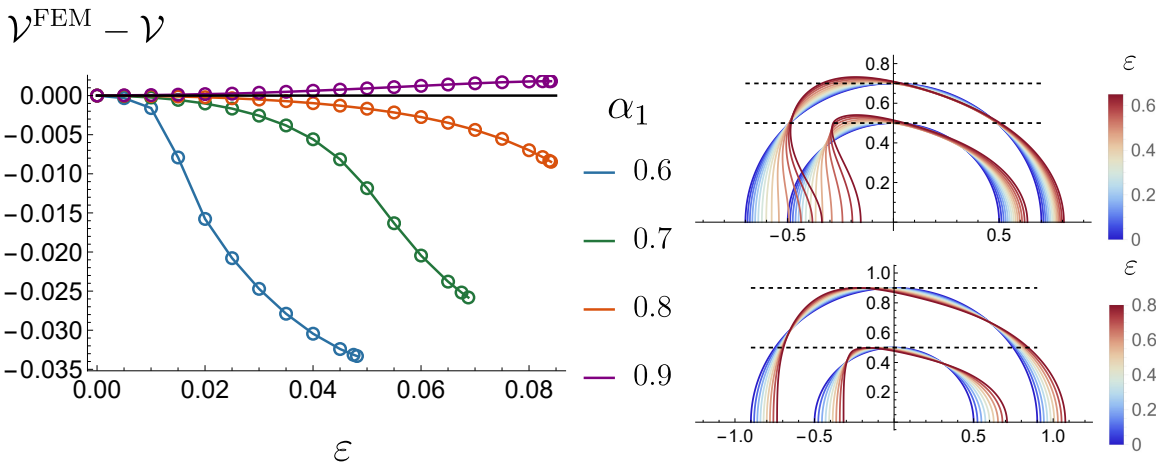

(a) (b)

Figure 4.11: (a) Difference between the FEM and MoR velocities, varying ϵ for several encapsulation sizes α_1. (b) Surface deformation for various ϵ with $\alpha_1 = 0.7$ (top) and $\alpha_1 = 0.9$ (bottom). In all plots $\tilde{\kappa}_0 = 10^{-5/2}$, $\gamma = 1$, and $\alpha_0 = 0.5$. The horizontal black dashed lines indicate the undeformed coating thickness at $\theta = \pi/2$.

as the encapsulation size is increased. The coating deformation is determined by the forces imposed on it and the resistance to deformation. Increasing the coating thickness increases the overall disturbance to the flow and thus the stresses imposed on the coating. However, we also introduce more material to the coating which increases its resistance to deformation. The interplay of these two effects in Figure 4.11a results in a smaller deformation when $\alpha_1 = 0.9$, than when $\alpha_0 = 0.6$ for the same ϵ. Consequently, the effect on the cell velocity decreases as α_1 is increased.

In Figure 4.12 we consider the extra pressure drop ΔP^+. Figure 4.12a presents the MoR solution, varying the encapsulation size α_1 for several cell sizes α_0 encapsulation sizes. We fix $\tilde{\kappa} = 10^{-5/2}$ and present results for both $\gamma = 10^{-2}$ and $\gamma = 1$. We remind the reader that the unbounded solutions do not capture any change in the pressure drop across the tube and so are omitted. As before, the FEM solutions with $\epsilon = 10^{-5}$ are in strong agreement with the MoR solutions. When the coated cell is small, the pressure drop across the tube is not strongly affected. Similar to in Figure 4.5a, with a larger γ, as the encapsulation size is increased the extra pressure drop is positive and increases with the encapsulation size. When γ is small (large slip), the extra pressure drop is negative and decreases with the encapsulation size. However, when the encapsulation size is large $\alpha_1 \geq 0.8$, the extra pressure begins to increase, despite the coating having a large slip. In both cases the effect of increasing the cell size is slight since the permeability is small; in general increasing the cell size increases the extra pressure drop since the disturbance to the flow is greater. In Figure 4.12b we

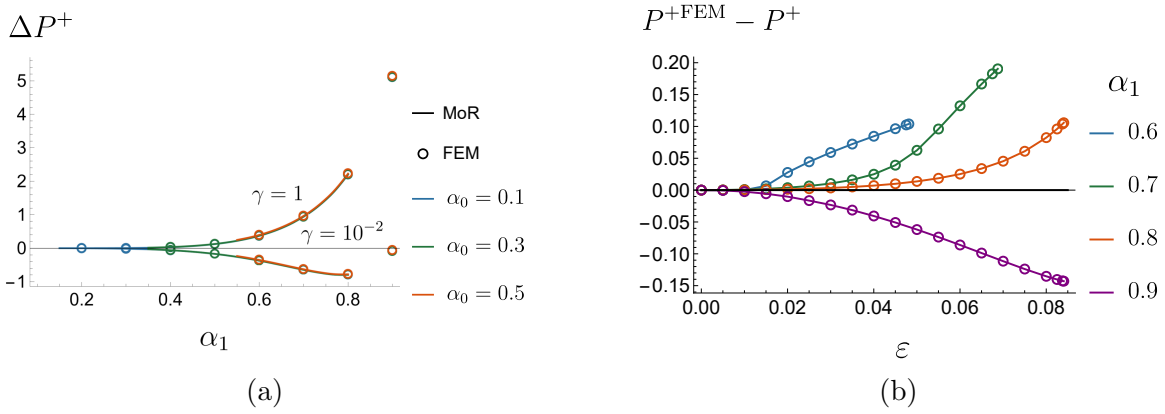

(a) (b)

Figure 4.12: (a) The extra pressure drop across the tube, varying the encapsulation size α_1 for several cell sizes α_0. We fix $\tilde{\kappa} = 10^{-5/2}$ and present results for both $\gamma = 10^{-2}$ and $\gamma = 1$. The solid lines correspond to our MoR predictions and the data points are FEM solutions with $\epsilon = 10^{-5}$. (b) The difference between the nonlinear FEM and MoR extra pressure drop predictions for fixed $\alpha_0 = 0.5$, $\tilde{\kappa}_0 = 10^{-5/2}$, $\gamma = 1$, and $\tilde{\lambda} = 1$ ($\nu = 0.25$), varying the encapsulation size α_1.

present the difference between the extra pressure drop as predicted by the FEM and MoR solution methods for increasing ϵ. We again fix $\tilde{\kappa}_0 = 10^{-5/2}$, $\gamma = 1$, and $\alpha_0 = 0.5$ and present results for increasing encapsulation sizes α_1. Similar to Figure 4.5 with $\gamma = 1$, when the encapsulation size is smaller the extra pressure drop increases with ϵ. However, when the encapsulation size is larger we observe the reverse. These dependencies are the reverse of those observed in Figure 4.11a and are interpreted similarly: when the coating bulges out toward the tube wall the drag of the coated cell increases such that it translates more slowly and a greater pressure is required to drive it downstream. When the encapsulation size is larger we have the reverse such that the extra pressure drop decreases with ϵ.

In Figure 4.13 we present the difference between the cell pressure as predicted by the FEM and MoR solutions methods, comparing against the Poiseuille flow contribution in Figure 4.13a and the MoR cell pressure in Figure 4.13b. Here, we fix $\tilde{\kappa}_0 = 10^{-5/2}$, $\gamma = 1$, $\tilde{\lambda} = 1$ ($\nu = 0.25$), and $\alpha_0 = 0.5$, varying ϵ for different encapsulation sizes α_1. We observe in Figure 4.13a that for small ϵ the cell pressure depends strongly on the change in the pressure drop across the tube presented in Figure 4.12a. We observe in Figure 4.13b that the cell pressure is typically under-predicted by the MoR, and increases with ϵ for all encapsulation sizes. This is expected from Figure 4.6 since $\gamma = 1$. We find that the cell pressure increases the most when $\alpha_1 = 0.6$, which we attribute to the large deformation due to a thin coating (see, for example, Figure 4.14).

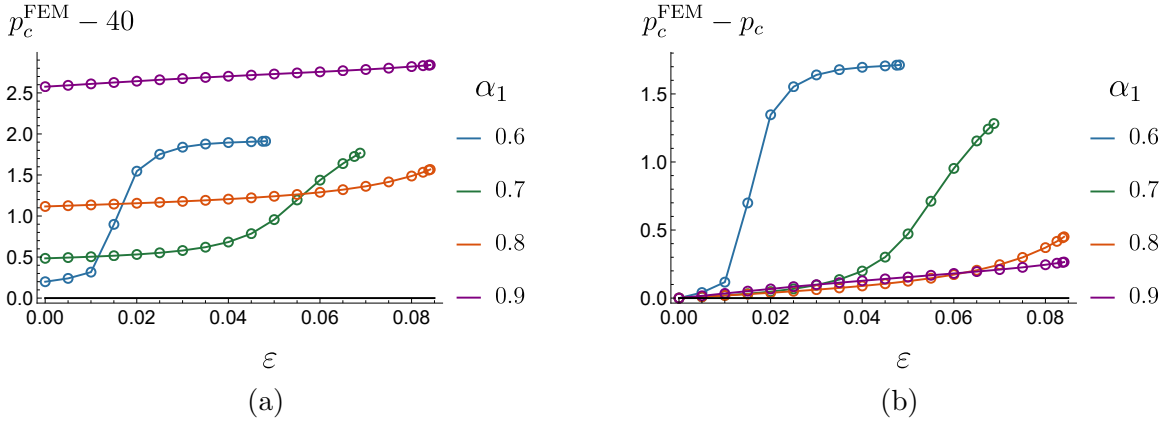

Figure 4.13: The difference between the FEM cell pressure and (a) the background Poiseuille flow contribution and (b) the leading-order MoR cell pressure predictions, varying ϵ and α_1 for fixed $\tilde{\kappa}_0 = 10^{-5/2}$, $\gamma = 1$, $\tilde{\lambda} = 1$ ($\nu = 0.25$), and $\alpha_0 = 0.5$.

Finally, we consider the coating deformation, again using $u_r(\alpha_0, 0)$ as a measure of the deformation magnitude. In Figure 4.14a we present the MoR predictions, along with the unbounded and FEM predictions with $\epsilon = 10^{-5}$. We fix $\tilde{\kappa}_0 = 10^{-5/2}$ and $\gamma = 1$, and present the surface deformation against the coating thickness for several cell sizes. Here, the cell size is important. For a small cell (blue), increasing the coating thickness leads to an increase in the deformation magnitude. Increasing the coating thickness, the disruption to the flow is increased, leading to larger tractions on the coating surface, and a larger deformation. For a large cell (orange), increasing the coating thickness decreases the deformation magnitude despite the increase in tractions associated with an increase in the size of coated cell. Under the same tractions, we expect a thinner coating to exhibit a larger deformation due to a reduction in the bending modulus (4.17). For a medium sized cell (green), we see the interplay between these two effects. The deformation initially decreases with increasing coating thickness due to the reduction in bending modulus, then later increases with the increase in tractions associated with an increase to the overall size of the coated cell. As expected, the unbounded solutions under-predict the coating deformation, with a poorer approximation for a larger encapsulation. In all cases, the FEM solutions with $\epsilon = 10^{-5}$ strongly agree with the MoR predictions.

In Figure 4.14b, we present the difference between the FEM and MoR deformation predictions at $\theta = 0$ for increasing ϵ, again fixing $\tilde{\kappa}_0 = 10^{-5/2}$, $\gamma = 1$, and $\alpha_0 = 0.5$. Each line corresponds to a different encapsulation size α_1. We see that the MoR solutions over-predict the cell deformation when the encapsulation size is smaller, similar to that observed in Figure 4.7. We expect this is associated with the bulging

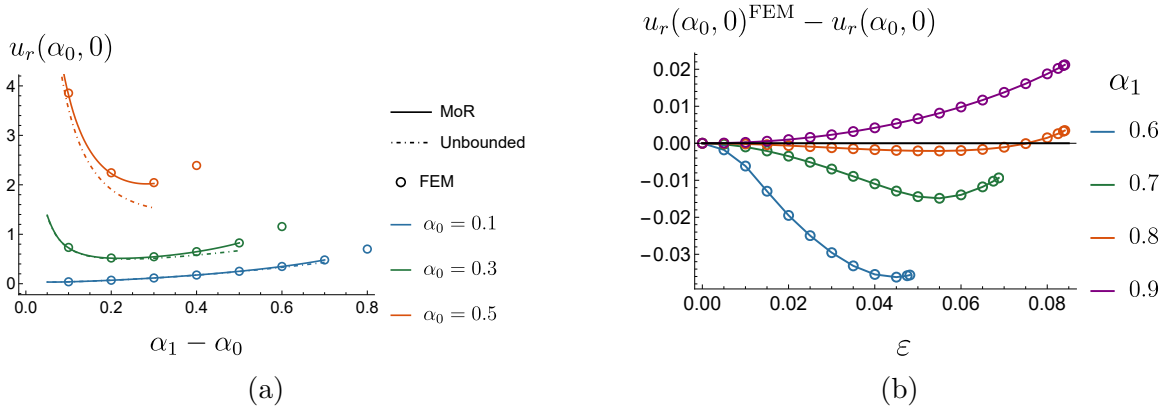

Figure 4.14: (a) The deformation magnitude, given by $u_r(\alpha_0, 0)$, with $\tilde{\kappa}_0 = 10^{-5/2}$, $\gamma = 1$, and $\tilde{\lambda} = 1$ ($\nu = 0.25$). The dependence on coating thickness is given for varying cell sizes. The solid lines correspond to our MoR predictions and the dot-dashed lines correspond to our unbounded predictions. The data points marked via a circles are our validatory FEM solutions with $\epsilon = 10^{-5}$. (b) The difference between the nonlinear FEM and MoR deformation predictions for fixed $\alpha_0 = 0.5$, $\tilde{\kappa}_0 = 10^{-5/2}$, $\gamma = 1$, and $\tilde{\lambda} = 1$ ($\nu = 0.25$), varying the encapsulation size α_1.

of the coating toward the tube wall presented in Figure 4.11b, resulting in a decreased cell velocity and increased extra pressure drop. When the encapsulation size is larger, the pressure in the gap between the coated cell and the tube wall is increased which compressed the coated cell toward the z-axis, preventing this bulging effect. In this case, the cell velocity increases with ϵ, the extra pressure drop decreases with ϵ, and the MoR solutions instead under-predict the cell deformation at $\theta = 0$.

4.6 Discussion

We present a model for a hydrogel-coated cell translating axially along the centre-line of a cylindrical tube and driven by Poiseuille flow. We present two implementations to solve the problem. The first utilises the MoR to solve the leading order fluid and solid problems in the limit of a small ratio of typical viscous fluid stresses to the elastic stiffness, and the second is a nonlinear FEM implementation which is used to validate the MoR solutions, as well as to show the impact of ϵ on the dependent variables. Additionally, we present the solutions from Chapter 3 which treat the external flow as unbounded. We find strong agreement between all three methods when the coated cell is small and stiff (small α_1 and ϵ), where, keeping ϵ small, the agreement between the MoR and FEM solutions persists for $\alpha_1 \leq 0.8$.

We investigate how the translational velocity of the cell, its pressure and surface

deformation, and the change in pressure drop across the tube length depend on the key material parameters and the problem geometry. We predict that for all geometries, a large slip (small γ) on the coating surface results in an increased mobility and a decreased pressure drop across the tube when compared with a small slip coating. Experimentally, this effect could improve the speed and efficiency of the transport of spherical particles in flow. We also identify two key mechanisms governing the magnitude of deformation; bending associated with a thinner coating and reduced bending modulus, and an increase in the blockage factor which generates larger fluid tractions, translating to larger deformations.

Chapter 5

Conclusions

5.1 Summary of work

We briefly describe the work contained in this thesis, detailing the key results. In Chapter 2 we considered an elastic particle translating axially along the centre-line of a cylindrical tube, subject to an axial body force and driving Poiseuille flow. We approached the problem in two ways: an asymptotic solution in the limit of a small ratio of typical viscous fluid stresses to elastic stiffness,

$$\epsilon = \frac{\mu_f V_0}{\mu_s \rho_0}, \tag{5.1}$$

which utilises the MoR to calculate the leading-order fluid flow, and a non-linear ALE FEM solution used to validate the MoR solutions and investigate their range of validity. Depending on the magnitude of the ratio of applied body force to viscous forces, the particle had either a bullet-like shape, an anti-bullet shape, or retained its original spherical shape. Additionally, by considering the first-order fluid problem in Section 2.4.1.4, the first-order correction to the translational velocity of the particle was shown to be zero. Using the non-linear solutions, we showed that for finite deformations, the particle velocity decreases with ϵ for small particles and increases with ϵ for large particles. We interpret this dependence by considering the minimum distance between the particle and the tube wall, which decreases with ϵ for small particles, and increases with ϵ for large particles.

In Chapter 3 we developed a framework to model the small deformation (small ϵ) of an initially spherical coated cell exposed to any unbounded Stokes flow. Using this framework we obtained analytical solutions for the translation, rotation, and deformation of the coated cell under a background shear and Poiseuille flow as functions of the Darcy number (dimensionless permeability of the coating), the slip parameter (controls the velocity jump between the tangential Stokes and Darcy velocities),

the Poisson's ratio (ratio of the transverse compressive strain to the extension strain developed in the coating), and the cell size. We additionally considered the special case of zero cell size, in which the solutions describe an initially spherical poroelastic particle in an unbounded flow. Under a shear flow, we showed that the leading-order rotation of the coated cell does not depend on its material parameters. Generally, we found that the surface deformation of the coated cell can be separated into a bulk deformation mode, in which the cell deformation is small and the outer coating deformation resembles that of spherical poroelastic particle, and a shell deformation mode, in which the outer coating and cell surface deformations are approximately equal and the magnitude of both is predominantly governed by the coating thickness. Additionally, we found that the magnitude of the surface deformations may either increase or decrease with increasing slip, depending on the Poisson's ratio and cell size. Under both flows, we predicted that the small deformation of the cell does not impact its pressure.

Finally, in Chapter 4 we considered the hydrogel-coated cell presented in Chapter 3, but now translating axially along the centre-line of a cylindrical tube and driven by Poiseuille flow. Similar to Chapter 2 we presented the leading-order fluid flow and coating deformation in the small deformation limit, along with a non-linear ALE FEM implementation. We additionally compared these predictions with our unbounded framework presented in Chapter 3. We found that a large slip increases the cell's translational velocity and decreases the pressure drop across the tube. This effect is exacerbated when the coating deformation is finite. We also identified two competing effects which govern the magnitude of the coating deformation; bending associated with a thinner coating and reduced bending modulus, and an increase in the blockage factor which generates larger fluid tractions leading to larger deformations. Similar to Chapter 3, we found that the cell pressure is not impacted by the leading-order deformation. Under finite deformations, we showed that the cell pressure was generally increased in comparison to the linearised predictions, indicating the cell is slightly pressurised.

5.2 Potential applications

The models developed in this thesis have the potential for impact across a wide range of applications. For example, the development of microfluidic systems for the characterisation of the material properties of spherical elastic particles relies on sound mathematical predictions of the resulting FSI problem. Existing microfluidic systems

for spherical elastic particles use tube flow or extensional flow [30], where the former is considered in Chapter 4. Both microfluidic systems may be considered using the unbounded framework presented in Chapter 3. Consequently, using these mathematical predictions, we anticipate similar microfluidic systems could be developed for the characterisation of material properties of a spherical poroelastic particle or a poroelastic spherical shell. For the case of a tube flow, both the deformation and velocity predictions from the bounded or unbounded frameworks could in theory be utilised, allowing two different material properties to be characterised simultaneously. In Chapter 4, we showed that the translational velocity is determined predominantly by the problem geometry, the permeability, and the slip parameter, since the effect of deformation is weak. Thus, we anticipate the translational velocity could be used to predict the slip parameter, and the deformation of the particle/coated cell used to predict its shear modulus. We note that through the inclusion of a body force in Chapters 3 and 4 the sedimentation dynamics of a poroelastic particle may be investigated under confinement, which are not currently well understood [72].

Recently, Xu et al. [61] investigated the impact of three different sets of boundary conditions coupling a Stokes flow to a poroelastic domain, concluding that a combination of complex driving flows and geometry are required to distinguish between them. The models presented in this thesis could be used to compare these different interfacial conditions to analyse the nuance of these choices of interfacial conditions, due to the added complexities of confinement and the blend of spherical and cylindrical domains. These predictions could then be validated via simple experiments to justify their choice for a given material.

As discussed in Chapter 1, characterising the mechanical cues imposed on a cell is important for understanding their corresponding changes in gene expression [15]. Fluid shear, membrane tension, surface deformation, and cell pressure have all been shown to reliably affect the intracellular signaling pathways governing a cell's response to mechanical stimuli. In Chapter 4, we provide predictions for the cell's pressure and surface deformation, and suggest that, though we assume the mechanical load experienced by the membrane is negligible compared with the coating, the cell membrane tension could be approximated by considering the coating hoop stress on the cell surface. Additionally, by mapping material points between the undeformed and deformed cell surfaces, further insight into the opening of ion channels on the cell membrane may be gained. We do not have an explicit read out for the shear modulation provided by the coating, as the total poroelastic shear stress on the cell surface is set to zero through the boundary conditions. To overcome this, fluid flow could

be permitted in the cell or the Brinkman regime could be used within the coating. When under tube confinement, we predict in Chapter 4 that given a fixed coating thickness, the local mechanical environment is dependent on cell size. To the best of our knowledge, the effect of cell size is not at present being considered within the context of cell therapies. We expect this is because the cell size is often small in comparison to an external length scale in *in-vitro* experiments, though this is not the case for vessels in the liver (see, for example, Table 1.1). Characterising these mechanical cues is also of importance to the development of drug delivery systems, which often utilise a spherical hydrogel particle [35], or hydrogel shell containing an aqueous core [31]. The mechanistic insights could be utilised to predict the required stiffness of the particle/coating to avoid the premature release of drug molecules.

5.3 Extensions and future work

We now consider some potential extensions to the models presented in this thesis. The MoR and FEM models in Chapters 2 and 4 may both be extended to include particles which are positioned off-axis. In this case, the results may be compared directly with the analytical solutions presented in Chapter 3 under a background Poiseuille flow to further quantify their range of validity. Additionally, multiple particles may be considered using the MoR [55], to understand the impact of the particle-particle interactions. Quantifying the impact of particle-particle interactions is of particular interest to the process of cell sorting. Lu et al. [137] considered a train of spherical capsules, predicting a critical separation distance past which the effect of the capsule interaction is small and the capsules behave identically (dilute suspension).

More complex physics may also be incorporated into our framework. Firstly, motivated by recent work manipulating the movement of magnetically labelled stem cells [138], an axial body force could be applied to the hydrogel coating in order to manipulate the translational velocity of the cell. When applied without the background Poiseuille flow, the effect of confinement could be investigated for a sedimenting encapsulation, the results of which could be experimentally validated and again used to characterise the material properties of the encapsulation. The general solutions for both a Brinkman medium and a poro-viscoelastic medium, which could be used to describe both the cell and coating domains, are also readily available using spherical harmonics (ignoring inertial terms). We note that a poro-viscoelastic in particular contains strong applications to cell modelling [49, 139]. The parameter values presented in Section 3.2.5 indicate a regime in which the elastic contribution of the cell

is comparable to that of the coating. In this case, the cell tension could be included in the model, or the cell could be modelled as an elastic or viscoelastic bulk [1, 71].

Additional extensions include the calculation of nutrient transport through the coating, to ensure the cells have enough nutrients to remain viable (alive) when in transit. In the simplest case, the nutrients could be treated as a passive tracer which advects with the flow. The effect of a hydrogel-coating on the adhesion of a cell to the endothelial layer is also of interest to the development of the cell therapy. If the injected cells do not attach at the target site, they are at risk of flowing through the liver and into the lungs which could be life threatening. Hodges and Jensen [80] used an asymptotic approach to describe the spreading and peeling of a cell onto and off an adhesive wall, using lubrication theory to account for the thin fluid layer between the cell and plane. The process of cell rolling was then described as a quasi-static combination of these two cases, with the leading edge spreading and the lagging side peeling. We suggest the inclusion of a thin, deformable porous layer which surrounds the cell as a starting point for addressing this question. The liver geometry involves vessels of many sizes and has complex branching. The magnitude of the confinement imposed on a coated cell is therefore time dependent as it transits through the circulation. The additional complexity of a branching channel could be investigated (see, for example, Häner et al. [77, 90]) to understand the mechanical cues imposed on the cell when coated, bridging the gap between the *in-vitro* and *in-vivo* scenarios.

The bio-inspired problems considered in this thesis have the potential for impact across a range of different fields in bio-medicine and bio-engineering, as well as providing fundamental insights into the impacts of confinement in several canonical FSI problems. Specifically, the results of Chapter 4 provide mechanistic insights which can be exploited in the development of next-generation cell therapies involving coated cells via a quantification of the mechanical cues imposed on the cell.

Appendix A

The method of reflections

We present further details of the method of reflections, used to provide semi-analytical solutions for the leading-order fluid problem. We begin by presenting the coordinate transformations necessary for converting between cylindrical and spherical coordinate systems. We then present general solutions for the Stokes equations in both spherical and cylindrical coordinates. Finally, we discuss the nature of convergence for this method.

A.1 Coordinate transformations

To be able to satisfy the systems of equations generated by the method of reflections, we must transform expressions between spherical and cylindrical coordinate systems. For both coordinate systems it is convenient to use the centre of the undeformed particle as the origin. By aligning the 'north pole' of the sphere with the positive z axis, we obtain the following relations,

$$\begin{pmatrix} \sin\theta & 0 & \cos\theta \\ \cos\theta & 0 & -\sin\theta \\ 0 & 1 & 0 \end{pmatrix} \begin{pmatrix} \boldsymbol{e}_\rho \\ \boldsymbol{e}_\phi \\ \boldsymbol{e}_z \end{pmatrix} = \mathcal{A} \begin{pmatrix} \boldsymbol{e}_\rho \\ \boldsymbol{e}_\phi \\ \boldsymbol{e}_z \end{pmatrix} = \begin{pmatrix} \boldsymbol{e}_r \\ \boldsymbol{e}_\theta \\ \boldsymbol{e}_\phi \end{pmatrix}, \qquad \text{with} \qquad \begin{matrix} z = r\cos\theta \\ \rho = r\sin\theta, \\ \phi = \phi \end{matrix} \tag{A.1}$$

where $\mathcal{A}$ is orthogonal. Applying these results we transform the fluid velocity, $\boldsymbol{v}$, and fluid stress, $\boldsymbol{\sigma}_f$, between these coordinate systems,

$$\boldsymbol{v}(r,\theta,\phi) = \mathcal{A}\boldsymbol{v}(\rho,\phi,z), \tag{A.2}$$

$$\boldsymbol{\sigma}_f(r,\theta,\phi) = \mathcal{A}\boldsymbol{\sigma}_f(\rho,\phi,z)\mathcal{A}^T. \tag{A.3}$$

A.2 Stream function in spherical coordinates

Assuming ϕ axisymmetry, the Stokes stream function series in spherical coordinates has the general solution,

$$\psi = \sum_{n=2}^{\infty} (A_n r^{-n+1} + B_n r^{-n+3} + C_n r^n + D_n r^{n+2}) \mathcal{C}_n(\cos\theta), \tag{A.4}$$

where $\mathcal{C}_n(\cos\theta)$ are the Gegenbauer polynomials of order n and degree $-1/2$ [107]. It will also be useful to define the Legendre polynomials of order $(n-1)$ as $\mathcal{P}_{n-1}(\cos\theta)$. To ensure the velocity field vanishes for $r \to \infty$, we set the coefficients $C_n = 0$ and $D_n = 0$. If calculating the leading-order solid displacement and pressure, we instead set the coefficients $A_n = 0$ and $B_n = 0$ in order to ensure the displacement remains finite at the origin. To recover the velocity field we use relations

$$v_r = -\frac{1}{r^2 \sin\theta} \frac{\partial \psi}{\partial \theta}, \tag{A.5}$$

$$v_\theta = \frac{1}{r \sin\theta} \frac{\partial \psi}{\partial r}, \tag{A.6}$$

to give relations for the velocity components (2.65) and (2.66) with $r = \alpha$.

For each odd term in the method of reflections $\boldsymbol{v}^{(0,\text{odd})} = \boldsymbol{v}^{(0,1)}, \boldsymbol{v}^{(0,3)}, \cdots$ we aim to satisfy the boundary conditions on the sphere (2.41) to obtain the coefficients A_n and B_n. To achieve this we first transform the previous even terms $\boldsymbol{v}^{(0,\text{even})} = \boldsymbol{v}^{(0,2)}, \boldsymbol{v}^{(0,4)}, \cdots$ to spherical coordinates. We then project these even terms to the particle surface, approximating them as functions of $\cos\theta$ such that we can exploit the linear independence of $\mathcal{P}_{n-1}(\cos\theta)$ and $\mathcal{C}_n(\cos\theta)$. To do this we use the use the expressions,

$$f(\cos\theta) = \sum_{n=2}^{\infty} \tilde{a}_n \mathcal{C}_n(\cos\theta), \tag{A.7}$$

$$g(\cos\theta) = \sum_{n=2}^{\infty} \tilde{b}_{n-1} \mathcal{P}_{n-1}(\cos\theta), \tag{A.8}$$

where f and g are arbitrary functions of $\cos\theta$ [55]. The coefficients $\tilde{a}_n$ and $\tilde{b}_{n-1}$ are given by

$$\tilde{a}_n = \frac{1}{2} n(n-1)(2n-1) \int_{-1}^{1} \frac{f(\cos\theta)\mathcal{C}_n(\cos\theta)}{(\sin\theta)^2} \, \mathrm{d}(\cos\theta), \tag{A.9}$$

$$\tilde{b}_{n-1} = \frac{1}{2}(2n-1) \int_{-1}^{1} g(\cos\theta)\mathcal{P}_{n-1}(\cos\theta) \, \mathrm{d}(\cos\theta). \tag{A.10}$$

Substituting the expressions for the velocity field in spherical coordinates (2.65) and (2.66) into the boundary conditions (2.62) and then using (A.7) and (A.8) gives the following summation,

$$\sum_{n=2}^{\infty} -\alpha^{-n-1}(A_n + B_n\alpha^2)\mathcal{P}_{n-1}(\cos\theta) = \sum_{n=2}^{\infty} \tilde{b}_{n-1}\mathcal{P}_{n-1}(\cos\theta) \tag{A.11}$$

$$\sum_{n=2}^{\infty} -\alpha^{-n-1}((n-1)A_n + (n-3)B_n\alpha^2)\csc\theta\,\mathcal{C}_n(\cos\theta) = \sum_{n=2}^{\infty} \tilde{a}_n \csc\theta\mathcal{C}_n(\cos\theta). \tag{A.12}$$

Equating each term in the summation results in the relations,

$$-\alpha^{-n-1}(A_n + B_n\alpha^2) = \tilde{b}_{n-1}, \tag{A.13}$$

$$-\alpha^{-n-1}((n-1)A_n + (n-3)B_n\alpha^2) = \tilde{a}_n. \tag{A.14}$$

By re-writing the cylindrical velocity expressions on the sphere surface using the expressions (A.7) and (A.8) we obtain the spherical coefficients A_n and B_n. Due to the complexity of the solutions we are forced to numerically calculate $\tilde{a}_n$ and $\tilde{b}_{n-1}$, rendering the method of reflections semi-analytic in nature.

A.3 Stream function in cylindrical coordinates

The general solution for the Stokes velocity field in cylindrical coordinates is

$$\boldsymbol{v} = \sum_{k=-\infty}^{\infty} \left[\nabla \times (\Omega_k \boldsymbol{e}_z) + \nabla\Psi_k + \rho\frac{\partial}{\partial\rho}\nabla\Pi_k + \frac{\partial\Pi_k}{\partial z}\boldsymbol{e}_z\right], \tag{A.15}$$

$$p = -2\sum_{k=-\infty}^{\infty} \frac{\partial^2\Pi_k}{\partial z^2}, \tag{A.16}$$

where Ω_k, Ψ_k and Π_k are cylindrical harmonic functions [107]. Following the framework in Yao et al. [55], we write the axisymmetric velocity (A.15) as,

$$\boldsymbol{v} = \left(\frac{\partial\Psi_0}{\partial\rho} + \rho\frac{\partial^2\Pi_0}{\partial\rho^2}\right)\boldsymbol{e}_\rho + \left(\frac{\partial\Psi_0}{\partial z} + \rho\frac{\partial^2\Pi_0}{\partial\rho\partial z} + \frac{\partial\Pi_0}{\partial z}\right)\boldsymbol{e}_z, \tag{A.17}$$

with

$$\Pi_0 = \frac{1}{\pi}\left(\int_0^\infty \frac{1}{\lambda}\pi_{a0}\mathcal{I}_0(\lambda\rho)\sin\lambda z\,\mathrm{d}\lambda + \int_0^\infty \frac{1}{\lambda}\pi_{c0}\mathcal{I}_0(\lambda\rho)\cos\lambda z\,\mathrm{d}\lambda\right), \tag{A.18}$$

$$\Psi_0 = \frac{1}{\pi}\left(\int_0^\infty \frac{1}{\lambda}\psi_{a0}\mathcal{I}_0(\lambda\rho)\sin\lambda z\,\mathrm{d}\lambda + \int_0^\infty \frac{1}{\lambda}\psi_{c0}\mathcal{I}_0(\lambda\rho)\cos\lambda z\,\mathrm{d}\lambda\right), \tag{A.19}$$

where $\mathcal{I}_0$ is the Bessel function of the first kind of order 0. To calculate an even component in the method of reflections, $\boldsymbol{v}^{(0,2)}$ for example, it remains to find the four unknown functions of λ: $\pi_{a0}, \pi_{c0}, \psi_{a0}$ and ψ_{c0}, such that $\boldsymbol{v}^{(0,2)}$ cancels $\boldsymbol{v}^{(0,1)}$ on the tube wall. We note that Equation (2.63) is of the form,

$$\boldsymbol{v}^{(0,2)}(1,z) = V_\rho \boldsymbol{e}_\rho + V_z \boldsymbol{e}_z, \tag{A.20}$$

where V_ρ and V_z come from transforming $\boldsymbol{v}^{(0,1)}$ to cylindrical coordinates and imposing $\rho = 1$. Substituting the expressions for Π_0 and Ψ_0 (A.18) and (A.19) into the velocity (A.17) and setting $\rho = 1$ gives the following relations,

$$\begin{aligned} V_\rho = \frac{1}{\pi}\int_0^\infty [\psi_{c0}\mathcal{I}_0'(\lambda) + \pi_{c0}\lambda\mathcal{I}_0''(\lambda)]\cos\lambda z\,\mathrm{d}\lambda \\ + \frac{1}{\pi}\int_0^\infty [\psi_{a0}\mathcal{I}_0'(\lambda) + \pi_{a0}\lambda\mathcal{I}_0''(\lambda)]\sin\lambda z\,\mathrm{d}\lambda, \end{aligned} \tag{A.21}$$

$$\begin{aligned} V_z = \frac{1}{\pi}\int_0^\infty [\psi_{a0}\mathcal{I}_0(\lambda) + \pi_{a0}\lambda\mathcal{I}_0'(\lambda) + \pi_{a0}\mathcal{I}_0(\lambda)]\cos\lambda z\,\mathrm{d}\lambda \\ + \frac{1}{\pi}\int_0^\infty [\psi_{c0}\mathcal{I}_0(\lambda) + \pi_{c0}\lambda\mathcal{I}_0'(\lambda) + \pi_{c0}\mathcal{I}_0(\lambda)]\sin\lambda z\,\mathrm{d}\lambda. \end{aligned} \tag{A.22}$$

We can then perform the following Fourier integrals to obtain,

$$\int_{-\infty}^\infty V_\rho \cos\lambda z\,\mathrm{d}z = \psi_{c0}\mathcal{I}_0'(\lambda) + \pi_{c0}\lambda\mathcal{I}_0''(\lambda), \tag{A.23}$$

$$\int_{-\infty}^\infty V_\rho \sin\lambda z\,\mathrm{d}z = \psi_{a0}\mathcal{I}_0'(\lambda) + \pi_{a0}\lambda\mathcal{I}_0''(\lambda), \tag{A.24}$$

$$\int_{-\infty}^\infty V_z \cos\lambda z\,\mathrm{d}z = \psi_{a0}\mathcal{I}_0(\lambda) + \pi_{a0}\lambda\mathcal{I}_0'(\lambda) + \pi_{a0}\mathcal{I}_0(\lambda), \tag{A.25}$$

$$\int_{-\infty}^\infty V_z \sin\lambda z\,\mathrm{d}z = \psi_{c0}\mathcal{I}_0(\lambda) + \pi_{c0}\lambda\mathcal{I}_0'(\lambda) + \pi_{c0}\mathcal{I}_0(\lambda). \tag{A.26}$$

These four equations can then be solved simultaneously to obtain equations for the four unknown functions of λ,

$$\psi_{c0} = \frac{[\mathcal{I}_0(\lambda) + \lambda\mathcal{I}_0'(\lambda)]\int_{-\infty}^\infty V_\rho\cos\lambda z\,\mathrm{d}z + \lambda\mathcal{I}_0''(\lambda)\int_{-\infty}^\infty V_z\sin\lambda z\,\mathrm{d}z}{\lambda{\mathcal{I}_0'}^2(\lambda) + \mathcal{I}_0(\lambda)[\mathcal{I}_0'(\lambda) - \lambda\mathcal{I}_0''(\lambda)]}, \tag{A.27}$$

$$\psi_{a0} = \frac{[\mathcal{I}_0(\lambda) + \lambda\mathcal{I}_0'(\lambda)]\int_{-\infty}^\infty V_\rho\sin\lambda z\,\mathrm{d}z - \lambda\mathcal{I}_0''(\lambda)\int_{-\infty}^\infty V_z\cos\lambda z\,\mathrm{d}z}{\lambda{\mathcal{I}_0'}^2(\lambda) + \mathcal{I}_0(\lambda)[\mathcal{I}_0'(\lambda) - \lambda\mathcal{I}_0''(\lambda)]}, \tag{A.28}$$

$$\pi_{c0} = -\frac{\mathcal{I}_0(\lambda)\int_{-\infty}^\infty V_\rho\cos\lambda z\,\mathrm{d}z + \mathcal{I}_0'(\lambda)\int_{-\infty}^\infty V_z\sin\lambda z\,\mathrm{d}z}{\lambda{\mathcal{I}_0'}^2(\lambda) + \mathcal{I}_0(\lambda)[\mathcal{I}_0'(\lambda) - \lambda\mathcal{I}_0''(\lambda)]}, \tag{A.29}$$

$$\pi_{a0} = -\frac{\mathcal{I}_0(\lambda)\int_{-\infty}^\infty V_\rho\sin\lambda z\,\mathrm{d}z - \mathcal{I}_0'(\lambda)\int_{-\infty}^\infty V_z\cos\lambda z\,\mathrm{d}z}{\lambda{\mathcal{I}_0'}^2(\lambda) + \mathcal{I}_0(\lambda)[\mathcal{I}_0'(\lambda) - \lambda\mathcal{I}_0''(\lambda)]}. \tag{A.30}$$

These expressions are then substituted back into (A.18) and (A.19) and then (A.17) to obtain the velocity field, with the integration in λ performed numerically. Here, we have detailed how to solve for $\boldsymbol{v}^{(0,2)}$ such that $\boldsymbol{v}^{(0,0)} + \boldsymbol{v}^{(0,1)} + \boldsymbol{v}^{(0,2)}$ satisfy the boundary conditions on the tube wall (2.63). Following this methodology we can find any $\boldsymbol{v}^{(0,\text{even})}$ to reimpose the boundary conditions on the tube wall.

A.4 Convergence

A.4.1 Elastic particle

Combining Equations (A.5), (A.6) and (A.17) we obtain the total velocity field. When calculating the total drag acting on the sphere, however, we need only consider the velocity contributions with j odd, which originate from imposing the boundary conditions on the sphere surface. Since the cylindrical expressions do not contain singularities within the sphere, the associated force integrates to zero via the divergence theorem,

$$F_z^{(i,2j)} = \oiint_{\partial V} \boldsymbol{e}_z \cdot \boldsymbol{\sigma}_f^{(i,2j)} \cdot \boldsymbol{n} \, \mathrm{d}S = 0, \tag{A.31}$$

where V is the sphere volume and ∂V its boundary. Thus, we write the total drag as,

$$F_z^{(i)} = F_z^{(i,1)} + F_z^{(i,3)} + \cdots , \tag{A.32}$$

where $F_z^{(i,j)}$ is the drag force associated with the velocity $\boldsymbol{v}^{(i,j)}$ and pressure $p^{(i,j)}$. Each component of the total drag can be obtained either by calculating the local stress field on the surface of the sphere or by using the stream function directly with $r = \alpha$ [107],

$$F_z^{(i,j)} = \int_0^\pi r^3 \sin\theta^3 \frac{\partial}{\partial r} \left(\frac{E^2 \psi^{(i,j)}(r,\theta)}{r^2 \sin\theta^2} \right) r \partial\theta. \tag{A.33}$$

The drag force provides us with a metric to define convergence of the total solution. Since the translational velocity of the particle is unknown, we use the wall corrections, for example $D^{(0)}(\alpha)$ and $K^{(0)}(\alpha)$, to define convergence, asserting they both be individually converged, see Figure A.1. We define convergence with respect to the reflection number j as when the latest contribution is at least five orders of magnitude smaller than the total value.

Further, we must also ensure n is large enough to accurately project cylindrical expressions onto the sphere surface. In Figure A.2 we calculate the difference between the leading-order velocity on the sphere surface at $\theta = \pi/2$ obtained from the expressions in cylindrical coordinates (A.17) and the corresponding projection

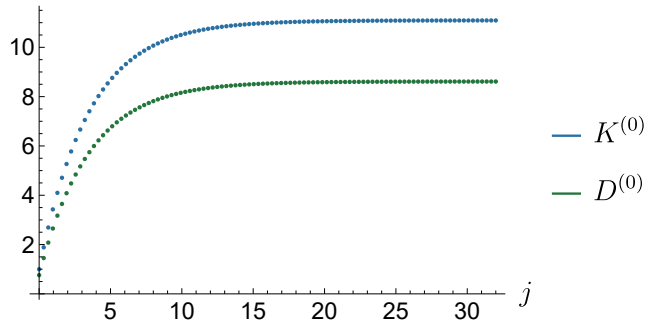

Figure A.1: Convergence of the wall correction factors with $\alpha = 0.6$ and $f = 0$. Here, j is the reflection number.

onto spherical coordinates via Equations (A.9) and (A.10) using either the first two ($n = 2, 4$) or three ($n = 2, 4, 6$) non-zero terms in the spherical stream function series. Since we can exactly represent Poiseuille flow via a spherical stream function series with non-zero terms corresponding to $n = 2$ and $n = 4$, this choice is the minimum required for the problem. However, if we impose the no-slip condition on the tube wall, and the particle is large enough to cause a substantial disturbance in the flow field, we must recruit higher order, even terms in n. By including terms with $n = 6$, we recover a more accurate approximation of how the tube wall impacts the resulting leading-order deformation of the elastic particle. For describing pressure-driven channel flow around a rigid sphere under no applied body force, including the first three non-zero terms in the spherical stream function series ensures we can accurately apply both sets of boundary conditions simultaneously for $\alpha \leq 0.7$. With larger α we would need to include higher terms in n to reduce the error associated with the projection. We expect the MoR to converge exactly for $n \to \infty$.

We acknowledge that for large particles ($\alpha = 0.8$) we seek 5-digit accuracy for convergence in j, though may admit up to $\sim 1\%$ errors when satisfying the no-slip boundary conditions on the particle surface. To avoid numerically recalculating the integrals (A.27)–(A.30) on each reflection, we instead precalculate all required integrals, storing values in a look-up table. Consequently, the calculation of each even reflection involves the addition of these precalculated integrals, and it is computationally efficient to include an arbitrary number of reflections in the velocity series. The number of required integrals to be precalculated scales quadratically with n. This does not strongly affect the runtime of the method when calculating the surface tractions imposed on the particle ($\sim<$ 1 second for reflection number $j < 1000$), however it does impact the runtime when visualising the resulting velocity field. While the MoR is meshless, in order to present the external flow field throughout the fluid domain, we

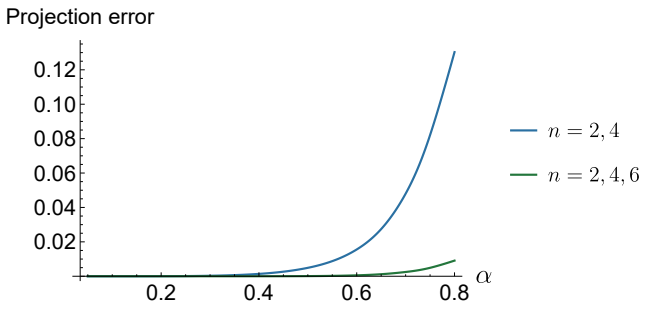

Figure A.2: The difference in predicted velocity on the undeformed particle surface with $\theta = \pi/2$ between the cylindrical terms and the projection to spherical coordinates in the method of reflections with $f = 0$. Graphs are shown including the first two ($n = 2, 4$) and first three ($n = 2, 4, 6$) non-zero terms in the spherical stream function series.

are required to calculate similar numerical integrals as presented in (A.18) and (A.19) across a the domain (see, for example, Figure 2.11, where we use a 100×100 grid mesh). For the first order flow fields presented in Figures 2.11d to 2.11f, we precalculate numerical integrals up to and including $n = 11$. We stress again that the the calculation of the surface tractions on the particle, necessary for the calculation of its displacement, remains small for larger n.

A.4.2 Coated cell

The accuracy and convergence of the coated cell model is similar to that of the spherical elastic particle. However, we note that the number of reflections required for convergence is not only dependent on the geometric parameters, but also the porous parameters. In Figure A.3 we present the reflection number j required for convergence of the MoR solution, varying $\tilde{\kappa}_0$ and γ for fixed geometry $\alpha_0 = 0.4$ and $\alpha_1 = 0.6$. It is clear that in general a greater $\tilde{\kappa}_0$ and γ require more terms for the same accuracy of solution. This is because a smaller Darcy number and slip result in a greater disturbance to the flow. Consequently, we expect that the unbounded solution presented in Chapter 3, which is equivalent to the MoR solution with $j = 1$, will in general be more accurate for a greater Darcy number and a larger slip.

We expect the discrepancy presented in Figure A.2 to be dependent predominantly on the encapsulation size and similarly choose $n = 2, 4, 6$ for the coated cell model, keeping $\alpha_0 \leq 0.8$.

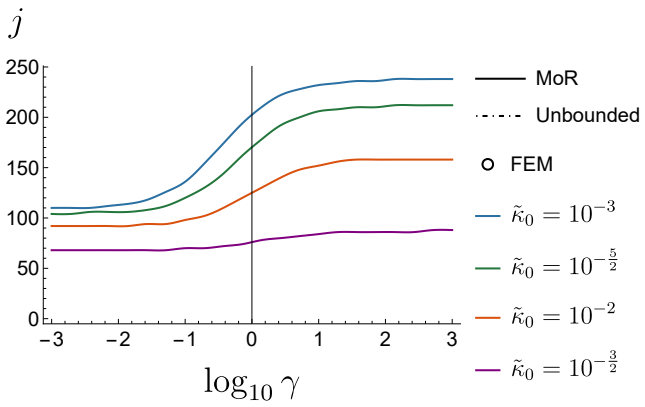

Figure A.3: Reflection number j required for convergence with $\alpha_0 = 0.4$ and $\alpha_1 = 0.6$.

Appendix B

Numerical Validation

B.1 Elastic particle

To validate the solid solver we employ the method of manufactured solutions. Given a prescribed particle displacement, we use the solid governing equations to find analytical expressions for the required surface tractions and body force. These tractions and the body force are then used to drive the particle displacement in the numerical model, and the solution is compared with the analytical displacement field. Due to the complexity of the model and geometry, we choose the one-dimensional displacement field,

$$\epsilon \boldsymbol{u}^{\text{test}} = \epsilon_t r \boldsymbol{e}_r, \tag{B.1}$$

where ϵ_t determines the magnitude of the particle displacement as a fraction of the particle radius and r is now the Lagrangian radial coordinate. Substituting (B.1) into the governing equations for the particle displacement we obtain the corresponding surface tractions, $\boldsymbol{\tau} = \boldsymbol{P} \cdot \boldsymbol{N}$, and body force,

$$\tau_r = \frac{1}{\epsilon}\left[1 + \epsilon_t - (1+\epsilon_t)^{-1} + (1+\epsilon_t)^2(-1 + (1+\epsilon_t)^3)\lambda_s\right], \quad \tau_\theta = 0, \quad \boldsymbol{f} = \boldsymbol{0}, \tag{B.2}$$

where Lamé's first parameter λ_s arises from the compressible neo-Hookean stress-strain relationship,

$$\boldsymbol{P} = \frac{\lambda_s}{\mu_s \epsilon}(J-1)J\boldsymbol{F}^{-T} + \frac{1}{\epsilon}\left(\boldsymbol{F} - \boldsymbol{F}^{-T}\right). \tag{B.3}$$

We note the switch from an incompressible particle to a compressible one is straightforward to implement and is necessary to obtain the above displacement field (B.1). We investigate the effect of increasing ϵ_t with no background flow ($\boldsymbol{v} = \boldsymbol{0}$) in Figure B.1, presenting log-log plots of the L^2-norm of the difference between the FEM displacement and (B.1). The typical error is of the order 1×10^{-4} and increases with

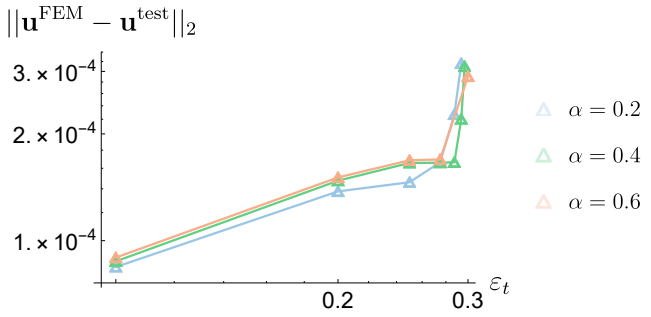

Figure B.1: L^2-norm of the difference between the FEM displacement and the test analytical displacement averaged over the solid domain for varying displacement magnitudes ϵ_t. The simulations used the element sizes 4×10^{-2}, 2×10^{-2}, and 5×10^{-3} in the fluid, solid and boundary domains, respectively. These element sizes were chosen as the standard values and were used consistently within this study.

ϵ_t. For each α, the error increases sharply as ϵ_t approaches 0.3, which is associated with the breakdown of the ALE method due to the large displacement.

To test the fluid and ALE solvers we impose the traction (B.3) and include a background Poiseuille flow. We decrease $\epsilon = 1 \times 10^{-10}$ such that the particle is effectively rigid to the imposed fluid stresses. Consequently, the fluid sees a rigid particle with inflated radius $r_s^{\text{test}} = \alpha(1 + \epsilon_t)$. The particle velocity of the inflated particle may then be compared with the MoR solutions for a particle with initial radius r_s^{test}. In these comparisons we acknowledge the MoR solutions are not exact, but expect the results for the particle velocity to be accurate to $\sim 1 \times 10^{-5}$ in all tested cases. We fix $\epsilon_t = 0.1$ and investigate the effect of mesh refinement in Figure B.2. We test the solid solver in Figure B.2a similarly to Figure B.1, and test the fluid and ALE solvers in Figure B.2b by presenting the norm of the absolute error between the FEM and MoR particle velocities. For each α, we include three mesh refinements and observe the convergence of the solid, fluid and ALE solvers. We note that the error in the particle velocity prediction appears to converge more slowly than the displacement since the particle velocity is also affected by the displacement predictions.

B.2 Coated cell

Due to the additional complexities introduced in the coated cell model presented in Section 4.4.2 we do not utilise the method of manufactured solutions to validate the ALE FEM solver. Instead, in Figure B.3 we conduct a mesh refinement study, fixing $\alpha_0 = 0.4$, $\alpha_1 = 0.6$, $\tilde{\kappa}_0 = 10^{-5/2}$, $\tilde{\lambda} = 1$ ($\nu = 0.25$), and $\epsilon = 0.09$, and varying the number of elements used in the mesh for several values of γ. When $\gamma = 1$, the

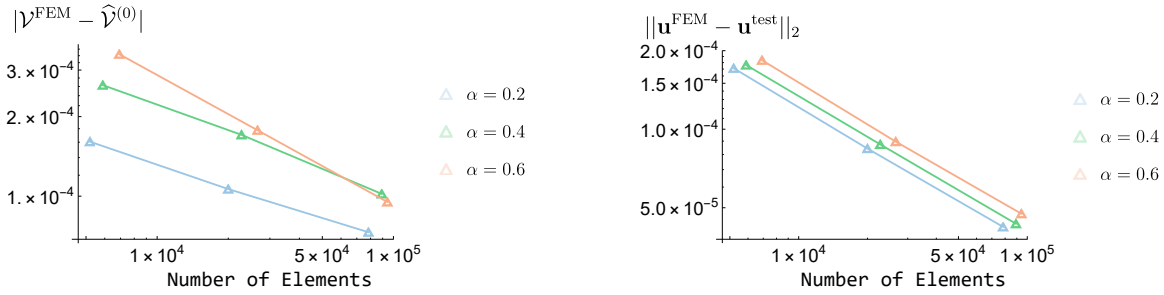

(a) (b)

Figure B.2: Mesh refinement plots testing the solid, fluid and ALE solvers with fixed $\epsilon_t = 0.1$. Within each plot, we halve each element size and calculate the corresponding error. The middle data points correspond to the standard element size used in Figure B.1. (a) Log-log plots of the L^2-norm of the difference between the FEM displacement and the test analytical displacement for varying displacement magnitudes, ϵ_t. The average slope is 0.52. (b) Log-log plots of the norm of the absolute error between the FEM and MoR particle velocities. The average slope is 0.38.

parameter values coincide with those chosen in Figure 4.7. We present log-log plots detailing the convergence of the cell velocity $\mathcal{V}$, cell pressure p_c, and the aspect ratio of the coated cell A_r, defined as the ratio of the maximal (vertical) width and the maximum (horizontal) length of the coated cell, in Figure B.3a, Figure B.3b, and Figure B.3c, respectively. In each plot we assume the 'true' solution is given by an element number of 1.5×10^5. It is clear that as the mesh is refined the result asymptotes, such that the result becomes independent of the mesh. The average slope in each plot is -1.01, -1.25, and -1.00 which are steeper than the convergence rates found in Figure B.2. For a fixed mesh size, the absolute error of the cell velocity decreases with γ (less slip), and the absolute error of the cell pressure and aspect ratio increase with γ (more slip). We expect this is because the cell velocity itself increases with γ, while the coating deformation (and thus its effect on the cell pressure) decrease with γ.

B.2.1 Convergence with large γ

The FEM implementation presented in Section 4.4.2 performs poorly when γ is large and ϵ is finite. We expect this is due to the reformatted interfacial condition (4.89) in which the large γ is multiplied by the small tangential velocity jump to recover an $\mathcal{O}(1)$ traction on the outer coating surface. With a large γ, the solver is not robust to parameter continuation in ϵ as this changes the slip flow over the outer coating surface. We note that multiplying the interfacial condition (4.89) by a factor of $1/\tilde{\gamma}$

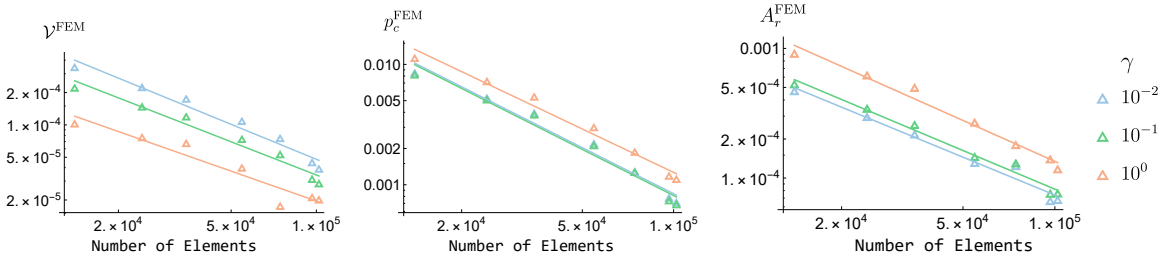

(a) (b) (c)

Figure B.3: Mesh refinement plots testing the FEM solver for the coated cell for several γ with fixed $\alpha_0 = 0.4$, $\alpha_1 = 0.6$, $\tilde{\kappa}_0 = 10^{-5/2}$, $\tilde{\lambda} = 1$ ($\nu = 0.25$), and $\epsilon = 0.09$ to coincide with the parameter values chosen in Figure 4.7c. We present log-log plots of the norm of the absolute error of (a) the cell velocity, (b) the cell pressure and (c) the aspect ratio of the coated cell, varying the number of elements used in the mesh for different γ. In each plot, we assume the 'true' solution is given by an element number of 1.5×10^5. The average slope in each plot is (a) -1.01, (b) -1.25, and (c) -1.00.

did not improve the solver robustness to increments in ϵ when γ is large, since we found that the surface traction was not accurately captured. We were, however, able to obtain solutions using the FEM implementation when γ is large and ϵ finite by using parameter continuation in ϵ when γ was small, and then fixing ϵ and performing parameter continuation in γ. Using this approach, we were able to reliably reach large γ for coatings with large deformations (ϵ).

Appendix C

Asymptotic reduction of a non-linear poroelastic particle in an unbounded flow

C.1 Governing equations

We again work in a frame of reference which translates with the coated cell, though now assume the coating may exhibit large deformations. The dimensional governing equations for the external Stokes flow are

$$\nabla \cdot \boldsymbol{\sigma}_f = \mathbf{0}, \tag{C.1}$$

$$\nabla \cdot \boldsymbol{v} = 0, \tag{C.2}$$

where $\boldsymbol{v}$ is the fluid velocity and $\boldsymbol{\sigma}_f$ is the stress tensor for a Newtonian fluid given by

$$\boldsymbol{\sigma}_f = -p_f \boldsymbol{I} + \mu_f \left[\nabla \boldsymbol{v} + (\nabla \boldsymbol{v})^T\right], \tag{C.3}$$

where p_f is the fluid pressure and μ_f is the fluid viscosity. The superscript T denotes the transpose. The net force $\boldsymbol{F}_{\text{force}}$ and torque $\boldsymbol{T}$ exerted on the particle by the surrounding fluid are given by the integrals

$$\boldsymbol{F}_{\text{force}} = \oiint_S \boldsymbol{\sigma}_f \cdot \boldsymbol{n} \, \mathrm{d}S = \mathbf{0}, \tag{C.4}$$

$$\boldsymbol{T} = \oiint_S \boldsymbol{r} \times (\boldsymbol{\sigma}_f \cdot \boldsymbol{n}) \, \mathrm{d}S = \mathbf{0}, \tag{C.5}$$

where we use the subscript force to distinguish the net force from the deformation gradient tensors presented below.

For the poroelastic coating, we write all non-linear equations using an Eulerian framework, similar to the presentation in MacMinn et al. [125] as this facilitates the

coupling to the external Newtonian fluid. To account for the rotation of the coated cell, we define $\boldsymbol{X}(\boldsymbol{y}, t)$ as the position of a material point in the undeformed configuration, $\boldsymbol{y}(\boldsymbol{x})$ as the position of this point in a frame which rotates with the angular velocity $\boldsymbol{\Omega}$, and $\boldsymbol{x}$ as the current position of this point. We define the deformation gradient tensors,

$$\boldsymbol{F}_0 = \left(\frac{\partial \boldsymbol{X}}{\partial \boldsymbol{y}}\right)^{-1}, \quad \text{and} \quad \boldsymbol{F}_1 = \left(\frac{\partial \boldsymbol{y}}{\partial \boldsymbol{x}}\right)^{-1}, \tag{C.6}$$

such that via the chain rule the deformation gradient tensor

$$\boldsymbol{F} = \left(\frac{\partial \boldsymbol{X}}{\partial \boldsymbol{x}}\right)^{-1} = \boldsymbol{F}_1 \boldsymbol{F}_0. \tag{C.7}$$

To be clear, $\boldsymbol{F}_0(\boldsymbol{y}, t)$ maps from the undeformed configuration to the rigid-body rotating state, then $\boldsymbol{F}_1(\boldsymbol{x})$ captures the steady mapping from the rotating state to the current position. Since we focus on capturing the shape change of the particle we define the particle deformation as

$$\boldsymbol{u}(\boldsymbol{x}) = \boldsymbol{x} - \boldsymbol{y}(\boldsymbol{x}), \tag{C.8}$$

where we have used $\boldsymbol{y}(\boldsymbol{x})$ as the reference state.

Since $\boldsymbol{F}_0$ describes a rigid-body rotation, we have

$$\det \boldsymbol{F}_0 = 1 \quad \text{and} \quad \boldsymbol{F}_0 \boldsymbol{F}_0^T = \boldsymbol{I}. \tag{C.9}$$

Using (C.9), we define the left Cauchy-Green deformation tensor

$$\boldsymbol{B} = \boldsymbol{F}\boldsymbol{F}^{\mathrm{T}} = \boldsymbol{F}_1 \boldsymbol{F}_0 \boldsymbol{F}_0^T \boldsymbol{F}_1^T = \boldsymbol{F}_1 \boldsymbol{F}_1^T, \tag{C.10}$$

and the Jacobian

$$J(\boldsymbol{x}) = \det(\boldsymbol{F}) = \det(\boldsymbol{F}_1) = \frac{1}{\det(\boldsymbol{F}_1^{-1})}, \tag{C.11}$$

which measures the local volume change within the particle. Here, $\boldsymbol{F}_0$ does not appear in (C.10) and (C.11) as no strain or volume change is generated by the rigid-body rotation. The Jacobian is directly related to the porosity via

$$J(\boldsymbol{x}) = \frac{1 - \phi_{f,0}}{1 - \phi_f(\boldsymbol{x})}. \tag{C.12}$$

We assume that the internal flow is governed by Darcy's law,

$$\phi_f(\boldsymbol{v}_p - \boldsymbol{v}_s) = -\frac{\kappa(\phi_f)}{\mu_f} \nabla p_p, \tag{C.13}$$

where $\boldsymbol{v}_p$ and $\boldsymbol{v}_s$ are the internal fluid and solid velocities measured in the translating frame (undeformed configuration) and, assuming finite deformations, the permeability $\kappa = \kappa(\phi_f)$ is non-uniform. In general the permeability will change as the solid skeleton deforms, which is captured through the dependence on porosity. It will be useful to define $\kappa_0 = \kappa(\phi_{f,0})$ as the uniform permeability field associated with the undeformed porosity.

We define the solid velocity implicitly through the velocity gradient tensor

$$\boldsymbol{L}_s = \nabla \boldsymbol{v}_s = \dot{\boldsymbol{F}} \boldsymbol{F}^{-1}. \tag{C.14}$$

Substituting (C.7) into (C.14) we have

$$\boldsymbol{L}_s = (\dot{\boldsymbol{F}}_1 \boldsymbol{F}_0 + \boldsymbol{F}_1 \dot{\boldsymbol{F}}_0) \boldsymbol{F}_0^T \boldsymbol{F}_1^{-1} = \dot{\boldsymbol{F}}_1 \boldsymbol{F}_1^{-1} + \boldsymbol{F}_1 \boldsymbol{W}_0 \boldsymbol{F}_1^{-1} = \boldsymbol{F}_1 \boldsymbol{W}_0 \boldsymbol{F}_1^{-1}, \tag{C.15}$$

where the superscript $\dot{\cdot} = \mathrm{d}/\mathrm{d}t$, $\boldsymbol{W}_0 = \dot{\boldsymbol{F}}_0 \boldsymbol{F}_0^{-1} = \boldsymbol{\Omega} \times \boldsymbol{I}$ is the spin tensor which describes the angular velocity of the rotating state, and $\dot{\boldsymbol{F}}_1 = 0$ due to the steady assumption [140].

Imposing conservation of mass on both the fluid and solid phases within the poroelastic coating we have

$$\nabla \cdot (\phi_f \boldsymbol{v}_p) = 0, \quad \nabla \cdot ((1 - \phi_f) \boldsymbol{v}_s) = 0, \tag{C.16}$$

such that $\nabla \cdot \boldsymbol{v}_p$ and $\nabla \cdot \boldsymbol{v}_s$ are in general non-zero. Adding the equations in (C.16) we define the total internal fluid flux

$$\boldsymbol{q} = \phi_f \boldsymbol{v}_p + (1 - \phi_f) \boldsymbol{v}_s \tag{C.17}$$

which has zero divergence.

To describe how the fluid and solid phases share internal stresses we write the total stress,

$$\boldsymbol{\sigma}_p = \boldsymbol{\sigma}' - p_p \boldsymbol{I}, \tag{C.18}$$

where $\boldsymbol{\sigma}'$ is Terzaghi's effective stress which is the force per unit area carried by the solid skeleton. Details of this stress decomposition may be found in [125]. Imposing mechanical equilibrium within the particle we have

$$\nabla \cdot \boldsymbol{\sigma}_p = \nabla \cdot \boldsymbol{\sigma}' - \nabla p_p = \boldsymbol{0}. \tag{C.19}$$

We adopt a compressible neo-Hookean model for the coating which will reduce to linear elasticity under the assumption of small strain,

$$\boldsymbol{\sigma}' = \lambda (J - 1) \boldsymbol{I} + \frac{\mu_s}{J} \left(\boldsymbol{B} - \boldsymbol{I} \right), \tag{C.20}$$

where λ is Lamé's first parameter, μ_s is the shear modulus, and $\frac{1}{2}(\boldsymbol{B}-\boldsymbol{I})$ is the solid strain. We remind the reader that $\boldsymbol{B}$ is related to the deformation gradient tensor via (C.10).

We model the cell as a sack of viscous fluid enclosed by an impermeable membrane. Since a closed spherical shell may not be bent without being stretched [126], the elastic resistance provided by this membrane is characterised predominantly by its stretching modulus K_c,

$$K_c = \frac{E_c h_c}{1-\nu_c^2}, \tag{C.21}$$

where E_c is the Young's modulus of the membrane, h_c is the membrane thickness, and ν_c is the Poisson's ratio of the membrane. Here, we neglect the elasticity of the membrane and assume the stretching stiffness of the hydrogel coating $K_h \gg K_c$.

Since the cell membrane is assumed to be impermeable (see Chapter 1) and we seek steady solutions, we assume no flow inside the cell. Moreover, we assume the pressure in the cell, denoted by p_c, enforces the volumetric constraint,

$$\iiint_{\Omega_c} \mathrm{d}V = V_c = \frac{4}{3}\pi a_0^3, \tag{C.22}$$

where V_c is the undeformed cell volume. In Chapter 3 it is convenient to use the undeformed cell pressure p_c^0 as the reference pressure in the system. However, in Chapter 4 we instead impose zero pressure at a point far downstream from the coated cell.

C.2 Boundary conditions

Far from the coated cell we expect any disturbance to the external flow caused by the coated cell to be small such that

$$\boldsymbol{v} - \boldsymbol{V}_\infty - \boldsymbol{V}_{tr} \to 0 \quad \text{as} \quad r \to \infty, \tag{C.23}$$

where $\boldsymbol{V}_\infty$ and $\boldsymbol{V}_{tr}$ are the external far-field flow and cell's constant translational velocity in the lab frame, respectively.

We define the deformed surfaces S_i as

$$\boldsymbol{r}_i = a_i \boldsymbol{e}_r + \boldsymbol{u}(\boldsymbol{r}_i), \tag{C.24}$$

On the outer coating surface S_1 we impose the continuity of normal fluid flux, continuity of total stress, continuity of fluid stresses and the Beavers & Joseph slip condition

[56],

$$\boldsymbol{v} \cdot \boldsymbol{n} = \boldsymbol{q} \cdot \boldsymbol{n}, \tag{C.25}$$

$$\boldsymbol{\sigma}_f \cdot \boldsymbol{n} = \boldsymbol{\sigma}_p \cdot \boldsymbol{n}, \tag{C.26}$$

$$\boldsymbol{n} \cdot \boldsymbol{\sigma}_f \cdot \boldsymbol{n} = -p_p, \tag{C.27}$$

$$\boldsymbol{t}^i \cdot \boldsymbol{\sigma}_f \cdot \boldsymbol{n} = \frac{\gamma \mu_f}{\sqrt{\kappa}}((\boldsymbol{v} - \boldsymbol{q}) \cdot \boldsymbol{t}^i), \tag{C.28}$$

where γ is defined as the slip parameter such that $\gamma = 0$ corresponds to a surface with perfect slip and $\gamma \to \infty$ corresponds to a surface with no-slip.

On the cell surface S_0, we impose no normal fluid flux and conservation of total stress,

$$\phi_f \boldsymbol{v}_p \cdot \boldsymbol{n}_0 = 0, \tag{C.29}$$

$$\boldsymbol{\sigma}_p \cdot \boldsymbol{n}_0 = -p_c \boldsymbol{n}_0. \tag{C.30}$$

C.3 Non-dimensionalisation

We non-dimensionalise lengths with the particle radius a_1, velocities with the velocity scale V_0 which is determined by the magnitude of the external far-field flow in (C.23), and the fluid pressure and stress with the viscous pressure scaling $\mu_f V_0/a_1$. Additionally, the permeability is scaled on κ_0. The stress condition (C.26) states that the total stress on the particle must balance with the viscous stress exerted by the external flow at the interface. Hence, the total stress, elastic stress, and pore pressure are also scaled on $\mu_f V_0/a_1$. We define the dimensionless parameter

$$\epsilon = \frac{\mu_f V_0}{\mu_s a_1}, \tag{C.31}$$

which is the ratio of typical viscous stresses in the external flow to the elastic stiffness of the solid skeleton. From the constitutive relation (C.20) we see that ϵ characterises the magnitude of the solid strain. It follows from the strain tensor that the solid displacement is non-dimensionalised on ϵa_1.

Applying the above non-dimensionalisations, the governing equations for the external Stokes flow are given by

$$\nabla \cdot \boldsymbol{\sigma}_f = \boldsymbol{0}, \tag{C.32}$$

$$\nabla \cdot \boldsymbol{v} = 0, \tag{C.33}$$

$$\boldsymbol{\sigma}_f = -p_f \boldsymbol{I} + \nabla \boldsymbol{v} + (\nabla \boldsymbol{v})^T, \tag{C.34}$$

$$\boldsymbol{F}_{\text{force}} = \boldsymbol{T} = \boldsymbol{0}, \tag{C.35}$$

where $\boldsymbol{F}_{\text{force}}$ and $\boldsymbol{T}$ are calculated by non-dimensionalising (C.4) and (C.5).

The non-linear governing equations in the coating are

$$\phi_f(\boldsymbol{v}_p - \boldsymbol{v}_s) = -\tilde{\kappa}_0 \kappa(\phi_f) \nabla p_p, \tag{C.36}$$

where $\boldsymbol{v}_s$ is given through

$$\nabla \boldsymbol{v}_s = \boldsymbol{F}_1 \boldsymbol{W}_0 \boldsymbol{F}_1^{-1} \tag{C.37}$$

and $\tilde{\kappa}_0 = \kappa_0 / a_1^2$ is the Darcy number, which represents the coating permeability in reference to its cross-sectional area,

$$\nabla \cdot (\phi_f \boldsymbol{v}_p) = 0, \quad \nabla \cdot ((1-\phi_f)\boldsymbol{v}_s) = 0, \tag{C.38}$$

$$\nabla \cdot \boldsymbol{\sigma}' - \nabla p_p = \boldsymbol{0}, \tag{C.39}$$

$$\boldsymbol{\sigma}' = \frac{1}{\epsilon} \frac{2\nu}{1-2\nu} (J-1)\boldsymbol{I} + \frac{1}{\epsilon}(\boldsymbol{B} - \boldsymbol{I}), \tag{C.40}$$

where Poisson's ratio, $\nu = \lambda / (2(\lambda + \mu_s))$, measures the magnitude of transverse strain induced in the coating when deformed and

$$\boldsymbol{F}_1 = (\boldsymbol{I} - \epsilon \nabla \boldsymbol{u})^{-1}. \tag{C.41}$$

The cell pressure p_c is used to enforce the constraint,

$$\iiint_{\Omega_c} \mathrm{d}V = V_c = \frac{4}{3}\pi \alpha_0^3, \tag{C.42}$$

where $\alpha_0 = a_0 / a_1$ is the dimensionless cell radius.

The far-field condition for the external Stokes flow is,

$$\boldsymbol{v} - \boldsymbol{V}_\infty - \boldsymbol{V}_{tr} \to 0 \quad \text{as} \quad r \to \infty. \tag{C.43}$$

The deformed surfaces S_i are implicitly determined by the equations

$$\boldsymbol{r}_1 = \boldsymbol{e}_r + \epsilon \boldsymbol{u}(\boldsymbol{r}_1), \tag{C.44}$$

$$\boldsymbol{r}_0 = \alpha_0 \boldsymbol{e}_r + \epsilon \boldsymbol{u}(\boldsymbol{r}_0). \tag{C.45}$$

We then have the dimensionless interfacial conditions on S_1

$$\boldsymbol{v} \cdot \boldsymbol{n} = \boldsymbol{q} \cdot \boldsymbol{n}, \tag{C.46}$$

$$\boldsymbol{\sigma}_f \cdot \boldsymbol{n} = \boldsymbol{\sigma}_p \cdot \boldsymbol{n}, \tag{C.47}$$

$$\boldsymbol{n} \cdot \boldsymbol{\sigma}_f \cdot \boldsymbol{n} = -p_p, \tag{C.48}$$

$$\boldsymbol{t}^i \cdot \boldsymbol{\sigma}_f \cdot \boldsymbol{n} = \frac{\tilde{\gamma}}{\sqrt{\kappa(\phi_f)}} (\boldsymbol{v} - \phi_f \boldsymbol{v}_p) \cdot \boldsymbol{t}^i, \tag{C.49}$$

where $\tilde{\gamma} = \gamma/\sqrt{\tilde{\kappa}_0}$. On S_0 we have

$$\phi_f \boldsymbol{v}_p \cdot \boldsymbol{n}_0 = 0, \tag{C.50}$$

$$\boldsymbol{\sigma}_p \cdot \boldsymbol{n}_0 = -p_c \boldsymbol{n}_0. \tag{C.51}$$

C.4 Asymptotic reduction

Similar to Section 2.3, we now assume $\epsilon \ll 1$, such that the particle strain and deformation are small, and expand the variables, $\boldsymbol{v}$, p_f, $\boldsymbol{\sigma}_f$, $\boldsymbol{F}_{\text{force}}$, $\boldsymbol{T}$, ϕ_f, $\boldsymbol{v}_p$, $\boldsymbol{v}_s$, κ, p_p, $\boldsymbol{u}, \boldsymbol{\sigma}'$, and p_c in powers of ϵ, e.g.

$$\boldsymbol{v} = \boldsymbol{v}^{(0)} + \epsilon \boldsymbol{v}^{(1)} + \cdots, \tag{C.52}$$

where the superscript (i) denotes the associated power of ϵ. We similarly expand the position of the deformed surfaces, $\boldsymbol{r}_i$, the force and torque, $\boldsymbol{F}$ and $\boldsymbol{T}$, and the coated cells translational and rotational velocities, $\boldsymbol{V}_{tr}$ and $\boldsymbol{\Omega}$. We proceed by assuming $\phi_{f,0}, \tilde{\kappa}_0, \tilde{\gamma}$ and ν remain fixed as $\epsilon \to 0$.

The leading-order incompressible Stokes equations are simply

$$\nabla p_p^{(0)} = \nabla^2 \boldsymbol{v}^{(0)}, \tag{C.53}$$

$$\nabla \cdot \boldsymbol{v}^{(0)} = 0. \tag{C.54}$$

In the limit of small ϵ we have the expansions

$$\boldsymbol{F}_1 = \boldsymbol{I} + \epsilon \nabla \boldsymbol{u} + \mathcal{O}\left(\epsilon^2\right), \tag{C.55}$$

$$\det(\boldsymbol{F}_1) = 1 + \epsilon \nabla \cdot \boldsymbol{u} + \mathcal{O}\left(\epsilon^2\right), \tag{C.56}$$

within the coating. The porosity is given by expanding (C.11) and (C.12) and using (C.56) to write

$$\phi_f = \phi_{f,0} + \epsilon(1 - \phi_{f,0}) \nabla \cdot \boldsymbol{u}^{(0)} + \cdot\,. \tag{C.57}$$

Expanding (C.36), the leading-order flow in the coating is governed by Darcy's law (C.36) with the constant porosity, $\phi_f^{(0)} = \phi_{f,0}$ and associated permeability $\tilde{\kappa}_0$,

$$\phi_{f,0}(\boldsymbol{v}_f^{(0)} - \boldsymbol{v}_s^{(0)}) = -\tilde{\kappa}_0 \nabla p_p^{(0)}. \tag{C.58}$$

We also expand the local continuity conditions (C.38) to give

$$\nabla \cdot \boldsymbol{v}_p^{(0)} = 0. \quad \nabla \cdot \boldsymbol{v}_s^{(0)} = 0. \tag{C.59}$$

Substituting (C.55) into (C.37) the velocity gradient tensor is constant to leading order, $\boldsymbol{L}_s^{(0)} = \boldsymbol{W}_0^{(0)}$, such that the solid velocity is the rigid-body rotation

$$\boldsymbol{v}_s^{(0)} = \boldsymbol{W}_0^{(0)}\boldsymbol{x} = r[\boldsymbol{\Omega} \times \boldsymbol{e}_r], \tag{C.60}$$

where $\boldsymbol{\Omega}$ remains to be determined. We note that in (C.60), $\boldsymbol{v}_s$ is identical to $\boldsymbol{v}_\Omega$ as given in (3.1).

The leading-order mechanical equilibrium equation for the solid skeleton is given by expanding (C.39),

$$\nabla \cdot \boldsymbol{\sigma}_p^{(0)} = \nabla \cdot \boldsymbol{\sigma}'^{(0)} - \nabla p_p^{(0)} = \boldsymbol{0}, \tag{C.61}$$

where expanding (C.40) and using (C.55) we reduce to a linearly elastic stress-strain relationship to leading order,

$$\boldsymbol{\sigma}'^{(0)} = \frac{2\nu}{1-2\nu}(\nabla \cdot \boldsymbol{u}^{(0)})\boldsymbol{I} + 2\boldsymbol{\varepsilon}, \tag{C.62}$$

where $\boldsymbol{\varepsilon} = \frac{1}{2}\left(\nabla \boldsymbol{u}^{(0)} + \left(\nabla \boldsymbol{u}^{(0)}\right)^T\right)$ is the linear elastic strain.

The leading-order far-field condition for the external Stokes flow is,

$$\boldsymbol{v} - \boldsymbol{V}_\infty - \boldsymbol{V}_{tr} \to 0 \quad \text{as} \quad r \to \infty. \tag{C.63}$$

Expanding the kinematic condition (C.44) we find

$$\boldsymbol{r}_1 = \boldsymbol{e}_r + \epsilon \boldsymbol{u}^{(0)}(r = 1), \tag{C.64}$$

$$\boldsymbol{r}_0 = \alpha_0 \boldsymbol{e}_r + \epsilon \boldsymbol{u}^{(0)}(r = \alpha_0), \tag{C.65}$$

such that $\boldsymbol{r}_i^{(0)} = \boldsymbol{e}_r$, implying interfacial conditions are applied on the undeformed particle surface with $\boldsymbol{n}_i = \boldsymbol{e}_r$, $\boldsymbol{t}_i^1 = \boldsymbol{e}_\theta$, and $\boldsymbol{t}_i^2 = \boldsymbol{e}_\phi$. Expanding the boundary conditions (C.46)–(C.49) to leading order, and noting that $\boldsymbol{v}_s$ in (C.60) has no radial component, we have on $r = 1$

$$\boldsymbol{v} \cdot \boldsymbol{e}_r = \phi_{f,0} \boldsymbol{v}_p \cdot \boldsymbol{e}_r, \tag{C.66}$$

$$\boldsymbol{\sigma}_f \cdot \boldsymbol{e}_r = \boldsymbol{\sigma}_p \cdot \boldsymbol{e}_r, \tag{C.67}$$

$$\boldsymbol{e}_r \cdot \boldsymbol{\sigma}_f \cdot \boldsymbol{e}_r = -p_p, \tag{C.68}$$

$$\boldsymbol{e}_\theta \cdot \boldsymbol{\sigma}_f \cdot \boldsymbol{e}_r = \frac{\gamma}{\sqrt{\tilde{\kappa}_0}}((\boldsymbol{v} - \boldsymbol{q}) \cdot \boldsymbol{e}_\theta), \tag{C.69}$$

$$\boldsymbol{e}_\phi \cdot \boldsymbol{\sigma}_f \cdot \boldsymbol{e}_r = \frac{\gamma}{\sqrt{\tilde{\kappa}_0}}((\boldsymbol{v} - \boldsymbol{q}) \cdot \boldsymbol{e}_\phi). \tag{C.70}$$

Similarly, expanding (C.50) and (C.51) we have on $r = \alpha_0$

$$\boldsymbol{v}_p \cdot \boldsymbol{e}_r = 0, \tag{C.71}$$

$$\boldsymbol{\sigma}_p \cdot \boldsymbol{e}_r = -p_c \boldsymbol{e}_r. \tag{C.72}$$

Expanding the force and torque balances (C.4) and (C.5) to leading order then gives

$$\boldsymbol{F}^{(0)}_{\text{force}} = \int_{\phi=0}^{2\pi}\int_{\theta=0}^{\pi} \boldsymbol{\sigma}_f^{(0)}|_{r=1}\cdot\boldsymbol{e}_r \ \sin\theta \ \mathrm{d}\theta \ \mathrm{d}\phi = \boldsymbol{0}, \tag{C.73}$$

$$\boldsymbol{T}^{(0)} = \int_{\phi=0}^{2\pi}\int_{\theta=0}^{\pi} \boldsymbol{r}\times(\boldsymbol{\sigma}_f^{(0)}|_{r=1}\cdot\boldsymbol{e}_r) \ \sin\theta \ \mathrm{d}\theta \ \mathrm{d}\phi = \boldsymbol{0}. \tag{C.74}$$

Dropping the superscripts, (C.53), (C.54), (C.57) to (C.70), (C.73) and (C.74) which form the leading-order problem to calculate the fluid flow and resulting deformation are equivalently presented in the main text as (3.3) to (3.18), (3.23) and (3.27) to (3.31). We note that this system of equations could equivalently be derived from a linearly poroelastic description.

C.5 The reduction to an impermeable, incompressible particle subject to no-slip boundary conditions

Through the interfacial conditions (3.28) and (3.29) we have

$$\sigma_{f,rr} = -p_p, \tag{C.75}$$

$$\sigma_{f,rr} = -p_p + \frac{2\nu}{1-2\nu}\nabla\cdot\boldsymbol{u} + 2\frac{\partial u_r}{\partial r}, \tag{C.76}$$

which combined also require (3.32),

$$2\frac{\partial u_r}{\partial r} = -\frac{2\nu}{1-2\nu}\nabla\cdot\boldsymbol{u}, \tag{C.77}$$

on $r=1$.

We now consider the limiting case of $\nu\to 1/2$. Defining the small parameter $\delta=(1-2\nu)\ll 1$, it may be shown that as $\delta\to 0$

$$\nabla\cdot\boldsymbol{u} = \mathcal{O}(\delta)+\cdots. \tag{C.78}$$

We then write the Darcy pressure as

$$p_p = p_{\text{elas}} + \frac{2\nu}{1-2\nu}\nabla\cdot\boldsymbol{u}, \tag{C.79}$$

where p_{elas} is the solid elastic pressure for the case of an impermeable, incompressible particle subject to no-slip boundary conditions, as obtained by Murata [3]. Since the particle is incompressible, p_{elas} acts as a Lagrange multiplier to enforce (C.78) when

$\delta \to 0$. Using the pressure decomposition (C.79), along with (C.77), both interfacial conditions (C.75) and (C.76) become

$$\sigma_{f,rr} = -p_{\text{elas}} + 2\frac{\partial u_r}{\partial r}, \tag{C.80}$$

such that we recover the expected stress balance between the Stokes flow and elastic particle. Using (C.79), it may be shown that our predictions for the solid elastic pressure are in perfect agreement with those presented by Murata [3].

Appendix D

Reformulation of the boundary/interfacial conditions

To exploit the orthogonality of the solid spherical harmonics we reformulate the boundary conditions for both the fluid and solid problems in terms of r-components and r-derivatives. This approach is similar to that developed by Happel and Brenner [107], and later extended by Murata [3] to consider an elastic in a general Stokes flow. We first formally define the solid spherical harmonics in Appendix D.1, before presenting the boundary conditions reformulations for the fluid and solid problems in Appendices D.3 and D.4, respectively.

D.1 Solid spherical harmonics

We assume the function $h(\boldsymbol{r})$ satisfies Laplace's equation such that

$$\nabla^2 h = 0. \tag{D.1}$$

Using a spherical coordinate system we have separable solutions,

$$h(\boldsymbol{r}) = \sum_{n=0}^{\infty} \sum_{m=-n}^{n} h^{\mathcal{R}}_{n,m} \mathcal{R}_{n,m}(\boldsymbol{r}) + h^{\mathcal{I}}_{n,m} \mathcal{I}_{n,m}(\boldsymbol{r}), \tag{D.2}$$

where $h^{\mathcal{R}}_{n,m}$ and $h^{\mathcal{I}}_{n,m}$ are constants, and $\mathcal{R}_{n,m}(\boldsymbol{r})$ and $\mathcal{I}_{n,m}(\boldsymbol{r})$ are the regular and irregular solid spherical harmonics, given by

$$\mathcal{R}_{n,m}(\boldsymbol{r}) = \sqrt{\frac{4\pi}{2n+1}} r^n Y_{n,m}(\theta,\phi), \quad \text{and} \quad \mathcal{I}_{n,m}(\boldsymbol{r}) = \sqrt{\frac{4\pi}{2n+1}} \frac{Y_{n,m}(\theta,\phi)}{r^{n+1}}. \tag{D.3}$$

Here, $Y_{n,m}(\theta,\phi)$ are Laplace's spherical harmonics. Restricting to the purely real case,

$$Y_{n,m}(\theta,\phi) = \begin{cases} (-1)^m \sqrt{\frac{(2n+1)}{2\pi}\frac{(n-|m|)!}{(n+|m|)!}}\mathcal{P}_{n,|m|}(\cos\theta)\sin|m|\phi, & m<0 \\ \sqrt{\frac{(2n+1)}{4\pi}}P_{n,m}(\cos\theta), & m=0 \\ (-1)^m \sqrt{\frac{(2n+1)}{2\pi}\frac{(n-m)!}{(n+m)!}}\mathcal{P}_{n,m}(\cos\theta)\sin m\phi, & m>0, \end{cases} \tag{D.4}$$

where $\mathcal{P}_{n,m}(\cos\theta)$ are the associated Legendre polynomials of degree n and order m. Written in this form we have the orthogonality relations,

$$\int_{\phi=0}^{2\pi}\int_{\theta=0}^{\pi} Y_{n,m}(\theta,\phi)Y_{p,q}(\theta,\phi)\sin\theta \,\mathrm{d}\theta\,\mathrm{d}\phi = \delta_{np}\delta_{mq}. \tag{D.5}$$

Throughout much of the above work, for example in Section 3.3.1, it is convenient to only consider the solid spherical harmonic functions of degree n. For clarity we write

$$h_n(\boldsymbol{r}) = \sum_{m=-n}^{n} h^{\mathcal{R}}_{n,m}\mathcal{R}_{n,m}(\boldsymbol{r}), \quad h_{-n-1}(\boldsymbol{r}) = \sum_{m=-n}^{n} h^{\mathcal{I}}_{n,m}\mathcal{I}_{n,m}(\boldsymbol{r}), \tag{D.6}$$

where again $h^{\mathcal{R}}_{n,m}$ and $h^{\mathcal{I}}_{n,m}$ are constant coefficients. Note

$$h(\boldsymbol{r}) = \sum_{n=-\infty}^{\infty} h_n(\boldsymbol{r}), \tag{D.7}$$

from (D.2).

D.2 Useful identities

We now present several identities involving the solid spherical harmonics which will be useful when reformulating the boundary conditions in Appendices D.3 and D.4. Assuming h_n is a solid spherical harmonic function of degree n,

$$x\frac{\partial h_n}{\partial x} + y\frac{\partial h_n}{\partial y} + z\frac{\partial h_n}{\partial z} = r\frac{\partial h_n}{\partial r} = nh_n, \tag{D.8}$$

$$\nabla^2(r^l h_n) = l(l+2n+1)r^{l-2}h_n. \tag{D.9}$$

We also quote the vector calculus identity with $\boldsymbol{A}$ an arbitrary vector,

$$\nabla\times(\nabla\times\boldsymbol{A}) = \nabla(\nabla\cdot\boldsymbol{A}) - \nabla^2\boldsymbol{A}. \tag{D.10}$$

D.3 Reformulation of the fluid problem boundary conditions

We use the interfacial conditions (3.28), (3.30), (3.31) and (3.33) to calculate the coefficients in the solid spherical harmonic functions $\Phi_{-n-1}, \Psi_{-n-1}, P_{-n-1}, p_n$, and p_{-n-1}. The normal flux condition (3.28), continuity of fluid stress (3.30), and no penetration (3.33) conditions are already in the desired form, since $\boldsymbol{v}_s$ has no radial component,

$$v_r|_{r=1} = \phi_{f,0} v_{p,r}|_{r=1} = -\tilde{\kappa}_0 \frac{\partial p_p}{\partial r}|_{r=1}, \tag{D.11}$$

$$\sigma_{f,rr}|_{r=1} = -p_p|_{r=1}, \tag{D.12}$$

$$v_{p,r}|_{r=\alpha_0} = -\tilde{\kappa}_0 \frac{\partial p_p}{\partial r}|_{r=\alpha_0} = 0. \tag{D.13}$$

Separating (3.31) into the θ and ϕ components, the Beavers & Joseph conditions are

$$\boldsymbol{e}_\theta \cdot \boldsymbol{\sigma}_f \cdot \boldsymbol{e}_r = \tilde{\gamma}(\boldsymbol{v} + \tilde{\kappa}_0 \nabla p_p - \boldsymbol{v}_s) \cdot \boldsymbol{e}_\theta, \tag{D.14}$$

$$\boldsymbol{e}_\phi \cdot \boldsymbol{\sigma}_f \cdot \boldsymbol{e}_r = \tilde{\gamma}(\boldsymbol{v} + \tilde{\kappa}_0 \nabla p_p - \boldsymbol{v}_s) \cdot \boldsymbol{e}_\phi, \tag{D.15}$$

applied on the undeformed particle surface ($r = 1$). We reformulate these interfacial conditions using the divergence and curl operators. Beginning with divergence, we write

$$\begin{aligned} &r\nabla \cdot (\boldsymbol{\sigma}_f \cdot \boldsymbol{e}_r(r=1)) - 2\sigma_{f,rr}|_{r=1} \\ &\qquad = \tilde{\gamma}\left(r\nabla \cdot (\boldsymbol{v}(r=1)) - 2v_r|_{r=1} + \tilde{\kappa}_0 \nabla^2 (p_p(r=1)) - 2\tilde{\kappa}_0 \frac{\partial p_p}{\partial r}|_{r=1} \right), \end{aligned} \tag{D.16}$$

and use the following relations,

$$r\nabla \cdot (\boldsymbol{v}(r=1)) = [r\nabla \cdot \boldsymbol{v}]_{r=1} - \left[r\frac{\partial v_r}{\partial r} \right]_{r=1}, \tag{D.17}$$

$$r\nabla \cdot (\boldsymbol{\sigma}_f \cdot \boldsymbol{e}_r(r=1)) = [r\nabla \cdot \boldsymbol{\sigma}_f]_{r=1} - [3P]_{r=1} - [\sigma_{f,rr}]_{r=1} - \left[r\frac{\partial \sigma_{f,rr}}{\partial r} \right]_{r=1}, \tag{D.18}$$

$$r\nabla^2 p_p(r=1) = \left[r\nabla^2 p_p \right]_{r=1} - \left[r\frac{\partial^2 p_p}{\partial r^2} \right]_{r=1}, \tag{D.19}$$

to write, noting that the divergence of $\boldsymbol{v}$, $\boldsymbol{\sigma}_f$ and $\boldsymbol{v_s}$ all equal zero,

$$\left[r\frac{\partial \sigma_{f,rr}}{\partial r} + 3(p_f + \sigma_{f,rr}) \right]_{r=1} = \tilde{\gamma}\left[r\frac{\partial v_r}{\partial r} + 2v_r + \tilde{\kappa}_0 \left(r\frac{\partial^2 p_p}{\partial r^2} + 2\frac{\partial p_p}{\partial r} \right) \right]_{r=1}. \tag{D.20}$$

To be clear, in the left-hand side of each of the relations (D.17)–(D.19) we evaluate the expression on $r = 1$ before applying any derivatives. On the right-hand side we perform any derivatives before evaluating on $r = 1$.

We then write the curl relation as

$$[\boldsymbol{r} \cdot \nabla \times (\boldsymbol{\sigma}_f \cdot \boldsymbol{e}_r)]_{r=1} = \tilde{\gamma} \, [\boldsymbol{r} \cdot \nabla \times \boldsymbol{v} - \boldsymbol{r} \cdot \nabla \times \boldsymbol{v}_s]_{r=1} \,, \tag{D.21}$$

since there are no r-derivatives present and the curl of ∇p_p is trivially zero.

The reformulated interfacial conditions (D.11) to (D.13), (D.20) and (D.21) allow us to apply the solid spherical harmonic identities in Appendix D.2 to solve the fluid problem separately for each degree n. For example, applying (D.8) to the general solution for the Stokes velocity and Darcy pressure, (3.39) and (3.43), we find the expressions

$$v_r = \sum_{n=1}^{\infty} \left[\frac{n}{r} \Phi_n^* + \frac{n}{2(2n+3)} r P_n^* \right] + \sum_{n=1}^{\infty} \left[-\frac{n+1}{r} \Phi_{-n-1} + \frac{n+1}{2(2n-1)} r P_{-n-1} \right], \tag{D.22}$$

$$r \frac{\partial v_r}{\partial r} = \sum_{n=1}^{\infty} \left[\frac{n(n-1)}{r} \Phi_n^* + \frac{n(n+1)}{2(2n+3)} r P_n^* \right] + \sum_{n=1}^{\infty} \left[\frac{(n+1)(n+2)}{r} \Phi_{-n-1} - \frac{n(n+1)}{2(2n-1)} r P_{-n-1} \right], \tag{D.23}$$

$$\frac{\partial p_p}{\partial r} = \sum_{n=1}^{\infty} \frac{n}{r} p_n - \frac{n+1}{r} p_{-n-1}. \tag{D.24}$$

$$r \frac{\partial^2 p_p}{\partial r^2} = \sum_{n=1}^{\infty} \frac{n(n-1)}{r} p_n + \frac{(n+1)(n+2)}{r} p_{-n-1}. \tag{D.25}$$

Using the constitutive relation (3.5) we then obtain

$$\sigma_{f,rr} = \sum_{n=1}^{\infty} \left[\frac{2n(n-1)}{r^2} \Phi_n^* + \frac{n^2 - n - 3}{2n+3} P_n^* \right] + \sum_{n=1}^{\infty} \left[\frac{2(n+1)(n+2)}{r^2} \Phi_{-n-1} - \frac{n^2 + 3n - 1}{2n-1} P_{-n-1} \right], \tag{D.26}$$

$$r \frac{\partial \sigma_{f,rr}}{\partial r} = \sum_{n=1}^{\infty} \left[\frac{2n(n-1)(n-2)}{r^2} \Phi_n^* + \frac{(n^2 - n - 3)n}{2n+3} P_n^* \right] + \sum_{n=1}^{\infty} \left[-\frac{2(n+1)(n+2)(n+3)}{r^2} \Phi_{-n-1} + \frac{(n^2 + 3n - 1)(n+1)}{2n-1} P_{-n-1} \right], \tag{D.27}$$

It may also be shown using (D.8) and (D.10) that

$$\boldsymbol{r}\cdot\nabla\times\boldsymbol{v}=\sum_{n=1}^{\infty}n(n+1)\Psi_n^*+\sum_{n=1}^{\infty}n(n+1)\Psi_{-n-1}, \tag{D.28}$$

$$\boldsymbol{r}\cdot\nabla\times(\boldsymbol{\sigma}_f\cdot\boldsymbol{e}_r)=\sum_{n=1}^{\infty}\frac{n(n+1)(n-1)}{r}\Psi_n^*-\sum_{n=1}^{\infty}\frac{n(n+1)(n+2)}{r}\Psi_{-n-1}, \tag{D.29}$$

$$\boldsymbol{r}\cdot\nabla\times\boldsymbol{v}_s=2r(\Omega_x\sin\theta\cos\phi+\Omega_y\sin\theta\sin\phi+\Omega_z\cos\theta). \tag{D.30}$$

Substituting the explicit representations (D.22)–(D.30) into the reformulated boundary conditions (D.11) to (D.13), (D.20) and (D.21) and grouping terms together we obtain the system of equations

$$n\Phi_n^*+\frac{n}{2(2n+3)}P_n^*-(n+1)\Phi_{-n-1}+\frac{n+1}{2(2n-1)}P_{-n-1} \\ =-\tilde{\kappa}_0(np_n-(n+1)p_{-n-1}), \tag{D.31}$$

$$2n(n-1)\Phi_n^*+\frac{n^2-n-3}{2n+3}P_n^*+2(n+1)(n+2)\Phi_{-n-1}+\frac{n^2+3n-1}{2n-1}P_{-n-1} \\ =-(p_n+p_{-n-1}), \tag{D.32}$$

$$\left[2n(n-1)(n-2)-n(n+1)\tilde{\gamma}\right]\Phi_n^*+\left[\frac{n(n^2-n+3)+9}{2n+3}-\frac{n(n+3)\tilde{\gamma}}{2(2n+3)}\right]P_n^* \\ -\left[(n+1)\left(2(n+2)(n+3)+n^2\tilde{\gamma}\right)\right]\Phi_{-n-1}+\left[4+\frac{n^2(n+4)}{2n-1}-\frac{(n-2)(n+1)\tilde{\gamma}}{2(2n-1)}\right]P_{-n-1} \\ =(n(n+1)+3)(p_n+p_{-n-1}), \tag{D.33}$$

$$(n-1)n(n+1)\Psi_n^*-n(n+1)(n+2)\Psi_{-n-1}=n(n+1)\tilde{\gamma}(\Psi_n^*+\Psi_{-n-1}) \\ -2(\Omega_z\cos\theta+\Omega_x\cos\phi\sin\theta+\Omega_y\sin\theta\sin\phi), \tag{D.34}$$

$$\tilde{\kappa}_0\left(\alpha_0^n n\frac{p_n}{r^n}-\frac{p_{-n-1}}{r^{-n-1}}\alpha_0^{-n-1}(n+1)\right)=0, \tag{D.35}$$

where in (D.31) we have $r=1$ and in (D.35) we have $r=\alpha_0$. By prescribing Φ_n^*,Φ_n^* and P_n^* through the far-field condition (3.27), we may exploit the linearity of the solid spherical harmonics to solve the system of equations (D.31)–(D.35) simultaneously for each degree n. This results in the solutions (3.49)–(3.53) and gives the unknown spherical harmonic functions, $\Phi_{-n-1},\Psi_{-n-1},P_{-n-1},p_n$, and p_{-n-1} which determine the exterior and interior flow profiles through the general solutions (3.39), (3.40) and (3.43).

D.4 Reformulation of the solid problem boundary conditions

We now reformulate the boundary conditions for the solid problem,

$$\sigma'_{rr}|_{r=1}= 0, \quad \sigma'_{r\theta}|_{r=1}= \sigma_{f,r\theta}|_{r=1}, \quad \sigma'_{r\phi}|_{r=1}= \sigma_{f,r\phi}|_{r=1}, \tag{D.36}$$

$$-p_p|_{r=\alpha_0}+\sigma'_{rr}|_{r=\alpha_0}= -p_c, \quad \sigma'_{r\theta}|_{r=\alpha_0}= 0, \quad \sigma'_{r\phi}|_{r=\alpha_0}= 0. \tag{D.37}$$

The first boundary condition in (D.36) and (D.37) (radial components) are already suitable and so we reformulate only the θ and ϕ components. The analysis is similar to that carried out in the previous section, though since the solid skeleton is compressible we have $\nabla \cdot \boldsymbol{u} \neq 0$. We begin by writing,

$$r\nabla \cdot (\boldsymbol{\sigma}' \cdot \boldsymbol{e}_r(r = \alpha_i)) - 2\sigma'_{rr}|_{r=\alpha_i}= r\nabla \cdot (\boldsymbol{\sigma}_f \cdot \boldsymbol{e}_r(r = \alpha_i)) - 2\sigma_{f,rr}|_{r=\alpha_i}, \tag{D.38}$$

where we may again use (D.18) to reformulate the right-hand side to the desired form. For the left-hand side we have,

$$\begin{aligned} r\nabla \cdot (\boldsymbol{\sigma}' \cdot \boldsymbol{e}_r(r = \alpha_i)) &= r\left[\nabla \cdot (\boldsymbol{\sigma}' \cdot \boldsymbol{e}_r)\right]_{r=\alpha_i} - \left[r\frac{\partial \sigma'_{rr}}{\partial r}\right]_{r=\alpha_i} \\ &= \left[\nabla \cdot (\boldsymbol{\sigma}' \cdot \boldsymbol{r})\right]_{r=\alpha_i} - \left[r\frac{\partial \sigma'_{rr}}{\partial r}\right]_{r=\alpha_i} \\ &= \left[\boldsymbol{r} \cdot \nabla \cdot \boldsymbol{\sigma}' + \mathrm{tr}(\boldsymbol{\sigma}') - r\frac{\partial \sigma'_{rr}}{\partial r} - \sigma'_{rr}\right]_{r=\alpha_i} \\ &= \left[r\frac{\partial p_p}{\partial r} + (3\lambda + 2\mu_s)(\nabla \cdot \boldsymbol{u}) - r\frac{\partial \sigma'_{rr}}{\partial r} - \sigma'_{rr}\right]_{r=\alpha_i}. \end{aligned} \tag{D.39}$$

Substituting (D.18) and (D.39) into (D.38), and using $\sigma'_{rr} = 0$ and $\sigma_{f,rr} = -p_p$ on $r = \alpha_1 = 1$ we obtain (3.66). By using $\sigma'_{rr} = p_p - p_c$ on $r = \alpha_0$, we similarly obtain (3.69). We may then write the relevant terms for these reformulated boundary conditions explicitly using the Papkovich-Neuber representation (3.58),

$$\begin{aligned} \sigma'_{rr} = \sum_{n=0}^{\infty} \Bigg[&\frac{1}{2r^2}(3 - 4\nu - n)n[\boldsymbol{r} \cdot \boldsymbol{\psi}_c]_n - \frac{1}{2r^2}(4(1 - \nu) + n)(n + 1)[\boldsymbol{r} \cdot \boldsymbol{\psi}_c]_{-n-1} \\ &+ \nu[\nabla_C \cdot \boldsymbol{\psi}_c]_n + \nu[\nabla_C \cdot \boldsymbol{\psi}_c]_{-n-1} + \frac{1}{2r^2}(3 - 4\nu - (n + 2))(n + 2)[\boldsymbol{r} \cdot \boldsymbol{\psi}_p]_n \\ &- \frac{1}{2r^2}(2 - 4\nu + n)(n - 1)[\boldsymbol{r} \cdot \boldsymbol{\psi}_p]_{-n-1} + \nu[\nabla_C \cdot \boldsymbol{\psi}_p]_n + \nu[\nabla_C \cdot \boldsymbol{\psi}_p]_{-n-1} \\ &- \frac{1}{r^2}(n + 1)(n + 2)\phi_n - \frac{1}{r^2}(n)(n - 1)\phi_{-n-1}\Bigg], \end{aligned} \tag{D.40}$$

$$(3\lambda+2\mu_s)\nabla_C\cdot\boldsymbol{u}=(1+\nu)\nabla_C\cdot\boldsymbol{\psi}$$
$$=(1+\nu)\sum_{n=0}^{\infty}[\nabla_C\cdot\boldsymbol{\psi}_c]_n+[\nabla_C\cdot\boldsymbol{\psi}_c]_{-n-1}+[\nabla_C\cdot\boldsymbol{\psi}_p]_n+[\nabla_C\cdot\boldsymbol{\psi}_p]_{-n-1}, \quad \text{(D.41)}$$

$$\frac{\partial\sigma'_{rr}}{\partial r}=\sum_{n=0}^{\infty}\Bigg[\frac{1}{2r^2}(3-4\nu-n)n(n-1)[\boldsymbol{r}\cdot\boldsymbol{\psi}_c]_n+\frac{1}{2r^2}(4(1-\nu)+n)(n+1)(n+2)[\boldsymbol{r}\cdot\boldsymbol{\psi}_c]_{-n-1}$$
$$+\nu(n-1)[\nabla_C\cdot\boldsymbol{\psi}_c]_n-\nu(n+2)[\nabla_C\cdot\boldsymbol{\psi}_c]_{-n-1}+\frac{1}{2r^2}(3-4\nu-(n+2))(n+2)(n+1)[\boldsymbol{r}\cdot\boldsymbol{\psi}_p]_n$$
$$+\frac{1}{2r^2}(2-4\nu+n)(n-1)n[\boldsymbol{r}\cdot\boldsymbol{\psi}_p]_{-n-1}+\nu(n+1)([\nabla_C\cdot\boldsymbol{\psi}_p]_n-\nu n([\nabla_C\cdot\boldsymbol{\psi}_p]_{-n-1}$$
$$-\frac{1}{r^2}(n+1)(n+2)n\phi_n+-\frac{1}{r^2}n(n-1)(n+1)\phi_n\Bigg], \quad \text{(D.42)}$$

where using (3.62) and (3.63) we have

$$[\boldsymbol{r}\cdot\boldsymbol{\psi}_p]_n=\frac{r^2}{1-\nu}\sum_{n=0}^{\infty}\frac{np_n}{2(2n+3)}, \quad [\boldsymbol{r}\cdot\boldsymbol{\psi}_p]_{-n-1}=\frac{r^2}{1-\nu}\sum_{n=0}^{\infty}\frac{(n+1)p_{-n-1}}{2(2n-1)} \quad \text{(D.43)}$$

$$[\nabla_C\cdot\boldsymbol{\psi}_p]_{-n-1}=\frac{1}{1-\nu}\sum_{n=0}^{\infty}\frac{np_n}{2n+3}, \quad [\nabla_C\cdot\boldsymbol{\psi}_p]_{-n-1}=\frac{1}{1-\nu}\sum_{n=0}^{\infty}\frac{(n+1)p_{-n-1}}{(2n-1)}. \quad \text{(D.44)}$$

For the curl reformulation we have the two boundary conditions (3.67) and (3.70), applied on $r=\alpha_1=1$ and $r=\alpha_0$, respectively. For the right-hand side of (3.67) we previously derived (D.29). The remaining terms required may be written using the Papkovich-Neuber representation (3.58) as,

$$\boldsymbol{r}\cdot\nabla\times(\boldsymbol{\sigma}'\cdot\boldsymbol{e}_r)=\sum_{n=0}^{\infty}\frac{1}{r}(1-\nu)\big[(n-1)(y\frac{\partial\psi_n^x}{\partial z}-z\frac{\partial\psi_n^x}{\partial y}+z\frac{\partial\psi_n^y}{\partial x}-x\frac{\partial\psi_n^y}{\partial z}+x\frac{\partial\psi_n^z}{\partial y}-y\frac{\partial\psi_n^z}{\partial x})$$
$$-(n+2)(y\frac{\partial\psi_{-n-1}^x}{\partial z}-z\frac{\partial\psi_{-n-1}^x}{\partial y}+z\frac{\partial\psi_{-n-1}^y}{\partial x}-x\frac{\partial\psi_{-n-1}^y}{\partial z}+x\frac{\partial\psi_{-n-1}^z}{\partial y}-y\frac{\partial\psi_{-n-1}^z}{\partial x})\big], \quad \text{(D.45)}$$

where we have used the fact that the curl of a gradient is zero.

The expressions (D.40) to (D.42) and (D.45) may be evaluated on the relevant undeformed particle surface ($r=\alpha_i$) and substituted into the reformulated boundary conditions (3.65)–(3.70), along with the relevant expressions for the fluid stress, in order to obtain the system of equations (3.71)–(3.76).

Bibliography

[1] A. Mietke, O. Otto, S. Girardo, P. Rosendahl, A. Taubenberger, S. Golfier, E. Ulbricht, S. Aland, J. Guck, and E. Fischer-Friedrich. Extracting cell stiffness from real-time deformability cytometry: Theory and experiment. *Biophysical Journal*, 109(10):2023–2036, 2015.

[2] M. M. Villone, F. Greco, M. A. Hulsen, and P. L. Maffettone. Numerical simulations of deformable particle lateral migration in tube flow of newtonian and viscoelastic media. *Journal of Non-Newtonian Fluid Mechanics*, 234:105–113, 2016. ISSN 0377-0257.

[3] T. Murata. Deformation of an elastic particle suspended in an arbitrary flow field. *Journal of the Physical Society of Japan*, 50(3):1009–1016, 1981.

[4] Y.-N. Young, Y. Mori, and M. J. Miksis. Slightly deformable Darcy drop in linear flows. *Physical Review Fluids*, 4:063601, 06 2019.

[5] National Records of Scotland. List of data tables, 2020. `https://www.nrscotland.gov.uk/statistics-and-data/statistics/statistics-by-theme/vital-events/general-publications/vital-events-reference-tables/2020/list-of-data-tables#section6`.

[6] Office for National Statistics. Deaths registered in england and wales, 2020. `https://www.ons.gov.uk/peoplepopulationandcommunity/birthsdeathsandmarriages/deaths/datasets/deathsregisteredinenglandandwalesseriesdrreferencetables`.

[7] S. Zhao, Z. Xu, H. Wang, B. E. Reese, L. V. Gushchina, M. Jiang, P. Agarwal, J. Xu, M. Zhang, R. Shen, Z. Liu, N. Weisleder, and X. He. Bioengineering of injectable encapsulated aggregates of pluripotent stem cells for therapy of myocardial infarction. *Nature communications*, 7, 2016.

[8] Y. Yang, S. Zhang, G. Jones, N. Morgan, and A. J. El Haj. Phosphorylcholine-containing polymers for use in cell encapsulation. *Artif. Cells Blood Substit. Immobil. Biotechnol.*, 32:91–104, 2004.

[9] L. Nevi, G. Carpino, D. Costantini, V. Cardinale, O. Riccioni, S. Di Matteo, F. Melandro, P. B. Berloco, L. Reid, E. Gaudio, and D. Alvaro. Hyaluronan coating improves liver engraftment of transplanted human biliary tree stem/progenitor cells. *Stem Cell Research and Therapy*, 8(68), 2017.

[10] M. C. Arno. Engineering the mammalian cell surface with synthetic polymers: Strategies and applications. *Macromolecular Rapid Communications*, 41(18): 2000302, 2020.

[11] T. T. Pham, P. L. Tran, C. D. Phung, H. T. Nguyen, C. H. Nguyen, C. S. Yong, J. O. Kim, S. Yook, and J.-H. Jeong. Surface-triggered in situ gelation for tunable conformal hydrogel coating of therapeutic cells and biomedical devices. *Advanced Functional Materials*, 31(21):2010169, 2021.

[12] A. K. Haudenschild, A. H. Hsieh, S. Kapila, and J. C. Lotz. Pressure and distortion regulate human mesenchymal stem cell gene expression. *Annals of Biomedical Bngineering*, 37:492–502, 2009.

[13] H. Zhang, A. Kay, N. R. Forsyth, K. K. Liu, and A. J. El Haj. Gene expression of single human mesenchymal stem cell in response to fluid shear. *Journal of Tissue Engineering*, 3, 2012.

[14] H. Li, A. Muhammad, and P. Norbert. Mechanosensitive channels and their functions in stem cell differentiation. *Experimental Cell Research*, 374(2):259–265, 2019. ISSN 0014-4827.

[15] B. Martinac, Y. A. Nikolaev, G. Silvani, N. Bavi, V. Romanov, Y. Nakayama, A. D. Martinac, P. Rohde, O. Bavi, and C. D. Cox. Cell membrane mechanics and mechanosensory transduction. *Current Topics in Membranes*, 86:83–141, 2020.

[16] J. Jin, R. Jaspers, G. wu, J. Korfage, J. Klein-Nulend, and A. Bakker. Shear stress modulates osteoblast cell and nucleus morphology and volume. *International Journal of Molecular Sciences*, 21:8361, 11 2020.

[17] F. M. Eroshkin and A. G. Zaraisky. Mechano-sensitive regulation of gene expression during the embryonic development. *Genesis*, 55(4):e23026, 2017.

[18] S. L. Waters, L. J. Schumacher, and A. J. El Haj. Regenerative medicine meets mathematical modelling: Developing symbiotic relationships. *npj Regenerative Medicine*, 6(1):24, 2021.

[19] C. Ashmore-Harris, E. Antonopoulou, S. M. Finney, M. R. Vieira, M. G. Hennessy, A. Muench, W.-Y. Lu, V. L. Gadd, A. J. El Haj, S. J. Forbes, and S. L. Waters. Exploiting in silico modelling to enhance translation of liver cell therapies from bench to bedside. *npj Regenerative Medicine*, 9(1):19, 2024.

[20] J. F. Butterworth, D. C. Mackey, J. D. Wasnick, G. E. Morgan, M. S. Mikhail, and G. E. Morgan. *Morgan & Mikhail's Clinical Anesthesiology*. 5. New York: McGraw-Hill, 2013.

[21] E. Yeom, Y. J. Kang, and S.-J. Lee. Changes in velocity profile according to blood viscosity in a microchannel. *Biomicrofluidics*, 8(3), 2014.

[22] K. Maezawa, R. Furushima-Shimogawara, A. Yasukawa, N. Ohta, and S. Iwanaga. Real-time observation of pathophysiological processes during murine experimental schistosoma japonicum infection using high-resolution ultrasound imaging. *Tropical Medicine and Health*, 46(1), 2018.

[23] S. Dasari, P. Weber, C. Makhloufi, E. Lopez, and C. L. Forestier. Intravital microscopy imaging of the liver following leishmania infection: An assessment of hepatic hemodynamics. *Journal of Visualized Experiments*, 101, 2015.

[24] T. Fukuda, E. Asou, K. Nogi, and K. Goto. Evaluation of mouse red blood cell and platelet counting with an automated hematology analyzer. *Journal of Vetinary Medical Science*, 79, 2017.

[25] Invitrogen. Invitrogen hepatic biology products and services, 2021. `https://tools.thermofisher.com/content/sfs/brochures/ADMEToxGoldStandard.pdf`.

[26] N. J. Yang and M. J. Hinner. Getting across the cell membrane: An overview for small molecules, peptides, and proteins. *Site-Specific Protein Labeling: Methods and Protocols*, pages 29–53, 2015.

[27] H. Ho, H. B. Yu, A. Bartlett, and P. Hunter. An in silico pipeline for subject-specific hemodynamics analysis in liver surgery planning. *Computer Methods in Biomechanics and Biomedical Engineering*, 23(4):138–142, 2020.

[28] M. Villone and P. L. Maffettone. Dynamics, rheology, and applications of elastic deformable particle suspensions: A review. *Rheologica Acta*, 58, 04 2019. doi: 10.1007/s00397-019-01134-2.

[29] M. M. Villone, J. K. Nunes, Y. Li, H. A. Stone, and P. L. Maffettone. Design of a microfluidic device for the measurement of the elastic modulus of deformable particles. *Soft Matter*, 15:880–889, 2019.

[30] Y. Chen, K. Guo, L. Jiang, S. Zhu, Z. Ni, and N. Xiang. Microfluidic deformability cytometry: A review. *Talanta*, 251:123815, 2023.

[31] K. O. Rojek, M. Cwiklinska, J. Kuczak, and J. Guzowski. Microfluidic formulation of topological hydrogels for microtissue engineering. *Chemical Reviews*, 122(22):16839–16909, 2022.

[32] C. A. Copos and R. D. Guy. A porous viscoelastic model for the cell cytoskeleton. *The ANZIAM Journal*, 59(4):472–498, 2018.

[33] I. Burova, I. Wall, and R. J. Shipley. Mathematical and computational models for bone tissue engineering in bioreactor systems. *Journal of Tissue Engineering*, 10:2041731419827922, 2019.

[34] Y. Leng, M. de Lucio, and H. Gomez. Using poro-elasticity to model the large deformation of tissue during subcutaneous injection. *Computer Methods in Applied Mechanics and Engineering*, 384:113919, 2021. ISSN 0045-7825.

[35] D. Caccavo. An overview on the mathematical modeling of hydrogels' behavior for drug delivery systems. *International Journal of Pharmaceutics*, 560:175–190, 2019.

[36] M. J. Penn and M. G. Hennessy. Optimal loading of hydrogel-based drug-delivery systems. *Applied Mathematical Modelling*, 112:649–668, 2022. ISSN 0307-904X.

[37] J. Li and D. J. Mooney. Designing hydrogels for controlled drug delivery. *Nature Reviews Materials*, 1(12):1–17, 2016.

[38] E. F. Yeo, H. Markides, A. T. Schade, A. J. Studd, J. M. Oliver, S. L. Waters, and A. J. El Haj. Experimental and mathematical modelling of magnetically labelled mesenchymal stromal cell delivery. *Journal of The Royal Society Interface*, 18(175), 2021.

[39] H. Zhang, N. H. Chen, A. El Haj, and K. K. Liu. An optical-manipulation technique for cells in physiological flows. *Journal of Biological Physics*, 36(2): 135–43, 2010.

[40] H. Brenner and J. Happel. Slow viscous flow past a sphere in a cylindrical tube. *Journal of Fluid Mechanics*, 4(2):195–213, 1958.

[41] T. Greenstein and J. Happel. Theoretical study of the slow motion of a sphere and a fluid in a cylindrical tube. *Journal of Fluid Mechanics*, 34(4):705–710, 1968.

[42] S. Leichtberg, R. Pfeffer, and S. Weinbaum. Stokes flow past finite coaxial clusters of spheres in a circular cylinder. *International Journal of Multiphase Flow*, 3(2):147 – 169, 1976. ISSN 0301-9322.

[43] S. Bhattacharya, C. Mishra, and S. Bhattacharya. Analysis of general creeping motion of a sphere inside a cylinder. *Journal of Fluid Mechanics*, 642:295–328, 2010.

[44] X. Yao, Marcos, and T. N. Wong. Slow viscous flow around two particles in a cylinder. *Microfluidics and Nanofluidics*, 21(161), 2017.

[45] P. M. Bungay and H. Brenner. The motion of a closely-fitting sphere in a fluid-filled tube. *International Journal of Multiphase Flow*, 1(1):25 – 56, 1973. ISSN 0301-9322.

[46] H. Y. Yeh and H. J. Keh. Axisymmetric creeping motion of a prolate particle in a cylindrical pore. *European Journal of Mechanics - B/Fluids*, 39:52 – 58, 2013. ISSN 0997-7546.

[47] S. Whittaker. Flow in porous media I: A theoretical derivation of Darcy's law. *Transport in Porous Media*, 1:3–25, 03 1986. ISSN 1573-1634.

[48] L. Durlofsky and J. F. Brady. Analysis of the Brinkman equation as a model for flow in porous media. *The Physics of Fluids*, 30(11):3329–3341, 11 1987. ISSN 0031-9171.

[49] B. S. Padmavathi, T. Amaranath, and S. D. Nigam. Stokes flow past a porous sphere using Brinkman's model. *Zeitschrift für Angewandte Mathematik und Physik ZAMP*, 44:929–939, 1993.

[50] S.-M. Yang and W.-H. Hong. Motions of a porous particle in Stokes flow: Part 1. Unbounded single-fluid domain problem. *Korean Journal of Chemical Engineering*, 5:23–34, 03 1988. ISSN 1975-7220.

[51] S.-M. Yang and W.-H. Hong. Motions of a porous particle in Stokes flow: Part 2. Linear flows near a fluid interface. *Korean Journal of Chemical Engineering*, 6:234–245, 07 1989. ISSN 1975-7220.

[52] S.-M. Yang and L. G. Leal. Motions of a porous particle in Stokes-flow near a plane-fluid interface. *Physiochemical hydrodynamics*, 11(4):543–569, 01 1989. ISSN 0191-9059.

[53] J. Prakash and G. P. R. Sekhar. Slow motion of a porous spherical particle with a rigid core in a spherical fluid cavity. *Meccanica*, 52:91–105, 2017.

[54] E. I. Saad and M. S. Faltas. Slow motion of a porous sphere translating along the axis of a circular cylindrical pore subject to a stress jump condition. *Transport in Porous Media*, 102:91–109, 2014.

[55] X. Yao, C. H. Ng, J. R. A. Teo, Marcos, and T. N. Wong. Slow viscous flow of two porous spherical particles translating along the axis of a cylinder. *Journal of Fluid Mechanics*, 861:643–678, 2019.

[56] G. S. Beavers and D. D. Joseph. Boundary conditions at a naturally permeable wall. *Journal of Fluid Mechanics*, 30(1):197–207, 1967.

[57] P. G. Saffman. On the boundary condition at the surface of a porous medium. *Studies in Applied Mathematics*, 50(2):93–101, 1971. ISSN 0022-2526.

[58] T. Levy and E. Sanchez-Palencia. On boundary conditions for fluid flow in porous media. *International Journal of Engineering Science*, 13(11):923–940, 1975. ISSN 0020-7225.

[59] J. A. Ochoa-Tapia and S. Whitaker. Momentum transfer at the boundary between a porous medium and a homogeneous fluid—I. Theoretical development. *International Journal of Heat and Mass Transfer*, 38(14):2635–2646, 1995. ISSN 0017-9310.

[60] M. Minale. Momentum transfer within a porous medium. II. Stress boundary condition. *Physics of Fluids*, 26(12):123102, 12 2014. ISSN 1070-6631.

[61] Z. Xu, J. Zhang, Y.-N. Young, P. Yue, and J. J. Feng. Comparison of four boundary conditions for the fluid-hydrogel interface. *Physical Review Fluids*, 7, Sep 2022.

[62] R. Ruiz-Baier, M. Taffetani, H. D. Westermeyer, and I. Yotov. The Biot–Stokes coupling using total pressure: Formulation, analysis and application to interfacial flow in the eye. *Computer Methods in Applied Mechanics and Engineering*, 389, 2022. ISSN 0045-7825.

[63] S. Badia, A. Quaini, and A. Quarteroni. Coupling Biot and Navier–Stokes equations for modelling fluid–poroelastic media interaction. *Journal of Computational Physics*, 228(21):7986–8014, 2009. ISSN 0021-9991.

[64] M. A. Biot. General theory of three-dimensional consolidation. *Journal of Applied Physics*, 12(2):155–164, 04 1941.

[65] M. A. Biot. Nonlinear and semilinear rheology of porous solids. *Journal of Geophysical Research*, 78(23):4924–4937, 1973.

[66] C. S. Peskin. The immersed boundary method. *Acta Numerica*, 11:479–517, 2002.

[67] W. Strychalski, C. A. Copos, O. L. Lewis, and R. D. Guy. A poroelastic immersed boundary method with applications to cell biology. *Journal of Computational Physics*, 282:77–97, 2015. ISSN 0021-9991.

[68] L. Li, J. Zhang, Z. Xu, Y.-N. Young, J. J. Feng, and P. Yue. An arbitrary Lagrangian-Eulerian method for simulating interfacial dynamics between a hydrogel and a fluid. *Journal of Computational Physics*, 451, 2022. ISSN 0021-9991.

[69] B. Nasouri, A. Khot, and G. J. Elfring. Elastic two-sphere swimmer in Stokes flow. *Physical Review Fluids*, 2, Apr 2017.

[70] T. Murata. On the deformation of an elastic particle falling in a viscous fluid. *Journal of the Physical Society of Japan*, 48(5):1738–1745, 1980.

[71] M. Mokbel, D. Mokbel, A. Mietke, N. Traber, S. Girardo, O. Otto, J. Guck, and S. Aland. Numerical simulation of real-time deformability cytometry to extract cell mechanical properties. *ACS Biomaterials Science & Engineering*, 3 (11):2962–2973, 2017.

[72] I. Noichl and C. Schönecker. Dynamics of elastic, nonheavy spheres sedimenting in a rectangular duct. *Soft Matter*, 18(12):2462–2472, 2022.

[73] J. M. Barakat, S. M. Ahmmed, S. A. Vanapalli, and E. S. G. Shaqfeh. Pressure-driven flow of a vesicle through a square microchannel. *Journal of Fluid Mechanics*, 861:447–483, 2019.

[74] E. M. Darling, M. Topel, S. Zauscher, T. P. Vail, and F. Guilak. Viscoelastic properties of human mesenchymally-derived stem cells and primary osteoblasts, chondrocytes, and adipocytes. *Journal of Biomechanics*, 41(2):454–464, 2008.

[75] L. Zhu, J. Barber, R. Zigon, S. Na, and H. Yokota. Modeling and simulation of interstitial fluid flow around an osteocyte in a lacuno-canalicular network. *Physics of Fluids*, 34(4), 2022.

[76] M. Ju, S. S. Ye, B. Namgung, S. Cho, H. T. Low, H. L. Leo, and S. Kim. A review of numerical methods for red blood cell flow simulation. *Computer Methods in Biomechanics and Biomedical Engineering*, 18(2):130–140, 2015.

[77] E. Häner, M. Heil, and A. Juel. Deformation and sorting of capsules in a T-junction. *Journal of Fluid Mechanics*, 885:A4, 2020.

[78] D. Barthès-Biesel. Motion and deformation of elastic capsules and vesicles in flow. *Annual Review of Fluid Mechanics*, 48(1):25–52, 2016.

[79] T. M. Geislinger and T. Franke. Hydrodynamic lift of vesicles and red blood cells in flow – from Fåhræus & Lindqvist to microfluidic cell sorting. *Advances in Colloid and Interface Science*, 208:161–176, 2014. ISSN 0001-8686. Special issue in honour of Wolfgang Helfrich.

[80] S. R. Hodges and O. E. Jensen. Spreading and peeling dynamics in a model of cell adhesion. *Journal of Fluid Mechanics*, 460:381–409, 2002.

[81] D. Barthès-Biesel and J. M. Rallison. The time-dependent deformation of a capsule freely suspended in a linear shear flow. *Journal of Fluid Mechanics*, 113:251–267, 1981.

[82] P. M. Vlahovska, Y. N. Young, G. Danker, and C. Misbah. Dynamics of a non-spherical microcapsule with incompressible interface in shear flow. *Journal of Fluid Mechanics*, 678:221–247, 2011.

[83] C. Quéguiner and D. Barthès-Biesel. Axisymmetric motion of capsules through cylindrical channels. *Journal of Fluid Mechanics*, 348:349–376, 1997.

[84] X.-Q. Hu, A.-V. Salsac, and D. Barthès-Biesel. Flow of a spherical capsule in a pore with circular or square cross-section. *Journal of Fluid Mechanics*, 705: 176–194, 2012.

[85] C. Schaaf and H. Stark. Inertial migration and axial control of deformable capsules. *Soft Matter*, 13:3544–3555, 2017.

[86] J. M. Barakat and E. S. G. Shaqfeh. The steady motion of a closely fitting vesicle in a tube. *Journal of Fluid Mechanics*, 835:721–761, 2018.

[87] J. M. Barakat and E. S. G. Shaqfeh. Stokes flow of vesicles in a circular tube. *Journal of Fluid Mechanics*, 851:606–635, 2018.

[88] D. R. Gossett, W. M. Weaver, A. J. Mach, S. C. Hur, H. T. K. Tse, W. Lee, H. Amini, and D. Di Carlo. Label-free cell separation and sorting in microfluidic systems. *Analytical and Bioanalytical Chemistry*, 397:3249–3267, 2010.

[89] Q. Guo, S. P. Duffy, K. Matthews, X. Deng, A. T. Santoso, E. Islamzada, and H. Ma. Deformability based sorting of red blood cells improves diagnostic sensitivity for malaria caused by *Plasmodium Falciparum*. *Lab on a Chip*, 16 (4):645–654, 2016.

[90] E. Häner, D. Vesperini, A.-V. Salsac, A. Le Goff, and A. Juel. Sorting of capsules according to their stiffness: From principle to application. *Soft Matter*, 17(13): 3722–3732, 2021.

[91] M. M. Villone, M. Trofa, M. A. Hulsen, and P. L. Maffettone. Numerical design of a t-shaped microfluidic device for deformability-based separation of elastic capsules and soft beads. *Physical Review E*, 96(5):053103, 2017.

[92] Z. Wang, Y. Sui, A.-V. Salsac, D. Barthès-Biesel, and W. Wang. Motion of a spherical capsule in branched tube flow with finite inertia. *Journal of Fluid Mechanics*, 806:603–626, 2016.

[93] Z. Wang, Y. Sui, A.-V. Salsac, D. Barthès-Biesel, and W. Wang. Path selection of a spherical capsule in a microfluidic branched channel: Towards the design of an enrichment device. *Journal of Fluid Mechanics*, 849:136–162, 2018.

[94] N. Grosjean, D. Iliev, O. Iliev, R. Kirsch, Z. Lakdawala, M. Lance, M. Michard, and A. Mikelić. Experimental and numerical study of the interaction between fluid flow and filtering media on the macroscopic scale. *Separation and Purification Technology*, 156:22–27, 2015.

[95] L. Yeghiazarian, K. Pillai, and R. Rosati. Thin porous media. *Transport in Porous Media*, 115:407–410, 2016.

[96] L. A. Taber and A. M. Puleo. Poroelastic plate and shell theories. In *Mechanics of Poroelastic Media*, pages 323–337. Springer, 1996.

[97] A. Mikelić and J. Tambača. Derivation of a poroelastic flexural shell model. *Multiscale modeling & Simulation*, 14(1):364–397, 2016.

[98] A. Mikelić and J. Tambača. Derivation of a poroelastic elliptic membrane shell model. *Applicable Analysis*, 98(1-2):136–161, 2019.

[99] S. Weinbaum, J. M. Tarbell, and E. R. Damiano. The structure and function of the endothelial glycocalyx layer. *Annual Review of Biomedical Engineering*, 9(1):121–167, 2007.

[100] T. W. Secomb, R. Hsu, and A. R. Pries. Motion of red blood cells in a capillary with an endothelial surface layer: Effect of flow velocity. *American Journal of Physiology-Heart and Circulatory Physiology*, 281(2):H629–H636, 2001.

[101] E. R. Damiano, B. R. Duling, K. Ley, and T. C. Skalak. Axisymmetric pressure-driven flow of rigid pellets through a cylindrical tube lined with a deformable porous wall layer. *Journal of Fluid Mechanics*, 314:163–189, 1996.

[102] W. Wang and K. H. Parker. The effect of deformable porous surface layers on the motion of a sphere in a narrow cylindrical tube. *Journal of Fluid Mechanics*, 283:287–305, 1995.

[103] W. L. Haberman. Motion of rigid and fluid spheres in stationary and moving liquids inside cylindrical tubes. *David Taylor Model Basin Report*, 1958.

[104] S. Wakiya. A spherical obstacle in the flow of a viscous fluid through a tube. *Journal of the Physical Society of Japan*, 8(2):254–256, 1953.

[105] J. Happel and B. Byrne. Correction-" motion of a sphere and fluid in a cylindrical tube". *Industrial & Engineering Chemistry*, 49(6):1029–1029, 1957.

[106] P. H. Wen, M. H. Aliabadi, and W. Wang. Movement of a spherical cell in capillaries using a boundary element method. *Journal of Biomechanics*, 40(8): 1786 – 1793, 2007. ISSN 0021-9290.

[107] J. Happel and H. Brenner. *Low Reynolds Number Hydrodynamics*. Number 1 in 5. Kluwer Academic Publishers, 1991.

[108] H. Masoud and H. A. Stone. The reciprocal theorem in fluid dynamics and transport phenomena. *Journal of Fluid Mechanics*, 879:P1, 2019.

[109] M. S. Alnaes, J. Blechta, J. Hake, A. Johansson, B. Kehlet, A. Logg, C. Richardson, J. Ring, M. E. Rognes, and G. N. Wells. The FEniCS project version 1.5. *Archive of Numerical Software*, 3, 2015. doi: 10.11588/ans.2015.100.20553.

[110] A. Logg, K. A. Mardal, and G. N. Wells. *Automated Solution of Differential Equations by the Finite Element Method*. Springer, 2012.

[111] F. Ballarin. Multiphenics – easy prototyping of multiphysics problems in FEniCS, 2022. `https://mathlab.sissa.it/multiphenics`.

[112] C. Geuzaine and J.-F. Remacle. Gmsh, 2022. `http://gmsh.info/`.

[113] A. S. Slyngstad. Verification and validation of a monolithic fluid-structure interaction solver in fenics. a comparison of mesh lifting operators. 2017. URL `https://api.semanticscholar.org/CorpusID:59394873`.

[114] M. Z. Wang, B. X. Xu, and C. F. Gao. Recent General Solutions in Linear Elasticity and Their Applications. *Applied Mechanics Reviews*, 61(3):030803, 05 2008. ISSN 0003-6900.

[115] P. Howell, G. Kozyreff, and J. Ockendon. *Applied Solid Mechanics*. Cambridge Texts in Applied Mathematics. Cambridge University Press, 2008.

[116] D. Weisz-Patrault, S. Bock, and K. Gürlebeck. Three-dimensional elasticity based on quaternion-valued potentials. *International Journal of Solids and Structures*, 51(19):3422–3430, 2014. ISSN 0020-7683.

[117] S. R. Atashipour and P. D. Folkow. On the complete solution of the three-dimensional solid space problems based on a novel curvilinear elasticity representation. *European Journal of Mechanics - A/Solids*, 97:104860, 2023. ISSN 0997-7538.

[118] P. F. Papkovich. Solution générale des équations differentielles fondamentales d'élasticité exprimée par trois fonctions harmoniques. *Comptes rendus de l'Acadé'mie des Sciences*, 195(3):513–515, 1932.

[119] H. V. Neuber. Ein neuer ansatz zur lösung räumlicher probleme der elastizitätstheorie. der hohlkegel unter einzellast als beispiel. *ZAMM-Journal of Applied Mathematics and Mechanics/Zeitschrift für Angewandte Mathematik und Mechanik*, 14(4):203–212, 1934.

[120] M. Stippes. Completeness of the papkovich potentials. *Quarterly of Applied Mathematics*, 26(4):477–483, 1969.

[121] T. Tran-Cong. On the completeness of the papkovich-neuber solution. *Quarterly of Applied Mathematics*, 47(4):645–659, 1989.

[122] K. Hackl and U. Zastrow. On the existence, uniqueness and completeness of displacements and stress functions in linear elasticity. *Journal of Elasticity*, 19: 3–23, 1988.

[123] S. Bock. On monogenic series expansions with applications to linear elasticity. *Advances in Applied Clifford Algebras*, 24(4):831–943, 2014. ISSN 1661-4909.

[124] H. Lamb. *Hydrodynamics*. Dover, New York Publications, 6 edition, 1945.

[125] C. W. MacMinn, E. R. Dufresne, and J. S. Wettlaufer. Large deformations of a soft porous material. *Physical Review Applied*, 5:044020, Apr 2016.

[126] L. D. Landau, L. P. Pitaevskii, A. M. Kosevich, and E. M. Lifshitz. *Theory of Elasticity*, volume 7. Elsevier, 2012.

[127] F. Y. M. Wan. Membrane and bending stresses in shallow spherical shells. *International Journal of Solids and Structures*, 3(3):353–366, 1967.

[128] E. Reissner. A note on membrane and bending stresses in spherical shells. *Journal of the Society for Industrial and Applied Mathematics*, 4(4):230–240, 1956. ISSN 03684245.

[129] M. E. Carr Jr and N. M. Hadler. Permeability of hyaluronic acid solutions. *Arthritis & Rheumatism: Official Journal of the American College of Rheumatology*, 23(12):1371–1375, 1980.

[130] S. H. Gehrke, J. P. Fisher, M. Palasis, and M. E. Lund. Factors determining hydrogel permeability. *Annals of the New York Academy of Sciences*, 831:179–207, 1997.

[131] M. B. Łabowska, K. Cierluk, A. M. Jankowska, J. Kulbacka, J. Detyna, and I. Michalak. A review on the adaption of alginate-gelatin hydrogels for 3d cultures and bioprinting. *Materials*, 14(4):858, 2021.

[132] S. Henon, G. Lenormand, A. Richert, and F. Gallet. A new determination of the shear modulus of the human erythrocyte membrane using optical tweezers. *Biophysical Journal*, 76(2):1145–1151, 1999.

[133] T. M. J. Evers, V. Sheikhhassani, H. Tang, M. C. Haks, T. H. M. Ottenhoff, and A. Mashaghi. Single-cell mechanical characterization of human macrophages. *Advanced NanoBiomed Research*, 2(7):2100133, 2022.

[134] T. Xia, R. Zhao, W. Liu, Q. Huang, P. Chen, Y. N. Waju, M. K. Al-ani, Y. Lv, and L. Yang. Effect of substrate stiffness on hepatocyte migration and cellular young's modulus. *Journal of Cellular Physiology*, 233(9):6996–7006, 2018.

[135] E. Reissner. On asymptotic solutions for nonsymmetric deformations of shallow shells of revolution. *International Journal of Engineering Science*, 2(1):27–43, 1964.

[136] S. M. Finney, M. G. Hennessy, A. Münch, and S. L. Waters. The impact of confinement on the deformation of an elastic particle under axisymmetric tube flow. *IMA Journal of Applied Mathematics*, 89(3):498–532, 09 2024.

[137] R. X. Lu, Z. Wang, A.-V. Salsac, D. Barthès-Biesel, W. Wang, and Y. Sui. Path selection of a train of spherical capsules in a branched microchannel. *Journal of Fluid Mechanics*, 923:A11, 2021.

[138] E. F. Yeo, H. Markides, A. T. Schade, A. J. Studd, J. M. Oliver, S. L. Waters, and A. J. El Haj. Experimental and mathematical modelling of magnetically labelled mesenchymal stromal cell delivery. *Journal of the Royal Society Interface*, 18(175):20200558, 2021.

[139] M. Moradi, W. Shi, and E. Nazockdast. General solutions of linear poro-viscoelastic materials in spherical coordinates. *Journal of Fluid Mechanics*, 946:A22, 2022.

[140] S. N. Atluri and A. Cazzani. Rotations in computational solid mechanics. *Archives of Computational Methods in Engineering*, 2:49–138, 1995.